

Efficient Water Oxidation: Nanostructured Titanium Oxides vs. Iron-Group Metal Electrodeposited GaAs

A Dissertation Presented to
the Faculty of the School of Engineering and Applied Science

In Partial Fulfillment of the Requirements for the Degree:

Doctor of Philosophy

By

Yin Xu

May 2021

APPROVAL SHEET

This
Dissertation
is submitted in partial fulfillment of the requirements
for the degree of
Doctor of Philosophy

Author: *Yin Xia*

This Dissertation has been read and approved by the examining committee:

Advisor: Giovanni Zangari

Advisor:

Committee Member: Robert Kelly

Committee Member: Stephen McDonnell

Committee Member: Petra Reinke

Committee Member: Joshua Choi

Committee Member:

Committee Member:

Accepted for the School of Engineering and Applied Science:



Craig H. Benson, School of Engineering and Applied Science

May 2021

Table of Contents

ABSTRACT	5
Chapter 1-Introduction	7
1.1 Hydrogen generation by water splitting.....	7
1.2 Photoelectrochemistry for energy conversion/storage	8
1.3 TiO ₂ based materials for solar water oxidation.....	9
1.4 Electrochemical anodic TiO ₂ nanotube arrays	11
1.5 Single crystal semiconductors as photoanodes	17
1.6 Motivation of the study	18
Chapter 2-Materials and methods	21
2.1 Anodization of TiO ₂ nanotube arrays	21
2.2 Various modification approaches of TiO ₂ NTs.....	22
2.3 Electrodeposition of metal on GaAs substrate	24
2.4 Characterization methods.....	25
2.5 Electrochemical/photoelectrochemical analysis	27
Chapter 3-Surface laser modification of TiO₂ nanotube arrays	35
3.1 Morphology and crystallinity changes induced by laser.....	35
3.2 Optimizing the laser energy fluence, PPA and length of the nanotube arrays towards photo water oxidation	41
3.3 Selectivity of surface water oxidation reaction.....	47
3.4 Conclusions.....	48
Chapter 4-Formation of TiO₂ sub-stoichiometries via hydrogen treatment	50
4.1 Morphology and phase changes induced by thermal reduction	51
4.2 Crystal structure and phase analysis by Rietveld refinement.....	56
4.3 Photoelectrochemical properties of TiO ₂ sub-stoichiometries.....	61
4.4 Water oxidation kinetics at the interface for TiO ₂ sub-stoichiometries	69
4.5 Thermal reduction vs. electrochemical reduction	70
4.6 Conclusions.....	74
Chapter 5-Introducing Ti³⁺/oxygen vacancies into TiO₂ nanotube arrays	77
5.1 Ti ³⁺ /oxygen vacancies introduced by Ar/NH ₃ thermal treatment	78
5.2 photoelectrochemical properties of Ar/NH ₃ modified TiO ₂ NTs.....	82
5.3 Stability of Ar/NH ₃ modified TiO ₂ NTs	90
5.4 Conclusions.....	92
Chapter 6-Improving surface oxidation kinetics with electrocatalysts by electrodeposition	94

6.1 Electrodeposition of porous Ni-Fe oxy-hydroxide catalysts.....	95
6.2 Growth of NiFeOH _x on the tops of regular anodic TiO ₂ nanotubes.....	98
6.3 Deposition of NiFeOH _x on the external walls of long large-gap TiO ₂ nanotubes.....	100
6.4 Growth of NiFeOH _x on the short large-gap TiO ₂ nanotubes.....	105
6.5 Conclusions.....	108
Chapter 7-Electrodeposition of Ni on GaAs through self-limiting electrodeposition	110
7.1 Self-limiting electrodeposition of continuous Ni thin film on GaAs	111
7.2 Self-limiting electrodeposition of discontinuous Ni nanoislands on GaAs	123
7.3 Conclusions.....	128
Chapter 8-Electrodeposition of binary/ternary Iron-group metal thin-film on GaAs through self-limiting electrodeposition	130
8.1 Self-limiting deposition of binary Iron-group alloys (Ni-Co and Ni-Fe).....	130
8.2 Electrochemical/photoelectrochemical water oxidation on binary Iron-group alloys	136
8.3 Self-limiting deposition of ternary Iron-group alloys (Ni-Co-Fe)	139
8.4 Electrochemical/photoelectrochemical water oxidation on ternary Iron-group alloys	143
8.5 Conclusions.....	146
Chapter 9-Conclusions and future work	147
9.1 Conclusions.....	147
9.2 Future work.....	150
Acknowledgements	153
Reference	155

ABSTRACT

Photoelectrochemical water splitting consists in the conversion of solar energy into chemical energy in the form of the hydrogen bond and simultaneously overcomes the intrinsic limitation of the intermittent property of the sunlight, allowing to provide energy in form of electricity reliably and continuously. Titanium oxide-based materials (such as TiO_2) and single crystal semiconductors (such as Si or GaAs) are among the most attractive photoanode candidates for efficient water oxidation. TiO_2 materials unfortunately suffer from the limited absorption of the solar spectrum, the poor charge transfer and the slow surface kinetics, while displaying a high stability and low cost. Si or GaAs in contrast have an ideal bandgap to maximize light absorption, but cannot be directly used as photoanodes, due to their limited stability and their susceptibility to photocorrosion, thus requiring a protective layer to enhance its functionality.

In the first part of the dissertation, we aim to investigate and improve the performance of titanium oxide nanomaterials by exploring (i) the generation of Ti^{3+} /oxygen vacancies by ammonia treatment, (ii) TiO_{2-x} sub-stoichiometries formation *via* extensive generation of oxygen vacancies and (iii) surface modification methods in order to widen the light absorption spectrum, improve charge transfer properties and increase interfacial water oxidation selectivity; finally efforts will be devoted to improve and optimize the various existing modification approaches simultaneously. The findings prove that there exists an optimum amount of oxygen deficiencies in TiO_{2-x} that maximizes the photoelectrochemical performance in the form of a well-defined concentration of point defects in the anatase phase of TiO_2 ; furthermore, surface modification with suitable water oxidation catalysts allows further improvement of the photoelectrochemical performance by accelerating the surface water oxidation kinetics, while minimizing the impact on the photo-

transmittance; the optimization of the photoelectrochemical properties is a synergic effect of increasing the light absorption, reducing the surface recombination and improving the conductivity in the bulk. Various modification methods on TiO₂ nanotube system were implemented to control the density of defects through oxygen removal; these include laser surface modification, introduction of Ti³⁺ by Ar/NH₃ treatment, high-temperature thermal hydrogen reduction and electrodeposition of water oxidation catalysts. The stability of anatase TiO₂ with nanotubular morphology is determined and various possible phase transformations of this materials are investigated. The density/types of the defects created were evaluated and quantified by using photoelectrochemical characterization, together with electrochemical analytical methods.

In the second part of the dissertation, we focus on investigating an electrodeposition method showing a self-limiting growth mechanism, in order to deposit Ni ultrathin film/nanoparticles on GaAs substrates. In addition, we extend the method to electrodeposit binary/ternary alloys following the same deposition behavior. We prove that the self-limiting deposition condition can be achieved for not only Ni layers, but also for other Iron-group mutual alloys such as Ni-Co, Ni-Fe and Ni-Fe-Co; the protective Ni layer allows an improved stability and surface water oxidation kinetics in an aqueous solution under photoelectrochemical measurements; the stability of this system can be further improved by adding a second or a third Iron-group element such as Co or Fe. Characterization methods including potential transient, XPS spectra and XPS depth profile, HR-TEM were applied to verify the self-limiting mechanism and to determine the thickness of the deposited protective layer. Photoelectrochemical and electrochemical characterization were used to evaluate the functionality of the metal-deposited GaAs as a photoanode candidate toward water oxidation and its performance.

Chapter 1-Introduction

1.1 Hydrogen generation by water splitting

Since the industrial revolution, fossil fuels have been dominating the global energy landscape despite the increasing concerns on the rapid depletion and the effect of the carbon dioxide emission on the earth's climate.¹ Since 1970s, sustainable energy, such as wind, solar and biomass, has increasingly attracted attention and various breakthroughs were made, stimulating scientists from various fields and developing novel concepts and devices, such as electrochemical energy conversion and solar cells.² Energy storage and the integration into the power grid system, however, hinders the implementation of these intermittent energy sources, as this requires complex control methods, modeling and identification of suitable technological processes.³ An appealing way to ensure continuity of energy supply is the conversion of electrical energy to chemical bonds of hydrogen gas via electrochemical or photoelectrochemical water splitting by renewable electricity or directly sunlight,⁴⁻⁶ owed to the relatively high gravimetric energy density and low greenhouse gas footprint of molecular hydrogen.^{7,8} In this scenario, many research interests focus on the well-known water splitting reaction. This process may be conceptually divided into two half-cell reactions: the oxygen evolution reaction (OER, $2H_2O \rightarrow 4H^+ + 4e^- + O_2 \uparrow$) and the hydrogen evolution reaction (HER, $2H^+ + 2e^- \rightarrow H_2 \uparrow$), either of which needs an appropriate catalyst to reduce the large overpotential barrier in order to accelerate the electrochemical kinetics. Compared with HER, catalysis of the OER requires four proton-coupled electron transfer to carry out this process and implement oxygen-oxygen bond formation, a more complicated and extremely more difficult with respect to kinetic rates.⁹ Conventional electrochemical cells for water splitting usually use electrocatalysts such as IrO_2 , RuO_2 , Ni oxides, etc., to minimize the overpotential and Tafel slope

in order to optimize the energy conversion efficiency.¹⁰ However, the onset potential at an electrocatalyst is always above the theoretical redox potential of water oxidation (1.23V vs. RHE) due to the thermodynamical energy barriers of this electrochemical reaction. Photoelectrochemical (PEC) cells on the other hand, utilizing both electrical energy and solar energy, are able to generate large photovoltages and significantly reduce the onset potential of water oxidation even below the limit of electrochemical cells, such that it lowers the electrical energy required to overcome the energy barrier for oxygen evolution.¹¹

1.2 Photoelectrochemistry for energy conversion/storage

It has been demonstrated through many efforts that PEC water splitting is among the most promising approaches to generate hydrogen directly from the solar irradiation.¹¹⁻¹³ This reaction typically involves three steps: (i) light absorption in a semiconductor followed by separation of photo-generated electron/hole pairs; (ii) transfer of the charge carriers either to the liquid/solid interface or to the external circuit; (iii) water splitting reaction by the charge carriers reaching the interface. Semiconductors are required to perform as the photo-electrodes in order to absorb photons to generate electron-hole pairs that can be further separated by electric fields. The energetic of this process is governed by the band edge positions of the semiconductor and the redox potential of the solution species. For an n-type semiconductor, the valence band edge is required to be below the OER potential, while a p-type semiconductor should have a conduction band above the HER potential. An electric field generated by band bending at the interface is present at the solid/liquid interface at equilibrium and a depletion region is created as shown in Figure 1.1. The holes (or electrons) drift to the interface and inject into water molecules (or protons) to carry out the OER (or HER). The other type of charge carriers spontaneously transfer to the other electrode to complete the overall reaction. The implementation of PEC cell for water splitting was first

demonstrated out by Fujishima and Honda in 1972, using TiO₂ as photoanode and platinum as cathode.¹⁴ TiO₂ based materials then became one of the most extensively studied candidates for high-efficient PEC cells ever since.

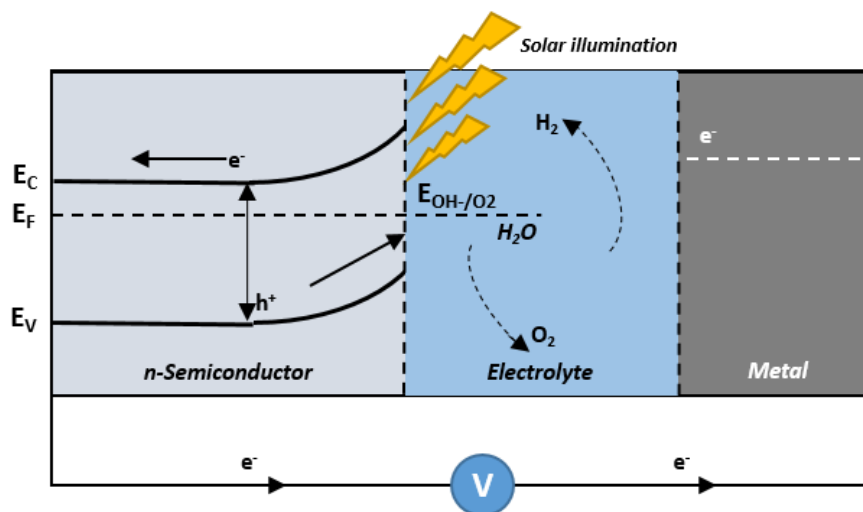


Figure 1.1 A typical PEC cell with n-semiconductor under light as the photoanode and metal as the cathode. Oxygen evolution occurs at the semiconductor/electrolyte interface under illumination.

1.3 TiO₂ based materials for solar water oxidation

Since the first reported photoelectrochemical water splitting on the TiO₂ surface, TiO₂ has been extensively investigated as a potential photoanode in the past decades.¹⁴ Typically as an n-type semiconductor, TiO₂ operates mainly as the UV-light absorber, which generates electron-hole pairs under irradiation and makes the photogenerated holes available at the solid/liquid interface to conduct water oxidation. TiO₂ is a main research focus in this field thanks to its high resistance to photocorrosion in strong alkaline solutions, low cost as an earth-abundant metal oxide and lack of toxicity. TiO₂ is well known to exhibit three main distinct crystal phases: anatase (tetragonal), rutile (tetragonal) and brookite (orthorhombic). The conventional unit cells for anatase, rutile and

brookite phase TiO_2 are shown in figure 1.2 (a). It has been demonstrated that the first two phases, especially anatase, exhibit photocatalytic activity towards water oxidation.¹⁵⁻¹⁸

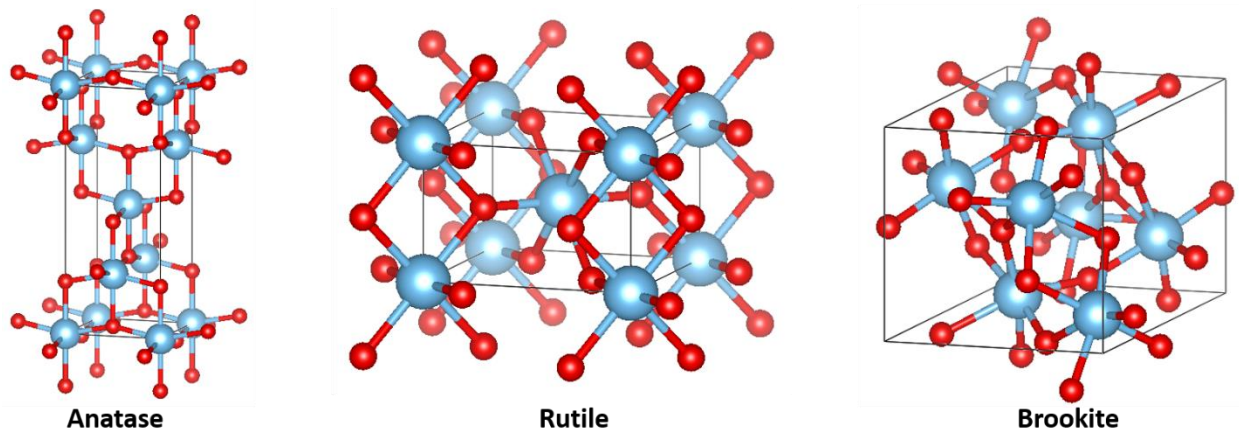


Figure 1.2 A conventional unit cell for Anatase, Rutile and Brookite TiO_2 .

The major drawback of TiO_2 is the relatively wide band gap of 3.0 eV (rutile) or 3.2 eV (anatase), limiting the light absorption to only the UV region of the solar spectrum, such that only 3-5% of the available photons can be captured, leading to the maximum conversion efficiency of 1.7%, as shown in Figure 1.3.¹⁹ The short minority charge carrier mean free path caused by defects known as trap states,²⁰ and the slow water oxidation kinetics at the electrode/electrolyte interface significantly reduce the amount of photogenerated holes that can reach the surface of TiO_2 to implement water oxidation. Furthermore, the sluggish charge transfer in the bulk material facilitates the recombination and leads to a short life time of the photogenerated electron/hole pairs. Based on these limitations, various efforts have been devoted to overcome the known limitations, mainly including i) fabricating nanostructures to increase the charge transfer and decrease the bulk recombination; ii) extrinsic metal/anion doping or introducing oxygen vacancies/ Ti^{3+} to modify

the band structure to improve the optical absorption; iii) surface modification to reduce the interfacial recombination and improve the water oxidation kinetics.

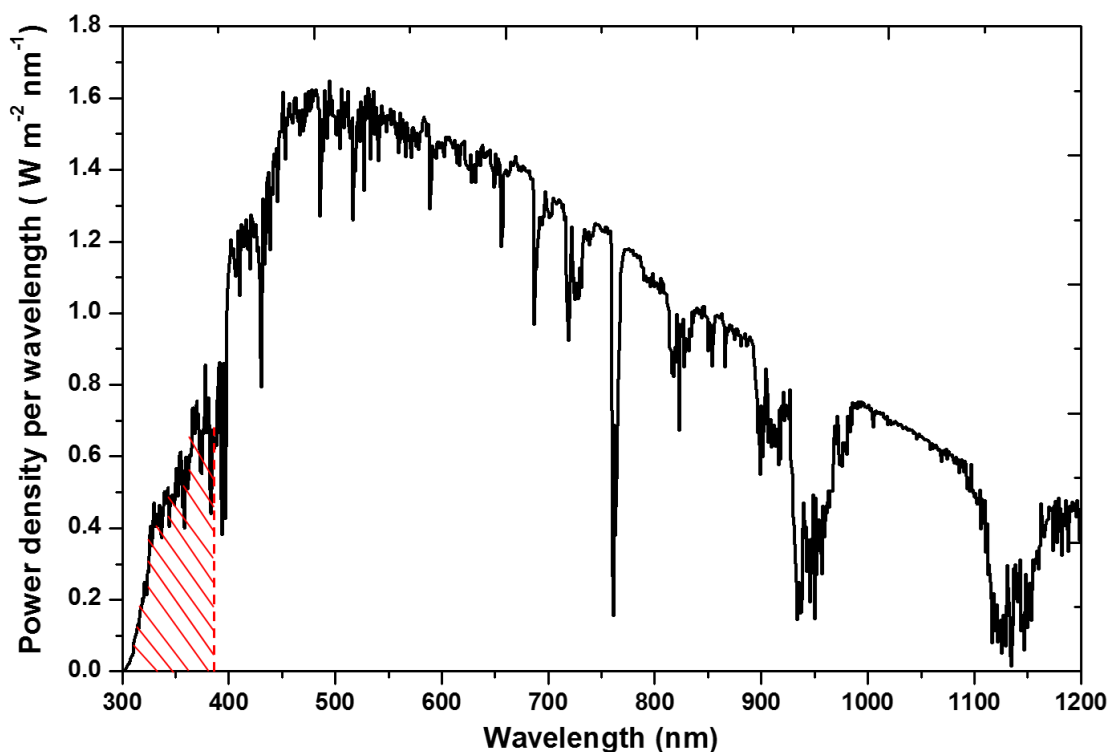


Figure 1.3 ASTM G173-03 reference spectra derived from SMARTS v.2.9.2 (global tilt, AM 1.5) as a function of wavelength. Anatase TiO₂ only absorbs photons with a wavelength less than ~387 nm as marked out in red.

1.4 Electrochemical anodic TiO₂ nanotube arrays

Synthesis of 1D TiO₂ nanotubular structures by electrochemical anodization of metal/alloy planar titanium foil is now considered to be one of the most cost-effective and versatile approaches to generate TiO₂ nanostructure as it can be tailored in terms of morphology, diameter of the pore

sizes, and length of the nanotubes by simply controlling the anodization parameters.¹² Initially, anodization of Ti foil in common acidic electrolyte usually only generates dense TiO₂ layers on the surface and cannot form porous structure. An appropriate balance between Ti dissolution condition (Ti to Ti⁴⁺ or [TiF₆]²⁻) and oxide layer growth is required in order to obtain tubular morphology. The growth process of TiO₂ NTs often entails the following: i) initial compact layer of TiO₂ is formed on Ti foil under high applied potential; ii) the as-formed oxide layer is attacked by the F⁻ ions. [TiF₆]²⁻ ions are generated and then injected into the electrolyte, meanwhile oxidation propagates further into the substrate; iii) relatively disorganized porous layer is formed with shadow gaps filled in due to the etching of the F⁻ ions ; iv) with the increasing of anodization time, the interior of the layer is dissolved and separated tubes are formed; v) the length of the tubes will increase according to the reaction time until the nanotube structure collapse.²¹ The ordering of the nanotube arrays is owed to the fact that the metal-oxide interface motion is regulated by the ionic migration and the stress-driven interface diffusion.^{22,23} This process is also displayed in the schematics in Figure 1.4.

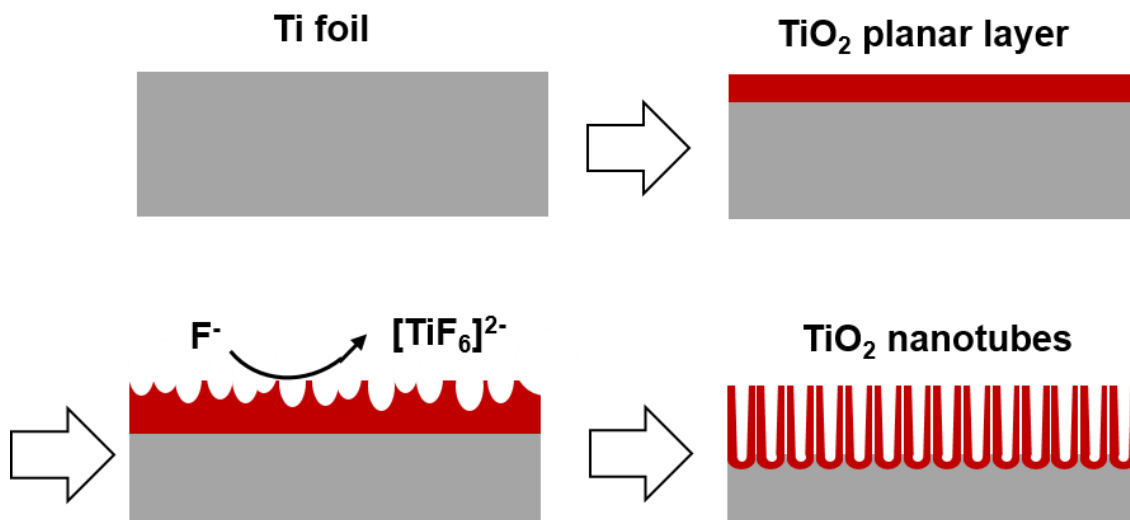


Figure 1.4 Schematics of the formation of anodized self-ordered TiO₂ nanotubes.

Aqueous electrolyte containing HF is able to generate TiO₂ nanotubes with relatively irregular shapes and a maximum thickness of 500 nm,²⁴ while KF or NaF based solution can extend the length of the NTs to several microns.^{25,26} Formation of TiO₂ NTs in organic solutions such as ethyl glycol or glycerol with low water content and ammonia fluoride (NH₄F) is now demonstrated to be an effective approach to generate well ordered TiO₂ nanotube arrays with a thickness up to several hundreds of microns due to the reduced etching rate.²⁷ In this dissertation, all the pristine TiO₂ nanotube arrays are prepared using ethyl glycol electrolyte containing ammonia fluoride unless otherwise mentioned. The as-grown TiO₂ NTs through anodization is typically amorphous and thus requires annealing to form crystalline phases such as anatase or rutile, and to increase the mechanical stability simultaneously. An annealing temperature of 350-400°C in air is found to be optimum to fabricate anatase TiO₂ in terms of charge transfer.²⁸ SEM images showing the top view and the cross section of the anodic TiO₂ nanotubes prepared using the anodization-annealing method are displayed in figure 1.5. In addition to the improved 1D charge transport property, inherent n-type doping and large surface area geometry compared to planar TiO₂ are achieved. Most importantly, the NTs structure also benefits from a short distance between the sites of water oxidation and the solution species such that all the photogenerated charge carriers are within diffusion length of ~100 nm.²⁵ However, TiO₂ NTs still suffer from its limitations, as previously mentioned.

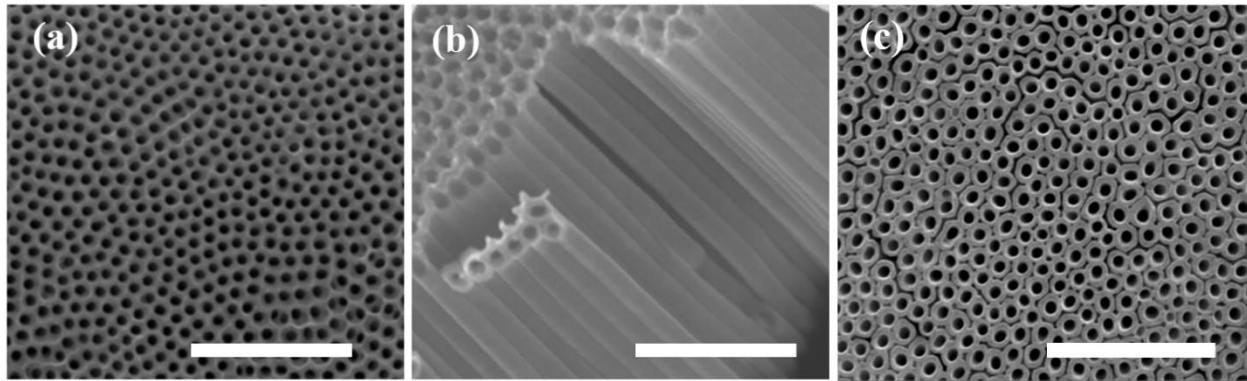


Figure 1.5 SEM images of anodic nanotube arrays (a) top view; (b) cross-section and (c) top view after removal of surface layer by Ar^+ sputtering.

Ti 3d and O 2p states are the relevant energy levels that form the edges of the conduction band and valence band respectively, and define the bandgap for TiO_2 materials.²⁹ Electronic and optical properties of TiO_2 strongly depend both on the bulk and most importantly to surface defects, and particularly on the formation, presence and concentration of bulk or surface Ti^{3+} states and oxygen vacancies (V_o).³⁰ The large bandgap of TiO_2 -based materials could be narrowed by introducing intrinsic defects such as oxygen vacancies and Ti^{3+} . These defects are usually present in small amount in the nanotube structures due to slightly Ti rich stoichiometry caused by the anodization condition while relatively large amount of these defects can be generated via proper chemical/electrochemical reduction methods.^{31,32} These defects are critical in understanding and enhancing the electrical/optical properties of TiO_2 . The typical point defects that commonly exist in TiO_2 based materials are summarized and the corresponding energy levels with respect to the conduction band or valence band of TiO_2 are displayed schematically in Figure 1.6. The unsaturated surface species such as Ti^{3+} , Ti^{2+} or even Ti^+ can be generated under high-vacuum, unreactive gases (Ar or N_2) or by generating reducing atmospheres using annealing under condition (H_2 or NH_3), where TiO_2 tend to split off O_2 or H_2O from the product and form bridge

oxygen and reduced Ti states.²⁹ During relatively long time annealing, the surface reduced Ti species can also diffuse deep into the bulk TiO₂. Similar results can be obtained by noble gas ion sputtering (Ar), ion-implantation (N or H) or plasma treatment.³³⁻³⁵

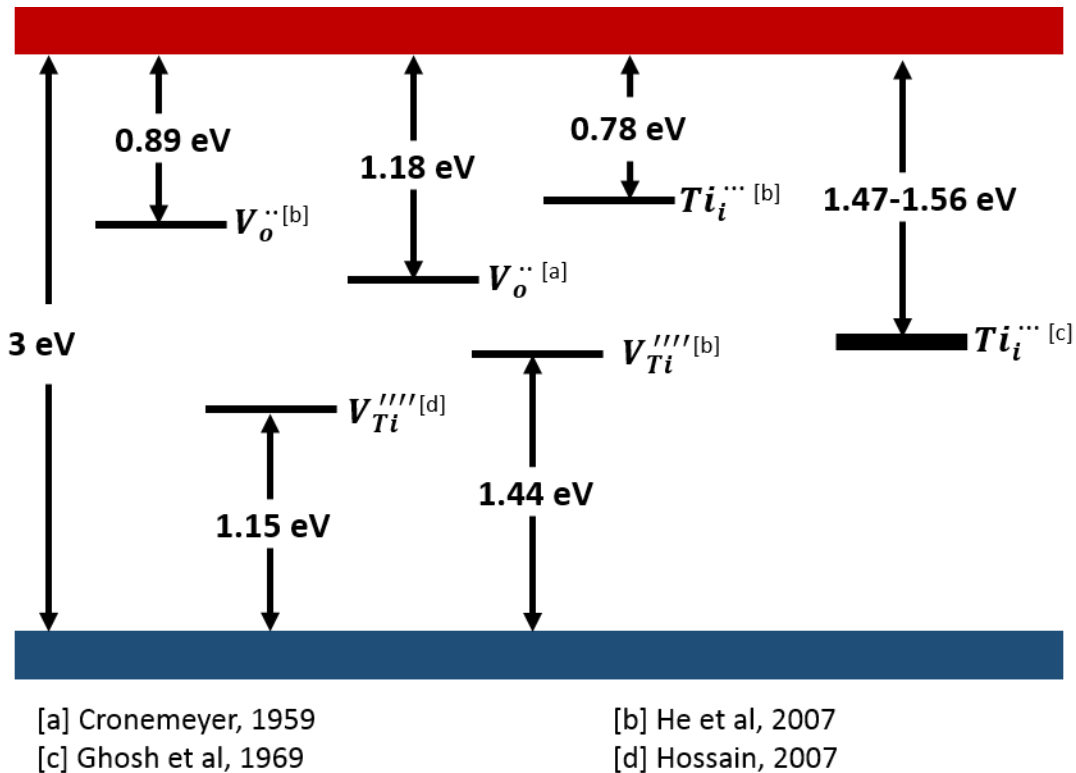


Figure 1.6 Energy levels of various point defects in TiO₂ with respect to the conduction band minimum and valence band maximum of TiO₂.³⁶⁻⁴⁰

Various defect states are generated in the bandgap by Ti³⁺ coupled with V_o, which generates isolated electronic states in the bandgap of TiO₂ and minimizes recombination. Introduction of defects is typically followed by a color change, from white/grey to dark blue or even black as a result of the extension of the solar absorption.⁴¹ For comparison, doping is also capable to increase the photon absorption by creating electronic states close to the conduction band, using transition

metal cations or the valence band with main group anions. However, these external dopants may sometimes behave as charge carrier recombination centers, decreasing the PEC performance, or may act as charge transfer mediators, optimizing the photoactivity depending on the dopant density, energy level, d-band configuration and uniformity.^{42,43}

Annealing TiO₂ in high vacuum or reduction atmosphere leads to a deviation from the 1:2 stoichiometry, forming oxygen-deficient TiO_{2-x}. Oxygen vacancies in TiO_{2-x} can be accommodated as point defects with the x value up to 10⁻⁴ to 10⁻³, while beyond this point the existing crystal structure is no longer stable and the off-stoichiometry is stabilized by phase transformation to Magneli phases (Ti_nO_{2n-1}, n=3 to 10) or even lower O-content phases (Ti₂O₃ or TiO), which exhibit gradually lowering bandgap and increasing metallic property. In particular, Ti₄O₇ has been reported to exhibit a much lower bandgap of 0.6 eV at room temperature compared to anatase TiO₂ (3.2eV), possibly broadening the absorption of TiO₂ from a wavelength of 387 nm to the far infrared region. Ti₂O₃ and Ti₃O₅ exhibit semi-metal behavior with a relatively high conductivity of ~0.1 Ω cm. Efforts related to tailor the bandgap and oxygen composition of TiO₂ sub-stoichiometries including Magneli phases are summarized in Figure 1.7, proposed by Nowotny et al.⁴⁴ This figure also implies a strong trend that an increase in the oxygen deficiency could effectively narrow the bandgap or introduce mid-gap states. Narrowed bandgap close to metal level however makes the incident radiation difficult to separate the electron/hole pairs, and thus it is possible to instead exhibit reduced photo-catalytic property. It is yet to be determined the exact amount of oxygen deficiency and reduction level that is optimum for photoelectrochemical water oxidation using TiO_{2-x} as the photoanode.

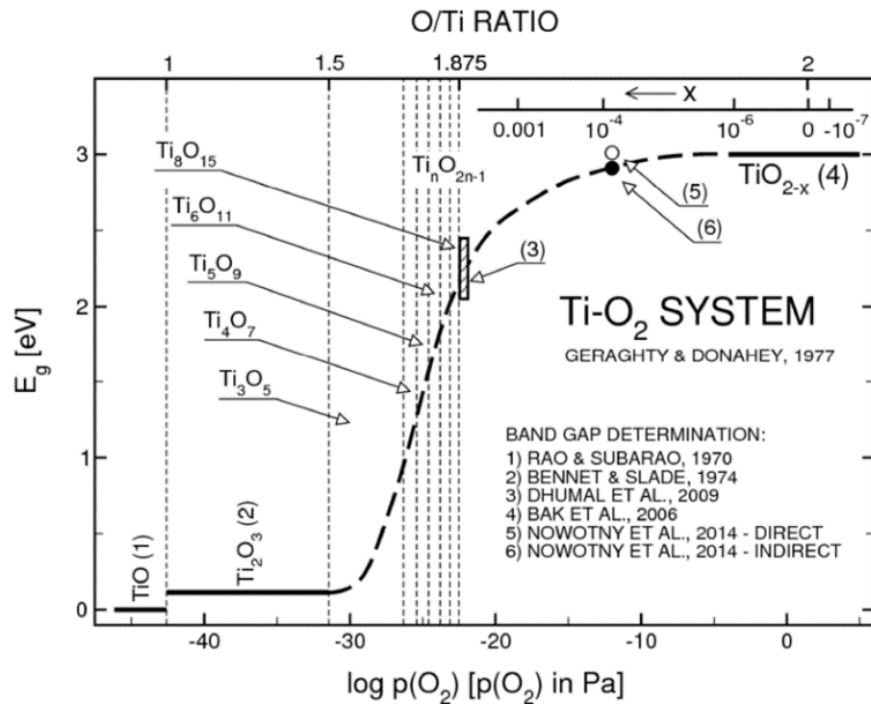


Figure 1.7 Bandgap of TiO_2 sub-stoichiometries a function of partial pressure of O_2 and O/Ti ratio. Reprinted from Ref ⁴⁴.

1.5 Single crystal semiconductors as photoanodes

Compared with wide-bandgap semiconductors such as TiO_2 , single crystal semiconductors with narrow bandgap such as Si, InP and GaAs have attracted more attention in the recent decade.⁴⁵⁻⁴⁷

Photon absorption, one of the essential limitations for TiO_2 -based materials, no longer exists in these single crystal semiconductors, as the narrow bandgaps allow the absorption of the solar spectrum up to the infrared region ($\lambda = 1128 \text{ nm}$ for Si; $\lambda = 926 \text{ nm}$ for InP; $\lambda = 874 \text{ nm}$ for GaAs).

Single crystal semiconductors, featuring no grain boundaries in the bulk and allowing precise control of the charge carrier concentration also enables negligible bulk recombination and controllable charge transfer properties. However, bare single crystal semiconductors as photoanodes exhibit poor photoelectrochemical performance due to the rapid decomposition and/or the formation of insulating oxides, preventing the charge transfer process and the redox

reaction, when in contact with aqueous electrolytes under light. Coating the single crystal semiconductor with a surface protective layer with sufficient photo transmittance, charge transfer and ideally high-catalytic activity is a general solution.

Various coating/deposition methods have been developed to stabilize the single-crystal semiconductor photoanode, including atomic layer deposition,^{46,48} electron beam deposition,⁴⁶ electrodeposition,⁴⁹ floating transfer,⁵⁰ spin coating,⁵¹ etc.⁵² Deposition of metal layer is usually more attractive among others because of its relatively simple fabrication and the capability to tailor the junction behavior by interfacial engineering. This metal layer does not only protect the semiconductor, but also generate the photovoltage through the formation of a Schottky junction, while also improving the reaction rate at the electrode/electrolyte interface. This layer should also be ultra-thin (less than 5 nm, usually less than 2 nm) to minimize the decrease of photoabsorption. Si is one of the most promising candidates among single crystal semiconductors thanks to its narrow bandgap, abundance and wide knowledge base. However, the narrow bandgap of 1.1 eV results in the limitation of photovoltage from water splitting.^{53,54} By contrast, GaAs with a relatively ideal bandgap of 1.43 eV allows the generation of a larger photovoltage to maximize the photoconversion efficiency. In this context, to deposit an ultra-thin metal layer on GaAs using a simple and inexpensive method with improved stability and photoelectrochemical activity is highly desirable.

1.6 Motivation of the study

In the first part of the dissertation (Ch.3 to Ch.6), we aim to investigate (i) the generation of point defects, (ii) the formation of TiO_{2-x} sub-stoichiometries by heavy reduction processes and (iii) surface modification methods in order to widen the light absorption spectrum, improve charge transfer properties and increase interfacial water oxidation selectivity. In addition, we seek to

improve and optimize the existing modification approaches simultaneously. The underlying hypothesis in this work is whether exists an optimum concentration of oxygen vacancies in TiO_{2-x} to maximize the photoelectrochemical performance either in the form as point defects in the anatase phase or in the form of a crystalline disorder in the newly formed phases. Surface modifications with proper OER catalysts allows further improvement of the photoelectrochemical performance by accelerating the surface water oxidation kinetics while minimizing the impact on the photo-transmittance; the optimization of the photoelectrochemical properties is a synergistic effect of increasing the light absorption, reducing the surface recombination and improving the conductivity in the bulk. In this work, various modification methods at TiO_2 nanotube system will be applied to control the density of defects through oxygen removal, including laser surface modification, introduction of Ti^{3+} by Ar/NH_3 treatment, high-temperature thermal hydrogen reduction and electrodeposition of OER catalysts; the schematics for the modification methods on TiO_2 NTs based on various reduction levels are shown in Figure 1.7. The stable range of anatase TiO_2 with nanotubular morphology will be determined and the resulting possible phase transformation will be investigated. The density/types of the defects created will be evaluated and quantified by using photoelectrochemical characterization, together with electrochemical impedance spectroscopy. Light absorption property of the modified TiO_2 NTs will be accessed by measuring the incident photon-to-current conversion efficiency (IPCE) change with various wavelength of the incident light.

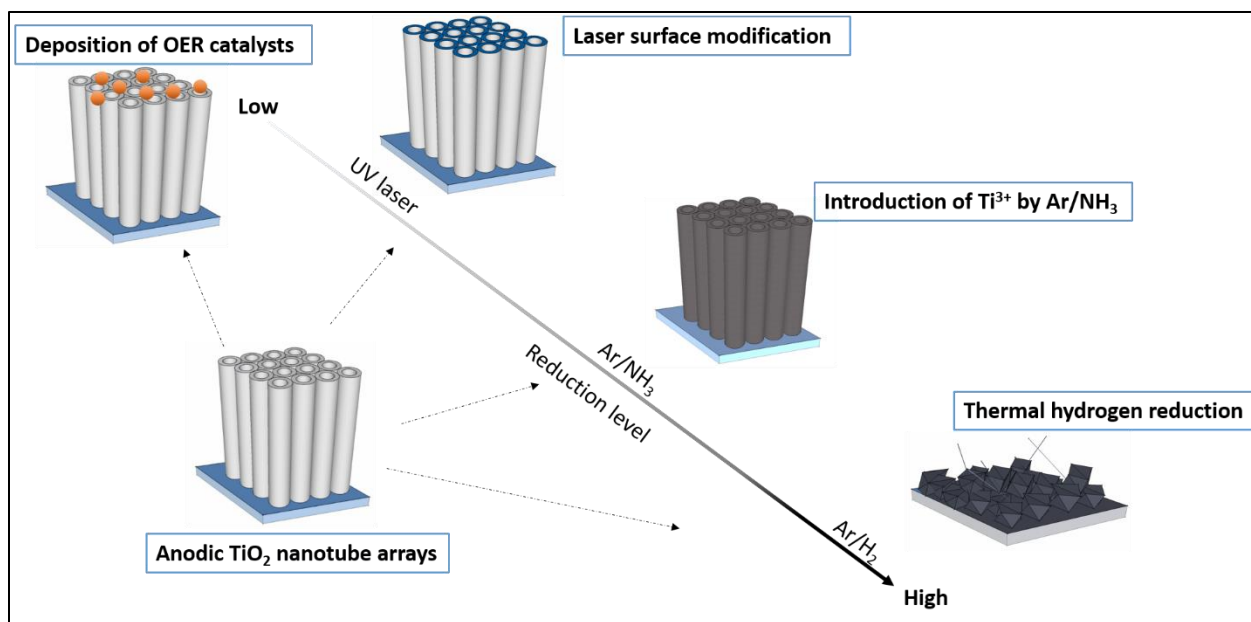


Figure 1.7 schematics for the various modification methods applied on TiO₂ nanotube arrays.

In the second part of the dissertation (Ch.7 and Ch.8), we focus on investigating an electrodeposition method that presents a self-limiting growth mechanism to deposit Ni ultrathin film/nanoparticles on GaAs substrates, and then we extend the method to electrodeposit binary/ternary alloys following the same deposition behavior. The hypothesis is: the self-limiting deposition condition can be achieved for not only Ni layer, but also for other Iron-group mutual alloys such as Ni-Co, Ni-Fe and Ni-Fe-Co; the protective Ni layer affords an improved stability and enhanced surface water oxidation kinetics in an aqueous solution under photoelectrochemical measurements; the stability of this system can be further improved by adding a second or a third Iron-group element such as Co or Fe. Various characterization methods, including potential transients, XPS spectra and XPS depth profile, XRR and HR-TEM will be applied to verify the self-limiting mechanism and to determine the thickness of deposited layer. Photoelectrochemical and electrochemical characterization will be utilized to evaluate the potential of the metal-deposited GaAs as photoanode candidate toward water oxidation.

Chapter 2-Materials and methods

2.1 Anodization of TiO₂ nanotube arrays

Anodization of compact-aligned TiO₂ nanotube arrays: Anatase compact-aligned TiO₂ nanotube arrays (or regular TiO₂ NTs, R-TiO₂) were synthesized using a double-anodization method followed by an annealing process.⁵⁵ Briefly, Titanium foils (Alfa Aesar, annealed, 99% purity, $2 \times 0.7 \times 0.0127$ cm³) were anodized in 0.3 wt% NH₄F (Sigma Aldrich, 99.99%, trace metals basis) and 2 vol% H₂O in ethylene glycol (Sigma Aldrich, 99.8%, anhydrous) before being sonicated in acetone, isopropanol and methanol (for 30 min each). The first anodization (Kepco BOP-100 voltage supply) was performed at 50V for 1 hour, using a Pt gauze as the counter electrode, to form the nanotubes. Successively, 1-hour sonication in DI water loosened the nanotubes from the substrate, allowing their removal with an adhesive tape, which uncovered a textured surface that template the successive growth. The second anodization was carried out under the same conditions, with the reaction time varying from 5 min to 1 hour to achieve a pre-determined thickness of the NT layer. Finally, the nanotubes were annealed at 350°C for 3 hours in an ambient environment to crystallize the anatase phase.²⁸

Anodization of TiO₂ nanotubes with gaps in between: The TiO₂ NTs with large gaps between the individual short nanotubes (LG (S)-TiO₂)⁵⁶ were obtained from the same Ti foil after the same cleaning process. The foil was anodized at an applied potential of 60V for 11 hours in a diethylene glycol electrolyte using the same anodization system⁵⁶. These short nanotubes were grown from a solution containing 2 wt% HF (1.12M) and 2wt% (1.24 M) water which remained straight after anodization. Relatively long (0.5-1.0 μm) LG-TiO₂ nanotubes with walls exposed on the surface were obtained from an electrolyte containing 2 wt% HF (1.12 M) and 4 wt% (2.49 M) water; these nanotubes collapsed on the surface in such a way that the nanotube walls were exposed on the

surface. Both types of as prepared NTs were annealed under 350°C in air for 3 h in order to crystallize the TiO₂ in the anatase structure.

2.2 Various modification approaches of TiO₂ NTs

Surface laser modification: For the surface layer modification, the nanotube samples were placed in a petri dish filled with 15 mL of DI water, facing upward, and irradiated with a pulsed UV laser. A Lambda Physik Compex 205 KrF pulsed excimer laser with a wavelength of 248 nm was used; the full width at half maximum (FWHM) of the pulse was 25 ns and the corresponding energy density was varied from 0.15 to 1 J cm⁻². The beam was directed towards the immersed TiO₂ nanotube array by a mirror and focused using a set of cylindrical lenses. The spot size of the laser source was kept constant at 0.26 × 1.33 cm (0.35 cm²). To increase the total energy absorbed and area of modification on the samples, pulses were overlapped by the translation of the sample with a Newport linear actuator at a speed of 0.26 mm s⁻¹. Pulses were overlapped by 90% and the total number of pulses across the modified area ranged from 10 to 40 pulse per area (PPA).

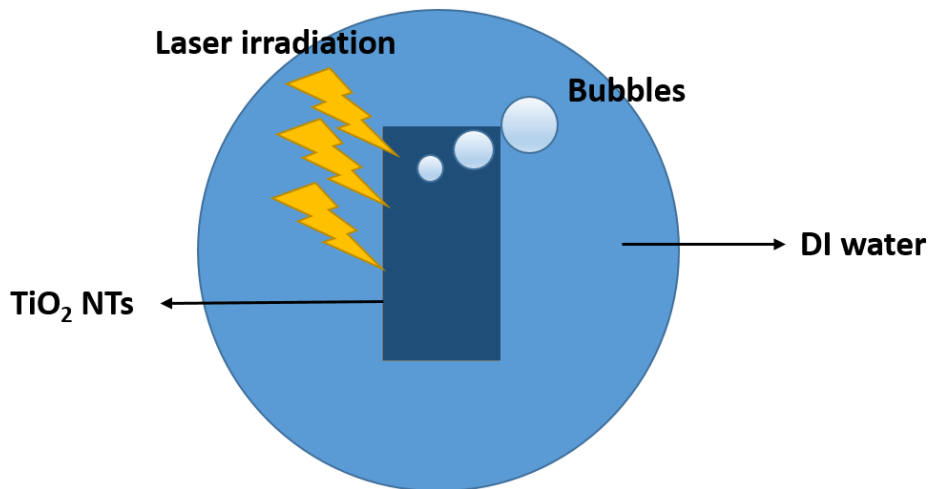


Figure 2.1 Schematics for laser surface modification of TiO₂ nanotubes in DI water under pulsed UV laser.

High-temperature hydrogen reduction: To synthesize TiO₂ sub-stoichiometries, the as-prepared TiO₂ NTs were annealed in a home-made tube furnace under a mixed gas flow of hydrogen and argon (5:95 by volume). Various reaction temperatures from 650°C to 850°C were held for 30 min before the system was naturally cooled down to room temperature in the same atmosphere. To further optimize the thermal reduction conditions, in another set of experiments the temperature was fixed at 800°C, testing the effect of reaction time from 5 min to 2 hrs. In parallel, electrochemical hydrogen doping (EC H-doping) was carried out in 0.5 M H₂SO₄ solution with an applied potential of -0.155 V_{SCE} for 3 s at pristine or thermally reduced Ti-O compounds as working electrodes.²⁰ The samples are labelled as H-TiO₂ and EC-TiO₂, referring to the thermally reduced and electrochemically reduced TiO₂, respectively. Specifically, TiO₂ reduced at various temperatures are denoted as H-650, H-700, H-750 and H-800, respectively, for the reduction time of 0.5 h.

Argon-ammonia thermal treatment: In order to obtain Ar/NH₃ modified TiO₂, the as prepared crystallized TiO₂ NTs were heated to 450°C in a tube furnace with an argon flow under the pressure of 500 mbar with a ramping rate of 4°C/min. When the temperature was stable at 450°C, Ar flow was turned off and NH₃ flow started to fill in the system with a flow of 500 sccm. The time to switch the gas was 7.5 min. The flow rate was set to 100 sccm after the pressure reached 500 mbar. Ar/NH₃ modified TiO₂ NTs were obtained after an annealing time of 1 to 4 hours before cooling down to room temperature under an argon flow overnight. Ar/NH₃ modified TiO₂ NTs with the length of 7 μm that were annealed for 1 hr, 2 hrs and 4 hrs have been labelled as AN-TiO₂, AN-TiO₂ (2h) and AN-TiO₂ (4h), respectively.

Electrodeposition of Ni-Fe-oxy-hydroxides on TiO₂ nanotubes: The electrodeposition of Ni-Fe oxy-hydroxides on TiO₂ nanotubes was carried out at room temperature, using a three-electrode

electrochemical cell comprised of a saturated calomel electrode (SCE) as the reference electrode and Pt mesh as the counter electrode. Ni-Fe oxy-hydroxides were deposited on various working electrodes, including a Au (120nm)/Si wafer, R-TiO₂, LG(L)-TiO₂ and LG(S)-TiO₂ substrates, respectively. Electrodeposition was carried out at constant current density (from – 0.1 to 15 mA cm⁻²) in a nitrogen-purged aqueous solution containing 0.09 M Ni(NO₃)₂·6H₂O and 0.01 M FeCl₂·4H₂O with a pH of 4.5 for 1 min, 2 min or 10 min.⁵⁷

2.3 Electrodeposition of metal on GaAs substrate

Self-limiting electrodeposition of Ni: The electrodeposition of Ni metal on GaAs substrate was carried out on an n-type GaAs substrate ((100) orientation, Si doped, $0.8-4 \times 10^{18}$ cm⁻³) at room temperature. Prior to deposition, the GaAs substrate was treated with acetone for 2 min and immersed in 10% ammonia solution for 2 min before rinsing in deionized (DI) water for 30 s to remove the oxide layer.⁵⁸ An Ohmic back contact between the GaAs substrate and the current collector was prepared by eutectic GaIn, which is liquid at room temperature. The as-etched GaAs substrate was used as the working electrode, while a Pt mesh was used as the counter electrode and a saturated calomel electrode (SCE) as the reference electrode. Electrodeposition of Ni on GaAs (Ni/GaAs) was carried out from the self-limiting chemistry as previously discussed, specifically consisting in an aqueous solution containing 15 mM NiCl₂·6H₂O and 0.1M KCl with a pH of 3.0 (adjusted by HCl). Galvanostatic deposition with a current density of 10 mA cm⁻² was performed varying deposition time from 0.2 to 120 s with an EG&G PAR Model 273A potentiostat. For comparison, a conventional deposition, in which the film thickness is growing with deposition time following Faraday's law, was carried out under a constant current density of 3.5 mA cm⁻² in a 0.1 M NiSO₄ solution with a pH of 2.5 using the same setup.

Electrodeposition of Iron-group mutual alloys: The electrodeposition of Iron-group mutual alloys was carried out in the same three-electrode electrochemical cell using Au/Si (Polycrystalline (111) textured on Si wafer) or GaAs (Si doped, $0.8-4 \times 10^{18} \text{ cm}^{-3}$, (100) orientation) substrate as the working electrodes. Au substrates were immersed in 0.5s H_2SO_4 for 30s, rinsed with DI water and dried by air gun to remove impurities and oxides on the surface before deposition. GaAs substrates were pre-treated by immersing in 10% ammonia solution for 2 min before rinsing in deionized (DI) water for 30 s. Pure Ni film was electrodeposited in a solution containing 15 mM $\text{NiCl}_2 \cdot 6\text{H}_2\text{O}$ and 100 mM KCl;⁵⁹ pure Co film was prepared using a solution containing 15 mM $\text{CoCl}_2 \cdot 6\text{H}_2\text{O}$ and 100 mM KCl; Ni-Co film was deposited in a solution containing $\text{NiCl}_2 \cdot 6\text{H}_2\text{O}$, $\text{CoCl}_2 \cdot 6\text{H}_2\text{O}$ (total concentration of $([\text{Ni}^{2+}] + [\text{Co}^{2+}])$ is 20 mM) and 100 mM KCl; Ni-Fe film was prepared in a solution containing $\text{NiCl}_2 \cdot 6\text{H}_2\text{O}$, $\text{FeCl}_2 \cdot 4\text{H}_2\text{O}$ (total concentration of $([\text{Fe}^{2+}] + [\text{Co}^{2+}])$ is 20 mM) and 100 mM KCl with N_2 purging for 0.5 h prior to the deposition. Ni-Fe-Co film was prepared in a solution containing 15 mM $\text{NiCl}_2 \cdot 6\text{H}_2\text{O}$, 5 mM $\text{FeCl}_2 \cdot 4\text{H}_2\text{O}$, 5 mM $\text{CoCl}_2 \cdot 6\text{H}_2\text{O}$ and 100 mM KCl. The solution pH was adjusted to 3.0 by 1 M HCl. All the films were deposited at a constant current density of 10 mA cm^{-2} with the deposition time ranging from 0.2 s to 60 s (EG&G PAR Model 273A potentiostat).

2.4 Characterization methods

Field emission-scanning electron microscopy (FEI Quanta 650 SEM) coupled with an Energy dispersive X-ray spectroscopy (EDS) was used to characterize the surface morphology, thickness of the films and atomic composition. X-ray photoelectron spectroscopy (XPS, ScientaOmicron UHV with R3000 detector) was used to study the oxidation state of Ti and O in Ti-O compounds in Chapter 4; XPS (PHI 5000 VersaProbe III, Al $K\alpha$) equipped with an argon ion sputtering gun was employed to characterize the oxidation state of elements and atomic composition through

depth profile in all the other chapters that involve XPS measurements. Electron paramagnetic resonance (EPR, Bruker EMX instrument, ER 4123D dielectric resonator) was performed using an applied microwave field of 9.82 GHz, 2.025mW microwave power and 1G p-p modulation amplitude at room temperature to investigate the bulk Ti^{3+} species by integrating the first 20 scans of spectra. X-ray diffraction (XRD) was performed with a Panalytical X'PERT diffractometer using a Cu $K\alpha$ radiation ($\lambda=1.54\text{\AA}$) in the Bragg-Brentano configuration. Grazing incidence X-ray diffraction (GI-XRD, PANalytical Empyrean X-ray diffractometer, Cu $K\alpha$, $\lambda=1.54\text{\AA}$) was used to estimate and compare the FWHM, and therefore the mean size of the crystallites. Due to the complexity of the pattern, the XRD data of the hydrogen treated Ti-O samples were analyzed with Rietveld refinement using GSAS-II.⁶⁰ The instrumental parameters were obtained with a NIST standard silicon, and were precluded from refinements. The background was fitted with a 12-term Chebyshev function. The texture of the phases was modeled by spherical harmonics and the phase fraction of each phase was constrained to adding up to 1 before being refined. The peak broadening was modeled by refining the microstrain only. The lattice parameters of each phase and the sample displacement were also refined, and all the refined parameters were subjected to a simultaneous refinement in the final step. High resolution TEM (HR-TEM), selected area diffraction (SAED) and fast Fourier transform (FFT) were obtained by using a FEI Titan 80-300 operating at 300 kV. TEM lamellae were prepared in a TESCAN GAIA 3 2016 FIB/SEM microscope equipped with a monoisotopic $^{69}\text{Ga}^+$ source and a Smaract nanomanipulator. Before starting the lamella preparation, the surface of the samples was protected first with a Pt layer deposited by electron beam deposition and next with a Pt layer deposited by ion beam deposition. The two-step deposition was required to avoid the impingement of the ion beam directly onto the sample surface. Indeed, Ion Beam Deposition results in damage of the surface, consisting of

sputtering/amorphization in a region with a thickness of tenths of nanometer. The application of a thin layer (< 100 nm) by electron beam deposition avoids this damage, preserving the chemical nature and the crystal structure of the topmost layer. The original thickness of the ion deposited Pt was $2\ \mu\text{m}$. Successively, lamellas were dug, cut and soldered to the nano-manipulator W needle, removed and soldered to the TEM sample holder. Once on the holder, the initial thinning was performed at 30 kV. Final thinning and polishing was performed with an acceleration potential down to 2 kV. The low energy of the ion beam was required to limit the thickness of the amorphous layer in the lamella allowing the HRTEM imaging of the crystal structure of the coating. A semiconductor parameter analyzer (HP 4156B Precision) was used to measure the dark current-potential curves.

2.5 Electrochemical/photoelectrochemical analysis

Cyclic Voltammetry/Linear Sweep Voltammetry/Chronoamperometry: Cyclic voltammetry (CV) is one of the most common and versatile electrochemical techniques for the study of electrochemical catalytic activities and is usually the initial step to understand the electrochemical performance of a materials system. The input signal for CV is a linear potential scan with a triangular waveform vs. time and the corresponding current is measured, while the potential input for liner sweep voltammetry (LSV) is linear, without a reversal. In this dissertation, CV and LSV are employed to evaluate the electrochemical/photoelectrochemical performance of the materials without/with standard solar illumination. Chronoamperometry measures the current of the electrochemical cell as a function of time at a fixed/stepped applied potential, and is utilized to investigate the stability of the working electrode performed in an electrochemical or photoelectrochemical cell. In this work, a three-electrode system was used with a saturated

calomel electrode (SCE) as the reference electrode, platinum gauze as the counter electrode and the materials of interest as the working electrode. All the potentials were converted to the reversible hydrogen electrode using the Nernst equation:

$$E_{RHE}^o = E_{app} + 0.059 \times pH + E_{SCE}^o \quad (2.1)$$

Photoelectrochemical measurements were carried out using an Oriel Sol 1A solar simulator emitting AM 1.5G sunlight irradiation with an intensity of 100 mWcm⁻² coupled with a Biologic SP-150 potentiostat. A horizontal configuration was used for the photoelectrochemical cell with the working electrode facing upward to the light source in a petri dish holding electrolyte. A vertical configuration was used for all the electrochemical measurements without standard light illumination. Various electrolytes were used, including 1M KOH (pH=13.6), 0.1 M phosphate buffer solution (0.02M KH₂PO₄+0.08M K₂HPO₄, pH=7.2) and Ferri/Ferrocyanide solution (50 mM K₃Fe(CN)₆, 350 mM K₄Fe(CN)₆ and 1 M Na₂SO₄, pH=6.7), according to different properties of the samples which will be specified in the successive chapters.

Incident-photon-to-charge-carrier-conversion efficiency: To measure the Incident-photo-to-charge-carrier-conversion efficiency (IPCE) as a function of wavelength, samples were placed in a vertical plastic cuvette containing electrolyte, which is connected to the SCE reference by a salt bridge containing saturated KCl solution. The incident lights at well-controlled wavelength were obtained by a tungsten/halogen lamp (Princeton Instruments TS428, 250W) through a monochromator (Princeton Instruments Acton SP1250). The incident light power density as a function of wavelength was measured by a Newport Model 1931-C power meter. The IPCE is calculated by comparing the flux of the photogenerated charge carriers that contribute to water oxidation and the incident photon flux. The charge flux is calculated from the photocurrent while

the photon flux can be calculated from the total power shining on the sample surface. Therefore, the IPCE can be calculated using the following equation:

$$IPCE = \frac{J(\lambda) \times h\nu}{P(\lambda) \times e} \quad (2.2)$$

where λ is the wavelength, $J(\lambda)$ is the photocurrent density measured at the given wavelength, h is the Planck constant, ν is the frequency of light, $P(\lambda)$ is the power of incident photons at the given wavelength.

Electrochemical Impedance Spectroscopy: Electrochemical impedance spectroscopy (EIS) allows the determination of capacitive and resistive features of heterogeneous systems by applying a sinusoidal voltage perturbation and measuring the corresponding current response using equivalent circuit models. In particular, the amplitude and phase angle of the current with respect to the potential at various frequencies can be measured. According to the AC electrical theory:

$$V(t) = V_0 + V_m \sin(\omega t) \quad (2.3)$$

$$I(t) = I_0 + I_m \sin(\omega t + \theta) \quad (2.4)$$

$$Z(\omega) = \frac{V(t)}{I(t)} \quad (2.5)$$

$$Z(\omega) = Z' + jZ'' \quad (2.6)$$

Where V_0 and V_m are the dc bias potential and the maximum potential of the applied sinusoidal voltage, respectively, I_0 and I_m are the steady-state current and the maximum current of the sinusoidal signal, θ is the phase angle.⁶¹ Under conditions of small voltage perturbations, of the order of 10 mV, the system of interest can be modeled by basic electrical components; Figure 2.2

shows the simplest equivalent RC circuit. For porous materials such as TiO₂ nanotubes arrays, a semi-infinite series of the RC circuit can be utilized.^{62–65}

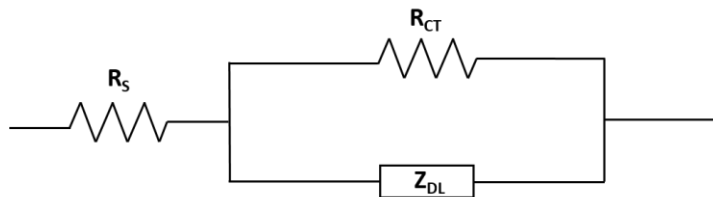


Figure 2.2 Equivalent RC circuit, R_s , R_{CT} and Z_{DL} represents solution resistance, charge transfer resistance and double layer capacitance, respectively.

Mott-Schottky Equation: Under equilibrium conditions, the Fermi-level of the semiconductor and the redox couple in the solution species are equal; these energy levels can however be separated by an external applied potential. The potential where the band bending effect is eliminated is defined as the flat band potential, V_{FB} . When the applied bias is more cathodic with respect to the flat band potential, electrons would accumulate at the interface and the energy bands bend upward; in contrast, at a more anodic potential, a depletion region is formed as the electrons are driven away from the interface and thus the energy bands bend downward. An inversion behavior as a p-type semiconductor is shown when the applied bias is sufficiently strong. The energy band structure changing with applied potential is shown in figure 2.3.

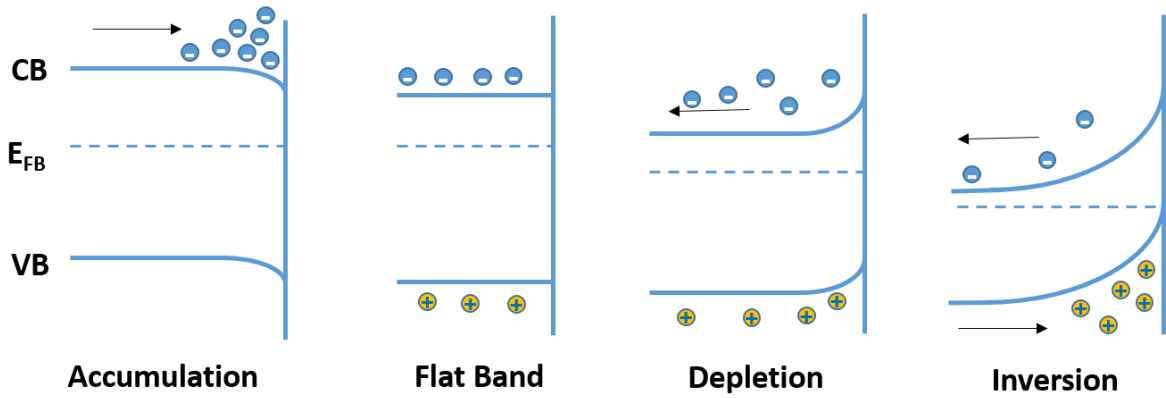


Figure 2.3 Band structure change with applied potential at the electrode/electrolyte interface for an n-type semiconductor.

The Mott-Schottky equation can only be used when the depletion condition is fulfilled; under these conditions it is possible to determine the flat band potential and the density of donors in the semiconductor. Poisson's equation in one dimension gives the relationship between the charge density and the potential difference in a phase as:

$$\frac{d^2\Phi}{dx^2} = -\frac{\rho}{\epsilon\epsilon_0} \quad (2.7)$$

where Φ is the electrostatic potential, ρ is the charge density at the position x away from the interface, ϵ is the relative permittivity, ϵ_0 is the permittivity of free space. The Mott-Schottky equation can be derived from the Poisson's equation assuming a Boltzmann energy distribution for the ions in solution, and an energy distribution of electrons in the space charge region. By using the Gauss's flux theorem the capacitance is linked to the potential at flat band:

$$\frac{1}{C^2} = \frac{2}{\epsilon\epsilon_0 e N_D} \left(E - E_{FB} - \frac{k_B T}{e} \right) \quad (2.8)$$

where C is the semiconductor capacitance, ϵ is the relative permittivity (~ 100 for TiO_2 to estimate the charge carrier concentration)^{66,67}, e is the electron charge, N_D is the density of donors, E is the applied potential, E_{FB} is the flat band potential, k_B is Boltzmann's constant, and T is the absolute temperature.

Capacitance values can be determined by identifying the frequency with the highest capacitance response, namely, the frequency with the largest imaginary impedance component. At the measured frequency, the capacitance is calculated from the following equation:

$$-\text{Im}(Z) = \frac{1}{2\pi f C} \quad (2.9)$$

Where $\text{Im}(Z)$ is the imaginary part of the impedance, f is the frequency and C is the capacitance.

⁶⁸ The value of charge density and flat band potential can be obtained from the linear region by plotting $1/C^2$ vs. applied potential.

In this work, the Mott-Schottky plots were obtained in a neutral acetate buffer solution (0.2 M Na_2SO_4 + 0.1 M NaCH_3COO) or in a 0.1 M neutral phosphate buffer solution (0.02M KH_2PO_4 +0.08M K_2HPO_4 , pH=7.2) with a frequency range between 11 kHz and 1 Hz and a potential amplitude of 20 mV_{RMS} in dark or under 1.5G solar illumination with a power intensity of 100 mW cm^{-2} .

Low Frequency Capacitance: The Mott-Schottky method also allows the determination of shallow donor states at relatively high frequencies (usually ≥ 100 Hz) while the deep level trap states can only be detected at low frequencies in a frequency range of 1mHz. The deep level trap states can be estimated by measuring the frequency dependent capacitance by EIS as they induce additional capacitance to the space charge layer. According to the work of Oskam et al⁶⁹⁻⁷¹, The frequency dependent capacitance C_P can be calculate by the equations below:

$$C_p = -[\omega * Im(Z)(1 + D^2)]^{-1} = \frac{e^2}{kT} \frac{k_2 k_1 n_s}{(k_1 n_s + k_2)^2} N \text{ (When } \omega = \text{small)} \quad (2.10)$$

$$D \equiv \frac{Re(Z) - R_\Omega}{-Im(Z)} \quad (2.11)$$

Where k_1 and k_2 are rate constants for the detrapping and trapping under steady state condition, and n_s is the electron density in the conduction band. The C_p value approaches a maximum when $k_1 n_s = k_2$. In this case:

$$C_p(max) = \frac{1}{4} \left(\frac{e^2}{kT} \right) N (cm^{-2}); \frac{k_2 k_1 n_s}{(k_1 n_s + k_2)^2} \Big|_{k_1 n_s = k_2} = \frac{1}{4} \quad (2.12)$$

Thus, the density of states N (deep level) can be derived from the above equation, when C_p is at its maximum. In this work, EIS was carried out in a neutral acetate buffer solution (0.2 M $Na_2SO_4 + 0.1$ M $NaCH_3COO$) in frequencies ranging from 200 kHz to 1m Hz in the dark.

Estimation of Water Oxidation Selectivity: The photogenerated holes reaching at the semiconductor/electrolyte interface may not immediately inject into the solution and react with the redox species; instead, significant recombination would occur with a low reaction kinetics on the surface as shown in Figure 2.4. In order to determine the fraction of photogenerated holes that reach the surface and participate in oxygen evolution, the photocurrent was measured in a neutral phosphate buffer solution without and with a hole scavenger species (SO_3^{2-}). The real photocurrent density reflecting the water oxidation (J_{OER}) can be estimated as the product of the maximum theoretical photocurrent (J_{MAX}), the charge separation efficiency in the bulk (η_{SEP}) and the water oxidation selectivity on the surface (η_{OER}) as shown in equation 2.13-2.15.

$$J_{OER} = J_{MAX} \times \eta_{SEP} \times \eta_{OER} \quad (2.13)$$

$$J_{SO_3^{2-}} = J_{MAX} \times \eta_{SEP} \times 100\% \quad (2.14)$$

$$\eta_{OER} = \frac{J_{MAX} \times \eta_{SEP} \times \eta_{OER}}{J_{MAX} \times \eta_{SEP} \times 100\%} = \frac{J_{OER}}{J_{SO_3^{2-}}} \quad (2.15)$$

In the phosphate buffer solution with the hole scavenger (SO_3^{2-}), the reaction occurring is the oxidation of $[SO_3^{2-}]$ to $[SO_4^{2-}]$, which is thermodynamically and kinetically more facile than the OER reaction and the oxidation selectivity is close to 100%,⁷²⁻⁷⁸ where the photocurrent density can be calculated using equation 2.14. Therefore, the water oxidation selectivity can be obtained by comparing the photocurrent density without and with the hole scavenger in the same condition as shown in equation 2.15, assuming the charge separation efficiency in the bulk remains the same.

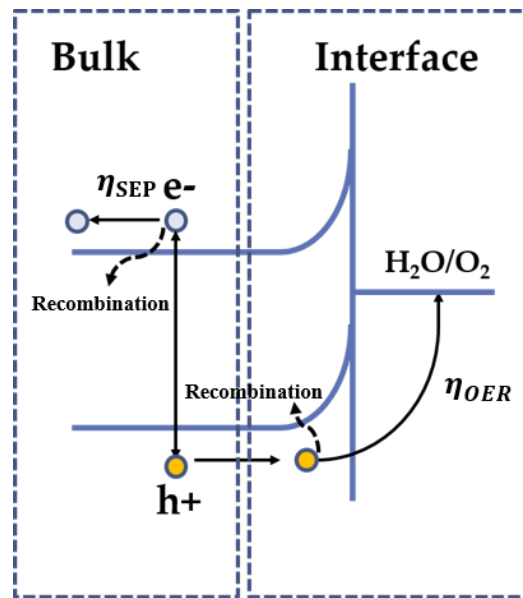


Figure 2.4 Schematics for the recombination occurring in the bulk and at the interface. η_{OER} and η_{SEP} represents the water oxidation selectivity at the surface and the charge separation efficiency in the bulk, respectively.

Chapter 3-Surface laser modification of TiO₂ nanotube arrays

Defects in TiO₂ include shallow donors, which enhance electronic conductivity, as well as deep level trap states, which in contrast facilitate recombination.^{67,79,80} Many efforts have been devoted to introduce surface defects at TiO₂; most of them, however require extreme conditions of high temperature and pressure or long reaction time. Yang et al. used molten Al to partially reduce the TiO₂ surface, creating a disordered TiO_{2-x} shell.⁸¹ Leshuk et al. prepared yellow and black TiO₂ by hydrogenation under a 300 ± 5 psig pure H₂ environment at 200 °C for 5 days or under flow of 10% H₂/ 90% Ar at 400-500 °C for 24-102 h.^{82,83} Lu et al. obtained black TiO₂ after hydrogenation at room temperature, but only after 15 days processing.⁸⁴ The development of rapid and simple approaches to induce surface disorder at TiO₂ nanotubes would be highly desirable. In this chapter, modification by irradiation from a KrF excimer laser ($\lambda = 248$ nm) on NT arrays immersed in DI water is carried out. The procedure results in a modified surface at the mouth of the NT arrays while maintaining the underlying NTs structure.⁸⁵

3.1 Morphology and crystallinity changes induced by laser

The effect of laser energy fluence was investigated by keeping the length of the tubes constant at 1 μm and the laser pulses per area (PPA) at 20. The secondary electron micrographs shown in Figure 3.1 reveal the surface morphology of the TiO₂ nanotubes after laser irradiation. The TiO₂ surface appears to have been partially melted and re-solidified, with the formation of discrete features at the NT surface after irradiation at laser fluences of 0.3 J cm⁻² or higher. The feature size was 1-2 μm for the lower energy densities (0.3-0.5 Jcm⁻²) and increased to 2-3 μm for higher fluences (0.5-1.0 Jcm⁻²), showing a more pronounced topographical variability. All of the irradiated surfaces maintained a porous morphology. A similar morphology, but with a smaller feature size (~ 500 nm) has been reported for TiO₂ films grown by sol-gel methods.⁸⁶ The

formation mechanism was related to the decomposition of organic material during synthesis in that work, while in our case the pores are probably generated by the entrapment of water within the molten material after laser irradiation followed by evaporation.

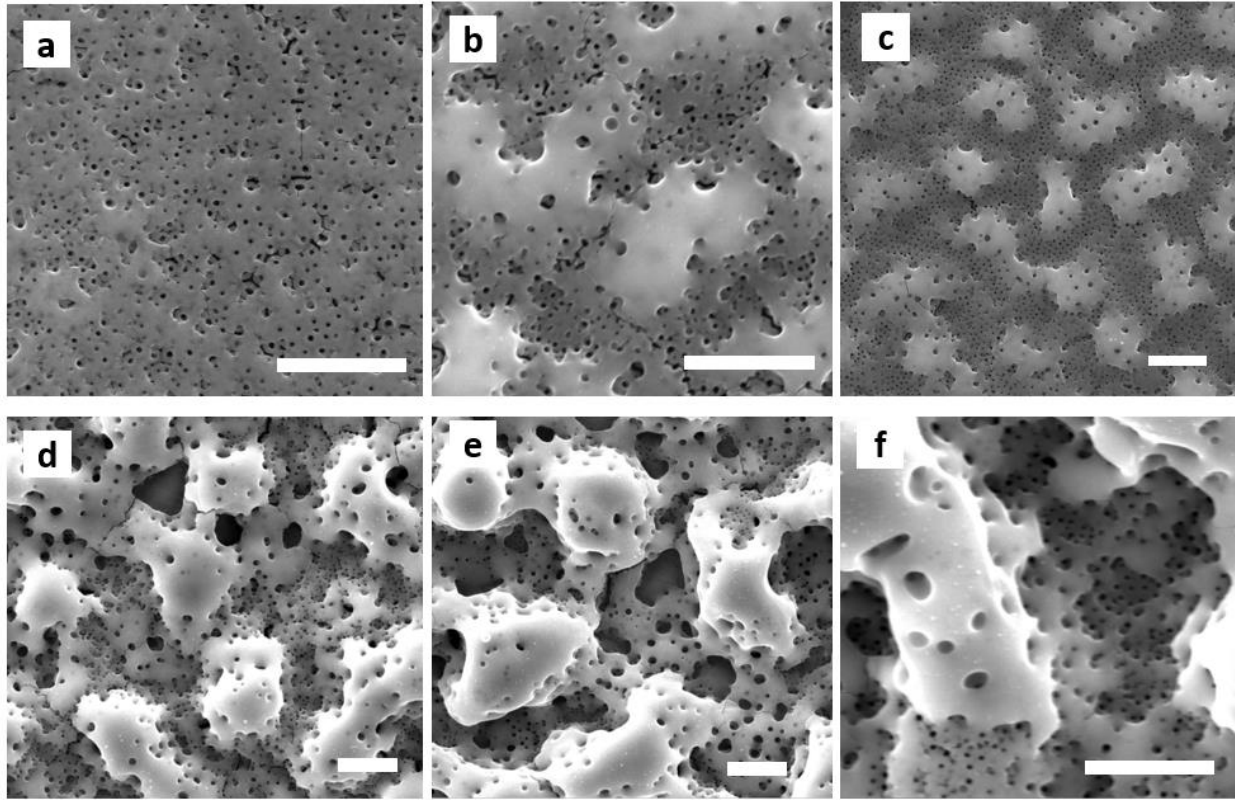


Figure 3.1 SEM images of the surface morphology for laser modified 1 μm long TiO_2 nanotube arrays; the PPA was kept constant at 20 while the energy fluence per pulse was (a) 0.15 Jcm^{-2} , (b) 0.3 Jcm^{-2} , (c) 0.4 Jcm^{-2} , (d) 0.5 Jcm^{-2} , (e) 0.8 Jcm^{-2} and (f) 1.0 Jcm^{-2} . The scale bars in each image correspond all to 1 μm .

The XRD patterns of NT arrays subjected to irradiation still show the anatase structure of the pristine nanotubes (Figure 3.2), while the main reflections become weaker with increasing laser fluence, suggesting degradation of the crystal structure. Specifically, the intensity of the (101), (200), (105), and (211) reflections of anatase TiO_2 reduces significantly, and only a weak (101) peak could be observed after irradiation.

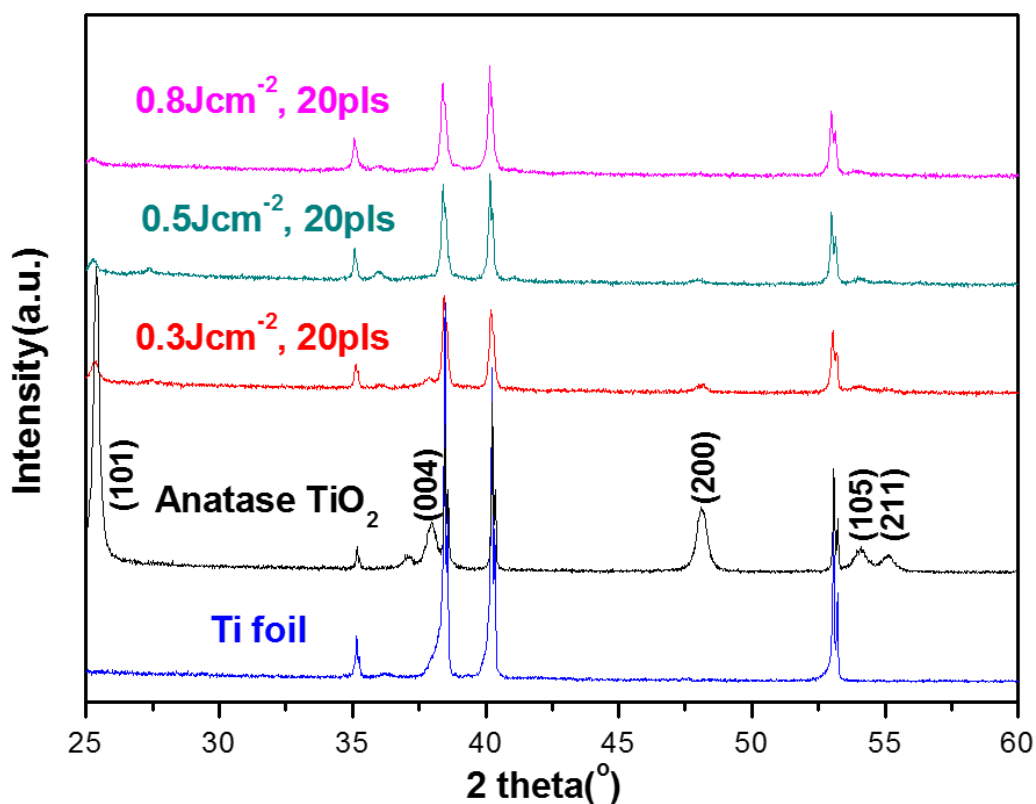


Figure 3.2 X-ray diffraction patterns of TiO_2 before and after laser treatment with different laser energy densities, as reported in the figure.

Figure 3.3 compares the photocurrent response of pristine anatase NTs with that of laser modified NTs at 0.15 to 0.4 J/cm^2 (20 PPA) as a function of potential. All samples exhibit an increasing photocurrent with applied potential, approaching a plateau between 0.6 and 1.2 V_{RHE} . The photocurrent at 1.23 V_{RHE} increases from 0.23 to 0.32 mA/cm^2 , a ~ 1.5 -fold enhancement, with increasing fluence from 0 (pristine NTs) to 0.3 J/cm^2 . NTs undergoing higher irradiation (0.4 J/cm^2) exhibit a current comparable with the pristine specimen, and an even higher fluence results in a decreased response as shown in Figure 3.4, possibly due to the morphology damage caused by the high-energy laser irradiation. It should be noted that the photocurrent on/off transients of the

pristine NTs, after the initial increase, exhibit a significant decay, suggesting significant recombination. The photocurrent transients of the modified samples on the other hand show a recombination feature that becomes less noticeable with increasing fluence, suggesting that laser irradiation may result in the partial annihilation of trap states.

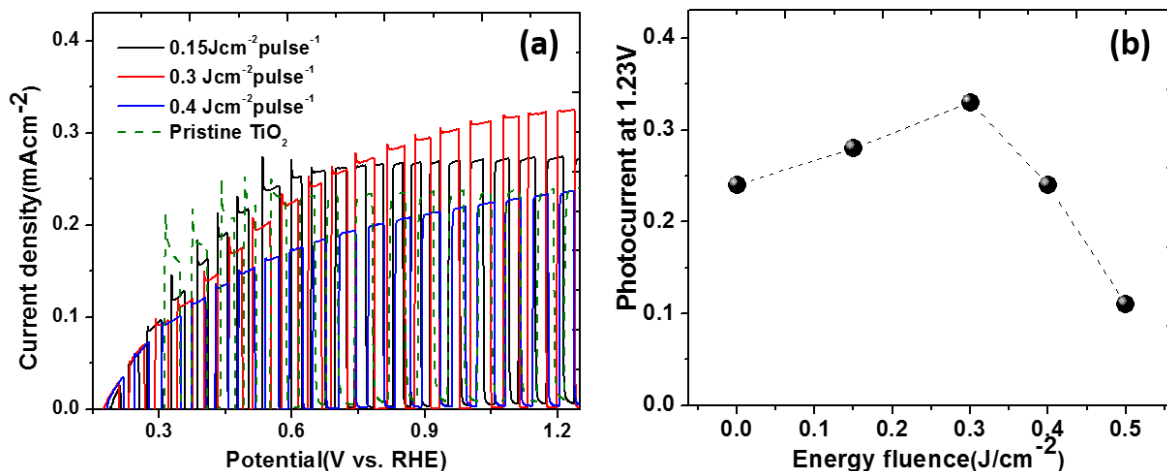


Figure 3.3 (a) The photocurrent density for laser modified TiO₂ arrays undergoing irradiation at various fluences in 1 M KOH solution (pH=13.6). Scan rate of 10 mV/s under 100 mW/cm² chopped illumination with relatively lower laser energy fluence (<0.5 J cm⁻² pulse⁻¹). (b) Comparison of the photocurrent at 1.23 V_{RHE} vs. energy fluence/pulse (0 to 0.5 J cm⁻² pulse⁻¹).

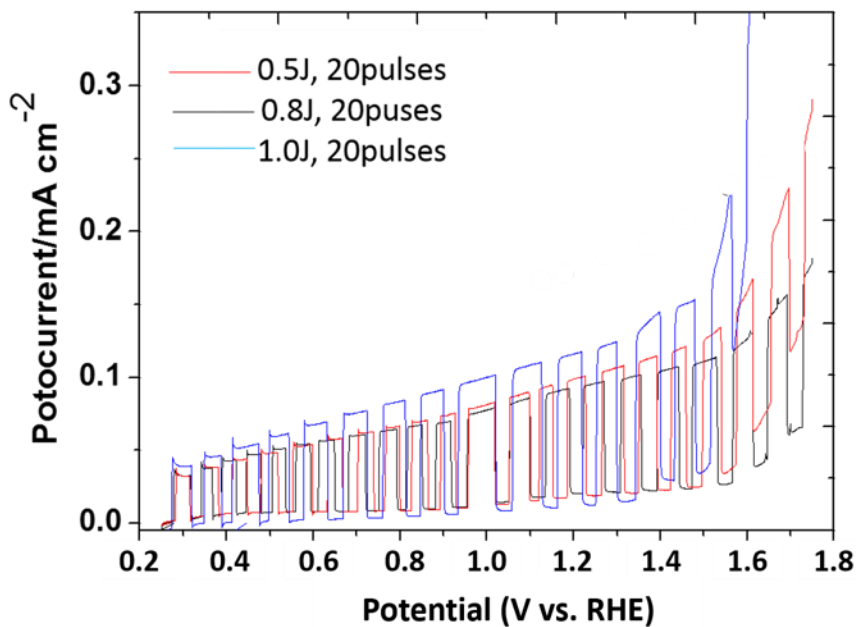


Figure 3.4 The photocurrent density for laser modified TiO₂ with relatively higher laser energy fluence (0.5 to 1.0 Jcm⁻²pulse⁻¹).

The Mott-Schottky plots for a pristine and a modified sample (0.3 J/cm², 30 PPA) are reported in Figure 3.5 (a). The donor density calculated from the slope of the linear region is $3.9 \times 10^{19} \text{ cm}^{-3}$ for the pristine sample, and is $2.66 \times 10^{20} \text{ cm}^{-3}$ for the modified one, suggesting an increase of shallow carrier density by almost one order of magnitude. As a consequence, a large negative shift of the flat band potential, from -0.2 to -1.28 V_{SCE}, is observed, resulting in a significant increase of the Fermi level, and highlighting the vastly different electronic properties of the modified layer. The density and energy of trap states are calculated from the maximum of the low frequency capacitance measured at various applied potentials;^{69,70} the results are displayed in Figure 3.5 (b) and (c). A quasi-exponential decrease of defect density is observed for both samples starting from the Fermi level. The pristine sample, Figure 3.4 (b), shows a maximum in capacitance at $\sim 0.5 \text{ V}_{\text{SCE}}$, revealing a significant trap state density of $9.3 \times 10^{16} \text{ cm}^{-3}$. The laser-modified TiO₂ in

contrast did not show any obvious maximum in capacitance within the potential window 0.4-0.8 V_{SCE}. Assuming that the trap states are located at the same potential of 0.5 V_{SCE}, calculation of a trap state density value of $2.3 \times 10^{16} \text{ cm}^{-3}$ is possible, which supports the notion that laser modification indeed decreases the density of trap states. This decrease in the density of trap states in laser-modified samples could be attributed to the trap state passivation by the hydrogen generated via water splitting occurring under laser irradiation and possibly by lattice disorder induced simultaneously at the TiO₂ NT surface.⁸⁷

The observed maximum in photocurrent at 0.3 J/cm^2 and 20 PPA can therefore be linked to the balance of two opposing effects: initially the photocurrent increases with the energy fluence due to the higher density of shallow carriers in the modified region; with higher energy fluence on the other hand the thickness of the modified region increases further, and the topography becomes more pronounced, likely leading to stronger light absorption by this layer, resulting eventually in a drop of the photocurrent.

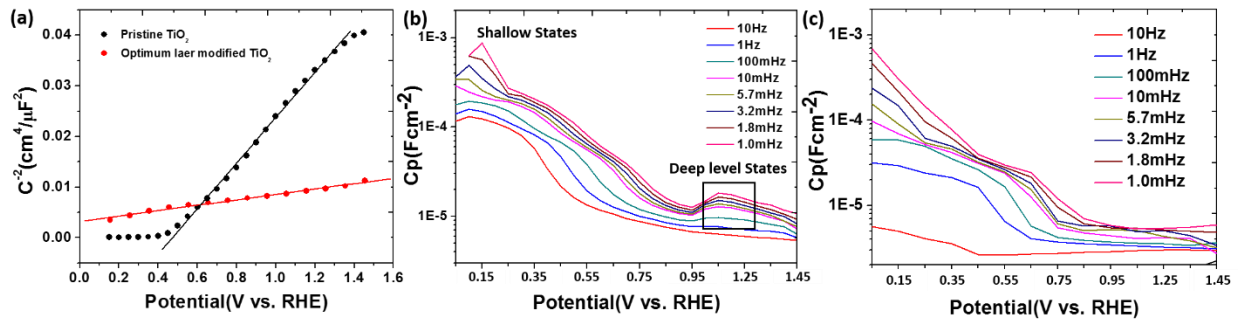


Figure 3.5 (a) Mott-Schottky plots of pristine and optimally laser modified TiO₂ (0.3 J/cm^2 , 30 PPA). Density of donors and flat band potential were computed according to Mott-Schottky equation based on flat semiconductor assumption. Low frequency capacitance measured from 107 Hz down to 1 mHz for pristine (b) and optimally laser modified TiO₂ (c); the data provide an estimate of the defect density vs. applied potential.

3.2 Optimizing the laser energy fluence, PPA and length of the nanotube arrays towards photo water oxidation

To investigate the influence of the number of laser PPA and of the nanotube length on the morphology and PEC properties, the irradiation energy was fixed at 0.3 J cm^{-2} while the number of pulses was varied. Figure 3.6 (a-d) displays the surface morphology evolution of the $1 \mu\text{m}$ long NTs with increasing irradiation PPA from 5 to 40. Similar to the effect of laser fluence, the morphology becomes more prominent and roughness increases, while the porous morphology is retained. Figure 3.6 (b, e, and f) show the effect of nanotube length (1, 4 and $11 \mu\text{m}$) on the surface layer morphology following irradiation with 0.3 J cm^{-2} , 20 PPA. From Figure 3.6 (b), the thickness of the laser modified region is approximately 300 nm. The surface features are more pronounced in the longer tubes, and more NTs are left exposed with increasing length; the lower degree of damage observed on the longer nanotubes may be linked to the higher thermal conductivity of TiO_2 , about 20 times that of water, which would facilitate thermal dissipation. The cross sectional images in the insets further demonstrate that only a local region at the surface is affected by laser irradiation, with minimal to no impact along the length of the tubes.

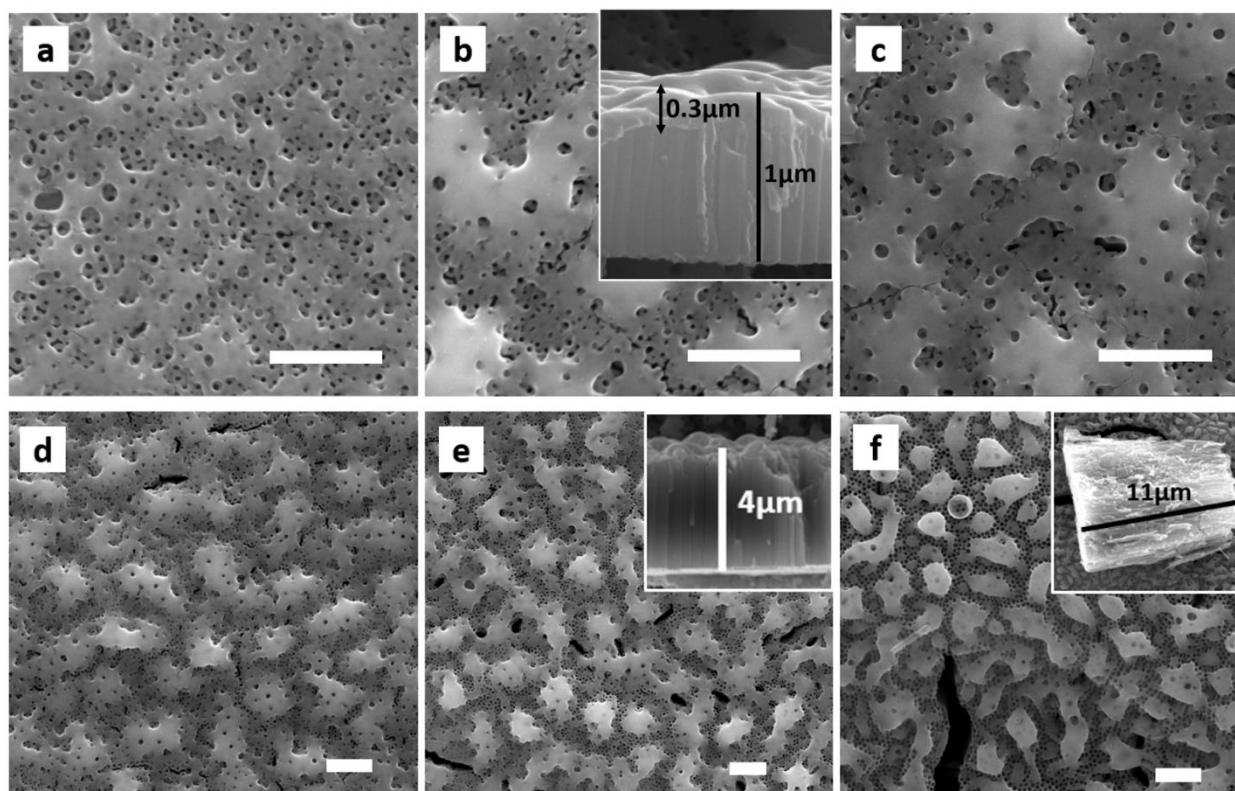


Figure 3.6 SEM images of the surface morphology for TiO₂ nanotube arrays irradiated at 0.3 J cm⁻² with various pulse numbers (a-c): (a) 5 PPA, (b) 20 PPA, (c) 30 PPA, (d) 40 PPA; and (e-f) 0.3 Jcm⁻², 20 PPA with various nanotube lengths: (e) 4 μm and (f) 11 μm. Insets present the cross section of the corresponding specimen. The scale bars correspond to 1 μm.

The effect of laser irradiation (0.3 Jcm⁻², 20 PPA) on the morphology of 4 μm long TiO₂ nanotubes was investigated in detail by high resolution TEM and electron diffraction, as shown in Figure 3.7. Figure 3.7 (a) displays the cross section of a nanotube array; the nanotubular morphology is preserved except for the boxed region, magnified in the inset, showing a ~ 300 nm thick layer, roughly corresponding to the region imaged by the SEM micrographs. Figure 3.7 (b) shows another NT array in cross section, where two boxes highlight regions at the top and the middle section of the NTs. The inset shows a magnified image from area 2, where the lighter contrast and

the fringes due to internal strains may suggest a stressed region with poorer crystallinity. Selected area electron diffraction (SAED) patterns of areas 1 and 2 in (b) are shown in Figure 3.7 (c) and (d), respectively. The first 4 rings in both SAEDs correspond to the (101), (004), (200) and (105) planes of anatase TiO₂, the same reflections observed in the XRD patterns. Figure 3.7 (c) evidences a lattice spacing identical to that of bulk anatase, with the spacings being 3.51, 2.45, 1.90 and 1.71 Å for these four planes, respectively. Figure 3.7 (d) in contrast exhibits slightly smaller d spacings, i.e. 3.50, 2.36, 1.88 and 1.67 Å for the same planes, respectively, confirming that this modified region is under significant stress. It should be noted however that the SAD pattern is actually a composition of the characteristic of the modified and unmodified regions since the electron beam penetrates a relatively thick region of the material. The TEM results are thus in good agreement with the XRD patterns, supporting the notion that degradation of the crystal structure is caused by laser irradiation.

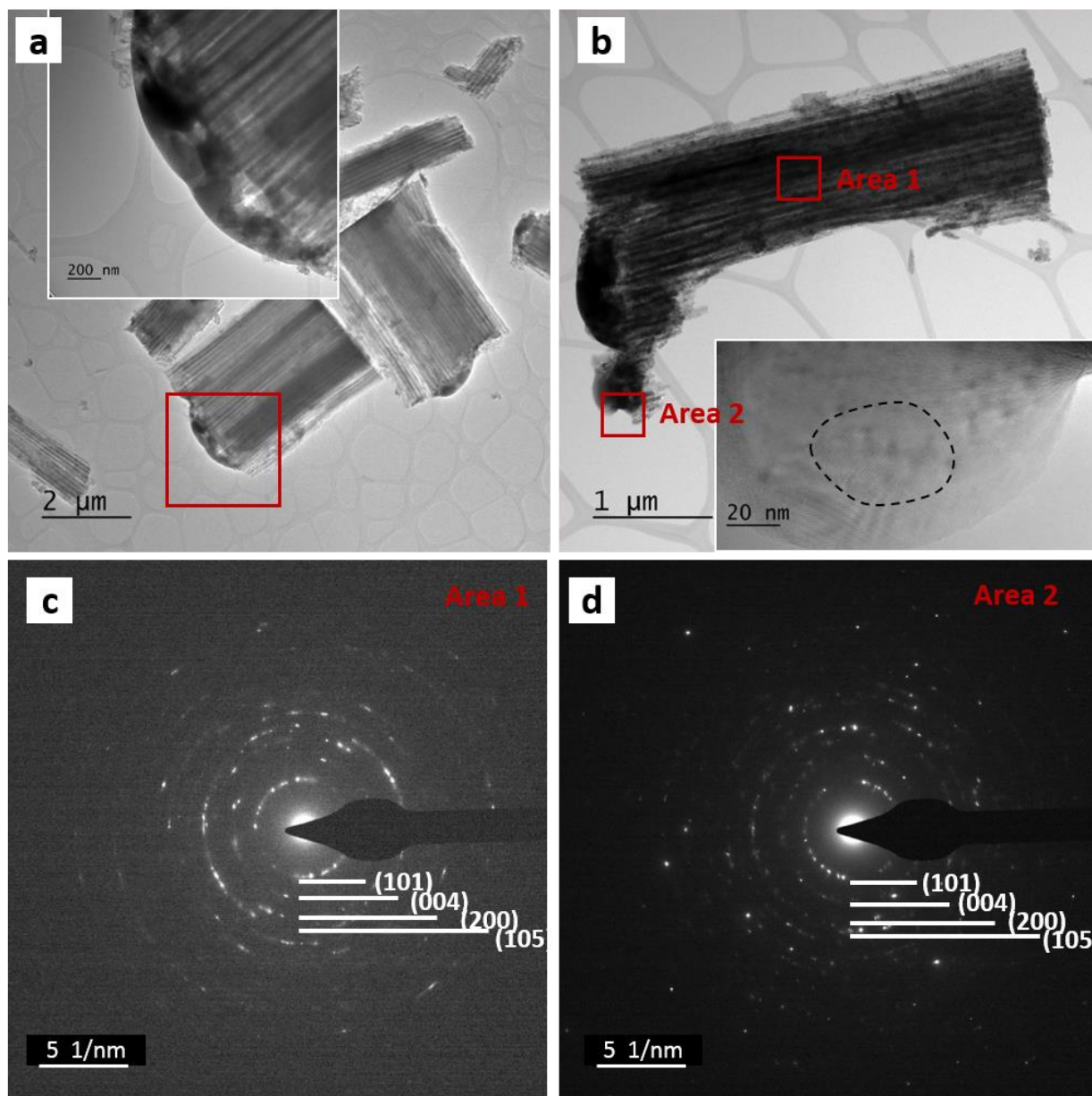


Figure 3.7 High resolution TEM images (a), (b), and selected area diffraction patterns (c), (d), of 0.3 Jcm^{-2} , 20 PPA laser treated $4 \mu\text{m}$ TiO_2 nanotube arrays. Area 1 and area 2 in (b) correspond to the nanotube wall area and the surface area modified by laser treatment, respectively.

The influence of PPA and the NT length on the photoelectrochemical performance was studied. As shown in figure 3.8 (a), the optimum number of pulses on $1 \mu\text{m}$ nanotube arrays is 30 PPA, resulting in a photocurrent of 0.36 mAcm^{-2} at $1.23 \text{ V}_{\text{RHE}}$, about 1.6-fold that of pristine NTs. The

occurrence of a maximum in photoresponse is explained again through the amount of energy absorbed by the NTs: at low PPA the improved charge transport owed to the increased charge carrier density enhances the photoresponse, while above 30 PPA, the increased thickness of the modified layer may limit the absorption and transport of the charge carriers, degrading performance. Figure 3.8 (b) shows that increasing the tube length leads to a photocurrent enhancement at low bias, but also results in a decrease of photoresponse at 1.23 V_{RHE} . For the 1 μm NTs, the photocurrent increases monotonously until saturation at 1.0 V_{RHE} , whereas for the 4 μm and 11 μm NTs, the photocurrent increases slightly only up to 0.5-0.6 V_{RHE} , decreasing thereafter with increasing bias. This decrease may be due to the fact that, as the applied bias increases the driving force for charge transport rises, the rate of e-h recombination is enhanced and the mean free path is decreased.⁸⁸ Electron collection at the back contact therefore decreases with higher NT length. As a result, the optimum laser irradiation conditions are obtained in 1 μm TiO_2 NT arrays undergoing modification with a fluence of 0.3 Jcm^{-2} and 30 PPA.

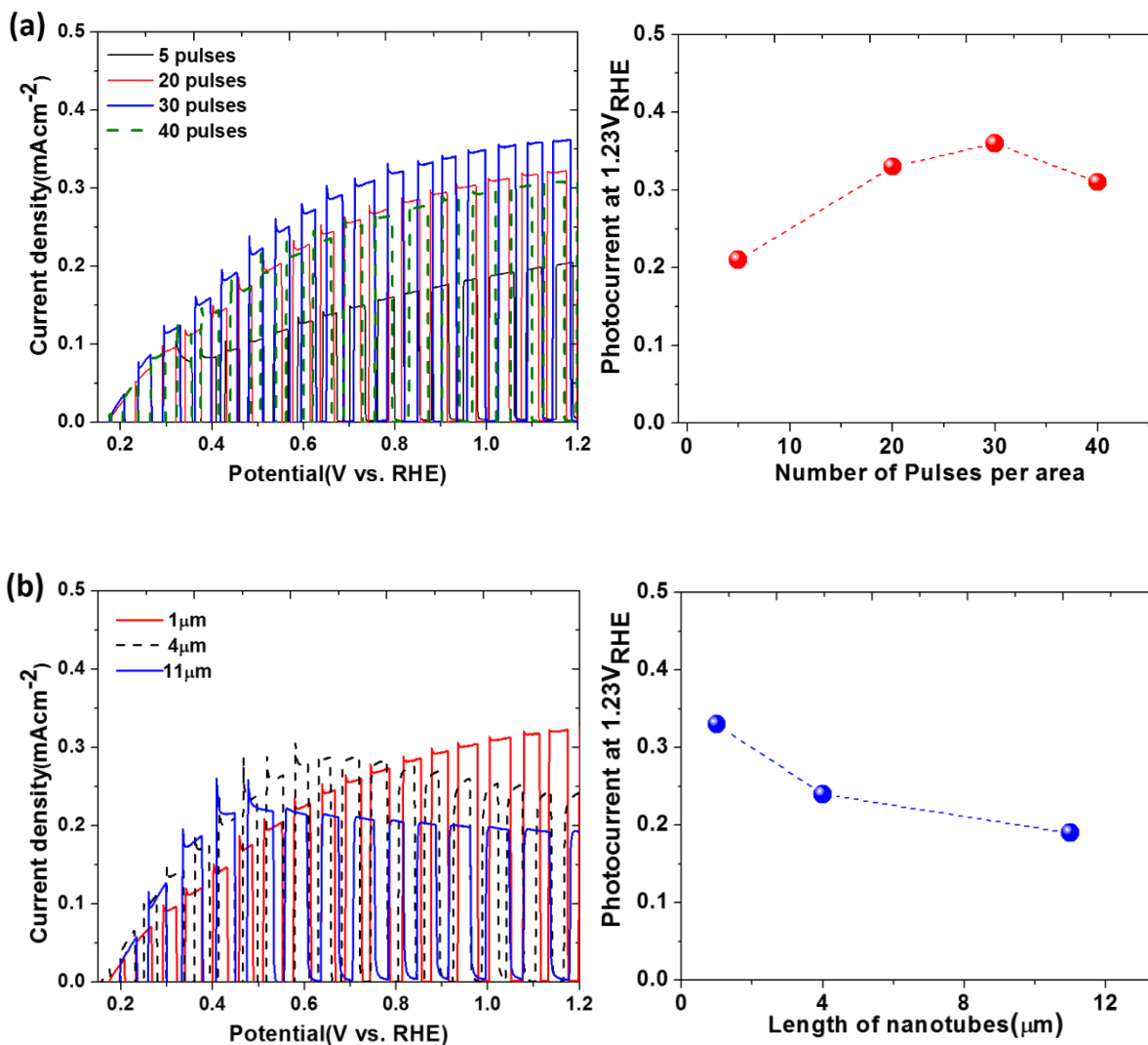


Figure 3.8 Photocurrent measurements for laser modified TiO₂ nanotube arrays (a) modified with various pulses times, and (b) with different nanotube lengths. Figures on the right compare the photocurrent at 1.23 V_{RHE} vs. (a) number of pulses per area, and (b) the nanotube length.

3.3 Selectivity of surface water oxidation reaction

The measured photocurrent during PEC measurements is often considered a proxy for the rate of PEC water splitting; however, other sources may be responsible for this photocurrent, including oxidation/dissolution of the electrode constituents or of species present in the electrolyte. In order to determine the fraction of photocurrent used to run water oxidation, photocurrent measurements were performed in a neutral phosphate buffer solution. Results for a representative set of samples with different irradiation energy, PPA, and tube length are shown in figure 3.9 (a) without hole scavenger solution and in figure 3.9 (b) with the hole scavenger. The water oxidation selectivity could be obtained by simply dividing the photocurrent values in figure 3.9 (a) by that in figure 3.9 (b).⁸⁹ Figure 3.9 (c) displays the water oxidation selectivity for nanotubes as a function of laser fluence, PPA, and nanotube length. The selectivity for pristine TiO₂ nanotube arrays reaches up to 65% at 1.23V_{RHE}. Optimally laser modified TiO₂ samples on the other hand exhibit a value of 78%, while for samples subjected to a lower PPA, the selectivity has a slight drop to 76%. The photocurrent saturates between 0.6 and ~1.0V_{RHE} while below this potential the water oxidation selectivity is low, suggesting that the hole injection process needed to oxidize water may be slow due to the small interface electric field, making this step rate-determining. By using low energy fluence or increasing the nanotube length, a drastic decay of the selectivity is observed; for example, 1μm nanotube arrays treated at 0.15 Jcm⁻², 20 pulses exhibit a value of 56%, while 4 μm NT arrays treated at 0.3 Jcm⁻², 20 pulses show water oxidation selectivity of 47% at 1.23V_{RHE}.

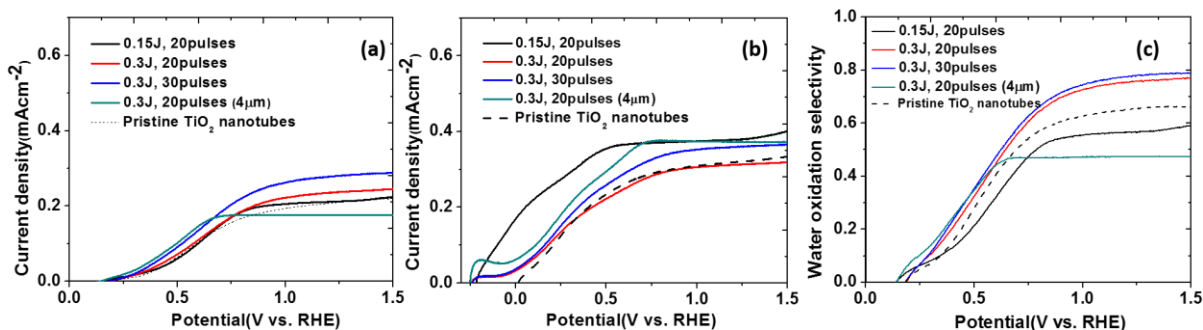


Figure 3.9 Photocurrent from laser-modified TiO₂ nanotube arrays (0.3 J cm⁻², 30 PPA) in 0.1 M phosphate buffer solution without (a) and with (b) Na₂SO₃ hole scavenger solution. (c) Water oxidation selectivity calculated by calculating the ratio of the photocurrent values in (a) vs. (b).

3.4 Conclusions

In this chapter, pulsed laser irradiation of anodized TiO₂ nanotube arrays was shown to be an effective and convenient method to enhance charge carrier density and induce crystal disorder on the anatase TiO₂ surface.⁸⁵ The process was carried out in DI water and completed in only ~ 60 s, resulting in the formation of a porous surface layer on top of a seemingly unaffected nanotube array. Optimum conditions to fabricate the laser-modified TiO₂ NT have been identified. The laser irradiation of 1μm length nanotube arrays at an energy fluence of 0.3 Jcm⁻² with 30 PPA yields optimal performance, showing a 1.6-fold increase in photocurrent with respect to the pristine TiO₂ NT arrays at 1.23 V_{RHE}. Comparing the photocurrent in neutral solution with and without a sulfite hole scavenger revealed evidence supporting the limiting performance factor under lower bias to be the oxygen oxidation kinetics. In addition, laser irradiation also increases the water oxidation selectivity, from 65% to 78% at 1.23 V_{RHE}. Electrochemical analysis reveals that laser irradiation enhances the photoelectrochemical response through an increased charge carrier donor density and a reduced amount of deep trap states. The observed decrease in crystallinity and the strain induced by a variation in lattice constant may also contribute to the enhanced performance via an enhanced

catalytic activity. The process has the potential to rapidly induce crystal disorder, but only to a limited extent (~1.6 fold saturated photocurrent density improvement) due to the limited penetration of the laser beam within the TiO₂ nanomaterial. It is of significance to develop other methods of modification which are not limited on/near the surface of TiO₂ NTs.

Chapter 4-Formation of TiO₂ sub-stoichiometries via hydrogen treatment

Hydrogen treatment at ambient pressure of TiO₂ is a typical approach to obtain the reduced TiO₂ with high level of defects (known as black TiO₂), where hydrogen reduces TiO₂ by fully or partially reducing Ti⁴⁺ to Ti³⁺ (or Ti²⁺) and creating oxygen vacancies with a corresponding change of physical and chemical properties.^{34,90-93} Wang et al.⁹⁰ reported the synthesis of hydrogenated black TiO₂ nanowires and NTs through annealing in a high purity hydrogen atmosphere at 200 to 500°C. Chen et al.⁹¹ treated bamboo-type TiO₂ in H₂ atmosphere at 400°C for 1h and demonstrated enhanced PEC and supercapacitor properties due to the increased conductivity. Zhu et al.⁹⁴ reduced TiO₂ NTs under a gas mixture of hydrogen and argon at 400 to 550°C, resulting in a reduced work function and an improved conductivity. Up to now, most of the studies based on the reduction of TiO₂ NTs have been restricted to relatively low annealing temperatures (<700°C) in order to maintain the nanotubular morphology. In this chapter, we perform the annealing of TiO₂ nanotubes in H₂ above 700°C, and investigate the degradation of the tubular morphology and the formation of a unique particle-nanowire porous structure; we also examine the corresponding phase transformation process and its relevance to PEC activity. Our strategy consists in inducing a superabundant density of oxygen vacancies, sufficient to form various Magneli phases with higher conductivity and lower band gap, thus enhancing both transport and radiation absorption. Furthermore, the density of states at the material surface is evaluated by electrochemical impedance spectroscopy while the interfacial recombination is studied by evaluating the hole transfer efficiency using a sulfite hole scavenger solution as well.⁹⁵

4.1 Morphology and phase changes induced by thermal reduction

The morphology of the thermally reduced Ti-O compounds was characterized by secondary electron micrographs. As shown in Figure 4.1, the H-650 sample (Figure 4.1 (b)) retains the same nanotube structure as the pristine anatase phase TiO₂ NTs (Figure 4.1(a)), while small particles are formed on the mouths of the tubes, increasing the surface roughness. After a 700°C annealing (Figure 4.1 (c)), the pore sizes of the nanotube mouths are observed to shrink, while the pore size decreases drastically with increasing reduction temperature, up to 750°C (Figure 4.1(d)), where the nanotube structure started to degrade. The TiO₂ NTs finally undergoes a complete morphology change at 800°C (Figure 4.1(e)), where the nanotube geometry is completely lost and a mixture of particles and nanowires form instead. Specifically, the particle size varies from 0.5 to 3 μm, with the aggregation caused probably by the fast adatom diffusion along high mobility direction and in part by internal stresses at high temperatures, while the length of the nanowires ranges from 2 to 10 μm. The cross sectional images for the TiO₂ NTs are shown in the insets, revealing that the NT lengths of around 4 μm remains intact for annealing temperatures lower than 800°C, while at 800°C (Figure 4.1(f)), the surface layer of the particle-nanowire has a thickness of ~4 μm, which is similar to the nanotube precursor. Therefore significant degradation of the NT morphology occurs between 750 and 800°C and a new microparticle-nanowire porous structure is formed.

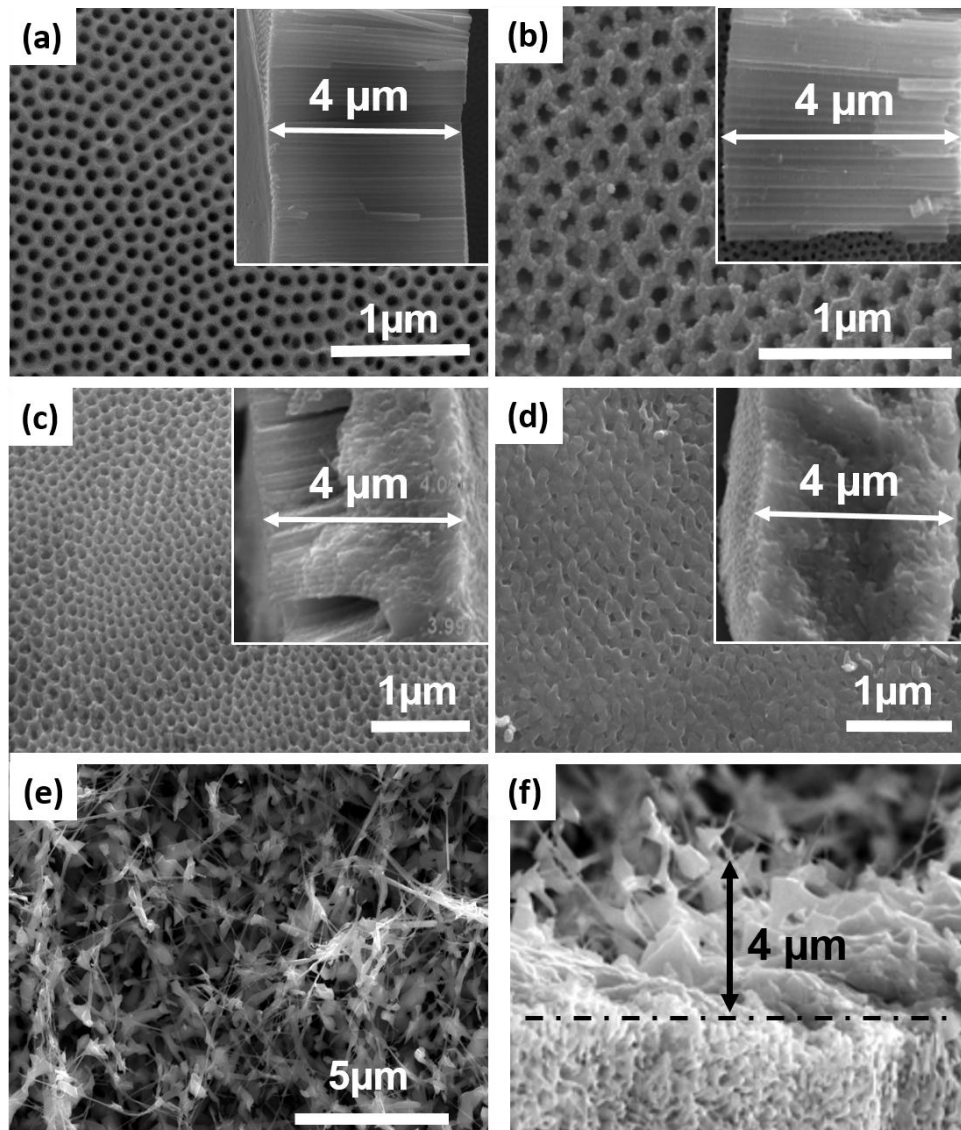


Figure 4.1 Top view SEM images of pristine and thermal hydrogen reduced Ti-O compounds under various reduction temperatures: (a) pristine without reduction, (b) 650°C, (c) 700°C and (d) 750°C (e) 800°C (top view) and (f) 800°C (cross section). The insets are the cross section images exhibiting the film thickness.

In order to elucidate the effect of thermal reduction on the structural changes, the crystal phases obtained under various annealing conditions are characterized by X-ray diffraction. From Figure 4.2 (a), the pristine TiO₂ indicates only anatase phase peaks due to the annealing process at 350°C in air, and the α -titanium hcp phase peaks coming from the substrate. For the H-750 sample, the

intensity of most of the anatase phase peaks decreases drastically while the (004) peak slightly increases. Meanwhile, several peaks belonging to rutile TiO_2 appeared as the rutile phase is thermodynamically preferred,⁹⁶ and the formation of corundum Ti_2O_3 was determined by the diffraction peaks from the (012), (110) and (113) planes. The phase change further progressed in the H-800 sample, where all the anatase peaks disappear. Intense reflections from corundum Ti_2O_3 demonstrate that this is one of the dominant phases in this reduced Ti-O compounds. On the other hand, it is also interesting to observe some weak peaks from the Ti_4O_7 Magnéli phase. Furthermore, the peak appearing at $\sim 43.8^\circ$ exhibits the presence of the TiO compound phase, as evidenced by the most intense diffraction from the (2-31) and (002) planes. It should be noted that the order of formation of the various phases does not correspond to an increasing oxygen deficiency. We hypothesize instead that the energy barrier for nucleation and the enthalpy of formation (ΔH_f) for each phase determines the rate of nucleation and growth. The values of ΔH_f for these phases correspond mostly to their order of appearance, supporting the hypothesis. These values can be found in Table 4.1.

Table 4.1. Formation enthalpy of different Ti-O phases

Phases	Formation enthalpy(kcal./mol)	ref
Ti	3.26	[97]
Anatase TiO_2	-224.4	[97]
Rutile TiO_2	-225.6	[98]
Ti_4O_7	-768.65	[97]
Ti_2O_3	-339.02	[97]
TiO	-118.05	[97]

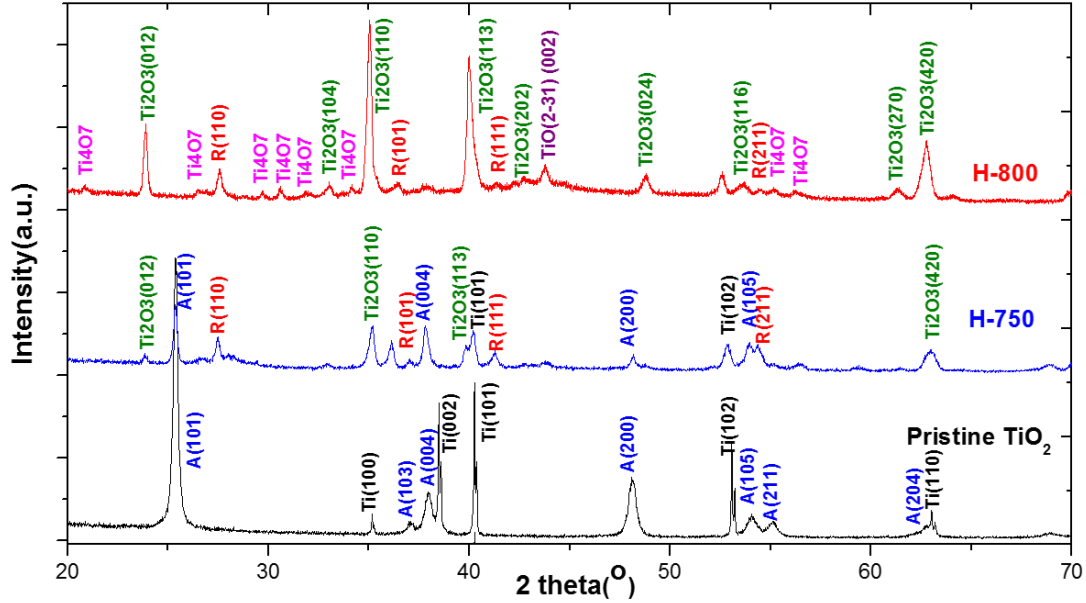


Figure 4.2 XRD patterns of thermal hydrogen reduced Ti-O compounds compared with pristine TiO₂ NTs with anatase phase.

The phase transformations occurring during the annealing process may explain the shrinking of the nanotubes and finally the collapse of the structure; the various phases being formed from the initial anatase in fact are likely nucleating both at the tube mouth and at the interface between the Ti and the TiO₂ NTs.⁹⁹ The new phases have a different crystal structure, preferential growth direction and density, inducing growth at the tubes facets and internal stresses that eventually cause the filamentary morphology seen in Figure 4.1 (e).

The TiO compound exhibits metallic-type conduction ($\sigma_{\text{TiO}} = \sim 105(\Omega \text{ cm})^{-1}$) in the rock salt structure,¹⁰⁰ and therefore a much higher electrical conductivity compared with semiconducting TiO₂. On the other hand the Ti₄O₇ phase, as a semiconductor, has been reported to exhibit a much narrower optical band gap of 0.6 eV at room temperature¹⁰¹ than that of the anatase TiO₂ (3.2 eV), possibly broadening the spectral response of TiO₂ from a wavelength of 387 nm to 2068 nm, in

the far infrared region. The presence of such a multiphase composite may thus enhance both absorption and the charge transfer process in a photoelectrochemical reaction.⁴⁴ In order to better understand these properties however, it is necessary to determine the distribution and connectivity of such phases, and whether photoactive phases are present at the surface or in the bulk. An ideal configuration would consist of a low bandgap semiconductor at the surface, with metallic phases in the inner volume to enhance charge carrier transport. The observed color change of the sample from brown (before) to black after the reduction reaction is consistent with the absorption of visible light as expected, and is shown in Figure 4.3.

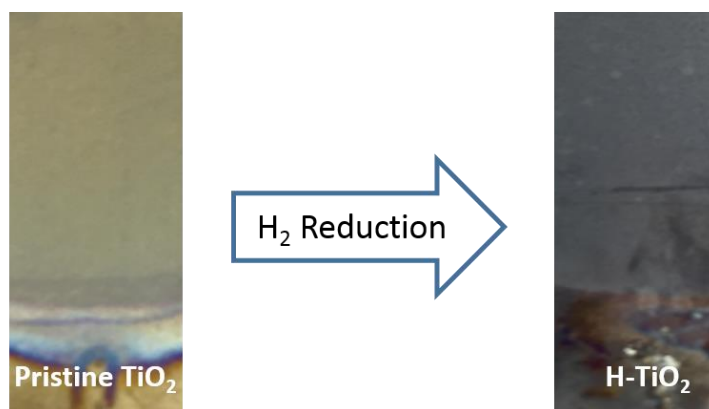


Figure 4.3 Photographs of pristine TiO_2 and thermal reduced Ti-O compounds.

In order to assess the change in oxidation state of Ti and better determine the oxide species present at the surface, X-ray photoelectron spectroscopy was employed to compare the difference between pristine TiO_2 and the reduced Ti-O composite annealed at 800°C ; the measurements were performed without previous sputter-etching. The high resolution O 1s and Ti 2p spectra are shown in Figure 4.4 (a) and (b), respectively. In Figure 4.4 (a), a more intense O 1s peak is observed at 530.2 eV. In addition, a broader shoulder is present for the H-800 sample compared to pristine TiO_2 . This shoulder is associated with Ti-OH bonding, which is 1.5 – 1.8 eV higher than the O 1s

binding energy, revealing that more hydroxyl groups are formed on the surface after the thermal reduction reaction.¹⁰² In Figure 4.4 (b), two peaks are observed, associated with the Ti 2p_{1/2} and 2p_{3/2} centered at binding energies of 464.6 eV and 458.9 eV, which are consistent with the standard values of TiO₂.¹⁰³ No obvious shift of binding energy, nor features related to Ti³⁺ are observed at 457.0eV^{104,105} for the reduced sample, suggesting a limited fraction of Ti³⁺ at the surface, as observed by others.¹⁰⁶ Despite the large phase fraction of Ti₂O₃ supported by XRD, there is no evidence for Ti³⁺ at the surface according to XPS, probably due to the interior location of this phase and the limited penetration length (~ 2 nm). Moreover, Ti³⁺ is susceptible to oxidation by environmental oxygen, and may not be stable for a long period of time on the very surface.¹⁰⁷

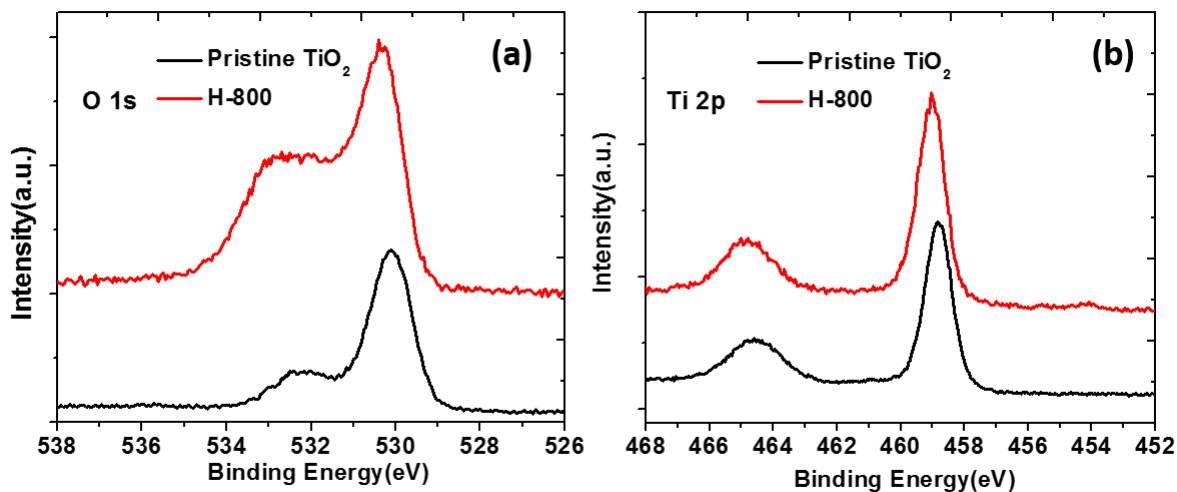


Figure 4.4 (a) High resolution O 1s XPS spectra and (b) High resolution Ti 2p XPS spectra of the pristine TiO₂ and H-800.

4.2 Crystal structure and phase analysis by Rietveld refinement

The crystal structures of rutile (TiO₂), anatase (TiO₂), and corundum (Ti₂O₃) are well known, while those of the Magnéli series are more complicated. To concisely describe the crystal structures of

the sub-stoichiometric Magnéli series ($\text{Ti}_n\text{O}_{2n-1}$) and their relationship to that of the stoichiometric end members (i.e. corundum ($n = 2$) and rutile ($n \rightarrow \infty$)), a unified representation scheme reported by Schwingenschlögl et. al is adapted in the following.¹⁰⁸ We start with a description of the crystal structure of rutile, whose unit cell is presented in Figure 4.5 (a). The titanium atoms form chains of infinite length along the c-axis. Each Ti atom is located at the inversion center of an oxygen octahedron. Adjacent oxygen octahedra filled with Ti atoms on the same chain are edge-sharing and have the same orientation; adjacent oxygen octahedra filled with Ti atoms on adjacent chains are corner-sharing and their orientations are related by a 90° rotation about the rutile c-axis. Octahedra of the same orientation form a chain along the rutile c-axis. Chains of octahedra of the same orientation line up along the rutile a- or b-axis to form a slab. Slabs of octahedra of different orientations stack alternately along the rutile a- or b-axis to form the entire oxygen sub-lattice. The oxygen sub-lattice of rutile can thus be envisioned as a network of oxygen octahedra, which is the common feature that unifies the sub-stoichiometric Magnéli series ($\text{Ti}_n\text{O}_{2n-1}$) and the stoichiometric end members (TiO_2 and Ti_2O_3). To represent the crystal structure of other members in the series, the oxygen sub-lattice of rutile is kept intact. Crystal directions for any member in the series can then be defined with respect to the principle axes of a rutile unit cell, which will be called the pseudo-rutile axes (a' , b' , c') in the subsequent context. The circles in Figure 4.5 (b), (c) and (d) show the projection of atoms along the pseudo-rutile a-axis of a slab consisting of two chains of octahedra. From Figure 4.5 (b), (c), and (d), one can see that different members in the $\text{Ti}_n\text{O}_{2n-1}$ series ($n \geq 2$) consist of Ti chains of different lengths, being aligned with the pseudo-rutile c' -axis. Notice that the chain length coincides with the degree of stoichiometry (n) in the chemical formula: the Ti chains in rutile TiO_2 ($n \rightarrow \infty$) are not interrupted at all; the Ti chains in Magnéli Ti_4O_7 ($n=4$) are interrupted every four Ti atoms; the Ti chains in corundum Ti_2O_3 ($n=2$) are

interrupted every two Ti atoms and etc. In general, for a member in the series of lower oxygen content (smaller n), the Ti chains are shorter (i.e. more frequently interrupted). With the above description, we intend to capture the common feature of the $\text{Ti}_n\text{O}_{2n-1}$ ($n \geq 2$) series and the correlation between their stoichiometries and their crystal structures. TiO ($n=1$) belongs to the monoclinic system and has a crystal structure that cannot be unified with the scheme described above. The crystal structure of TiO is shown in Figure 4.5 (e) using the representation proposed by Valeeva et al., where the atoms and vacancies are projected in the $[110]_{C2/m}$ direction onto the $(21-1)_{C2/m}$ plane.¹⁰⁹

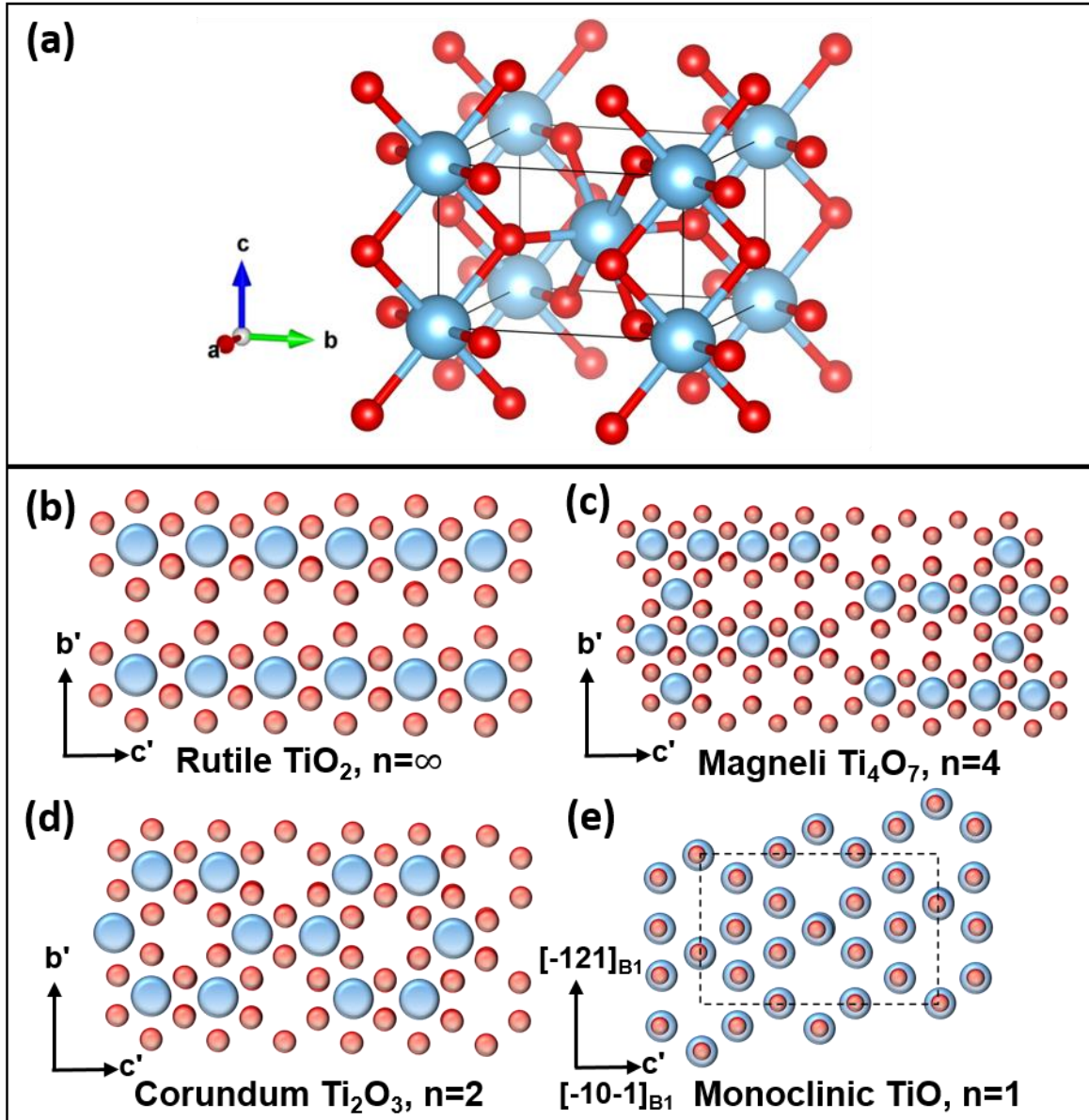


Figure 4.5 (a) A conventional unit cell of rutile TiO_2 and the projections along a' axis of O-Ti-O reflecting the crystal structures with a decreasing stoichiometry of (b) rutile TiO_2 , (c) Magnéli Ti_4O_7 , (d) Corundum Ti_2O_3 and (e) Monoclinic TiO . The blue and red spheres represent Ti and O atoms respectively.

Rietveld refinement was carried out to further confirm the presence of the phases and to evaluate the phase fractions, in particular those of Ti_4O_7 and TiO that have low symmetry, triclinic and

monoclinic structure, respectively. The refinement results are displayed in Figure 4.6. The phase fraction of Magnéli Ti_4O_7 , monoclinic TiO , Corundum Ti_2O_3 and Rutile TiO_2 was determined by Rietveld refinement to be 11.2, 64.3, 22.9 and 1.64 At%, respectively, indicating that the first three sub-stoichiometric phases are dominant, while the rutile phase almost disappears. Detailed parameters for the refinement are provided in Table 4.2. Being the only metallic phase in the Ti-O composite, and one of the main phases, TiO should contribute most of the charge carriers. A rough estimate of the average charge carrier density of the compounds can be obtained by dividing the theoretical value of TiO ($4.75 \times 10^{22} \text{ cm}^{-3}$) by the overall sample volume, resulting in an average electronic density of $\sim 3 \times 10^{22} \text{ cm}^{-3}$.¹¹⁰

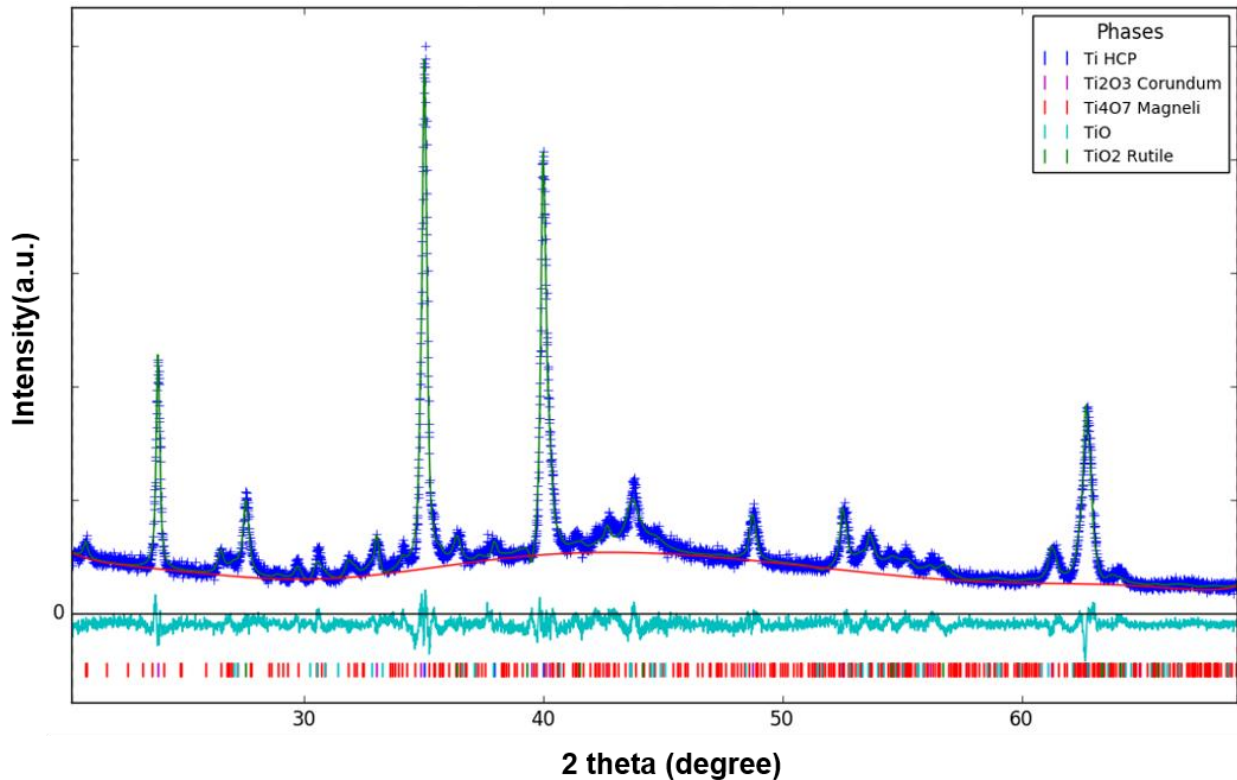


Figure 4.6 Rietveld refinements of H-800 sample. The blue line represents the XRD pattern, red line represents fitting of background, cyan line represents the deviation between measured and fitting results, and vertical bars show the positions of featured peaks of various phases.

Table 4.2 Detailed Rietveld refinement parameters and results from H-800 sample

No. of observations	6095				
No. of parameters	68				
wR	7.60%				
R	6.04%				
R _{brg}	5.60%				
wR _{brg}	7.60%				
wR _{min}	5.09%				
chi ²	13566.2				
GOF	1.50				
Chemical Formula	Ti	Ti ₂ O ₇	TiO	TiO ₂	Ti ₂ O ₃
Space Group	P 63/m m c	P-1	A 2/m	P 42/m n m	R -3 c
Weight Fraction	0.01445	0.30603	0.37097	0.01228	0.29627
Weight Fraction Sig	0.00153	0.03091	0.04362	0.02078	0.04238
Thin Film Wt.%	N.A.	31.1%	37.6%	1.2%	30.1%
Thin Film Wt.% Sig	N.A.	3.1%	4.4%	2.1%	4.3%
Mustrain	6180.7	14783.6	22802.7	16631.4	7831.5
Mustrain Sig	93.2	940.5	882.2	543.1	156.6
R _f	2.18%	6.58%	3.42%	3.42%	4.35%
Lattice Parameters					
a (Å)	2.964832	5.617060	9.118012	4.593041	5.154219
b (Å)	2.964832	7.113574	4.149516	4.593041	5.154219
c (Å)	4.753734	12.460166	5.794634	2.934250	13.720864
alpha (°)	90.000	94.9299	90.000	90.000	90.000
beta (°)	90.000	95.1425	107.4165	90.000	90.000
gamma (°)	120.000	108.7673	90.000	90.000	120.000

4.3 Photoelectrochemical properties of TiO₂ sub-stoichiometries

Linear sweep voltammograms collected from the samples H-650, H-750 and H-800 as a function of potential are shown in Figure 4.7 (a). All these photocurrents increase with applied potential and reach saturation values before 1.0 V_{RHE}, while the slight increase afterwards for H-650 is mainly attributed to the dark current increase. The onset potential of the reduced samples and the pristine TiO₂ are found to be almost identical at ~ 0.16V_{RHE}. As shown in Figure 4.7 (b), a slight

photocurrent increase at $1.23V_{RHE}$ is observed for H-650 from 0.23 mAcm^{-2} to 0.25 mAcm^{-2} compared with pristine TiO_2 , while for H-750 the value increases to 0.35 mAcm^{-2} . The optimum photoresponse occurs at the reduction temperature of 800°C , where the Ti-O compound exhibits a photocurrent of 0.54 mAcm^{-2} , which results in a 2.4-fold enhancement compared to pristine TiO_2 . Photocurrent densities measured in a wider range of reaction temperatures is displayed in Figure 4.8 (a) and (b). The photoresponse of thermally reduced compounds is related to the reduction temperature: from 650°C to 800°C , the photocurrent density increases with the annealing temperature, while from 800°C to 850°C the response starts to decay. To further understand the correlation between annealing conditions and the Ti-O stoichiometry, EDS measurements were carried out, and the oxygen/titanium ratio is plotted in Figure 4.7 (b). Below 750°C , the oxygen content decreases with increasing annealing temperature from an atomic O/Ti ratio of 1.75 at 650°C to 1.39 at 750°C , while this same ratio rises to 1.50 at 800°C ; this may be due to the significant morphology change. The associated EDS mapping is provided in Figure 4.9. The corresponding photoconversion efficiency (η) as a function of applied potential is shown in Figure 4.7 (c); this is calculated from the equation: $\eta = J_o(1.23 - V_{RHE})/P_{light}$, where J_o is the photocurrent density, V_{RHE} is the applied potential vs. the reversible hydrogen reference, and P_{light} is the power density of the light source. According to this equation, best materials achieve the maximum photocurrent at a relatively low applied bias. From Figure 4.7 (c), the H-650 sample shows a maximum conversion efficiency of 0.12% at $0.48V_{RHE}$ similar to the pristine TiO_2 (0.12% at $0.53V_{RHE}$), while for H-700 and H-750 the efficiency increased to 0.13% and 0.19% and occurred at decreasing applied potential of $0.53V_{RHE}$ and $0.47V_{RHE}$, respectively. The H-800 sample exhibits the maximum conversion efficiency of 0.33% at $0.45V_{RHE}$.

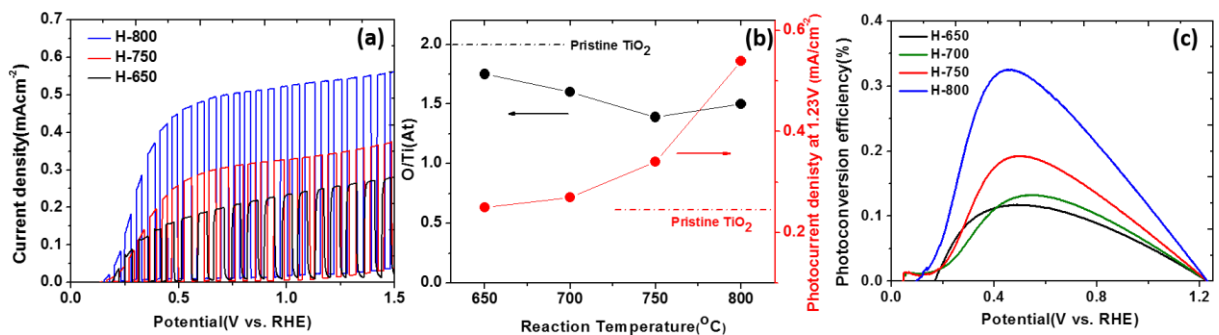


Figure 4.7 (a) Linear sweep voltammograms collected from reduced Ti-O compounds at different annealing temperatures, in a 1 M KOH solution with a scan rate of 10mV/s under 100mW/cm² pulsed illumination. (b) Atomic percent ratio of oxygen/titanium measured with EDS (black dots) and the measured photocurrent density for reduced Ti-O compounds at 1.23V_{RHE} (Red dots). (c) Calculated photoconversion efficiencies for the reduced Ti-O compounds as a function of applied potential.

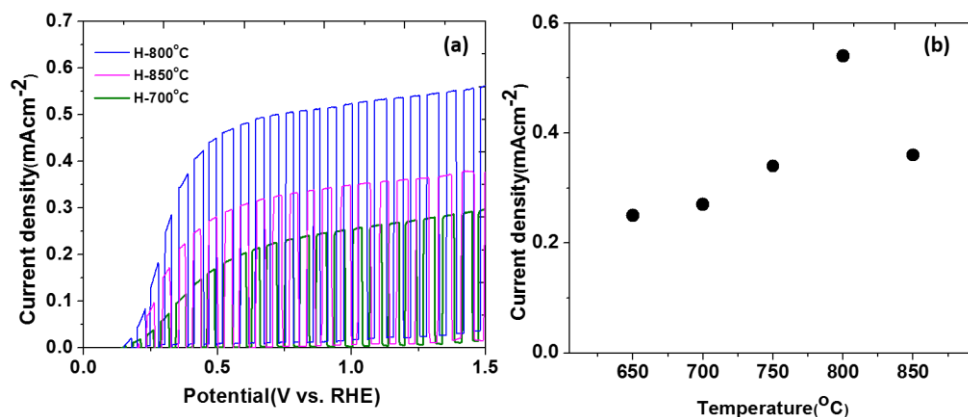


Figure 4.8 (a) Photocurrent density vs. applied potential for H-700, H-800 and H-850 in 1M KOH solution under pulsed AM 1.5G solar illumination. (b) Dependency of photocurrent density at 1.23V_{RHE} vs. reduction temperature. The optimum condition occurs at 800°C.

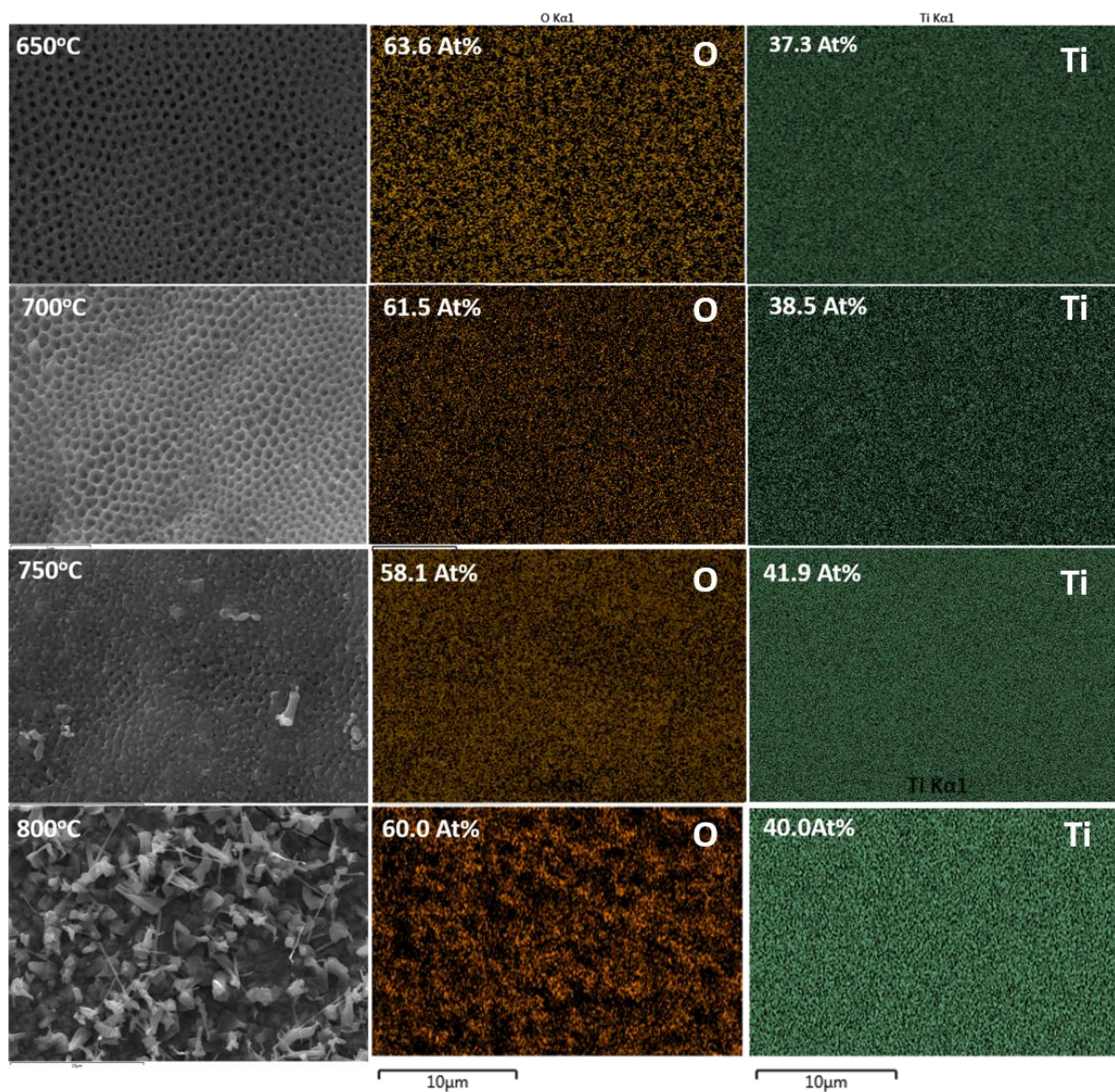


Figure 4.9 EDS mapping of (a) H-650, (b) H-700, (c) H-750 and (d) H-800 from the top view of Nts. The elemental distribution is uniform for the first three samples, while for H-800, the particles on the surface are oxygen-rich.

Aside from the generation of oxygen deficient Ti-O compounds at higher temperature as indicated by XRD analysis, oxygen loss could also be associated with the incorporation of H into the TiO₂ structure; this has been reported by Amano et al. in powder rutile TiO₂ annealed at 700°C in H₂, where Ti-OH bond formation was detected.¹⁰⁶ The incorporation of hydrogen has been known to

contribute to n or p-type conductivity, depending on the type of the host material.¹¹¹ According to these authors, H-incorporation in TiO₂ allows for the alignment of the energy level of hydrogen to be around the conduction band minimum of TiO₂, possibly resulting in an increase of n-type conductivity in the host TiO₂. This may partially explain the enhanced photocurrent response for the TiO₂ NTs at 700°C, 750°C and 800°C.

The dependence of photocurrent density on reduction time at 800°C has also been investigated as shown in Figure 4.10; the optimal reaction time is 0.5 h, with a 2h reduction process showing the same current response.

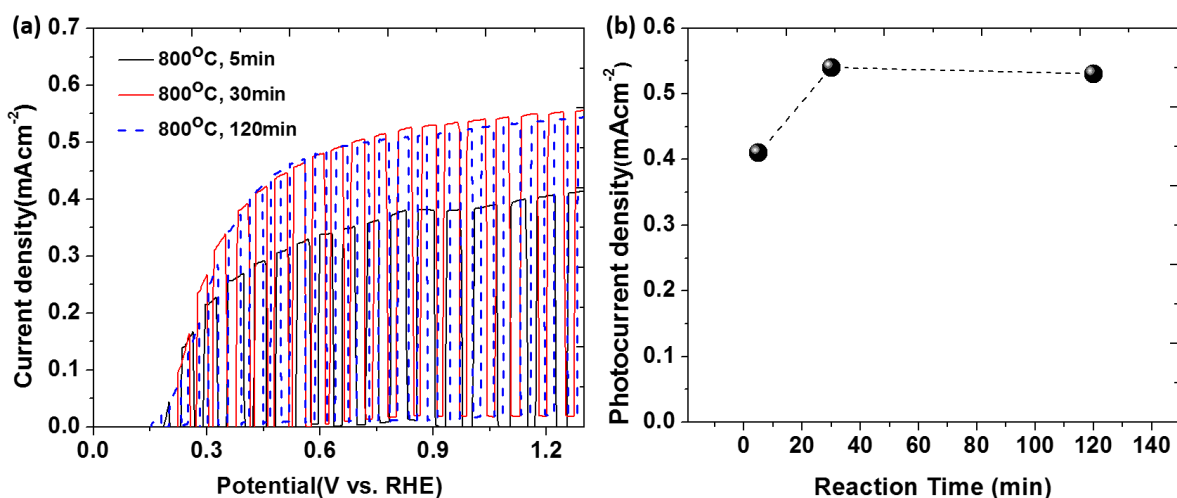


Figure 4.10 (a) Linear sweeps voltammograms collected from Ti-O compounds reduced at 800°C for 5min, 30min and 120min. (b) Measured photocurrent density at 1.23V_{RHE}. The photocurrent density increases from 0.4 mA cm⁻² for 5min reduced sample to 0.54 mA cm⁻² for the 30min reduced Ti-O compound, while the values of 30 min and 120 min are almost the same, indicating the reduction time of 30 to be the optimal condition.

To investigate the dependence of PEC properties on the donor density, Mott-Schottky plots were measured by EIS for the pristine TiO₂, H-750 and H-800; the data are presented in Figure 4.11. All samples exhibit a positive slope, confirming n-type doping. The density of donors for pristine

TiO₂ is $3.92 \times 10^{19} \text{ cm}^{-3}$ as shown in Figure 4.11 (a), in accordance with the reported value for anatase TiO₂.¹¹² An enhancement in doping level of ~1 or 2 orders of magnitudes is achieved for H-750 ($2.48 \times 10^{20} \text{ cm}^{-3}$) and H-800 ($9.38 \times 10^{21} \text{ cm}^{-3}$), as shown in Figure 4.11 (b) and (c). The high density of charge carriers for H-800 is mainly attributed to the dominance of metallic TiO, with a charge carrier density of $\sim 4.75 \times 10^{22} \text{ cm}^{-3}$. These results imply that the increase of charge carrier density on the surface induced by the thermal reduction largely contributes to the modification of PEC properties.

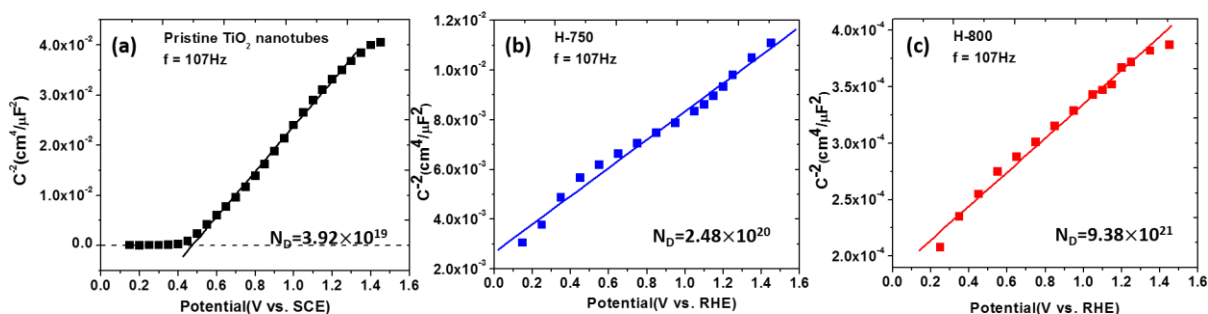


Figure 4.11 Mott-Schottky plots and calculated density of donors for (a) pristine TiO₂, (b) H-750 and (c) H-800 measured by EIS at a fixed frequency of 107 Hz measured.

It should be noted that this calculation is based on the assumption that the capacitance is mainly contributed by the bulk space charge, neglecting the presence of surface states. However, the H-750 and H-800 samples consist of large fractions of substoichiometric Ti-O compounds instead of pure TiO₂, and the contribution of the capacitance from surface states may not be negligible. This may lead to a deviation from the linear fits of ideal Mott-Schottky plots, as shown in Figure 4.11 (b) and (c), where varying slopes are observed. In order to investigate this effect in detail, M-S plots were measured using various frequencies in the range from 11 kHz to 1 Hz, as shown in Figure 4.12. From Figure 4.12 (a) (b) and (c), the traces collected at high frequency present similar slopes, while at medium and low frequencies, the slopes depend on frequency, probably due to the

contribution of surface states to the capacitance, leading to a higher calculated value of donor density. For the H-800 sample instead, the slopes measured at medium and low frequencies show much less deviation from linearity, as shown in Figure 4.12 (d) (e) and (f), suggesting that the main contribution to the overall capacitance is from the bulk space charge, and the estimated density of donors on this sample is closer to the real value. On the other hand, since both materials consist of semiconducting and metallic phases, it may be inappropriate to utilize the Mott-Schottky model. Despite the fact that these results may not provide an accurate value, these estimates are reasonable if compared to the charge carrier density obtained by the crystallographic phase composition as previously discussed.

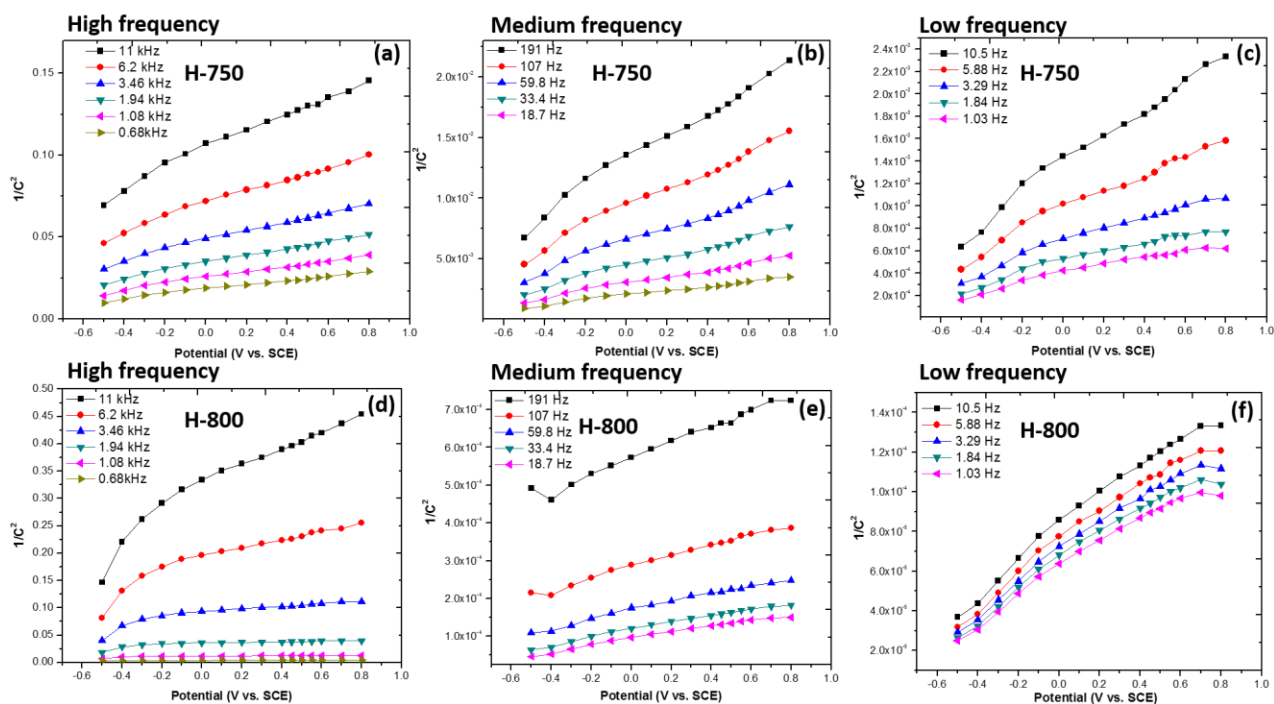


Figure 4.12 Mott-Schottky plots for (a) high frequency (b) medium frequency and (c) low frequency for H-750, and (d) high frequency (e) medium frequency and (f) low frequency for H-800. High frequency represents the range from 11k Hz to 0.68k Hz, medium frequency represents the range from 191Hz to 18.7Hz, and the low frequency represents the range from 10.6Hz to 1.03Hz. This denomination is only for the more precise discussion.

The observed formation of conducting and semiconducting phases could possibly increase charge carrier density and may enhance transport and light absorption, respectively, while the significant oxygen loss may facilitate formation of active Ti^{3+} sites, although we have not been able to detect such species, probably due to the limited lifetime.¹¹³ Measurements of Incident Photon to Current Efficiency (IPCE) and the absorption on H-800 samples in Figure 4.13 (a) and (b) however have shown that absorption is enhanced, but this does not result in visible light induced photocurrent, suggesting limited coupling between photoexcited orbitals and the electronic states responsible for the photocurrent. This leads us to hypothesize that a combination of enhanced transport and improved catalytic activity/selectivity could be responsible for the observed PEC response.

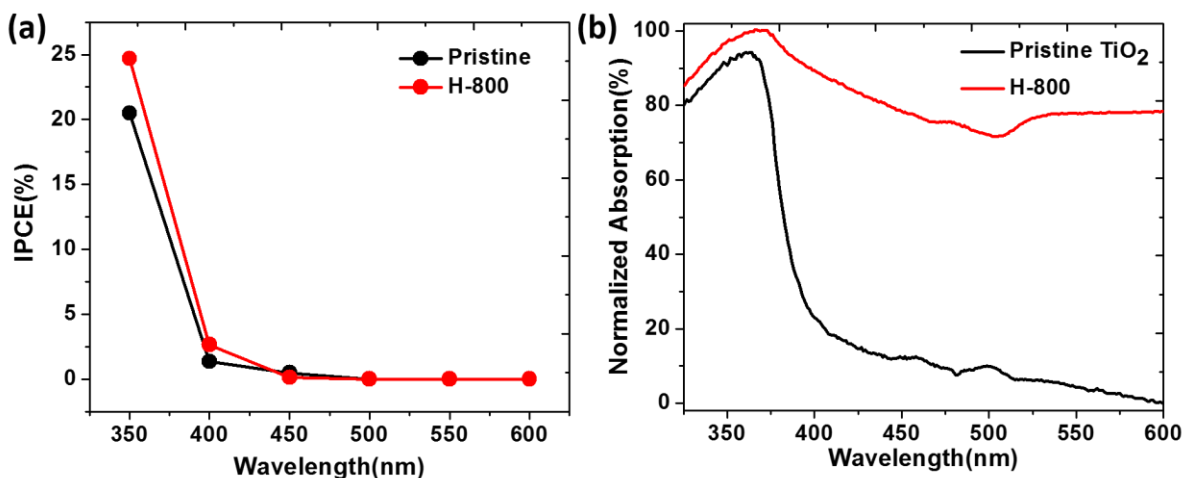


Figure 4.13 (a) IPCE vs. wavelength of pristine TiO_2 and H-800 sample measured by using a 250W QTH lamp powered by Princeton Instrument TS-428 PSU. IPCE increase is only observed in the UV region. (b) Absorption spectrum measured by using a Cary Varian 5E UV-VIS-NIR spectrophotometer. H-800 sample shows absorption improvement in the visible region compared with pristine TiO_2 .

4.4 Water oxidation kinetics at the interface for TiO₂ sub-stoichiometries

The water oxidation selectivity can be determined by comparing the measured photocurrent in the electrolyte of choice to that tested in the same solution with a fast-oxidizing species with a ~ 100% oxidation selectivity, assuming that the charge separation yield is the same in the bulk material, as discussed in the previous chapters. In Figure 4.14 (a) and (b), photocurrent densities from thermally reduced Ti-O compounds in 0.1 M phosphate buffer solution without and with 1 M Na₂SO₃ are plotted, and from these data water oxidation selectivity is calculated by simply dividing the two sets of photocurrent values. In Figure 4.14 (c), the water oxidation selectivity of H-650 is seen to constantly increase with the applied potential, possibly due to the lifetime increase of the surface holes that are kept from recombination by the increasing bias.¹¹⁴ The water oxidation selectivity of all other samples reaches a saturation value between 0.6 and 1.0 V_{RHE}, similar to the potential range where photocurrent saturates. This finding can be rationalized assuming that the interfacial recombination is the rate determining step before the saturation potential, where the hole injection process is limited by the small interface electric field. On the other hand, the water oxidation selectivity calculated at 1.23V_{RHE} is shown in Figure 4.14 (d) as a function of reduction temperature; the yield of H-650 reaches 60%, close to that of a pristine TiO₂ (65%). Ti-O compounds treated at higher temperature in contrast show a vast increase in the water oxidation selectivity, which reaches 85%, 87% and 92% for H-700, H-750 and H-800 respectively, indicating that the interface recombination no longer limits the PEC reaction at higher potential. Saturation of the photocurrent is associated to the maximization of the space charge layer within the nanotubes or in the filamentary morphology of H-800.¹¹⁵ Another possibility is that saturation could result from the Fermi level pinning, if a sufficiently high defect density are generated.¹¹⁶ We conclude that for reduced Ti-O compounds the interfacial recombination is no longer the rate-

determining process at high bias; the effects of space charge layer limitations or Fermi level pinning instead dominate.

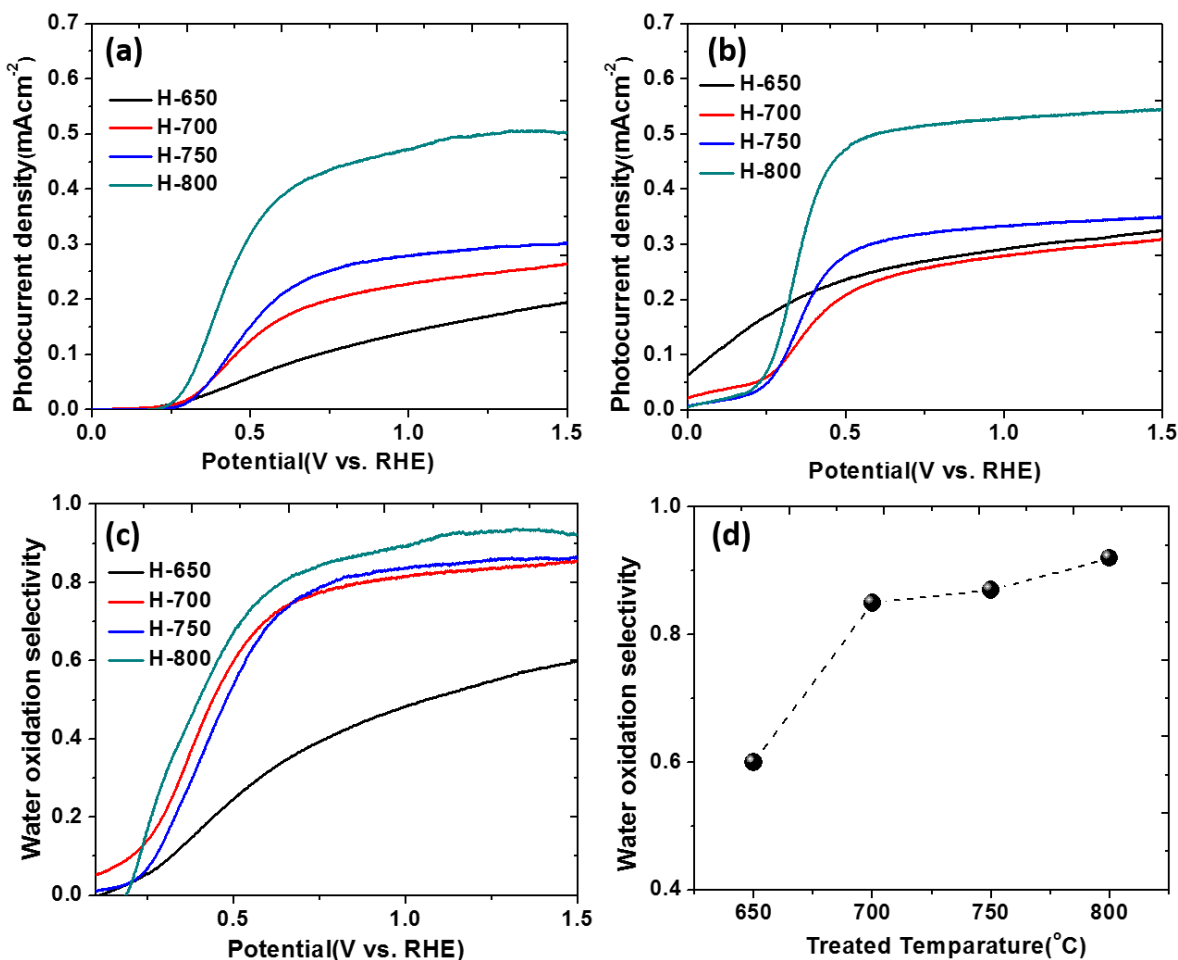


Figure 4.14 Photocurrent density from thermal reduced Ti-O compounds in 0.1 M phosphate buffer solution without (a) and with (b) 1M Na₂SO₃ hole scavenger solution. (c) Calculated water oxidation selectivity by comparing the photocurrent density values in (a) and (b). And (d) water oxidation selectivity as a function of annealing temperature at 1.23V_{RHE}.

4.5 Thermal reduction vs. electrochemical reduction

In our previous work^{20,114}, we showed that electrochemical (EC) doping with hydrogen can cause photocurrent increase due to trap state passivation. On the other hand, hydrogen doping has also

been reported as an effective modification method to improve the photoelectrochemical properties of transition metals.¹¹⁷⁻¹¹⁹ In order to compare EC vs. thermal reduction and, by combining the two, hopefully improve the PEC performance of the thermal reduced Ti-O compounds, pristine TiO₂ NTs and thermally reduced Ti-O compounds were EC doped with H⁺ at a negative potential bias. EC-doping is reported not to change the structure and morphology of TiO₂ NTs²⁰, which is also confirmed by our results in Figure 4.15 (a) and (b).

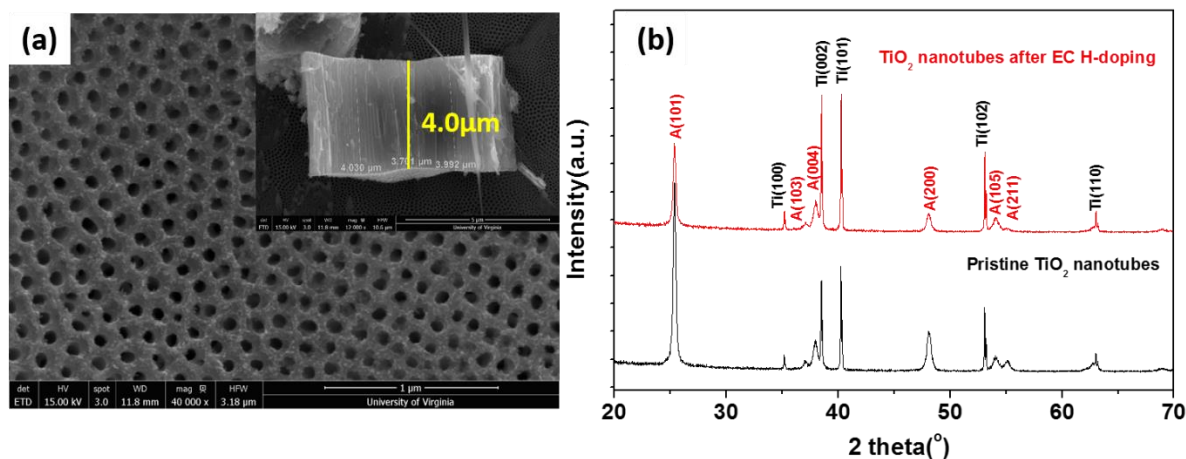


Figure 4.15 (a) SEM image of the top view and cross-section of the EC-doped TiO₂ NTs. (b) XRD patterns of the pristine TiO₂ and EC-doped TiO₂ NTs. No obvious morphology or phase change is observed for the doped TiO₂ compared with pristine TiO₂.

Figure 4.16 (a) compares the pulsed photo response of pristine TiO₂, EC-doped TiO₂ (EC-TiO₂) and a thermally reduced Ti-O compound (H-800). The photocurrent is saturated before 1.0 V_{RHE} for both the pristine TiO₂ and thermally reduced Ti-O compound, while it increases gradually for the EC-doped TiO₂, such that at 1.5 V_{RHE}, the photocurrent in the EC-TiO₂ equals that of the thermal reduced sample, which shows around 2.5-fold improvement compared to pristine TiO₂. The unsaturated photocurrent of EC-doped TiO₂ is attributed in part to a significant series resistance, and possibly with the unpinning of the Fermi level caused by the passivated trap

states.^{20,116} However, the early saturation potential makes thermally reduced Ti-O superior to EC-doped TiO₂ due to a larger photoconversion efficiency as shown in Figure 4.17. Figure 4.16 (b) exhibits the photocurrent density at 1.23V_{RHE} for thermally reduced Ti-O compounds without and with further EC-doping. For the H-650 sample, a large photocurrent increase of 0.2 mA cm⁻² is observed, while only a 0.04 mA cm⁻² increment is found in H-700. For H-750 and H-800.

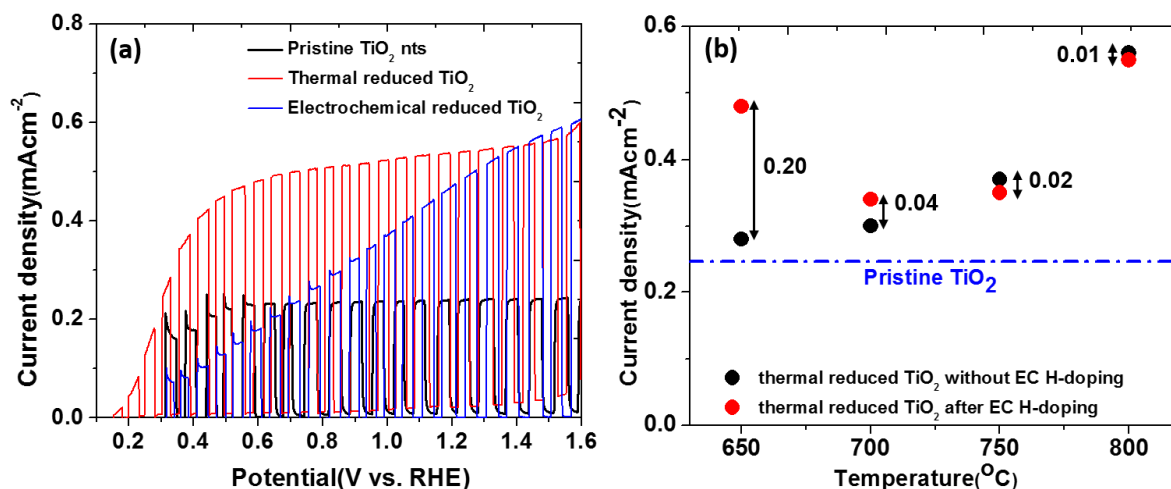


Figure 4.16 (a) Linear sweep voltammograms of pristine TiO₂ NTs, thermal reduced Ti-O compounds and EC reduced TiO₂ NTs. (b) A comparison of photocurrent density of thermal reduced Ti-O compounds without and with further EC H-doping. The differences between the values are marked.

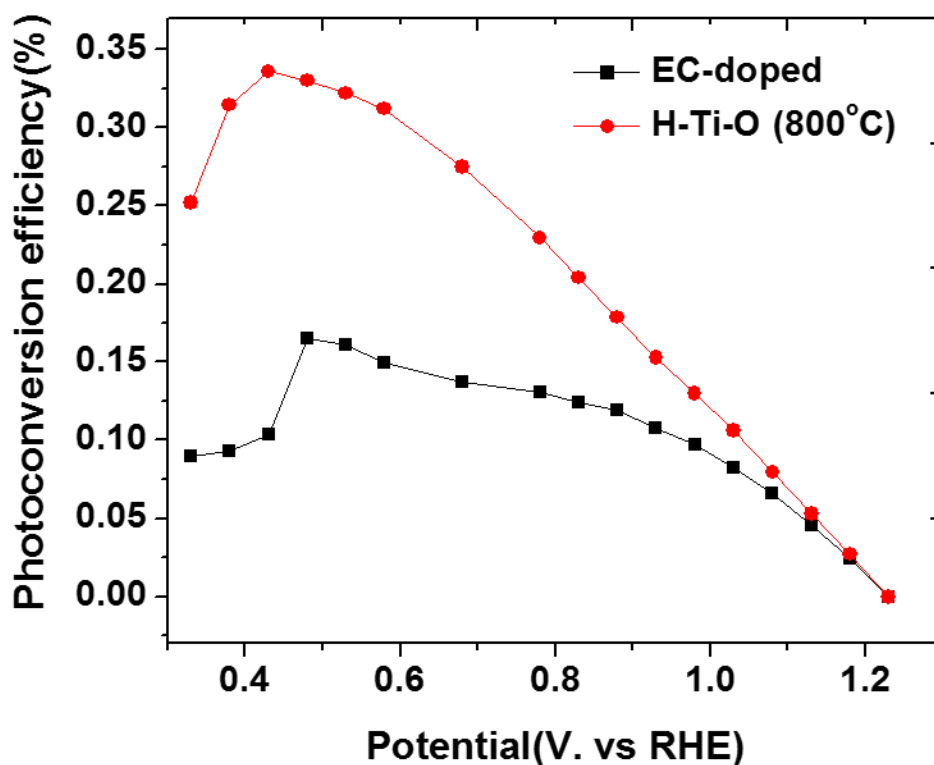


Figure 4.17 Calculated photoconversion efficiencies for the thermal-reduced Ti-O compounds and EC-doped TiO₂. The thermal reduced sample exhibit enhanced conversion efficiency.

The difference in photoresponse is quite small, and even the curves of the linear sweep voltammograms stay the same as shown in Figure 4.18, indicating that no obvious EC-doping effect occurs for Ti-O compounds under high temperature reduction. As aforementioned, low concentration point defects ($<10^{-4}$) often act as trap states facilitating recombination, while Li or H dopants effectively fill these sites, passivating the defects and leading to a higher photocurrent density. On the other hand, highly reduced materials exhibit large fractions of substoichiometric phases, wherein trap states could be generated by line defects due to the shear planes formation;¹²⁰ the point defects passivated by H or Li in comparison are negligible with respect to the defects induced by annealing.

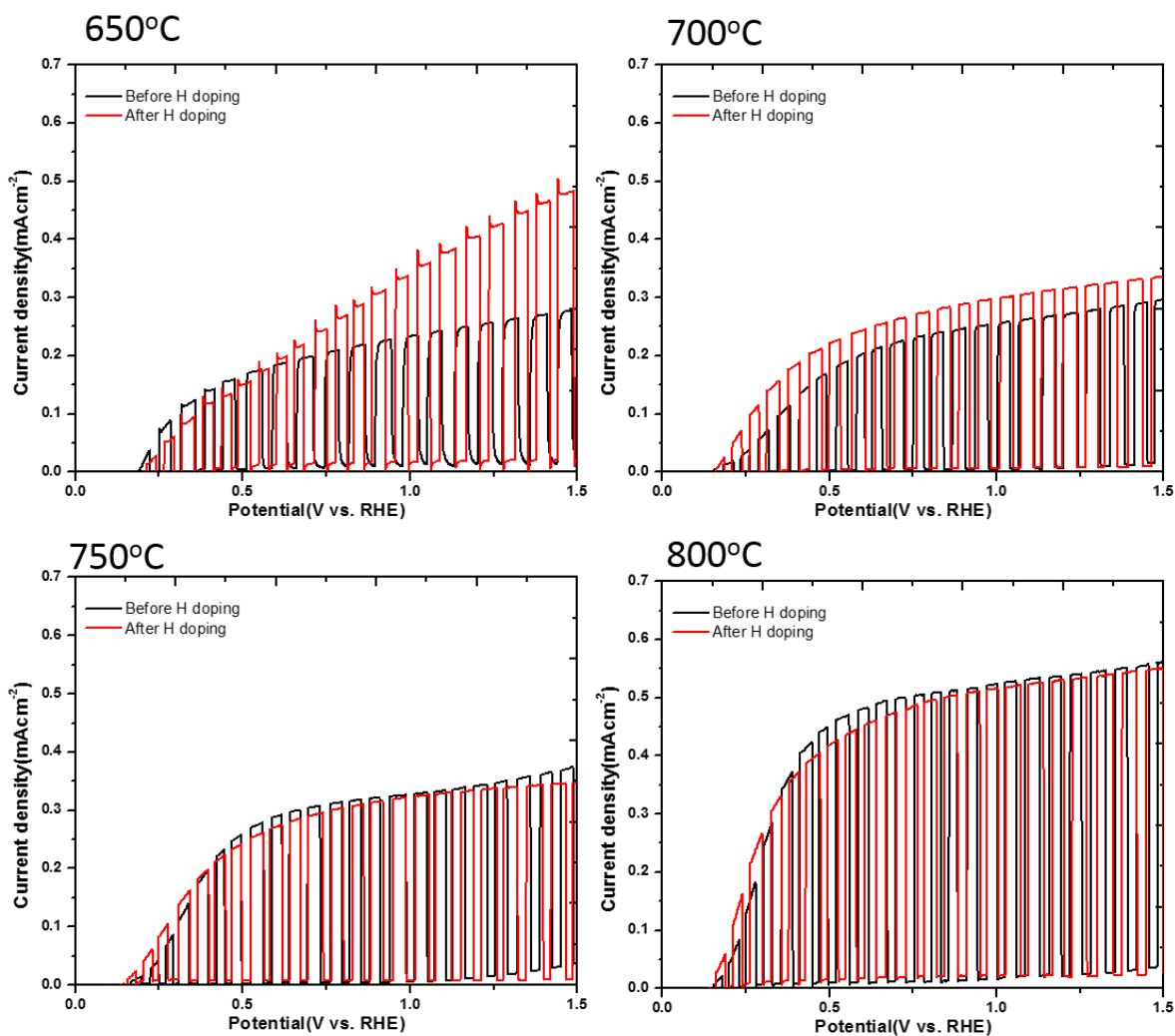


Figure 4.18 Linear sweeps voltammograms of thermal reduced Ti-O compounds prepared at various temperatures without (black curves) and with further EC-doping (red curves). For H-750 and H-800, the curves without and with EC doping stay almost the same, proving the non-effect of EC-doping on the high-temperature reduced Ti-O compounds.

4.6 Conclusions

In this chapter, thermal reduction under high annealing temperature is demonstrated to be an effective method to induce morphology changes and to form substoichiometric phases in anatase TiO₂ NTs.⁹⁵ Despite the complete degradation of the TiO₂ tubular structure at high reduction

temperature, TiO₂ NTs serve as a promising precursor to form a microparticle-nanowire porous structure consisting of sub-stoichiometric Ti-O phases including corundum Ti₂O₃, monoclinic TiO, the Ti₄O₇ Magnéli phase and a small fraction of rutile TiO₂, which exhibits enhanced photocurrent density and energy conversion efficiency. Specifically, the newly formed structure at 800°C shows a 2.5-fold increase in photocurrent at 1.23V_{RHE} and a 2.8-fold increase in photoconversion efficiency at a reduced bias with respect to the pristine TiO₂ NTs. This improvement is probably due to the increased amount of density of states at the surface measured with EIS as well as by reduced interfacial recombination process owing to an accelerated water oxidation kinetics. In particular, the density of surface defects in thermal-reduced Ti-O compounds is observed to increase by 2 orders of magnitude compared with pristine TiO₂, and analysis of the water oxidation selectivity indicates an improvement from ~65% to 92% for the reduced Ti-O compounds at 1.23V_{RHE}. The enhanced water oxidation selectivity implies that the hole injection process on the interface is no longer the rate determining step at higher bias for the reduced samples. Compared with laser surface modification and electrochemical reduction, the formation of TiO_{2-x} sub-stoichiometries under heavy reduction environment exhibit an enhanced photoelectrochemical, which is attributed to an increased number of donors as well as a higher conductivity. However, the light absorption is only limited in the UV region and no photoresponse is observed when the wavelength is larger than 450 nm. This may be due to the fact that photogenerated electron/hole pairs cannot be effectively separated in highly conductive TiO or Ti₂O₃ such that the photoactive species in the abovementioned Ti-O compound is decreased despite the improved charge transfer property. Introduction of defects into the TiO₂ NTs without significant phase/morphology change is therefore desirable, in order to better understand and

investigate the optimum amount of oxygen deficiencies for a maximized solar energy conversion efficiency.

Chapter 5-Introducing Ti^{3+} /oxygen vacancies into TiO_2 nanotube arrays

Since the work of Asahi et al.,⁴¹ nitrogen doping has been considered to be among the most promising approaches to fabricate the high defective TiO_2 (so-called black TiO_2).^{33,41,121} The experimentally determined energy levels of these localized oxygen vacancies are estimated at 0.75-1.18 V below the conduction band minimum,³⁷ while a high vacancy concentration induces a vacancy band just below the conduction band,³² which is proven to increase photoabsorption and catalytic activity.^{106,122} Different methods have been used to intercalate nitrogen in TiO_2 , resulting in a variety of complex species, with different contributions to absorption. Most nitrogen doping methods are accompanied by an increase in the density of oxygen vacancies (V_O), due to the lowering of their formation energy.^{123,124} As a consequence, Ti^{3+} reduced species are also generated, thus increasing the density of the active sites, but making it difficult to identify the main contribution leading to the enhanced photocatalytic activity. For example, some studies consider the catalytic activation of NH_3 treated TiO_2 only from the Ti^{3+} reduced species and oxygen vacancies, while N only stabilize the generated defects.¹²⁵⁻¹²⁸ Other researches however imply a synergistic effect of the co-dopants, oxygen vacancies and substitutional N dopants, where the p states of N dopants contribute to the band-gap narrowing by mixing with O 2p states.^{129,130} In addition, N doping is often achieved by flowing NH_3 at about 550-600°C. Under these conditions NH_3 decomposes forming hydrogen, which contributes additional reduction of TiO_2 and introduces another source of dopants.¹³¹ In this chapter, we use a mild thermal treatment method involving the sequential flow of gaseous Ar- NH_3 -Ar (AN) at 450°C with the aim to achieve N doping in TiO_2 , and in turn inducing formation of a significant amount of Ti^{3+} /oxygen vacancy

pairs, as proven by XPS, EPR and EDS. This treatment maintains the nanotubular morphology and the anatase phase structure of the pristine TiO₂ NTs.¹³²

5.1 Ti³⁺/oxygen vacancies introduced by Ar/NH₃ thermal treatment

X-ray Photoemission Spectroscopy was used to investigate the surface composition of the TiO₂ NTs and the changes in oxidation state change of the elements. The high resolution Ti 2p spectrum is shown in Figure 5.1 (a); the peaks at the binding energy of 458.9 eV and 464.6 eV are assigned to the Ti 2p 3/2 and Ti 2p 1/2, respectively. These features are observed both for the pristine and the argon-ammonia treated TiO₂ (AN-TiO₂), and exhibit the character of Ti⁴⁺. No shifts were observed in the XPS peak positions following the NH₃ treatment. The Ti³⁺ peak expected around 457.0 eV was also absent, probably due to the rapid oxidation of the surface Ti³⁺ species.¹⁰⁶ This indicates that Ti⁴⁺ is dominant on the surface for both pristine and AN-TiO₂. The O 1s spectrum in Figure 5.1 (b) shows only the one peak located at 530.2 eV, which corresponds to the lattice oxygen of TiO₂, revealing that only limited amounts of adsorbed oxygen or hydroxide species are present at the surface.¹³³ Figure 5.1 (c) shows the N 1s spectrum region; the N 1s peak is located at ~400 eV and assigned to the molecular γ -N₂ chemisorption, as well as that located at ~396 eV representing atomic β -N are both absent, demonstrating that the Ar/NH₃ treatment^{41,134} results in limited (or none) N insertion; we hypothesize therefore that this mild treatment leads to a weak adsorption of N, eventually resulting in its desorption upon the final Ar gas injection. The absence of a signal from N 1s in XPS has been previously reported for N-doped TiO₂.¹³⁵ Failure to observe a dopant in XPS is not surprising given that the XPS detection limit is 0.1-1 atom%.¹³⁶ XPS spectrum for pure Ar treated TiO₂ NTs is present in Figure 5.1 (d) and no obvious change is shown after the Ar treatment as well.

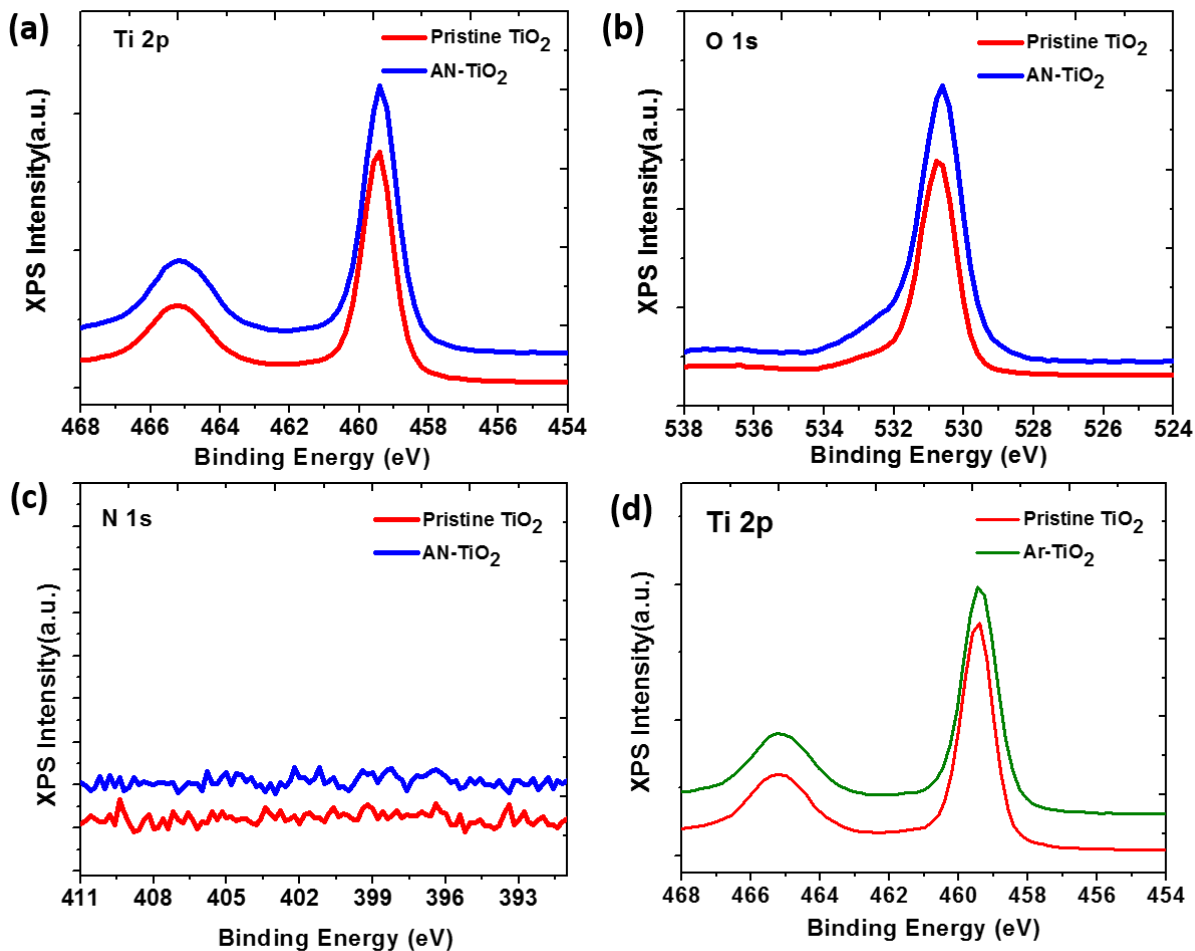


Figure 5.1 (a) Ti 2p, (b) O 1s, (c) N 1s XPS patterns for pristine TiO₂ NTs and AN-TiO₂ NTs. (d) Ti 2p XPS patterns for pristine TiO₂ and pure Ar treated TiO₂.

In order to further characterize the effects of the Ar-NH₃-Ar treatment, EPR measurements are carried out and the results are shown in Figure 5.2. The absence of a *g*-factor of 2.02 assigned to the O₂⁻ from adsorbed O₂ by surface Ti³⁺ (Ti³⁺-O₂) for both pristine and AN-TiO₂ further verify the lack of Ti³⁺ surface species caused by oxidation.^{129,137} For the pristine TiO₂, a weak peak at a *g*-factor of 1.996 indicates the presence of Ti³⁺ in the bulk material, while for the AN-TiO₂, a sharp peak with higher intensity is found at the same position, suggesting a large amount of Ti³⁺ bulk

species introduced by the Ar/NH₃ treatment.¹³⁸ It should also be noted that the commonly observed EPR signal of $g=2.005-2.003$ for the paramagnetic (Nb[•]) bulk centers in nitrogen-doped TiO₂ is also absent, which supports the XPS observation that only trace amounts of N are present.^{139,140}

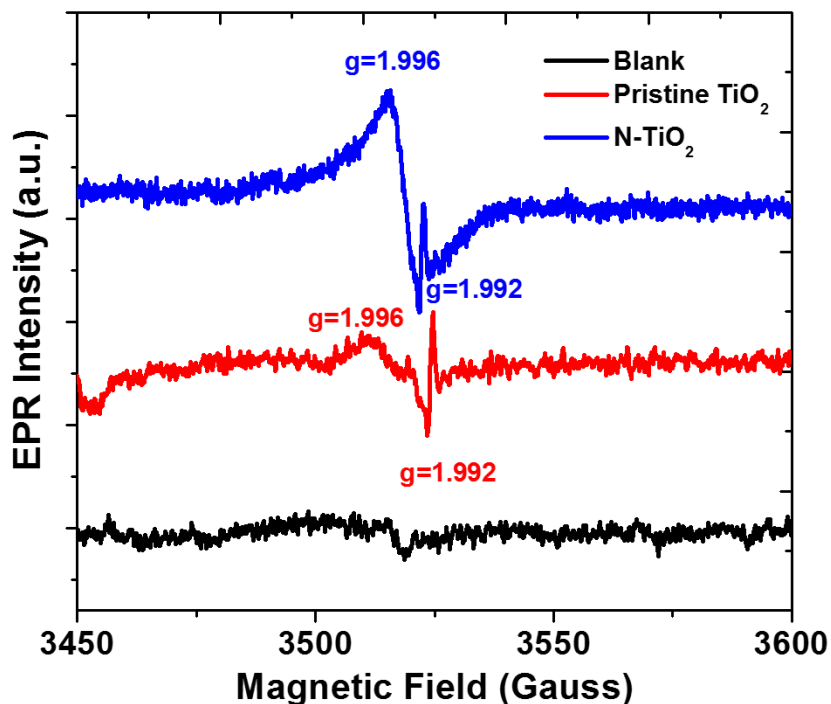


Figure 5.2 EPR spectra for the background, pristine TiO₂ and Ar/NH₃ treated TiO₂ NTs.

The morphology of the AN-TiO₂ is characterized by secondary electron micrographs as shown in Figure 5.3 (a). The AN-TiO₂ retains the same nanotubular structure, and the tube length is fixed to 7 μm , controlled by the anodization time. The average pore size of the nanotube mouths is ~ 80 nm, and the wall thickness is ~ 30 nm, which is unchanged compared to pristine TiO₂ NTs. XRD patterns are shown in Figure 5.3 (b) for the pristine anatase TiO₂ NTs and AN-TiO₂ treated under different reaction time. No shift in the peak positions or emergent new peaks were observed in the modified sample, confirming that the anatase phase of TiO₂ is retained. However, there is a pronounced

increase of the anatase (004) peak for all treated samples, suggesting a preferred orientation. From the SEM and XRD measurements, either morphology or phase structure barely change after the Ar/NH₃ treatment, due to the relatively low temperature of 450°C, which is in agreement with observations conducted at similar temperatures, as reported by other works.^{90,91} To investigate the atomic composition change due to the presence of Ti³⁺, XPS sputter profiling is performed with Ar ion milling. The composition as a function of etching depth up to 150 nm is displayed in Figure 5.3 (c). In order to eliminate the effect of Ar ion etching on the atomic composition, a comparison of pristine TiO₂ with AN-TiO₂ is carried out. For the AN-TiO₂, a decrease in O fraction and increase in Ti are observed compared to pristine TiO₂ as shown in figure 5.3 (c), which implies the generation of Ti³⁺ and the corresponding oxygen vacancies upon the Ar/NH₃ treatment. In parallel, the N fraction remains undetectable along the depth, confirming the absence of N insertion in the bulk. Average atomic compositions along a 150 nm etching depth for pristine TiO₂ and three AN-TiO₂ samples treated for different times are shown in Figure 5.3 (d). Pristine TiO₂ exhibits an excess of oxygen, probably due to a highly oxidized surface, while all the AN-TiO₂ samples show an O/Ti ratio less than the stoichiometric value of 2. Furthermore, this ratio decreases further with treatment time, indicating that the concentration of Ti³⁺ species can be increased by lengthening the time of treatment. This also demonstrates that the main contribution of the Ar/NH₃ treatment is to introduce Ti³⁺ into the materials, thus increasing the oxygen vacancy density.

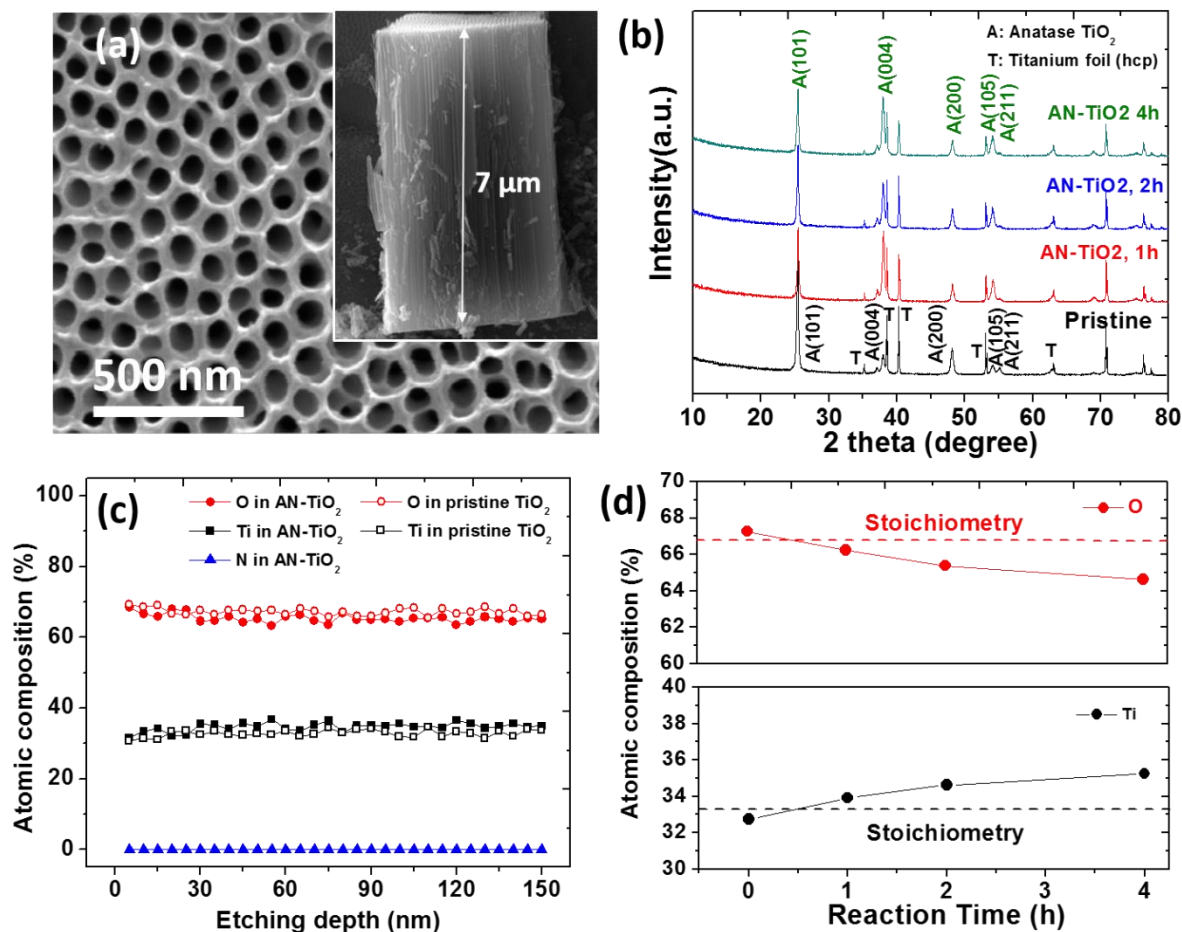


Figure 5.3 (a) FE-SEM image of AN-TiO₂ NTs (the inset was taken from the cross-section direction). (b) XRD patterns of pristine and AN-TiO₂ samples annealed under different times. (c) XPS determined atomic composition vs. Ar ion etching depth of pristine TiO₂ and AN-TiO₂ (2h). (d) Average atomic composition calculated from the top 150 nm layer thickness of the pristine and AN-TiO₂ NTs based on XPS intensity.

5.2 photoelectrochemical properties of Ar/NH₃ modified TiO₂ NTs

Linear sweep voltammograms under chopped illumination are shown in Figure 5.4 (a) for the pristine TiO₂ and AN-TiO₂ NTs. The photocurrent for the pristine TiO₂ saturates at ~ 0.5 V_{RHE} and the maximum value is ~ 0.23 mA cm⁻², probably owed to the limited mean free path of the charge

carriers. In contrast, the photocurrent generated by the AN-TiO₂ keeps increasing and reaches 0.93 mAcm⁻² at 1.23V_{RHE}, a 4-fold improvement with respect to the pristine materials. The dark current remains zero for both measurements, suggesting that no side reaction occurs. The PEC performance of pure Ar-treated TiO₂ is also compared in the same figure, where only a slight improvement of 0.08 mA/cm² is obtained, implying the synergetic effect of Ar and NH₃. In order to investigate this improvement, the incident photon-to-current conversion efficiency (IPCE) in the wavelength region of 350 to 700 nm is shown in Figure 5.4 (b). The IPCE for AN-TiO₂ at 350 nm, a wavelength close to the absorption limit of the anatase TiO₂ bandgap (3.2 eV, 388 nm), is close to 100%, demonstrating the absorption enhancement in the UV region. The IPCE of AN-TiO₂ remains above 10% up to 500 nm while the IPCE value for pristine TiO₂ remains zero above 450 nm, which demonstrates a wider spectral response and visible light-induced photocurrent. This behavior is also in agreement with the color change from brown to black before and after the treatment.

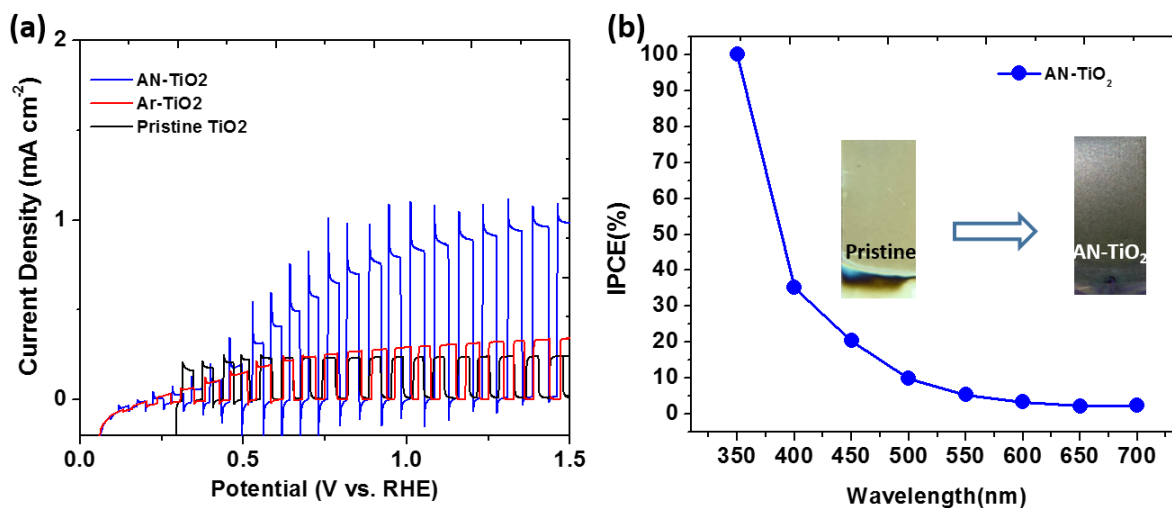


Figure 5.4 (a) Linear sweep voltammograms under AM 1.5G chopped illumination of the pristine TiO₂ NTs and AN-TiO₂ NTs. (b) IPCE of the incident light of AN-TiO₂ NTs.

Linear sweep voltammograms under illumination for the AN-TiO₂ treated under different durations are displayed in Figure 5.5 (a). At higher applied potential ($>1 V_{\text{RHE}}$), the photocurrent density increases with the reaction time, suggesting stronger absorption and/or improved transport. Above $1.55 V_{\text{RHE}}$, the current density for all the three samples are above 1 mA cm^{-2} , comparable with the theoretical maximum for pure TiO₂ of $\sim 1.1 \text{ mA cm}^{-2}$.¹⁴¹ Figure 5.5 (b) summarizes the potential values where the photocurrent density reaches 1 mA cm^{-2} . This value drops with increasing reaction time, and in particular, for AN-TiO₂ (4h), the potential to reach 1 mA cm^{-2} is $1.18 V_{\text{RHE}}$, less than the standard potential of water oxidation, demonstrating a significant advantage when performing photo-induced water oxidation. It should be noted that no obvious change in the XPS spectra is observed with the various treatment time as shown in Figure 5.6, due to the fact that the surface is oxidized in air after the treatment while the informational thickness of XPS measurements is usually less than 10 nm.

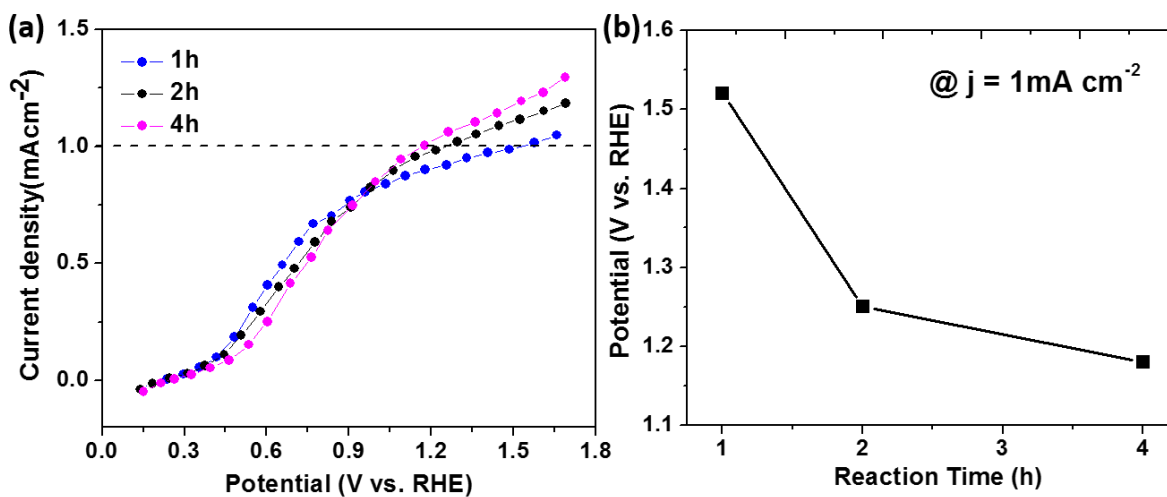


Figure 5.5 (a) Linear sweep voltammetry under AM 1.5G illumination of Ar/NH₃ modified TiO₂ NTs under different reaction times. (b) The potential at which the current density reaches 1 mA cm⁻² for AN-TiO₂ NTs with different reaction time.

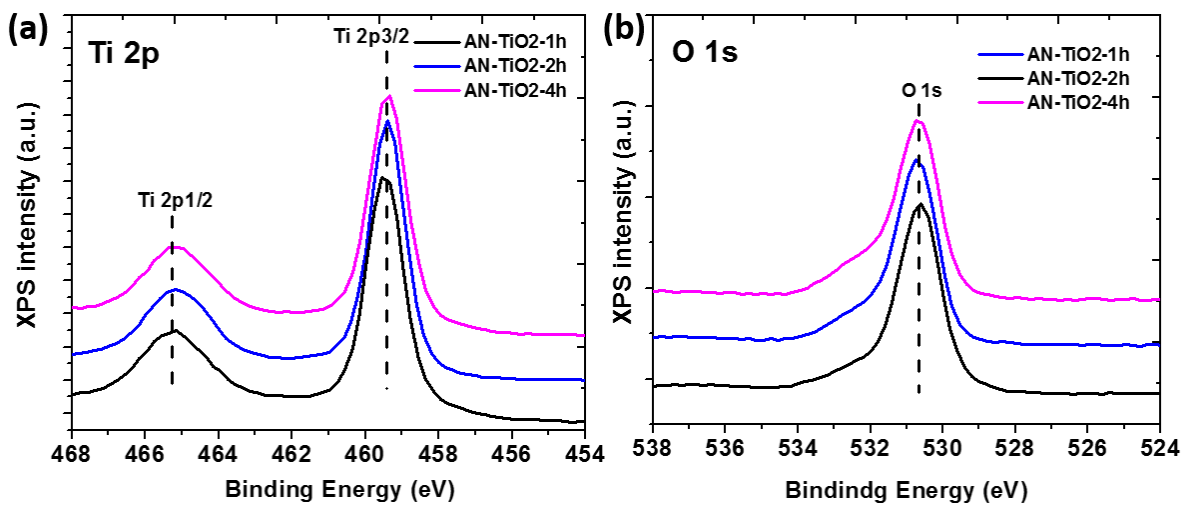


Figure 5.6 (a) Ti 2p, (b) O 1s of XPS spectrum of AN-TiO₂ treated with different reaction times under NH₃.

In order to compare the majority carrier densities and the flat band potentials, Mott-Schottky plots were generated for the AN-TiO₂, AN-TiO₂ (2h) and AN-TiO₂ (4h) at various frequencies, from 100 kHz to 1 Hz. The frequency (~100Hz) showing the maximum imaginary component in the impedance was used to determine the capacitance from the space charge; the corresponding Mott-Schottky plots are shown in Figure 5.7 (a).⁶⁸ The positive slopes confirm the n-type nature of the modified TiO₂.^{142,143} The largest charge carrier density for the pristine sample, as calculated from the linear region is $3.92 \times 10^{19} \text{ cm}^{-3}$, to be compared with the values of $4.99 \times 10^{20} \text{ cm}^{-3}$, $7.04 \times 10^{20} \text{ cm}^{-3}$, $3.61 \times 10^{21} \text{ cm}^{-3}$ for the TiO₂ treated with Ar/NH₃ for 1, 2 and 4 hrs, respectively, as shown in Figure 5.7 (b). This suggests an increase in carrier densities by 1-2 orders of magnitude due to the NH₃ treatment. This result demonstrates that the charge carrier density is increased by extending the treatment time, which is in agreement with the trend of the photoresponse, confirming that the enhanced charge carrier density is an important contributor to the PEC performance improvement.

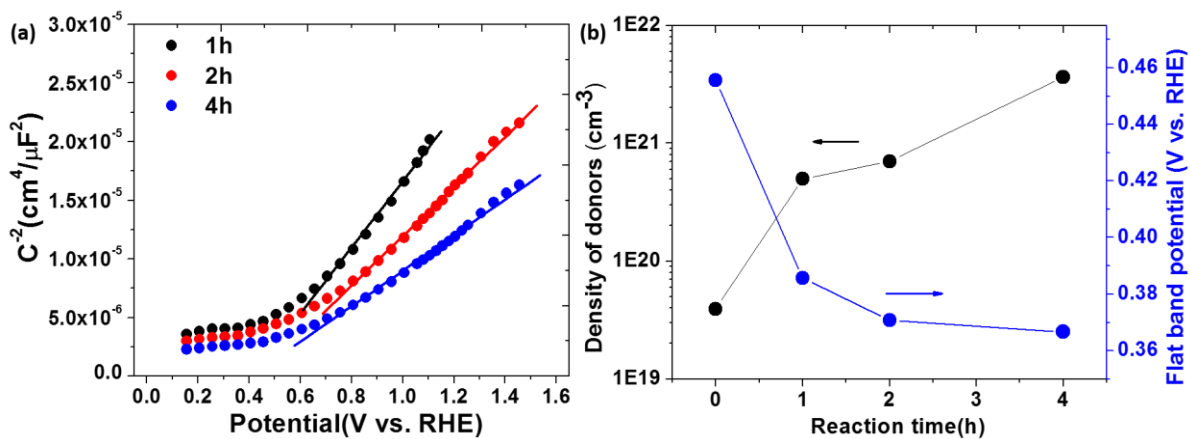


Figure 5.7 (a) Mott-Schottky plots measured at a frequency of 100 Hz for the AN-TiO₂ with different reaction times. (b) Calculated density of donors (black) and flat band potential (blue) as a function of reaction time in NH₃.

Additionally, the Mott-Schottky plots without/with light are compared in Figure 5.8. The fitted slope of the Mott-Schottky curve under illumination is similar to the slope in the dark, as the density of donors calculated from the capacitance of the depletion layer is an intrinsic behavior of the material and should not change with the incident light. However, the flat band potential, depending on Fermi level position, shifts anodically by $\sim 0.3\text{V}$ with the photon excitation. The shift direction is determined by the type of the charge carriers that are stored in the depletion region and thus a positive shift of the potential is a good indicator that the stored charge carriers are photogenerated holes,¹⁴⁴ in agreement with the n-type semiconductor nature of the AN-TiO₂.

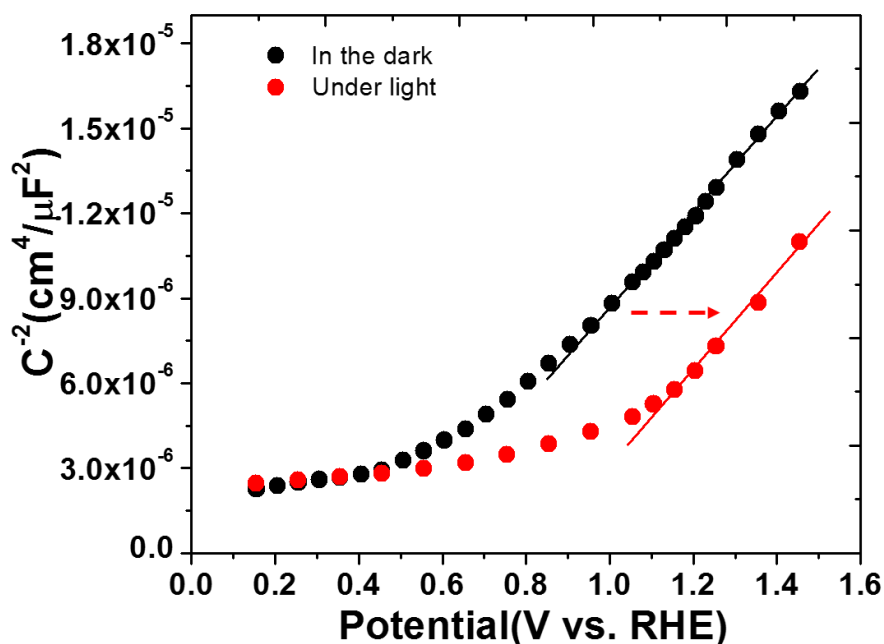


Figure 5.8 Mott-Schottky plots of the AN-TiO₂ (4h) in the dark and under 1.5G solar illumination.

The flat band potentials are obtained from the X-axis intercepts of the Mott-Schottky plots. The pristine sample shows a flat band potential (V_{FB}) of $0.456\text{V}_{\text{RHE}}$, similar to the values reported by

previous publications.^{66,145} The AN-TiO₂ samples instead exhibit a cathodic shift of the V_{FB}, with this value dropping to 0.386 V, 0.371 V and 0.367 V for AN-TiO₂, AN-TiO₂ (2h) and AN-TiO₂ (4h), respectively. The more positive V_{FB} observed in the pristine TiO₂ implies that a significant external bias is required to neutralize the band bending, allowing minority carriers to reach the surface and carry out water oxidation. This is due to the large band bending generated by a large difference between the Fermi level of TiO₂ and the redox potential of OH⁻/O₂. In contrast, this energy difference in the AN-TiO₂ samples is lowered, as indicated by the reduced V_{FB}, which can be further reduced by extending the treatment time as shown in figure 5.7 (b).

In order to investigate the dependence of the photo-catalytic properties on the length of the nanotube arrays, TiO₂ NTs were then grown with lengths of 1, 3, 6 and 8 μm by varying the anodization time. The cross section SEM images of the AN-TiO₂ with different lengths are shown in Figure 5.9 (a); the morphology retains the nanotube geometry, and the diameter of the nanotubes remains the same as pristine TiO₂ NTs. The linear sweep voltammograms under AM 1.5G illumination of AN-TiO₂ NTs with various lengths are compared in Figure 5.9 (b). The photocurrent densities at 1.5 V_{RHE} are 0.68 mA cm⁻², 0.91 mA cm⁻², 1.10 mA cm⁻² and 1.25 mA cm⁻², respectively for the 1, 3, 6 and 8 μm nanotube lengths, indicating a clear trend of increasing photoresponse with the length of the nanotube arrays. Typically, longer TiO₂ NT arrays capture more photons and thus generate larger amounts of photo-generated electron/hole pairs; these charge carriers however are prone to recombination during the extended travel path, such that an optimum thickness exists that maximizes photocurrent.^{114,146} For pristine TiO₂ nanotubular structures, UV photons are mainly absorbed in the first 1-2 μm layer from the surface and the electron mean free path needs to be comparable with the remaining tube length for electrons to reach the back contact before recombination.^{147,148} The optimum thickness for efficient photo-

catalysis therefore often does not exceed 3 μm .¹⁴⁹ For the AN-TiO₂ samples, this thickness is shown in Figure 5.9 (c) to go beyond 8 μm , probably due to the higher conductivity caused by the increased charge carrier density introduced by the treatment, as demonstrated by the Mott-Schottky method. Furthermore, the onset potential undergoes a cathodic shift from 0.243 V to 0.189 V with the increase in the NT length, which indicates an increased photovoltage, probably also due to the reduced V_{FB} .

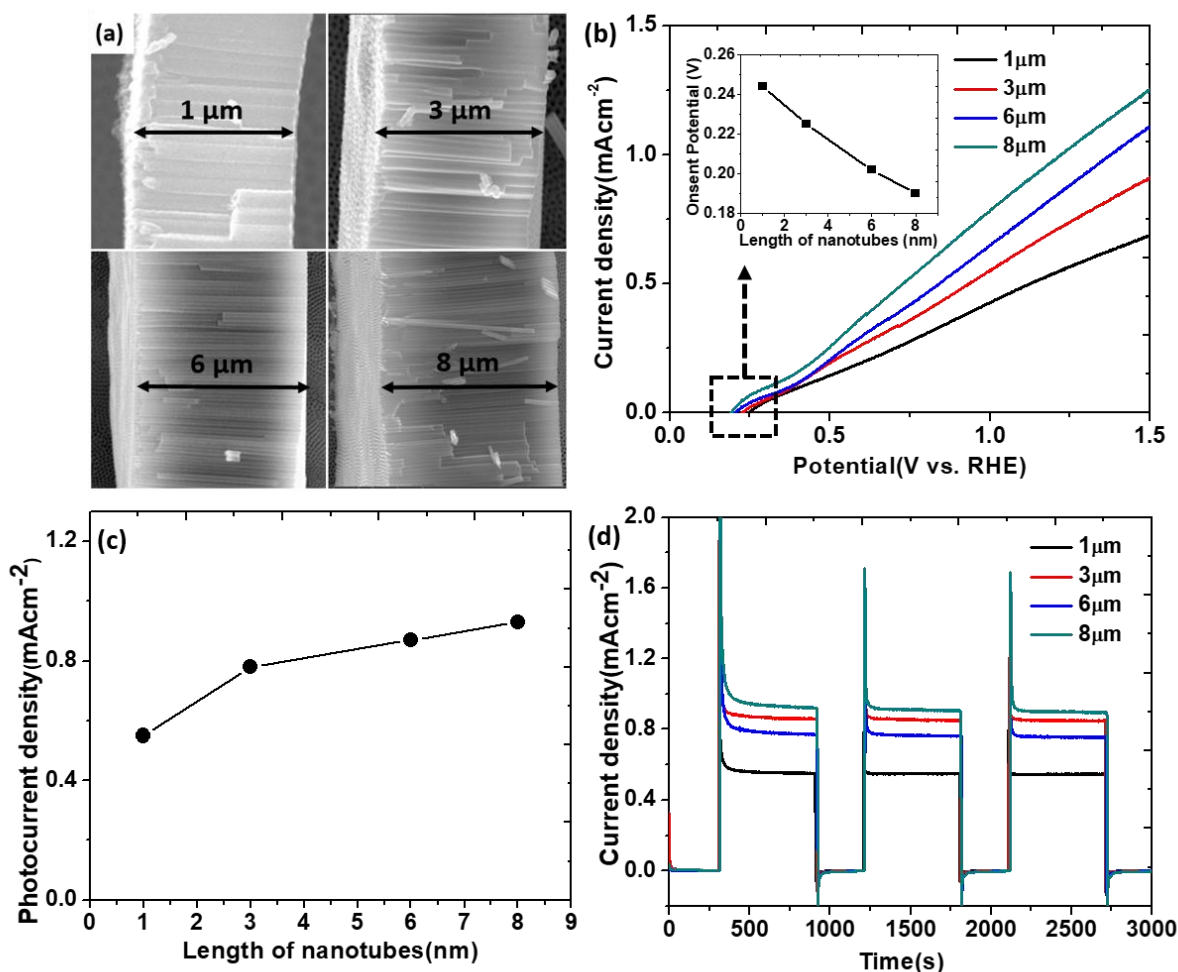


Figure 5.9 (a) Cross section FE-SEM images of AN-TiO₂ NTs various tube lengths. (b) Linear sweep voltammograms under AM 1.5G illumination of AN-TiO₂ NTs with various lengths. The inserted plot shows the onset potential vs. NT length. (c) Measured photocurrent density at 1.23 V_{RHE} as a function of NT length. (d) Stability test of NH₃ TiO₂ NTs at 1.23 V_{RHE} for 3000 s.

5.3 Stability of Ar/NH₃ modified TiO₂ NTs

The short term stability of the various AN-TiO₂ was measured for 3000 s under chopped illumination as shown in Figure 5.9 (d), showing no decay in the photocurrent within these time scales. The medium term stability are first evaluated by comparing the photocurrent density at 1.23 V_{RHE} of a fresh sample with the same sample placed in air for 1 week as shown in Figure 5.10 (a).

The photocurrent remains stable for the first 10 mins and no obvious decay was observed. The two photocurrent values coincide, suggesting that the Ti^{3+} species in the AN-TiO₂ are stable after exposure in air for a period of one week, thus implying good stability. The photocurrent density however drops to half the value when stored in air for 6 months. In order to better understand the photocurrent decay after a long term air exposure, the composition along the length of the AN-TiO₂ NTs is shown in Figure 5.10 (b). The oxygen fraction is much higher on the top 1 μm of the nanotube surface, while the O atomic fraction gradually decreases to the stoichiometric composition (O/Ti=2.0) at 2.8 μm from the top surface; the stoichiometry at the bottom half of the nanotube instead was found to be below 2.0, similar to the composition of the AN-TiO₂ fresh sample. The change of composition along the NT array reveals therefore that the top layer of up to $\sim 3 \mu\text{m}$ is highly oxidized in air, while the inner layer still retains a large amount of Ti^{3+} reduced species; this surface oxidation may explain the photocurrent drop after 6-month air exposure. In addition, we note that the photocurrent density of AN-TiO₂ after 6 months in air is still higher than that of pristine TiO₂ NTs.

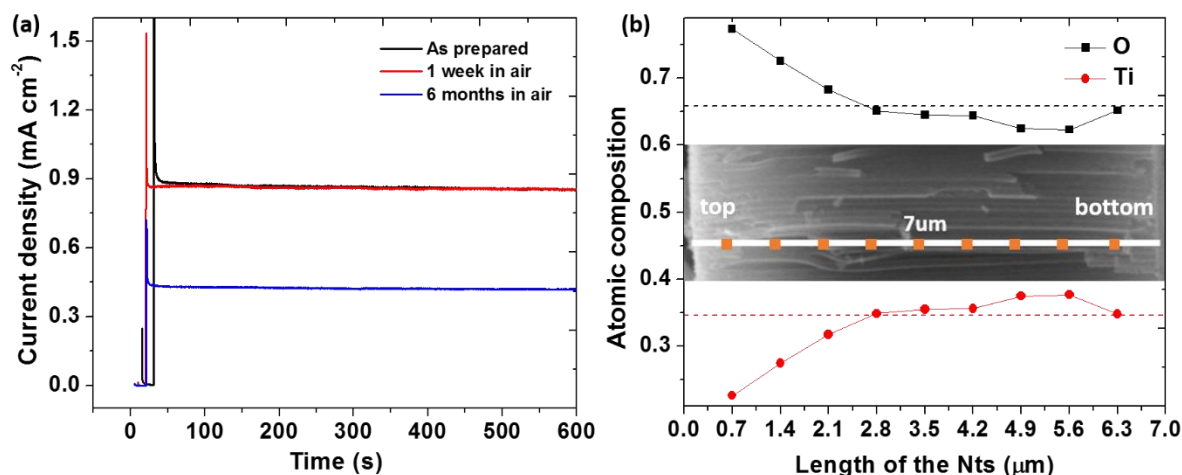


Figure 5.10 (a) Chronoamperometry plot at 1.23 V_{RHE} under illumination for the same AN-TiO₂ sample placed in air for different times. (b) EDS determined atomic composition along the length of the nanotube array for AN-TiO₂ NTs placed in air for 6 months. (The orange dots inserted in the SEM image indicate the locations of each EDS measurement)

5.4 Conclusions

In this chapter, TiO₂ NTs have been synthesized *via* a sequential Ar-NH₃-Ar flow at 450°C. From XPS and EPR, we prove that little amounts of nitrogen is incorporated in TiO₂, while a large density of Ti³⁺ species is generated, both at the surface and in the bulk.¹³² When performing as a photo-catalyst in alkaline solution, the Ar/NH₃ modified TiO₂ NTs (AN-TiO₂) exhibit a 5-fold enhancement in photocurrent compared with pristine TiO₂ NTs, due to the broadened photon absorption both in the ultraviolet and visible region of the solar spectrum. Furthermore, the photoresponse of AN-TiO₂ NTs can be optimized by increasing the reaction time. In particular, a photocurrent of 1 mA cm⁻² is obtained at 1.18 V_{RHE} when the reaction time in NH₃ is set as 4 hrs. We also demonstrate that the performance improvement reflects the increased density of charge carriers as well as the reduced flat band potential as an effect of the treatment. An increase of the

AN-TiO₂ layer thickness is also observed to further increase the photo-catalytic performance. In addition, no obvious decay in photocurrent is observed when the photoanode is operated in 1 M KOH under illumination at 1.23 V_{RHE} for 10 min, or after being stored in air for 1 week, while this value drops by half after exposure in air for 6 months, due to the progressive oxidation of Ti³⁺ species in the first 3 μm layer from the surface. Compared with laser surface modification, hydrogen thermal reduction and electrochemical reduction methods, Ar/NH₃ treatment on TiO₂ exhibit an superior enhancement on the TiO₂ NTs with a photoreaction response increase of 4-5 folds compared with pristine TiO₂ NTs, which is close to the theoretic maximum photocurrent of TiO₂, due to a relatively optimized introduction of the oxygen vacancies/Ti³⁺. To further improve the PEC performance of the modified TiO₂ based materials, depositing electrocatalysts on the TiO₂ surface is another possibility, while the influence and effectiveness is yet to be investigated.

Chapter 6-Improving surface oxidation kinetics with electrocatalysts by electrodeposition

Electrodeposited Ni or Ni-Fe oxy-hydroxides are among the non-noble metal catalysts with highest turn-over in alkaline electrolytes. For instance, metallic Ni in alkaline solutions forms spontaneously a variety of (double) hydroxides and oxy-hydroxides, which show a wide range of electrocatalytic activity.¹¹⁷ The catalytic performance in these materials seems however to be mainly related to Fe ions, sometimes introduced inadvertently as impurities, being present as Fe^{3+} in Ni-Fe hydroxide at open circuit, but oxidizing to Fe^{4+} at potential corresponding to oxygen evolution.¹⁵⁰ Studies of loading Ni-Fe (oxy) hydroxides on anodic TiO_2 nanotube arrays by electrodeposition methods are rarely reported and the influence of the loaded catalysts on the photoanode performance is not fully understood. In this chapter, we aim to combine anodized TiO_2 nanotubes and electrodeposited, highly efficient OER catalysts to investigate the effect of interfaces and potential synergetic effects related to charge redistribution. We first carry out the electrodeposition of Ni-Fe oxy-hydroxides on the surface of a Au/Si substrate to determine the intrinsic electrocatalytic behavior. Successively, the same procedure is applied on the anodic TiO_2 NT systems with various morphologies, including compact-aligned self-ordered TiO_2 NTs (or regular TiO_2 NTs, R- TiO_2), large-gap TiO_2 nanotube arrays with walls exposed (LG(L) TiO_2), and short large-gap TiO_2 individual nanotubes (LG(S) TiO_2), in order to investigate the influence of the surface morphology on the electrodeposition. The electrochemical/photoelectrochemical performance will be measured using the linear sweep voltammetry without/with light in alkaline solution, trying to evaluate the water oxidation kinetics of the Ni-Fe-oxy-hydroxides deposited TiO_2 NTs and the application as a photoanode candidate.¹⁵¹

6.1 Electrodeposition of porous Ni-Fe oxy-hydroxide catalysts

The surface morphology of Ni-Fe oxy-hydroxides (NiFeOH_x) deposited on Au/Si substrates is shown in Figure 6.1. A nanoflake morphology was observed onto the surface of the Au/Si substrate at a deposition time of 2 min as shown in Figure 6.1 (a), while the amount of the nanoflakes and their density increase with increasing deposition time, forming pseudo-crystals in the vertical direction at 10 min deposition time. The results are similar to those reported in the work of Boettcher.¹⁵² The films were deposited under current control, with the current density varying from -15.0 to -0.1 mA cm^{-2} as shown in Figure 6.1(c). The Ni fraction ($\text{Ni at\%}/(\text{Ni at\%} + \text{Fe at\%})$) changes slightly from 89% to 78% in the range of -15.0 to -3.0 mA cm^{-2} , then drops from 78% to 63% from -3.0 to 0.1 mA/cm^2 . At higher current density (-15.0 to -3.0 mA cm^{-2}), Ni and Fe are probably depositing at their limiting current (the limiting current for Fe is calculated to be $j_{\text{lim}} = -0.277 \text{ mA cm}^{-2}$; for Ni $j_{\text{lim}} = -2.45 \text{ mA cm}^{-2}$, assuming a 0.5 mm Nernst layer) and thus the mass transfer is the rate determining step, while the excess current density mainly contributes to the hydrogen evolution reaction, resulting in a local increase pH that contributes to the precipitation of oxy-hydroxides. At lower current density (-3.0 to 0.1 mA cm^{-2}), the charge transfer process dominates and the deposition rate of Ni is relatively slower, leading to a decreased Ni fraction. During the deposition, oxygen content slightly varies with the applied current density, remaining at 63%~67% ($\text{O at\%}/(\text{Fe at\%} + \text{Ni at\%} + \text{O at\%})$) as shown in Figure 6.1 (d).

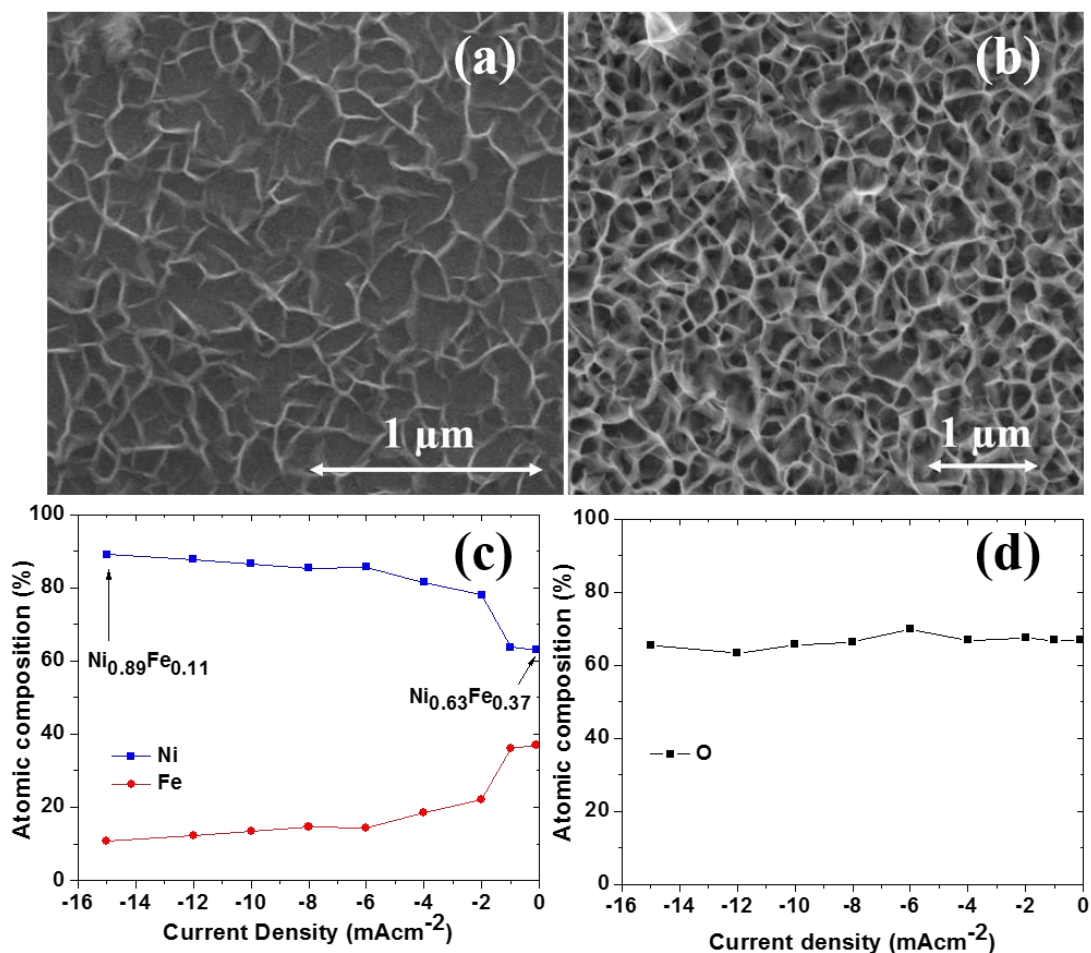


Figure 6.1 Surface morphology of electrodeposited NiFeOH_x on Au/Si substrate for 2min (a) and 10 min (b). Atomic fraction as a function of applied current density during the electrodeposition of Nickel/Iron (c) and Oxygen (d).

The catalytic activity towards the OER was initially evaluated by performing cyclic voltammetry at Ni-Fe oxy-hydroxides grown for 10 min and 1 min in 1 M KOH; these data are presented in Figure 6.2 (a). The applied potential at a current density of 10 mA cm⁻² was 1.51 V and 1.57 V vs. RHE for the 10 min deposited and 1 min deposited films, respectively. The cathodic shift of the polarization curve from 1 min to 10 min deposited oxy-hydroxides indicates an enhanced water oxidation kinetics for the sample grown at a longer deposition time. The enhanced OER activity of the thicker film is attributed in part to the increased surface area, contributed by both the vertical

growth and the increase of density of the ridges. The catalyst deposited for the longer time shows a relatively high resistivity, but under OER conditions the material becomes conductive and this constrain is not limiting.¹⁵² The catalyst electrodeposited for 10 min onto TiO₂ NTs systems will be discussed later. It also needs to be noted that an oxidation peak at ~1.45 V and a reduction peak at ~1.36 V are observed, corresponding to the oxidation and reduction, respectively, of the NiFe layer, which occurs in parallel with the oxidation evolution at relatively low bias. The electrochemical kinetics was investigated quantitatively by constructing Tafel plots as shown in Figure 6.2 (b) and (c); different Tafel slopes are observed in the low overpotential region. The thicker film exhibits an increase in Tafel slope at around 3 mA/cm², similar to the typical behavior observed at IrO₂ based oxide electrodes;¹⁵³ on the other hand the thinner film shows a decrease in Tafel slope (~29 mV/dec) above 10⁻³ mA/cm², which is not yet understood. At high rates of the OER, about above 40 mA/cm², the reaction rate seems to be limited by an ohmic drop, or to an intense bubble formation that limits the OER reaction.

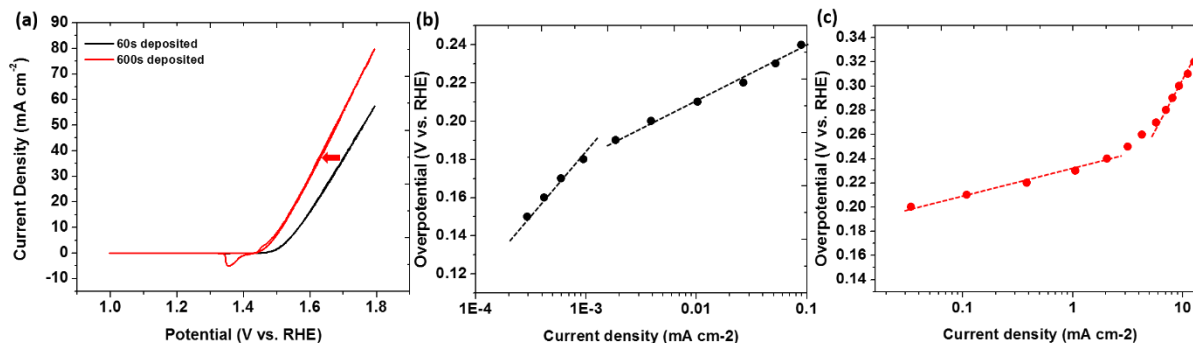


Figure 6.2 (a) Linear sweep voltammeteries of 600s and 60s deposited NiFeOH_x films in 1M KOH. Tafel plots measured in the same solution for (b) 60s-deposited and (c) 600s-deposited NiFeOH_x.

6.2 Growth of NiFeOH_x on the tops of regular anodic TiO₂ nanotubes

After the NiFeOH_x film had been proven to be an efficient catalyst towards water oxidation, the deposition of NiFeOH_x on TiO₂ nanotubes was further carried out to investigate the water oxidation kinetics and charge transfer at the TiO₂ nanotube interface. The schematics of electrodeposition of NiFeOH_x on different TiO₂ systems are shown in Figure 6.3. Three different nanotube structures were used as substrates for deposition, while the NiFeOH_x layers were deposited on different parts of the nanotubes. First, regular TiO₂ nanotubes (R-TiO₂) were investigated.

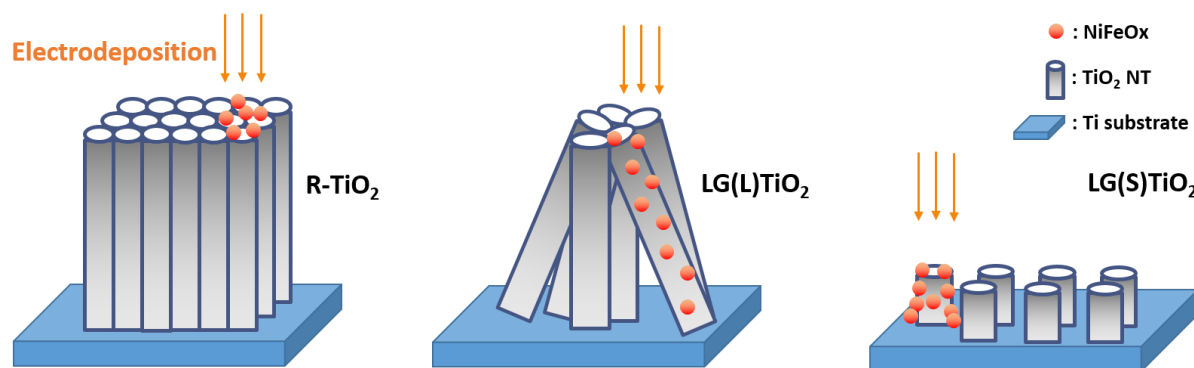


Figure 6.3 Schematics of electrodeposition of NiFeOH_x on different TiO₂ nanotube systems.

The surface morphology of pristine R-TiO₂ and NiFeOH_x onto R-TiO₂ are shown in Figure 6.4 (a) and (b). The pristine R-TiO₂ showed a relatively smooth surface with aligned pores. The nanotube diameters range from 50 to 100 nm. The deposition of NiFeOH_x on R-TiO₂ resulted in the nanotube mouths being covered with a relatively rough layer consisting of 10-20 nm size particles. From the elemental analysis shown in Figure 6.4 (c), peaks from Fe and Ni were detected, demonstrating the presence of a Ni-Fe-based layer on the TiO₂ surface. It should be noted that the

EDS signals from Ni and Fe are weak compared with Ti and O, indicating a low thickness of the Ni-Fe coating.

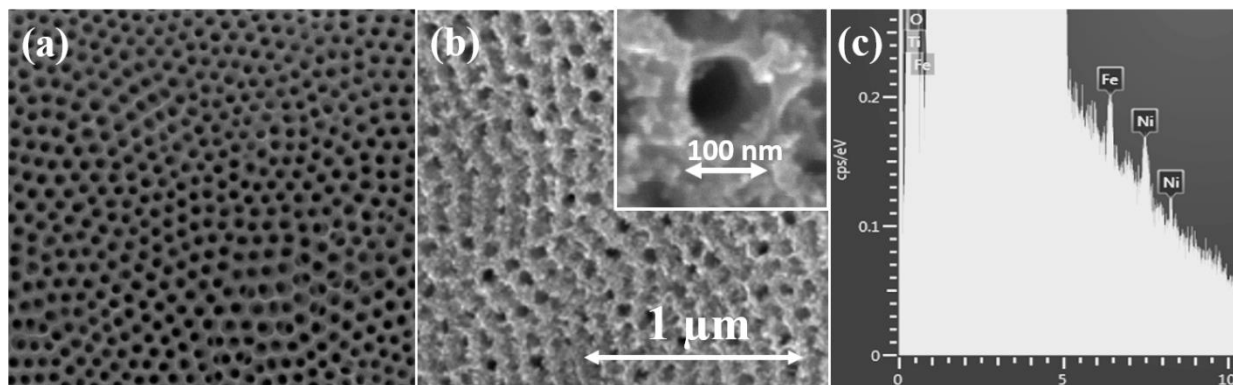


Figure 6.4 Top view SEM images of pristine regular TiO₂ NTs(a) and NiFeOH_x deposited regular TiO₂ NTs(b). EDS spectrum of NiFeOH_x deposited NTs.

The linear scan voltammetry of pristine R-TiO₂ and NiFeOH_x/TiO₂ were carried out under chopped light to investigate the impact of the catalyst on TiO₂ NTs as shown in Figure 6.5 (a). The photocurrent onset for the pristine R-TiO₂ was 0.1 V vs. RHE; the photocurrent increased until ~0.5 V vs. RHE, when a plateau in the photocurrent density (0.23 mA cm⁻²) was observed, corresponding to the saturation photocurrent density. A similar photoinduced behavior was observed for the NiFeOH_x deposited onto R-TiO₂, which showed a small shift in the photocurrent onset, probably due to variations in charge density at the interface. The photocurrent density in the latter case was lower at 0.14 mA cm⁻², probably as a consequence of the strong light absorption by the NiFeOH_x, which did exhibit wide band semiconductor behavior¹⁵⁰, causing significant absorption and/or inducing recombination at the NiFeOH_x/TiO₂ interface. The dark current of the NiFeOH_x/R-TiO₂ increased at a higher bias (>1.5V) due to the intrinsic catalytic property of the loaded NiFeOH_x catalyst, which was not observed for pristine R-TiO₂. To better understand the origin of the photoresponse, a current-transient was recorded in the first 300 s at an applied

potential of 1.23V vs. RHE as shown in Figure 6.5 (b). The current density increased to 0.11 mA cm⁻² when the light was turned on due to the transient increased amount of electron-hole pairs excited by the incident photons. A photocurrent decay appeared immediately after the light was switched on, which is a good indicator of the accumulation of photogenerated holes on the surface. This is an evidence of capacitive behavior¹⁴⁴, suggesting that the holes' lifetime was insufficient to allow injection into the solution. This implies that the decreased PEC conversion after NiFeOHx deposition is originated from both the reduced photon absorption and the recombination of the trapped photogenerated holes at or near the interface.

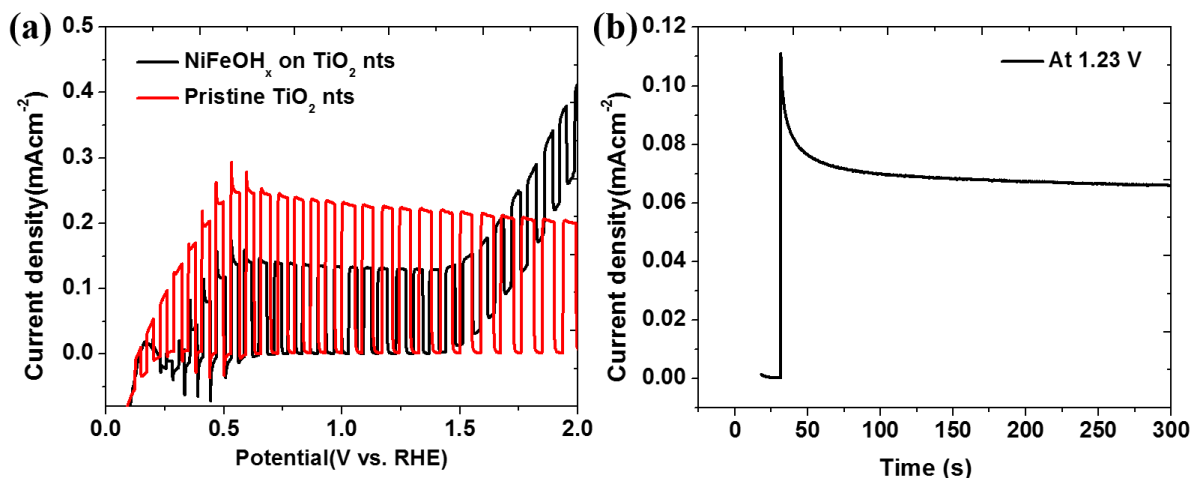


Figure 6.5 (a) Linear scanning voltammograms of pristine regular TiO₂ NTs and NiFeOHx deposited NTs under chopped irradiation of 100mW/cm² using AM 1.5G solar simulator. (b) Photocurrent transient for NiFeOHx deposited NTs in the first 300s at 1.23V vs. RHE.

6.3 Deposition of NiFeOHx on the external walls of long large-gap TiO₂ nanotubes

Electrodeposition of NiFeOHx catalysts was further investigated on TiO₂ nanotubes with large gaps in between to increase the accessibility of the deposit at the external walls, in order to assess the impact of a higher catalysts loading. The preparation of this type of nanotubes was carried out

in an electrolyte with lower polarity, which resulted in a lower density of nucleation sites, caused by a weaker electric field strength compared to conventional TiO₂ NTs anodization.⁵⁶ Figure 6.6 (a) depicts the surface morphology of the LG (L) TiO₂, where the nanotubes bend and stick to each other to form nanotube bundles, with a relatively high exposure of wall surfaces. The length of these nanotubes was 0.5~1.0 μm as shown in Figure 6.6 (b). After NiFeOH_x deposition, the morphology of the TiO₂ bundles remains unaffected while the NiFeOH_x catalyst coats the walls of the nanotube bundle with a nano-flake like deposit as shown in Figure 6.6 (c).

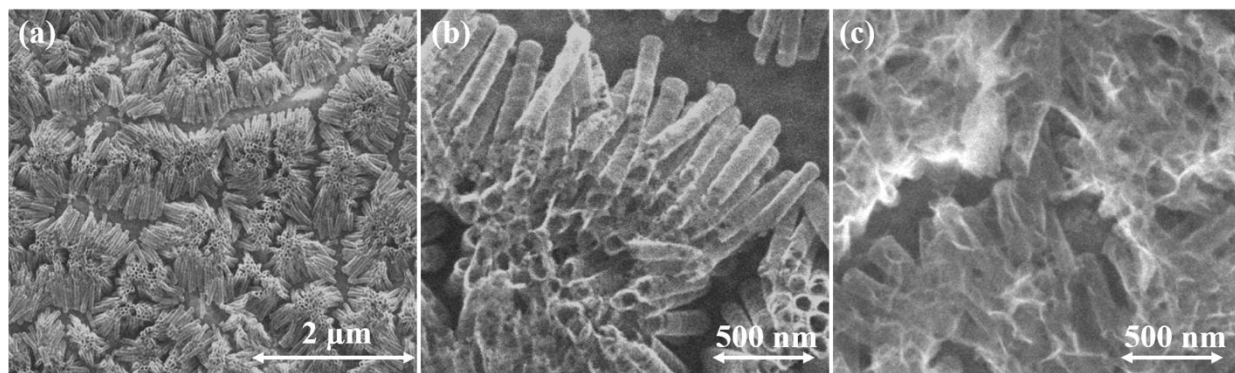


Figure 6.6 (a) (b) Surface morphology of regular LG(L) TiO₂ from different magnitudes and (c) of the NiFeOH_x deposited LG(L) TiO₂ NTs

XPS spectra of NiFeOH_x deposited on LG (L)-TiO₂ were collected for the elements Ni, Fe, O and Ti and the results are shown in Figure 6.7. Figure 6.7 (a) shows the main Ni peak appearing at a binding energy of ~855.6 eV, mainly resulting from the Ni (OH)₂ (855.3 eV) or/and NiOOH (855.8 eV). Moreover, the XPS signals from metallic nickel in the range of 852.6 - 852.9 eV are absent, further confirming that Ni on the surface is mainly in the form of Ni(OH)₂ and/or NiOOH. Peaks from the Fe 2p_{3/2} appear in a wide range of ~715-709 eV as shown in Figure 6.7 (b). The broad peak is probably generated by a convolution of FeO (709.4 eV), Fe₂O₃ (710.9 eV), and FeOOH (711.8 or 711.3 eV),¹⁵⁴ while precise identification of the various contributions is difficult as the

peak intensity is quite low due to a relatively small deposit amount, making in particular the detection of Fe oxides or Fe oxy-hydroxides - the minority fraction in the catalyst - difficult. No obvious signal from metallic Fe (707.0 eV) is shown as well.¹⁵⁵ Furthermore, a doublet at a binding energy of 532.6 eV and 531.8 eV is present in Figure 6.7 (c). The former peak correspond to the absorbed water or possibly absorbed O₂¹⁵⁶ while the latter is in agreement with oxygen in NiOOH.¹⁵⁷ No XPS signal from the Ti 2p spectrum is shown in Figure 6.7 (d), which evidences that there is no TiO₂ exposed on the surface, and that the NiFeOHx film has reached coalescence. An X-ray diffraction pattern of the catalyst is shown in Figure 6.7 (e), showing that all the main peaks are from the titanium substrate. One broad peak with relatively weak intensity located at $2\theta = 43.58^\circ$ is however observed, which is a good indicator of the presence of NiFe in the film as it matches very well with the diffraction of (111) plane from Al(FCC) NiFe with a corresponding lattice parameter of $a=3.59 \text{ \AA}$. A Ni atomic fraction of 45% is calculated using the King tables¹⁵⁸ which are constructed using the average atomic volume over the entire crystal. A slight deviation of the calculated Ni composition from the EDS measured value is probable, because the King tables are generated from bulk alloys while in our case the deposited NiFe is a thin film on TiO₂.

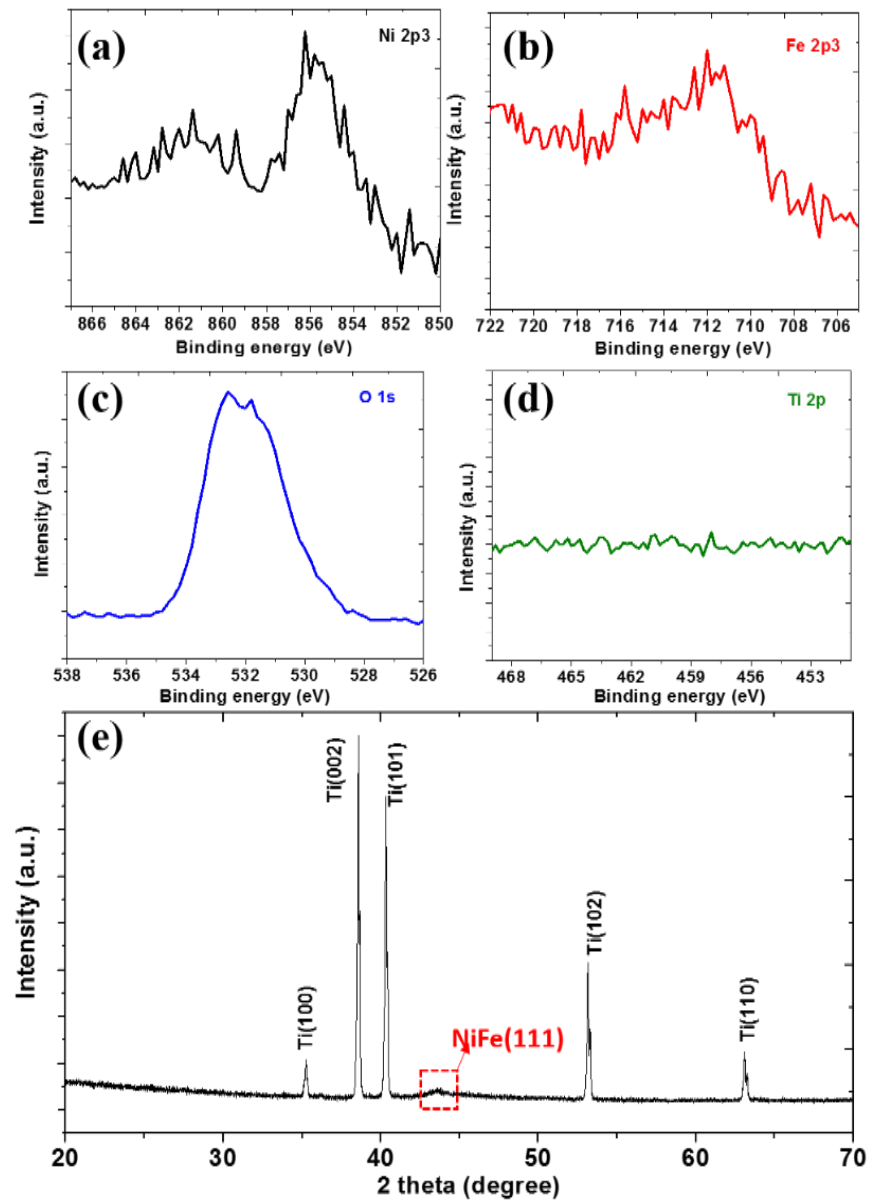


Figure 6.7 (a) Ni 2p₃, (b) Fe 2p_e, (c) O 1s and (d) Ti 2p XPS spectrum for NiFeOH_x deposited LG (L)TiO₂ NTs; (e) X-ray diffraction pattern for NiFeOH_x deposited LG(L) TiO₂ NTs.

In order to investigate the photoelectrochemical performance of the NiFeOH_x deposited on LG (L) TiO₂, a linear scan voltammetry of NiFeOH_x deposited onto LG (L) TiO₂ was measured. The catalyst film was grown for a deposition time of 2 min or 10 min using a constant deposition

current density of -0.1 mA cm^{-2} , and the photocurrent was measured under chopped light; the results are shown in Figure 6.8 (a) and (b). The pristine LG (L) TiO_2 showed a photocurrent onset of $\sim 0.2 \text{ V}$ and the photocurrent density was saturated at $\sim 1.0 \text{ V}$ vs. RHE, with a value of $\sim 0.19 \text{ mA cm}^{-2}$. Compared to pristine R TiO_2 NTs, which showed a photoinduced limiting current density of $\sim 0.23 \text{ mA cm}^{-2}$, the former value was slightly lower, probably as a consequence of the lower density and poor alignment of nanotubes on the LG (L) TiO_2 substrate, which is less ordered with respect to the regular TiO_2 nanotubes. In the voltage range from 0 to 1.0 V vs. RHE, as shown in Figure 6.8 (a), the photocurrent density of the NiFeOHx deposited onto LG (L) TiO_2 is reduced compared to pristine LG (L) TiO_2 , similar to the results of the NiFeOHx deposited onto regular TiO_2 . The photocurrent density at saturation for the samples with a deposition time of 2 min and 10 min were 0.15 mA cm^{-2} and 0.10 mA cm^{-2} , respectively. It should be noted that the onset potential for the pristine LG (L) TiO_2 is 0.16 V vs. RHE while the LG (L) TiO_2 coated with NiFeOHx showed an increased value to 0.24 V vs. RHE, which suggests a significant variation of the charge carrier density at the interface. The rapid decrease in the photocurrent density in Figure 6.8 (a) imply that defects at the interface increases after the deposition, which facilitates the recombination and suppresses hole injection. The photocurrent density decreases with increasing reaction time owed to the fact that thicker NiFeOHx absorbs light more efficiently, reducing the photons that reach the TiO_2 surface, thus decreasing the generation of electron/hole pairs. In the potential range from 1.0 to 2.0 V vs. RHE as shown in Figure 6.8 (b), the photocurrent density from the pristine LG (L) TiO_2 remains the same, probably due to space charge layer limitations¹¹⁵ or Fermi level pinning caused by the increased amount of defect states.^{20,116} The NiFeOHx deposited onto LG (L) TiO_2 , showed an increase of the dark current at higher bias ($>1.5 \text{ V}$ vs. RHE), due to the intrinsic catalytic activity of the NiFeOHx. The applied potential at a current

density of 1.0 mA cm^{-2} for the 2 min and 10 min deposited LG (L)-TiO₂ are 1.82V and 1.64V, respectively, suggesting poor catalytic activity. The increased amount of the catalyst was probably responsible for the enhanced electrocatalytic activity.

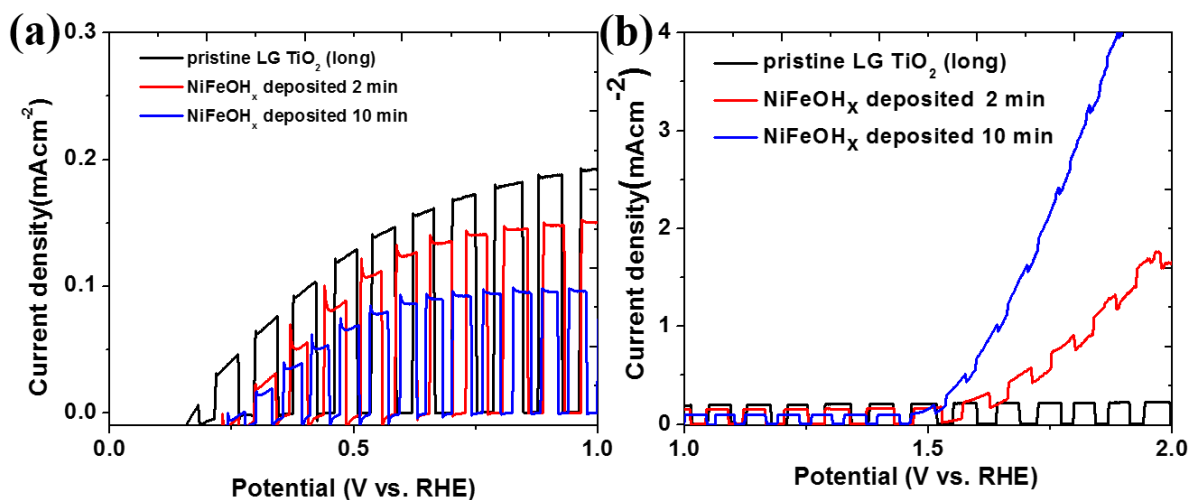


Figure 6.8 Linear scanning voltammograms of pristine LG (L) TiO₂ and NiFeOH_x deposited LG(L) TiO₂ for 2 min and 10 min in the potential range from 0.2 to 1.0V vs. RHE (a) and from 1.0 to 2.0 vs. RHE (b) under chopped light.

6.4 Growth of NiFeOH_x on the short large-gap TiO₂ nanotubes

In order to investigate the effect of a different geometry on the deposition of NiFeOH_x, the catalyst was further deposited on the entire walls of short large-gap TiO₂ nanotubes (LG (S) TiO₂). From Figure 6.9 (a), short nanotubes with a length of less than 300 nm are grown on the Ti substrate with relatively large gap between 0 and ~400nm. Unlike the regular anodic TiO₂ or LG (L) TiO₂ with the nanotubes clustered, the nanotubes of LG (S) TiO₂ are separate in such a way that the deposition may occur on the whole walls of each individual nanotube as shown in Figure 6.9 (b).

A nanoflake structure was again observed on the NiFeOHx coated on LG(S) TiO₂, similar to the growth on Au/Si substrate.

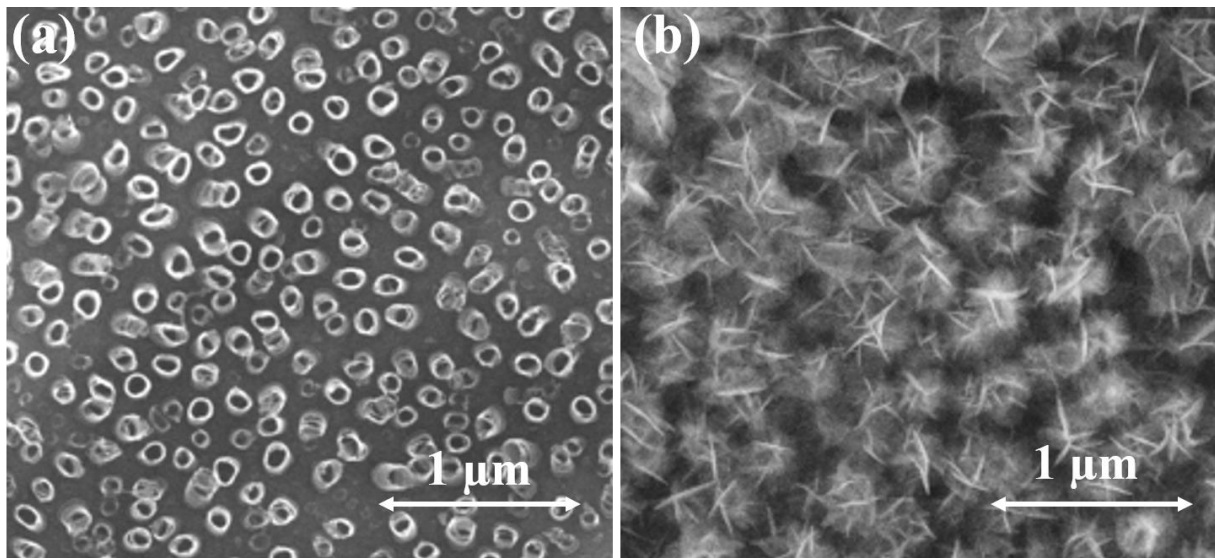


Figure 6.9 Top view morphology of pristine LG(S) TiO₂ NTs (a) and NiFeOHx deposited LG(S) TiO₂ NTs.

The photoelectrochemical performance of the pristine and NiFeOHx modified onto LG (S) TiO₂ is shown in Figure 6.10 (a) and (b). The pristine LG (S) TiO₂ shows a photocurrent density that does not saturate until the potential reaches 1.0V vs. RHE. The saturated current density (0.13mA cm⁻²) is less than the pristine regular TiO₂ and LG (L) TiO₂, probably owed to a limited amount of photogenerated holes caused by the reduced tube length and a less effective charge transfer efficiency due to the decreased density of the nanotube distribution. After deposition, the saturated photocurrent density decreases to 0.093 mA cm⁻² at 1.0V vs. RHE as shown in Figure 6.10 (a), mainly caused by the blocking of incident photons by the NiFeOHx layer. In the potential range of 1.0 to 2.0 V vs. RHE as shown in Figure 6.10 (b), the dark current for the NiFeOHx deposited onto LG (S) TiO₂ increases after 1.5V. Specifically, a current density benchmark of 1.0 mA cm⁻²

is reached at a potential of 1.57V, while a current density of 10 mA cm⁻² is obtained at 1.85V, which indicates an improved water oxidation activity thanks to the loading of NiFeOH_x catalysts.

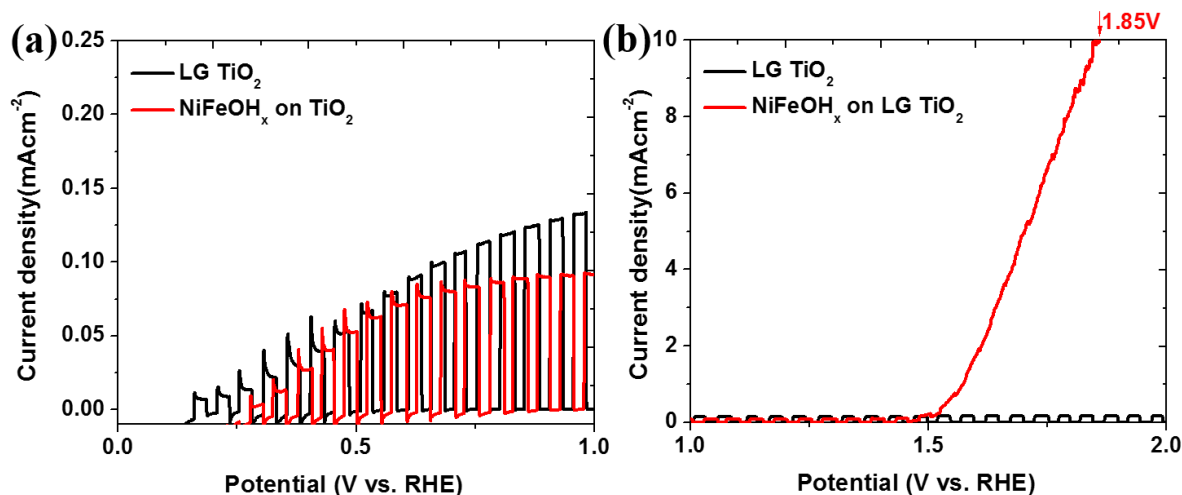


Figure 6.10 Linear scanning voltammograms of pristine LG(S) TiO₂ and NiFeOH_x deposited LG(S) TiO₂ for 2min and 10min under chopped irradiation in the potential range from 0.2 to 1.0V vs. RHE (a) and from 1.0 to 2.0V vs. RHE (b).

The photocurrent densities observed after the deposition on various TiO₂ nanotube systems reflect the water oxidation activity; these data are summarized in Figure 6.11. At relatively low applied potential (at 1.23V vs. RHE) the Ni-Fe oxy-hydroxide layer plays mainly the role of reducing the absorption of photons that reach the TiO₂ surface, negating the catalytic enhancement and leading to a decreased photocurrent density; instead, at relatively high bias (at 1.63V vs. RHE) the oxygen evolution is enhanced due to the intrinsic electrocatalytic properties of the loaded catalysts. The largest improvement is observed on the LG (S) TiO₂ system. This is probably owed to the minimal amount of introduced defects at the interface during electrodeposition, which is evidenced by comparing the photocurrent measurements shown in Figure 6.5 (a), Figure 6.8. (a) and Figure 6.10

(a). The transient decay of the photocurrent when light is on reflects the amount of defects in the material as those defects increase capability to store the photogenerated charge carriers ¹⁴⁴. From these results, the LG (S) TiO₂ shows the minimum decay in terms of the current density, leading to an optimal performance.

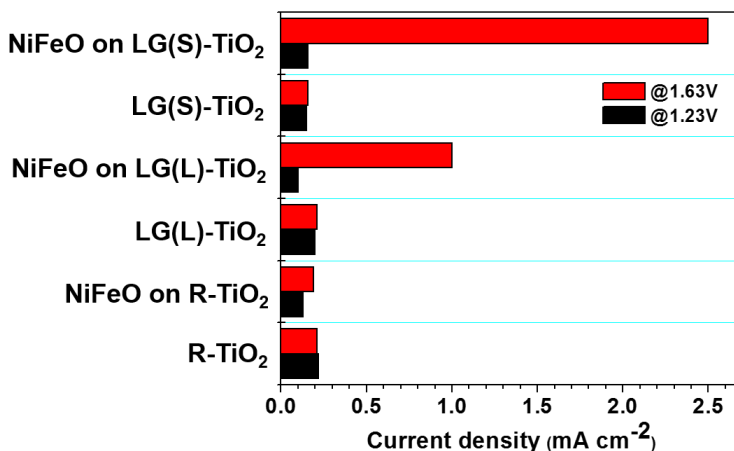


Figure 6.11 Comparison of current density of the three TiO₂ NTs systems at the potential of 1.23V and 1.63V vs. RHE.

6.5 Conclusions

In this Chapter, the galvanostatic electrodeposition of Ni-Fe oxy-hydroxides onto anodic TiO₂ nanotubes and the corresponding formation of supported OER catalysts is demonstrated and their performance is explored.¹⁵¹ In order to investigate the effect of deposition on different nanotube structures, electrolytes with different polarity were used to tailor the morphology of the anodized nanotube process, and different nanotube structures with large gaps in between were formed. Ni-Fe oxy-hydroxides are deposited on the tops, external walls and entire walls of nanotubes. At low applied potential ($\leq 1.5V$ vs. RHE), where the water oxidation is mainly induced by the photo-

generated holes from TiO_2 , the photoresponse is reduced and the onset potential is increased due to the introduction of defects at the interface during deposition and the reduced absorption of photons by the deposited layer. At high applied potential range ($>1.5\text{V}$ vs. RHE), where the electrochemical water oxidation dominates, the oxygen evolution is enhanced thanks to the intrinsic activity of the deposited NiFe oxy-hydroxides. For all the three TiO_2 systems, the trends are similar, while the largest improvement in terms of electrochemical activity towards water oxidation is observed on the short TiO_2 nanotubes with large gaps in between. Even though integration of TiO_2 with a water oxidation catalyst does not lead to enhancement in the photoresponse at low overpotential, the overall OER performance of the TiO_2 NTs systems could be improved at high overpotential.

Chapter 7-Electrodeposition of Ni on GaAs through self-limiting electrodeposition

In this chapter, the photoanode is switched to GaAs, as GaAs exhibits a direct and relatively ideal bandgap of 1.43 eV (at 298 K) to maximize the photoconversion efficiency by providing a visible light absorption (up to 867nm) of the solar spectrum compared to wide-bandgap semiconductors such as TiO₂ (up to 388 nm), and a larger photovoltage as compared to narrower bandgap semiconductors such as silicon which also features an indirect band-gap.^{159,160} The main limitation that hinders the application of GaAs in solar water splitting is the intrinsic instability in aqueous solutions under illumination,^{161,162} resulting in decomposition of GaAs and/or formation of an insulating oxide layer which would terminate the photoelectrochemical reaction towards water splitting.¹⁶³ Studies of photoelectrochemical water splitting at GaAs have been reported early on, most of them focusing on growing protective metallic layers on GaAs surface to prevent rapid photocorrosion.^{164,165} Growth of a thin metal on a semiconductor electrode affects its energetics, for instance by inducing band bending and forming a Schottky heterojunction. In the case of a continuous metal layer, the semiconductor substrate would be completely screened from the electrolyte. This results in a significantly improved protection, but the Schottky barrier would pin the Fermi level of the semiconductor to that of the deposited metal layer *via* surface states, precluding band-bending at the surface of the semiconductor, and thus usually leading to a limited photovoltage value.¹⁶⁶ For a discontinuous layer (disperse nanoparticles, NPs) in contrast, the Fermi level is no longer pinned to the metal layer when the NPs size is much lower than the depletion width at the semiconductor/electrolyte interface; in this case the inhomogeneous nature of the NP surface results in different morphologies and a range of barrier height values at each metal particle.^{166,167} Under these circumstances the photovoltage can be tuned by controlling the

particle size and surface coverage due to a pinch-off effect.^{168,169} In the following work, the protective, ultrathin Ni metal film is grown by electrodeposition, using a self-limiting chemistry proposed by Vereecken¹⁷⁰, whereby the absence of a boric buffer in a Nickel electrolyte induces over time an increase of pH at the film surface, resulting eventually in the precipitation of Ni hydroxide/oxy-hydroxide and terminating growth. Under these conditions, growth inhibition enhances the nucleation rate¹⁷¹, resulting in a high particle density and a very small coalescence thickness occurring within ~ 1 s, ideally suitable to achieve dense, continuous films at very low thickness. The self-limiting deposition mechanism of the protective layer was investigated through potential transients, XPS spectra and XPS depth profile using Ar⁺ ion milling. The Ni deposited on GaAs was then used as the photoanode under 1.5 G solar illumination in a K₃Fe(CN)₆/K₄Fe(CN)₆ aqueous solution to investigate the photoelectrochemical performance at both continuous and discontinuous films. The photocorrosion resistance of continuous vs. discontinuous Ni layers was also investigated in order to optimize layer properties towards water photo-oxidation.

7.1 Self-limiting electrodeposition of continuous Ni thin film on GaAs

A typical potential transient of the self-limiting electrodeposition of Ni on GaAs is shown in figure 7.1 (a). After a fast rise, the potential starts to decrease after ~ 0.2 s due to the electrode charging and the formation of the electrochemical double layer. A bump appears from 0.4 s to 0.6 s, as marked in the red rectangle. This is likely caused by the self-limiting nucleation, due to the formation of a hydroxide layer as a local pH gradient increase in the absence of buffering species.¹⁷² The potential transient, and in particular the bump, are main features of the self-limiting electrodeposition.⁵⁹ A slight increase in the potential is shown at ~ 0.8 s, which probably corresponds to the completion of the hydroxide formation.⁵⁹ When the deposition time is longer

than 1 s, Ni growth is terminated by the hydroxide layer formation, and the applied current density mainly contributes to the hydrogen evolution reaction. Intense bubble formation at the electrolyte surface was indeed observed after 1 s of deposition. In order to further validate the self-limiting deposition mechanism, both X-Ray Reflectometry (XRR) and XPS were used to determine the film thickness. The Ni layer thickness was determined by fitting XRR data as shown in Figure 7.1 (b); the average thickness was calculated to be 3 to 5 nm regardless of the deposition time, which varied between 10 and 30 s deposition of Ni on GaAs.

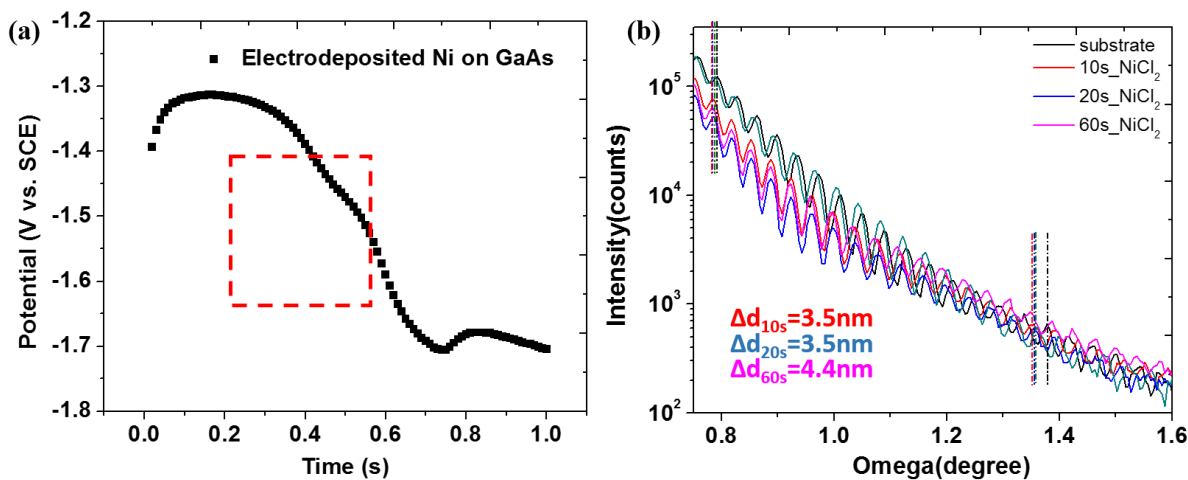


Figure 7.1 (a) Potential transient in the first second for the self-limiting Ni deposition; (b) X-ray reflectometry (XRR) patterns for the ruthenium sputtered silicon substrate (Ru/Si), Ni films grown on the Ru/Si deposited under self-limiting conditions at various deposition time. From calculation, the three Ni films have similar thickness, which is 3.5 nm, 3.5 nm and 4.4 nm for a deposition time of 10s, 20s and 60s respectively.

In comparison, the XPS intensity of various elements as a function of depth are shown in figure 7.2. Region I of the depth profile shows no major difference in the XPS Ni profiles for 10 and 30 s deposition, confirming that the deposited Ni layer thickness is self-limiting and independent of deposition time. The interface between the Ni film and the GaAs substrate, as shown in the second

region of the depth profile, exhibit a thickness of ~12 nm, much broader than the Ni layer, indicating extensive intermixing. In region II, the two Ga profiles are reproducible, while the As fraction vs. depth shows a different trend, which we ascribed to a reaction between As and Ni, possibly forming a compound NiAs.¹⁷³ The XPS depth profile for Ga, As and Ni are summarized in Figure 7.3.¹⁷⁴ The XPS signal from Ga and As is uniform and equiatomic in the third region, where the milling depth is larger than 16 nm, while only a small amount of Ni can be detected.

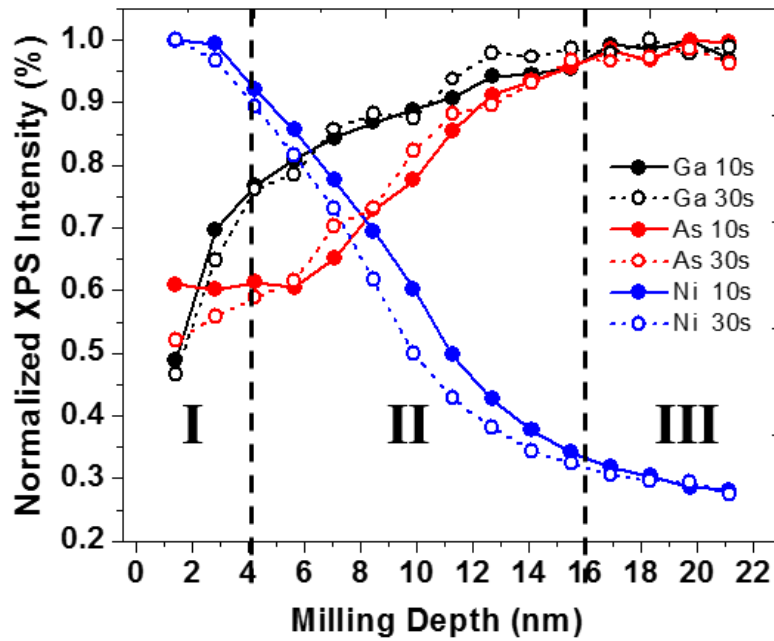


Figure 7.2 (a) XPS depth profile using Ar⁺ ion milling for Ni deposited GaAs for 10s, 30s and 60s.

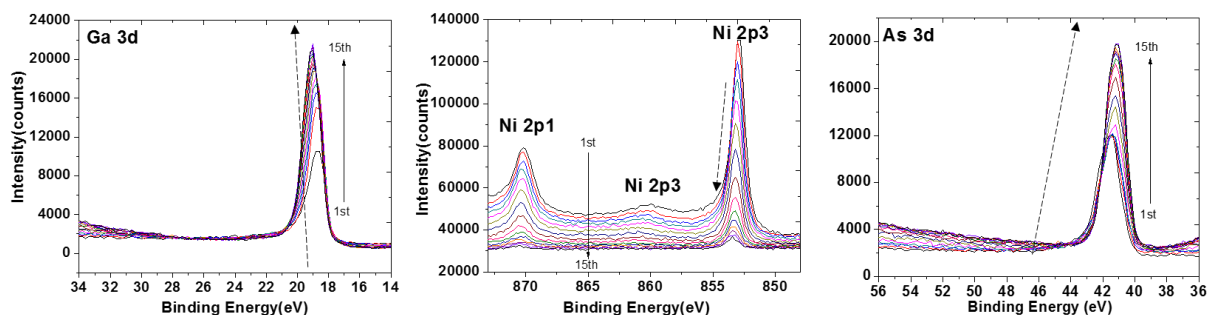


Figure 7.3 XPS spectrum of Ga 3d, Ni 2p3 and As 3d from 1st sputtering cycle to the 15th sputtering cycle, each Ar sputtering process removes ~1.4 nm of the top layer. The binding energy of the Ga 3d shifts to a higher value with the increasing number of sputtering while that of the As 3d shifts to a lower binding energy, which implies that Ni is diffusing into the GaAs substrate and causes the chemical state change of Ga and As.

The surface chemical state of the Ni/GaAs is further studied by XPS by comparing the pristine surface with a 6 s Ar ion milling. As shown in figure 7.4 (a), the peaks occurring at a binding energy of 852.9 and 870.2 eV are assigned to the Ni metal 2p_{3/2} and 2p_{1/2}, while the peaks located at 861.4 and 856.2 eV correspond to the Ni oxyhydroxide,¹⁷⁵ showing that the surface is mainly composed of metallic Ni and Ni oxy-hydroxides prior to Ar ion sputtering. The peak intensity from metallic Ni increases significantly, while the NiOOH peaks disappear after milling off a layer of ~1.4 nm from the surface. The results reveal that the layer underneath the surface is mainly composed of Ni metal, while Ni hydroxide or oxide is present in minimal amount. The high resolution of the XPS spectrum of O 1s of the protective Ni film before and after Ar milling is shown in figure 7.4 (b), where the oxygen peak occurring at 531.6 eV is due to adsorbed water molecules (H-O-H bond at 532.0-532.4eV), and the peak occurring at 529.8 eV is probably a convolution of the hydroxide (Ni-O-H bond at 530.5-530.6eV) and an oxide peak (Ni-O-Ni bond at 528.7-529.1eV).¹⁷⁶ These peaks disappear after removal of the top layer, thus confirming the

results extracted from the Ni spectrum. The XPS spectrum further support the self-limiting deposition hypothesis, since the top layer is covered with hydroxide or oxyhydroxide, while the layer underneath the surface is metallic Ni formed in the first stages of the electrodeposition before the self-limiting process is completed.

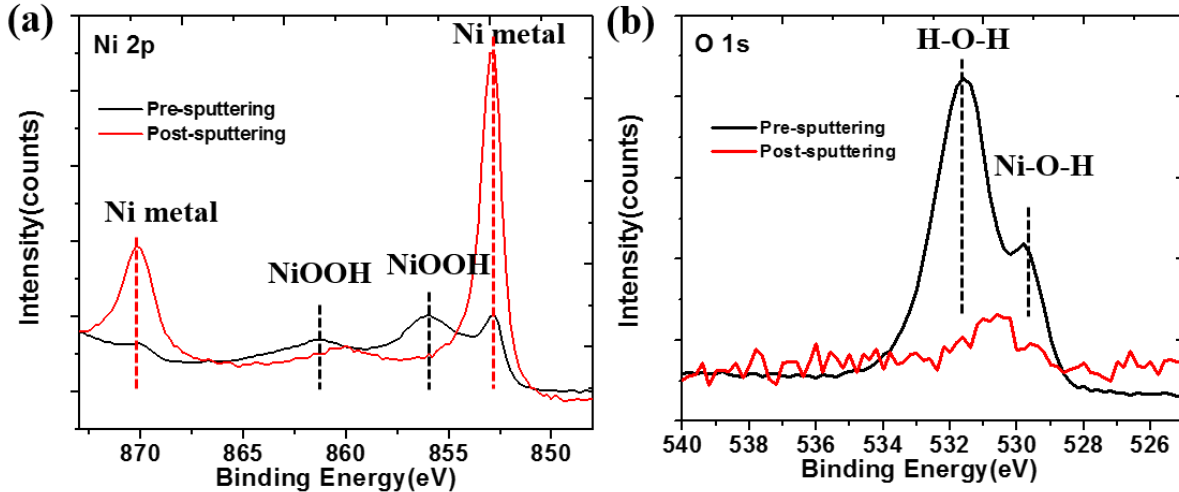


Figure 7.4 Ni 2p XPS spectrum (a) and O 1s XPS spectrum (b) for the Ni-deposited GaAs before and after sputtering off a flat surface layer of ~ 1.45 nm by Ar⁺ ion milling.

The FIB cross-section of the Ni film deposited for 1.0 s was investigated using HR-TEM. As shown in Figure 7.5 (a), the surface of the deposited sample is covered with an amorphous layer with a thickness of 1-3 nm, corresponding to the Ni oxy-hydroxides, while a metallic Ni layer with the thickness of ~ 4 nm is present underneath; both layers are continuous and no pin holes can be observed in the view, which further suggests that the self-limiting 1 s Ni deposition is capable of forming an ultra-thin continuous metallic Ni layer. The FFT analysis of the Ni film in figure 7.5 (b) shows fringes perpendicular to the matrix, representing the (111) planes of Ni with a face-centered-cubic structure. The d-spacing between these planes is 0.199 nm, close to the calculated value (0.1992 nm) for the Ni (111) planes, confirming that the electrodeposited Ni layer is

crystalline. From the indexed FFT pattern, the zone axis of the Ni layer is determined to have a [110] direction. The selected area diffraction pattern of the substrate shows the zinc blende structure of GaAs as displayed in figure 7.5 (c), where the zone axis is also along the [110] direction. Therefore, the epitaxial relationship $\text{Ni}(110)[110] \parallel \text{GaAs}(001)[110]$ is verified. This result is in good agreement with reported literature using galvanostatic electrodeposition methods to grow Ni thin film on GaAs.^{177–180} It should be noted that, with Si substrates, the formation of a metallic deposit on Si results spontaneously in the formation of a thin oxide layer⁴⁹, thus forming a MIS junction. At the GaAs substrate however, no such oxide is formed due to the dissolution of GaAs during the deposition of Ni. We therefore suggest that the thin NiOH/NiOOH layer may take the place of the oxide, thus generating a MIS-like barrier. This difference may be responsible for the lower barrier height with respect to electroplated Co on Si.⁴⁹

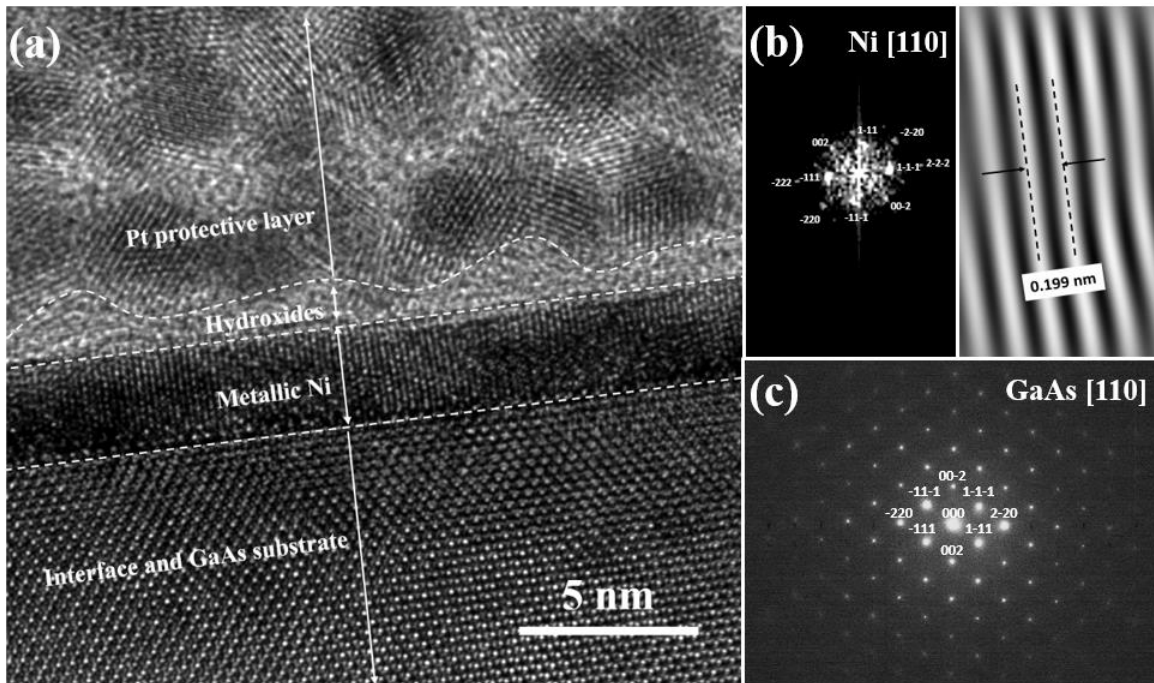


Figure 7.5 (a) HR-TEM cross-section image of 1.0s deposited Ni/GaAs; (b) FFT and the lattice parameter of the metallic Ni layer; (c) Selected Area Diffraction pattern of the GaAs substrate.

The photoelectrochemical performance of Self-limiting deposited Ni/GaAs (SL-Ni/GaAs) was investigated in an aqueous solution of $\text{K}_3\text{Fe}(\text{CN})_6/\text{K}_4\text{Fe}(\text{CN})_6$ under chopped light. Linear sweep voltammograms at the bare GaAs substrate, as well as the SL-Ni/GaAs films deposited for 1 and 10 s are reported in figure 7.6 (a). The onset potential of bare GaAs is $\sim 0.2\text{V}$ and the photocurrent saturates at a potential of $\sim 0.75\text{V}$ vs. RHE, with a maximum photocurrent density of less than 2 mA cm^{-2} ; such low photoactivity is probably owed to the decomposition of GaAs in solution under negative bias. The photoresponse of Ni films grown for 1 and 10 s Ni exhibits a similar onset potential ($\sim 0.77\text{V}$ vs. RHE), which is mainly contributed from the oxidation of $\text{Fe}(\text{CN})_6^{4-}$ to $\text{Fe}(\text{CN})_6^{3-}$. The thin Ni film grown for at least 1 s is continuous and the Fermi level of GaAs is pinned to Ni, such that the onset potential no longer shifts with deposition time. SL-Ni/GaAs deposits grown for 1 and 10 s exhibit a photocurrent saturating at $\sim 1.1\text{V}$ vs. RHE, and the photocurrent density at saturation is 4.9 mA cm^{-2} and 8.9 mA cm^{-2} , respectively. The photoconversion efficiency (η) as a function of applied potential is calculated and shown in figure 7.6 (b). The SL-Ni/GaAs film deposited for 1 s exhibits a maximum conversion efficiency of 0.67% at 1.0 V and the 10 s-deposited SL-Ni/GaAs shows a maximum conversion efficiency of 1.44% at the same applied potential. In comparison, conventional galvanostatic electrodeposition of Ni on GaAs (C-Ni/GaAs) shows a Ni film thickness that increases with deposition time according to the Faraday's law. In order to electrodeposit a continuous film using the conventional galvanostatic method, a thickness of at least $\sim 10\text{ nm}$ is needed, as the Ni islands are larger as shown in Figure 7.7 and require more time to form a continuous film in comparison with the self-limiting deposition method. The photocurrent transients generated by galvanostatic growth of C-Ni/GaAs with various thicknesses (10, 30 and 60 nm) are compared at a potential of 1.23V vs. RHE as shown in figure 7.6 (c). C-Ni/GaAs films grown to a thickness of $\sim 30\text{ nm}$ and $\sim 60\text{ nm}$ yield a

photocurrent of less than 0.5 mA cm^{-2} , while the photocurrent density for the 10 nm C-Ni/GaAs reaches 6.0 mA cm^{-2} . The linear scanning voltammetry of 60 nm-thick C-Ni/GaAs under chopped light is shown in figure 7.6 (d). The onset potential ($\sim 0.75\text{V}$ vs. RHE) is similar to that of SL deposited Ni/GaAs ($\sim 0.77\text{V}$ vs. RHE), which is also attributed to the Fermi level pinning effect at a continuous film. The results imply that the photoresponse of the SL-Ni/GaAs is superior to that of C-Ni/GaAs, due to the immediate coalescence and the nanoscale thickness. This layer is thus capable to maximize photon absorption of the protective layer, while affording the in-situ generation of the hydroxide/oxyhydroxides surface, resulting in a higher water oxidation catalytic activity.⁹ As a consequence, the following discussion will focus on SL-Ni/GaAs unless otherwise mentioned.

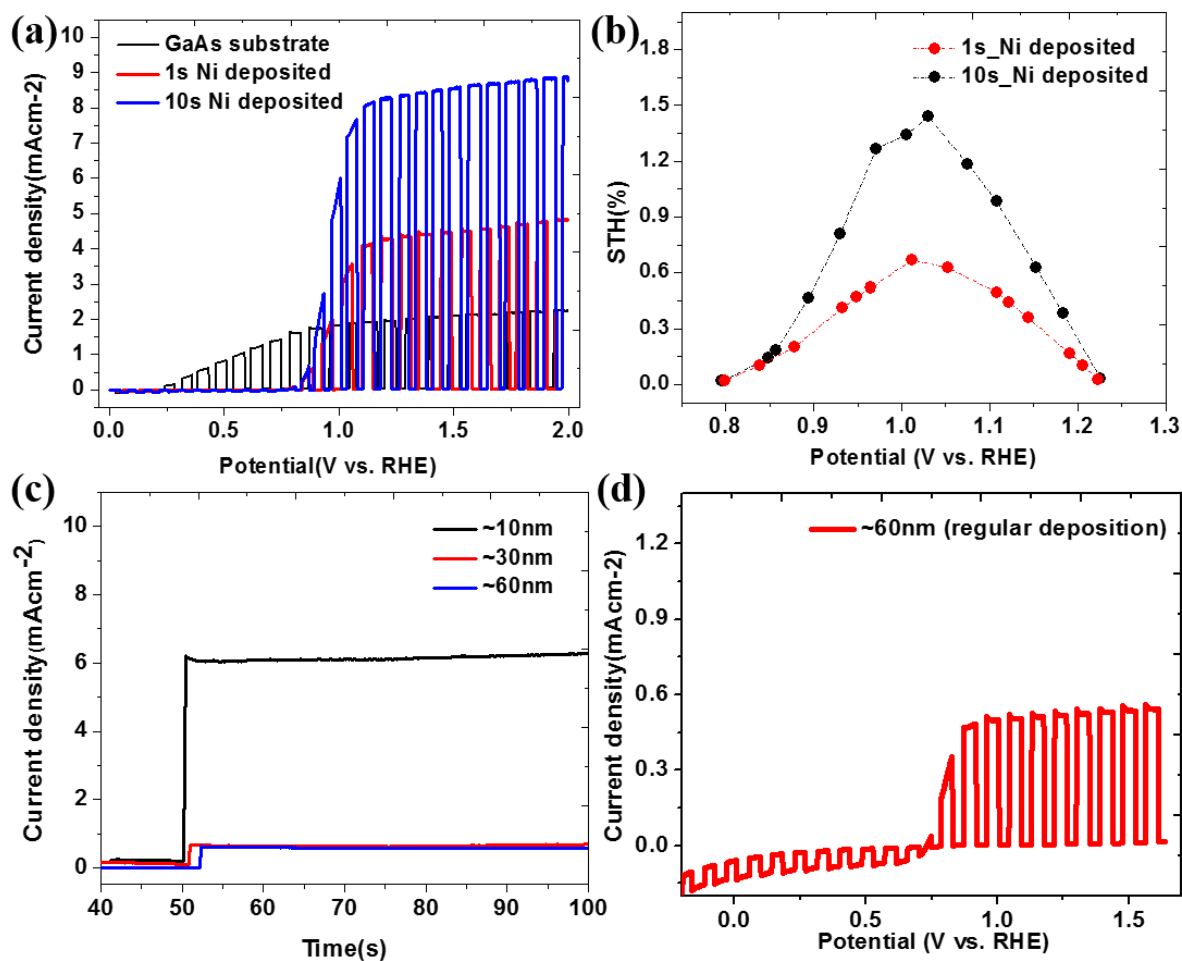


Figure 7.6 (a) Linear scanning voltammetries of GaAs substrate, Ni deposited GaAs for 1s and 10s under AM 1.5G chopped light; (b) Solar-to-hydrogen (STH) efficiency of Ni deposited GaAs at various applied potentials; (c) Chronoamperometry of Ni deposited GaAs using a conventional deposition method with various thickness at 1.23V vs. RHE. (d) Linear scanning voltammetries of Ni deposited GaAs using a conventional method with a thickness of ~60 nm under chopped illumination.

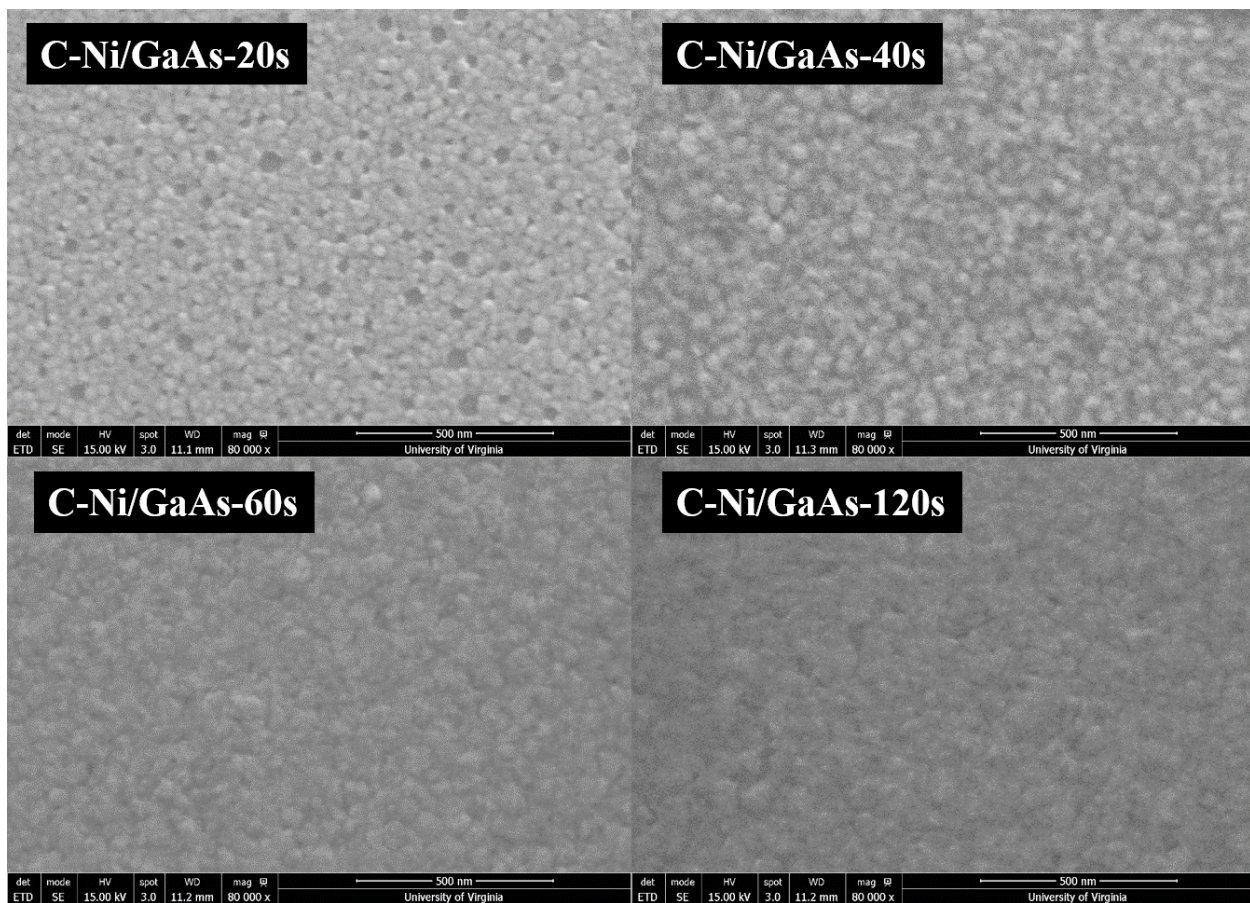


Figure 7.7 SEM images of Ni deposited GaAs with a conventional deposition method in NiSO₄ solution. The film thickness is determined to be ~10, 20, 30 and 60 nm for the 20s, 40s, 60s and 120s deposited film respectively, from ref ¹⁸¹. Coalescence is almost reached for the 20s-deposited C-Ni/GaAs while there are still large pinholes on the surface. For the 40s-deposited C-Ni/GaAs, the surface roughness remains high, and for a longer deposition time (40 and 60 s), relatively smooth surface are obtained.

The surface morphology of SL-Ni/GaAs as a function of deposition time was investigated by FE-SEM, as shown in figure 7.8. Films deposited for 10 s exhibit a smooth surface, while small defects – not necessarily going through the protective film – start to show on the 30 s deposit. When the deposition time reaches 60 s, roughening becomes more obvious and the particle size increases. As mentioned above, hydrogen evolution dominates the reaction when the film is no longer

growing due to hydroxide termination, and the generated hydrogen bubbles would significantly and continuously damage the thin film. Spherical particles start to grow as the deposition time increases to 120 s and surface roughness further increases. Ni particles probably grow in the area where the layer is peeled off by the hydrogen bubbles, and the self-limiting mechanism stops, as evidenced by the SEM and EDS results shown in Figure 7.9 (a) and (b).

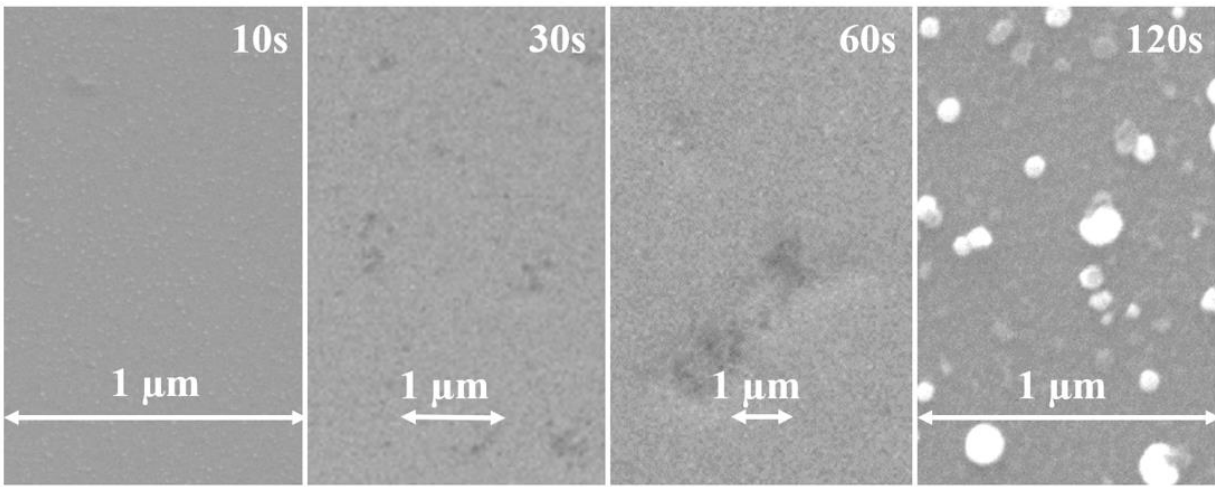


Figure 7.8 FE-SEM images of SL-Ni/GaAs with various deposition time from 10s to 120s

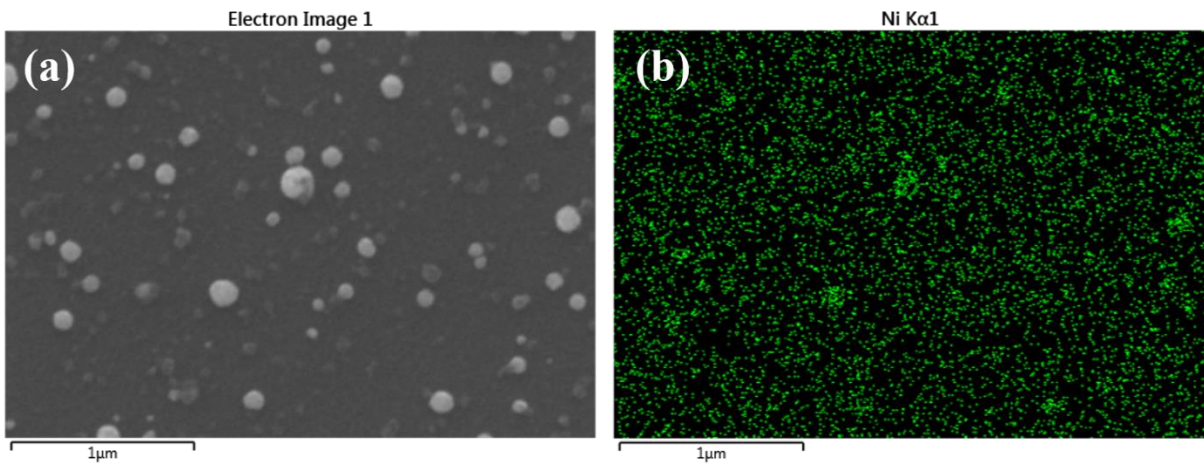


Figure 7.9 (a) FE-SEM image and (b) EDS mapping of the self-limiting deposition Ni/GaAs for 120s. From the mapping data, the particles on the surface shows more intense EDS signal, indicating that they are mainly composed of Ni.

The photocurrent vs. time for various films grown between 0 and 60 s was compared in aqueous $\text{K}_3\text{Fe}(\text{CN})_6/\text{K}_4\text{Fe}(\text{CN})_6$ solution under light at 1.23V vs. RHE as shown in figure 7.10 (a). The photocurrent of bare GaAs drops immediately after the light is turned on as a result of photocorrosion in solution. For all the SL-Ni/GaAs layers, the photocurrent density stays constant during the first 100 s, implying a significant improvement in stability after depositing the Ni protective layer. The photocurrent density vs. deposition time at the same applied potential is compared in figure 7.10 (b). A photocurrent density of 8.91, 7.71, 7.28, 6.37 mA cm^{-2} is obtained for the 10, 20, 30 and 60 s SL-Ni/GaAs, respectively, and the optimum photoresponse is determined to be 10 s. The decreased photocurrent density with a longer deposition time is the result of the damage of the continuous film by the hydrogen bubbles, as already mentioned. From the photoelectrochemical measurements, the self-limiting deposition of continuous Ni film on GaAs provides high photocurrent density and improved stability. However, the onset potential in the photo oxidation is relatively high ($\sim 0.75\text{-}0.80\text{V}$) leading to a limited photovoltage ($\sim 0.09\text{-}0.14\text{V}$, calculated using the reference anode, as a result of the Fermi level pinning effect. To reduce this effect, GaAs coated by discontinuous Ni nanoislands is further investigated.

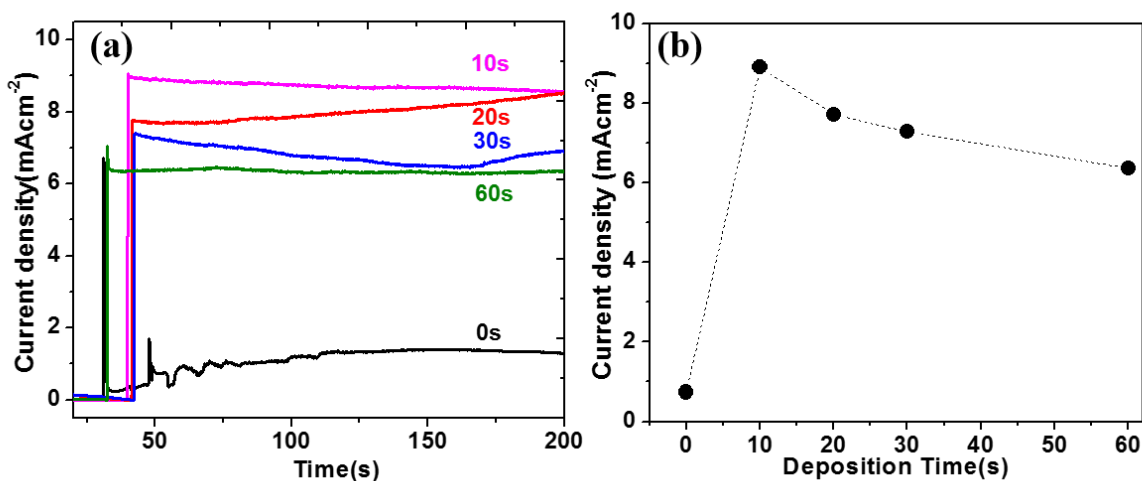


Figure 7.10 (a) FE-SEM images of SL-Ni/GaAs with various deposition time from 10s to 120s; (b) Chronoamperometry of SL-Ni/GaAs at 1.23V vs. RHE under illumination. (c) Photocurrent density at 1.23 V_{RHE} vs. deposition time of the SL-Ni/GaAs.

7.2 Self-limiting electrodeposition of discontinuous Ni nanoislands on GaAs

A SL deposition time of less than 1 s results in a discontinuous Ni film on GaAs. The surface chemical states of various elements for the SL-Ni/GaAs film deposited for 0.5 s are investigated by XPS and are shown in figure 7.11 (a). Based on the measured Ni 2p spectrum, the surface is mainly composed of metallic Ni, with a binding energy at 852.8eV, and Ni hydroxide (or oxyhydroxide), with binding energy of 855.8eV and 861.4 eV. This result is similar to that for the continuous SL-Ni/GaAs, except that the relative intensity acquired from metallic Ni is higher as the formation of the hydroxide/oxyhydroxide layer is incomplete. XPS peaks from Ga 3d (19.0 eV) and As 3d (41.8 eV) are shown in figure 7.11 (b) and (c), indicating that the GaAs surface is not fully covered by the Ni film, and a fraction of the GaAs surface is still exposed. Figure 7.11 (d) shows the O 1s spectrum, with a result similar to that for continuous SL-Ni/GaAs. The oxygen peak located at 531.6 eV is due to the adsorbed water molecules (H-O-H bond at 532.0-532.4eV),

and the peak occurring at 529.8 eV is from the combined peak of hydroxide (Ni-O-H bond at 530.5-530.6eV) and an oxide (Ni-O-Ni bond at 528.7-529.1eV).

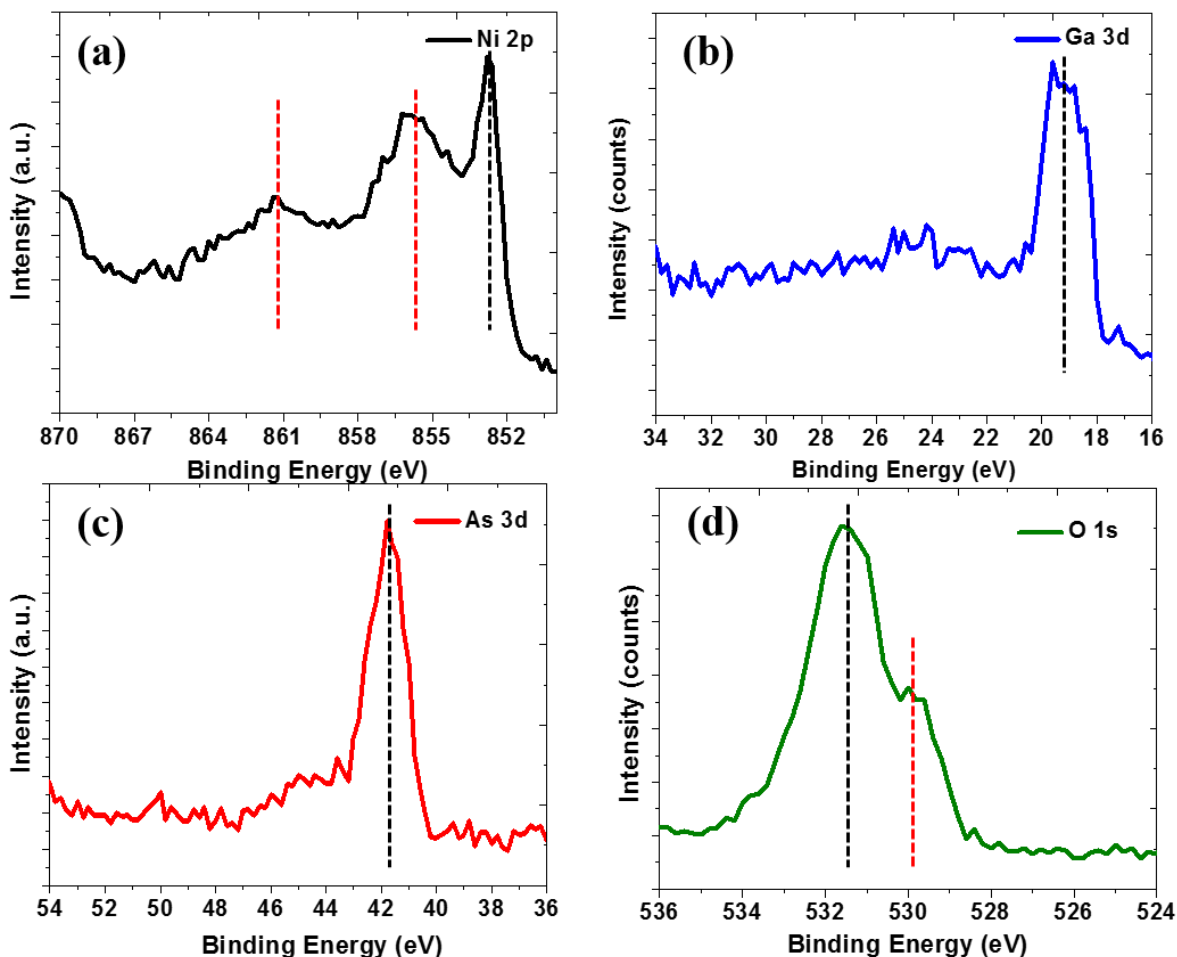


Figure 7.11 (a) Ni 2p; (b) Ga 3d; (c) As 3d and (d) O 1s XPS spectrum of 0.5s-deposited Ni on GaAs.

Linear sweep voltammetry carried out at SL-Ni/GaAs with a deposition time of ≤ 1.0 s under chopped light are shown in Figure 7.12 (a). As the deposition time decreases from 1.0 s to 0.5 s, the onset potential shifts substantially from 0.77 to 0.47V vs. RHE, leading to an increase in the photovoltage from 0.12 to 0.42 V. At a growth time of 0.2 s, the onset potential further decreases

to 0.39V vs. RHE, resulting in a photovoltage of 0.50 V. The saturated photocurrent density of the SL-Ni/GaAs film grown for 0.5 s is 8.0 mA cm⁻² at 1.1 V vs. RHE, while 0.2 s growth results in a value reaching 9.2 mA cm⁻² at 1.0 V vs. RHE, a higher value than the maximum photocurrent density (8.9 mA cm⁻²) obtained from continuous Ni layers. In comparison, linear sweep voltammetry of short-time deposited Ni on GaAs using a galvanostatic deposition method (C-Ni/GaAs) measured in the same condition are shown in figure 7.12 (b). For the 0.2 and 0.5 s deposited C-Ni/GaAs, the saturated photocurrent density is respectively 1.28 mA cm⁻² and 0.64 mA cm⁻². The low photocurrent density is attributed to the limited amount of Ni nanoislands being grown, due to the short deposition time. As the deposition time increases to 1.0 s, the saturated photocurrent density increases to 6.0 mA cm⁻² at ~1.0 V vs. RHE. The onset potential of the 1.0 s C-Ni/GaAs shifts cathodically from 0.75 V to 0.53 V vs. RHE compared to the continuous film, probably owed to the reduced Fermi level pinning effect. The photoconversion efficiency (η) for the short-time deposited Ni/GaAs with a self-limiting and a conventional method are shown in figure 7.12 (c) and (d). For the SL deposited Ni nanoislands, a maximum photoconversion efficiency of 3.82% is obtained at 0.72V vs. RHE for the 0.2s deposited SL-Ni/GaAs. The conventional deposition of Ni nanoislands shows optimum photoconversion efficiency is 1.83% at 0.86 V.

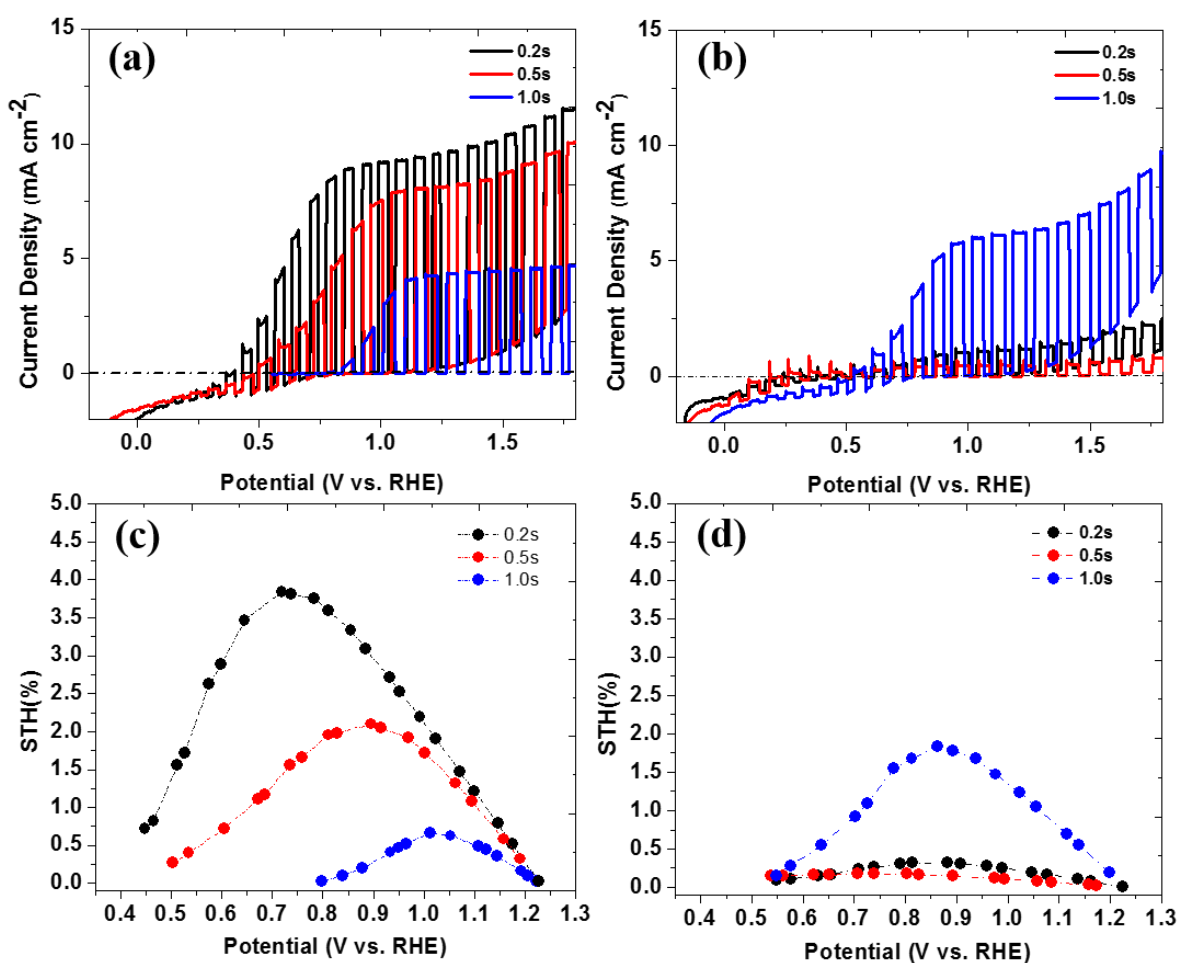


Figure 7.12 Linear Sweep voltammeteries of short time ($\leq 1.0s$) self-limiting deposited Ni on GaAs (a) and regular deposited Ni on GaAs (b); Solar-to-hydrogen efficiency of self-limiting deposited Ni on GaAs (c) and regular deposited Ni on GaAs (d).

A complete comparison of the photoelectrochemical performance and photoconversion efficiency between SL-Ni/GaAs and C-Ni/GaAs is displayed in Table 7.1, highlighting the superior photoanode property of the former. The self-limiting deposition results in a lower nanoisland size and a higher density of nucleation sites, while the growth is inhibited. This feature is beneficial as the number of Ni nanoislands serving as the charge carrier transport windows is increased¹⁶⁷ while simultaneously the Fermi level pinning effect is suppressed.

Table 7.1 Comparison of photoelectrochemical performance and energy conversion efficiency of SL-Ni/GaAs and C-Ni/GaAs.

Deposition condition	Saturated Photocurrent density (mA cm^{-2})	Photovoltage (V)	Maximum STH
0.2s_SL	9.2	0.50	3.82%
0.5s_SL	8.0	0.42	2.10%
1.0s_SL	4.9	0.12	0.67%
0.2s_C	1.28	0.66	0.32%
0.5s_C	0.64	0.66	0.18%
1.0s_C	6.0	0.36	1.83%

Barrier heights calculated from the dark saturation current are shown in figure 7.13 (a). The Schottky junction barrier height of films grown for < 1 s is relatively low (0.51 eV for 0.2 s, and 0.52 eV for 0.5 s) compared to a continuous film (0.71 eV for 10 s), which could be rationalized by considering that the 10-second growth results in a continuous oxyhydroxide, yielding a higher barrier height. ($\Phi_{\text{Ni}} = 5.04\text{-}5.35$ eV; $\Phi_{\text{NiOOH}} = 5.96$ eV).^{182,183} For a longer deposition time, the barrier height decreases to 0.66 eV, probably as a result of the pinholes generated by the hydrogen evolution. The photocurrent transients in the first 300 s in $\text{K}_3\text{Fe}(\text{CN})_6/\text{K}_4\text{Fe}(\text{CN})_6$ at 1.23V vs. RHE are shown in Figure 7.13 (b). For all the three films, a rapid decrease in photocurrent density is shown immediately after illumination, indicating the accumulation of photogenerated holes on the surface, as defects at the SL-Ni/GaAs surface are able to store the charge carriers and induce recombination.¹⁴⁴ For the films grown for 0.2 s and 0.5 s, a decay in photocurrent density, dropping to 2.3 mA cm^{-2} and 4.2 mA cm^{-2} respectively, while the decrease in photocurrent density for the film grown for 1.0 s is lower ($\sim 1.1 \text{ mA cm}^{-2}$). These results imply that, even though the discontinuous Ni nanoislands improve the photocurrent density and maximize the photovoltage by alleviating the Fermi level pinning effect, the reduced photocorrosion is reduced compared with the overlay of a continuous Ni film.

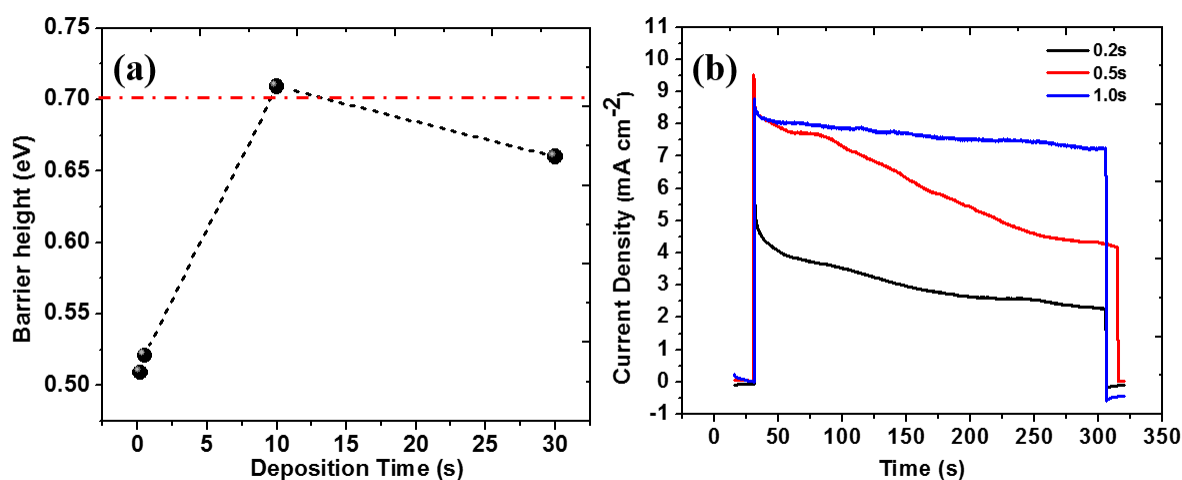


Figure 7.13 (a) Barrier height as a function of the deposition time of self-limiting Ni deposited GaAs; (b) Stability test of short time deposited Ni on GaAs at 1.23V vs. RHE under light.

7.3 Conclusions

In this Chapter, the self-limiting (SL) Ni electrodeposition on GaAs is carried out to grow a bilayer Ni/Ni-oxyhydroxide/hydroxide, leading to a continuous ultra-thin layer or discontinuous nanoparticles by controlling deposition time. The SL mechanism of Ni on GaAs is validated by XPS spectra, XPS depth profiles, XRR and HR-TEM, as the film thickness is independent of deposition time once the film reaches coalescence ($t > 1.0s$). The deposited Ni layer acts as a protective layer to limit the photocorrosion behavior of n-GaAs in aqueous solution while under solar illumination. SL-Ni/GaAs films exhibit a photocurrent density of 8.9 mA cm^{-2} at an optimum deposition time of 10 s with a relatively low photovoltage (0.09-0.14V) as a result of the Fermi level pinning effect, which leads to a limited maximum photoconversion efficiency of 1.44%. In contrast, discontinuous Ni nanoislands generate a higher photo response of 9.2 mA cm^{-2} and the photovoltage is significantly improved to 0.50 V, leading to a vastly enhanced photoconversion efficiency up to 3.84%. The stability under PEC test, however, is reduced compared to a

continuous film and a photocurrent decay is shown in the first 300 s at an applied potential of 1.23V vs. RHE. The reported work provides new opportunities for electrodepositing ultrathin metal layer or nanoscale catalytic metal particles on semiconductors for fabricating photoanodes and adds to the understanding of self-limiting deposition mechanism in a galvanostatic electrodeposition condition.

Chapter 8-Electrodeposition of binary/ternary Iron-group metal thin-film on GaAs through self-limiting electrodeposition

In this Chapter, we applied Galvanostatic electrodeposition for two binary Iron-group mutual alloy films (Ni-Co, and Ni-Fe) and one ternary Iron-group mutual alloy film in a self-limiting deposition condition, where a local pH gradient is created in a short time by the compact hydroxide/oxyhydroxide layer on the surface that can further terminate the growth, leading to the formation of a continuous ultrathin (oxy) hydroxide/metal film. The self-limiting deposition mechanism is verified by potential transient, XPS spectrum and XPS depth profile, from which an independence of the film thickness towards deposition time is demonstrated. Adding an additional element during deposition is proven to introduce a slower nucleation as a result of the smaller grain size of the deposited nanoislands. The electrochemical catalytic activity of the Iron-group alloy films was investigated and the water oxidation on the trinary film exhibits significantly improved kinetics. Furthermore, the Iron-group mutual alloy films were deposited on GaAs, which showed enhanced stability in photoelectrochemical water oxidation while retained a high photoresponse simultaneously.

8.1 Self-limiting deposition of binary Iron-group alloys (Ni-Co and Ni-Fe)

Potential transients of Ni and CoNi deposition in the first second is shown in Figure 8.1 (a). Typically, the potential transients is an indicator of the nucleation and first stage of growth. For either deposition, a rapid increase in the potential occurs in the first ~0.2 s corresponding to the charging of the electrode and the formation of electrochemical double layer before the nucleation initiates. A bump in the potential appears at 0.4 s to 0.6 s for Ni deposition while a similar bump for Ni-Co deposition appears at 0.6 to 0.8 s, which indicates the formation of

hydroxide/oxyhydroxide layer induced by the local pH gradient without buffer species.¹⁷² A second bump is shown at ~ 0.8 s for Ni and at ~ 1.0 s for Ni-Co deposition, corresponding to the completion of the surface hydroxide/oxyhydroxide formation. This surface layer is usually compact and is able to terminate further growth, resulting in an ultrathin metal/ (oxy) hydroxide layer with full coalescence, which is a significant feature of the self-limiting deposition.⁵⁹ The current density is mainly contributed by intense hydrogen evolution after the continuous surface layer is formed, as bubble formation was observed after ~ 1 s of deposition. It needs to be noted the Ni-Co deposition has a delayed nucleation (~ 0.2 s) at both initial state (first bump in potential transient curve) and the completion of the nucleation (second bump) compared to pure Ni deposition, as more nucleation sites with smaller sizes are formed by adding Co. The chemical state changes of the as-deposited Ni-Co film on Au were further investigated by XPS. The XPS spectrum of the Ni-Co film without/with a 6 s Ar milling (\sim removal of 1.5 nm surface layer) is compared as shown in Figure 8.1 (b-d). The peak located at a binding energy of 854.6 eV for the pre-sputtered Ni-Co film is assigned to the Ni $2p_{3/2}$ in NiO, indicating that the surface Ni mainly exists in the form of NiO. A metallic Ni peak with a binding energy of 853.0 eV appears after sputtering while a shoulder peak at 856.2 eV next to the NiO peak is associated with NiOOH as shown in figure 8.1 (b). For Co spectrum, a broad peak with its maximum intensity located at 780.4 eV is shown for both of the pre-sputtered and post-sputtered Ni-Co film in figure 8.1 (c), which is corresponding to Co $2p_{3/2}$ in the form of Co_2O_3 or Co_3O_4 . The broad peak probably consists of multiple peaks from other Co oxides, hydroxides, or oxyhydroxides, which is however difficult to specify. The oxygen peak located at 530.0 eV before Ar sputtering is associated with the O-H bond from absorbed water or surface hydroxides/oxyhydroxides, while the intensity of this peak

decreases after sputtering and another peak located at 532.0 eV corresponding to Ni^{3+} or Co^{3+} is present. This result is in good agreement with the Ni 2p and Co 2p spectrum.

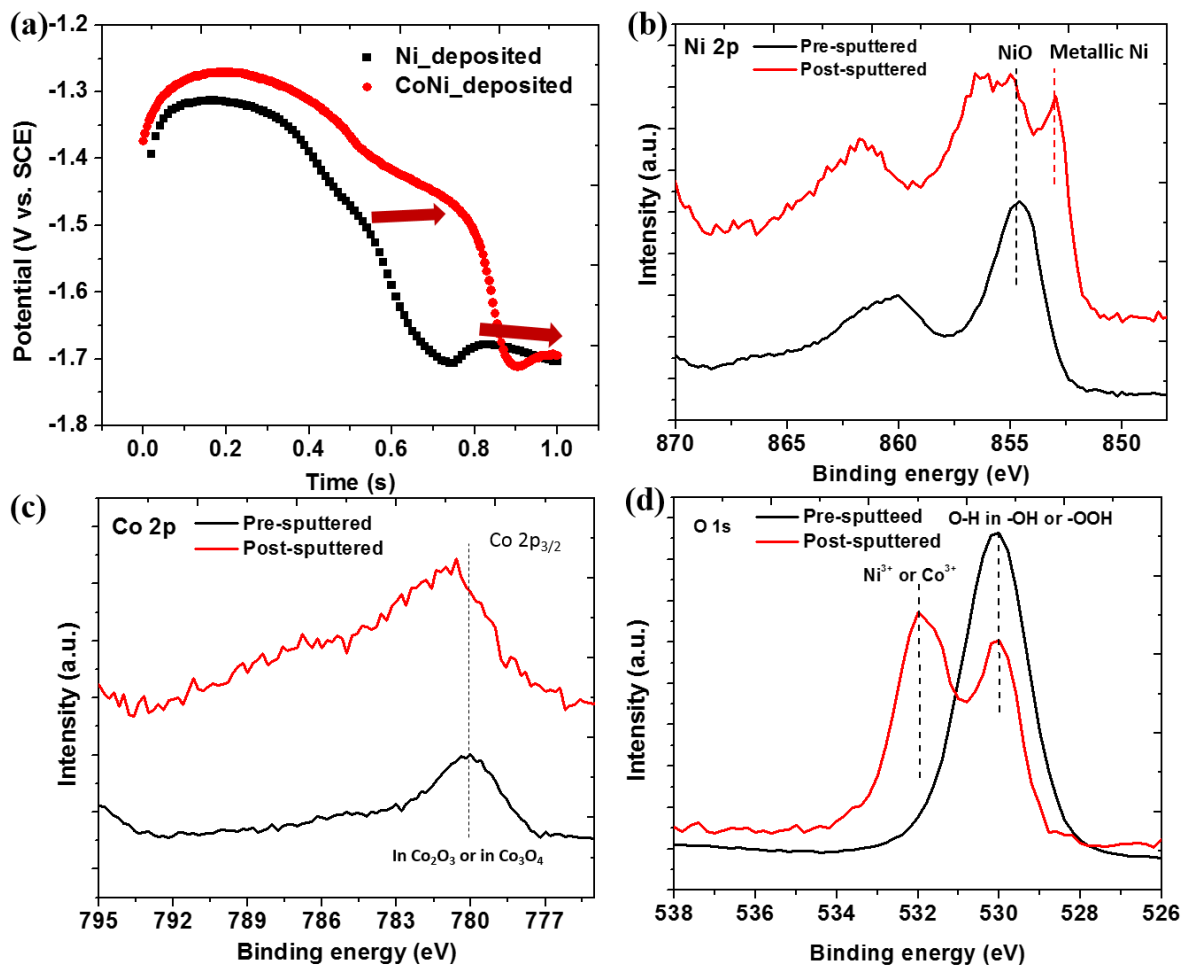


Figure 8.1 (a) Potential transients of Ni and Ni-Co on Au in the first second of galvanostatic electrodeposition. XPS spectrum of Ni (b), Co (c) and O (d) for Ni-Co film before/after 6s Ar sputtering (Removed layer thickness is $\sim 1.45\text{nm}$).

Potential transient of Ni-Fe deposition is shown in figure 8.2 (a). Similar to the case of Ni-Co, the first bump occurs at $\sim 0.6 - 0.8$ s while the second bump is not found in the first second of deposition, which indicates a similar self-limiting growth and an even slower nucleation process for

Ni-Fe deposition compared to pure Ni deposition and Ni-Co deposition. XPS spectrums of the Ni-Fe deposited film are shown in figure 8.2 (b) (c) and (d) without/with 6s Ar sputtering. Prior to sputtering, the peaks occurring at a binding energy of 852.6 eV is assigned to metallic Ni while the one located at 855.6 eV can be assigned to NiOOH as shown in figure 8.2 (b). The NiOOH peak disappears while the intensity of metallic Ni peak increases after Ar sputtering, showing Ni in the film underneath the surface mainly exists in the form of metallic Ni. For Fe spectrum shown in Figure 8.2 (c), a broad peak with the maximum intensity located at 712.2 eV is associated with FeOOH, while multiple overlapped peaks from other Fe oxides/hydroxides possibly contribute to the main peak as well.

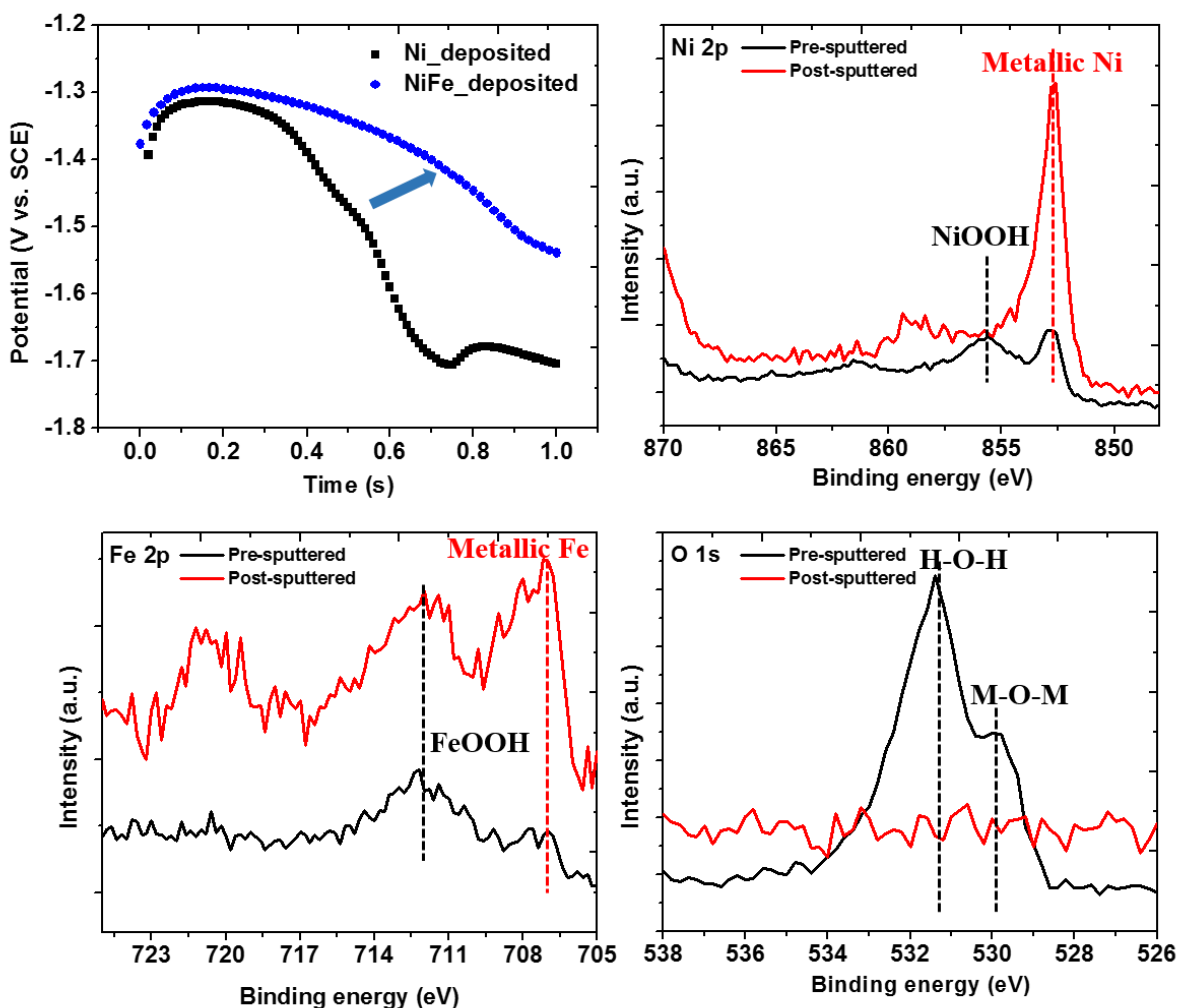


Figure 8.2 (a) Potential transients of Ni and Ni-Fe on Au in the first second of galvanostatic electrodeposition. XPS spectrum of Ni (b), Fe (c) and O (d) for Ni-Fe film before/after 6s Ar sputtering.

In order to further demonstrate the self-limiting mechanism for Ni-Co and Ni-Fe deposition, elemental composition measured by XPS along the out-of-plane depth of the film vs. different Ar milling depth was investigated for the films deposited with different time. As shown in Figure 8.3 (a), for both the 10 s deposited and 60 s deposited Ni-Co, Ni and Co deposition starts to decrease with a corresponding increase of Au composition after the first Ar sputtering, indicating that

interdiffusion occurs among Ni, Co and Au substrate. When the milling depth reaches ~17 nm, the composition of Au becomes ~100% and stays constant while all the other elements cannot be detected, such that a layer thickness of ~17 nm of the surface plus the interdiffusion layer is determined for both 10s deposited and 60s deposited Ni-Co. The independence of layer thickness on different deposition time further confirms the self-limiting deposition mechanism, as once the compact surface hydroxide/oxyhydroxide layer is formed, the film thickness is no longer increasing with time. Oxygen composition for both films drops to zero at a depth of ~5 nm, implying a low thickness of the surface hydroxide/oxyhydroxide layer (≤ 5 nm). The depth profile of Ni-Fe/Au was shown in Figure 8.3 (b). Ni and Fe composition decreases after the first sputtering for both 10 s and 60 s deposition, as a result of the interdiffusion of Ni, Fe and Au. The composition variation when the Ar milling depth is less than 10 nm between the 10s and 60s deposited films is probably due to the anomalous electrodeposition between Ni and Fe¹⁸⁴, in which case a slight change in the initial ratio of the Ni and Fe could result in a relatively larger difference in the products. However, the composition of Au along the depth for the 10 s Ni-Fe deposition overlaps with that for the 60 s Ni-Fe deposition while at ~20 nm the Au composition reaches ~100%. This indicates the Ni-Fe deposition is also independent of deposition time when the formation of surface hydroxide/oxyhydroxide layer is formed, and thus follows the self-limiting deposition mechanism. The grain size difference was further compared by GI-XRD as shown in figure 8.3 (d). The peak located at $2\theta = 44.5^\circ$ corresponds the diffraction from Ni (111) plane. The full width at high maximum (FWHM) becomes broader for the Ni-Fe/GaAs, demonstrating that the grain size is finer for the Ni-Fe according to Scherrer equation. From the previous discussion, the self-limiting growth during deposition occurs in Ni, Ni-Co, and Ni-Fe deposition, while both the Ni-Co and Ni-Fe deposition have a slower nucleation process compared to Ni deposition.

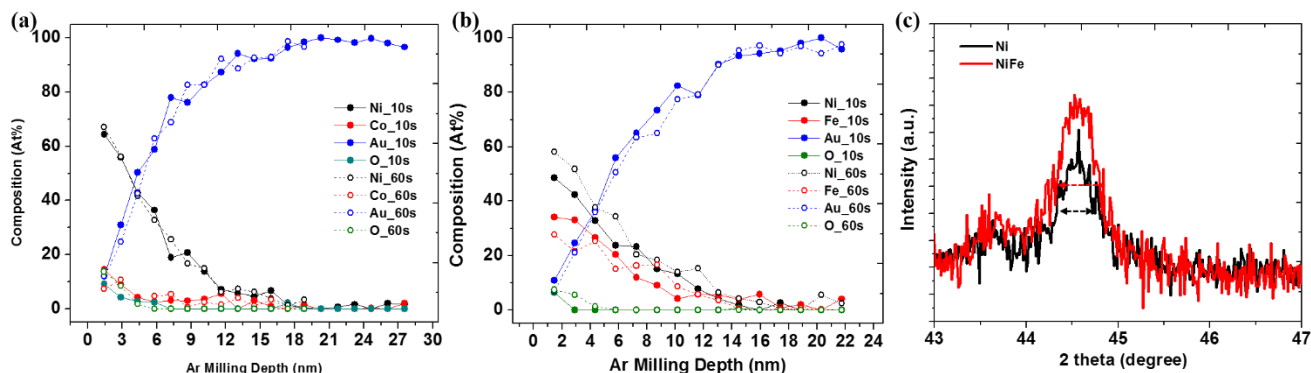


Figure 8.3 Elemental composition vs. Ar milling depth for Ni-Co/Au (a) and Ni-Fe/Au (b) for different deposition time. (c) GI-XRD for Ni and Ni-Fe film.

8.2 Electrochemical/photoelectrochemical water oxidation on binary Iron-group alloys

The catalytic activity towards water oxidation for Co, Ni, Ni-Co and Ni-Fe were estimated by cyclic voltammetry measured in 1 M KOH as shown in figure 8.4 (a). The overpotential when the current density reaches 10 mA cm^{-2} is 0.644V, 0.462V, 0.428V and 0.326V for Ni, Co, Ni-Co and Ni-Fe film respectively as shown in figure 8.4 (b). The onset potential is significantly reduced at the surface of binary alloy films (Ni-Fe and Ni-Co) compared with pure metallic layer (Ni or Co). The Tafel plots were measured in the same condition to further estimate the electrochemical kinetics as shown in figure 8.4 (c), where a Tafel slope of 93 mV/dec and 49 mV/dec is obtained for Ni-Co and Ni-Fe film, while a Tafel slope of 137 mV/dec and 273 mV/dec is shown respectively for pure Ni and Co film. The enhanced OER catalytic property is owed to an optimized bond strength between metal site and oxygen for NiOOH^{185} as well as the additional active sites created by Fe or Co^{186} .

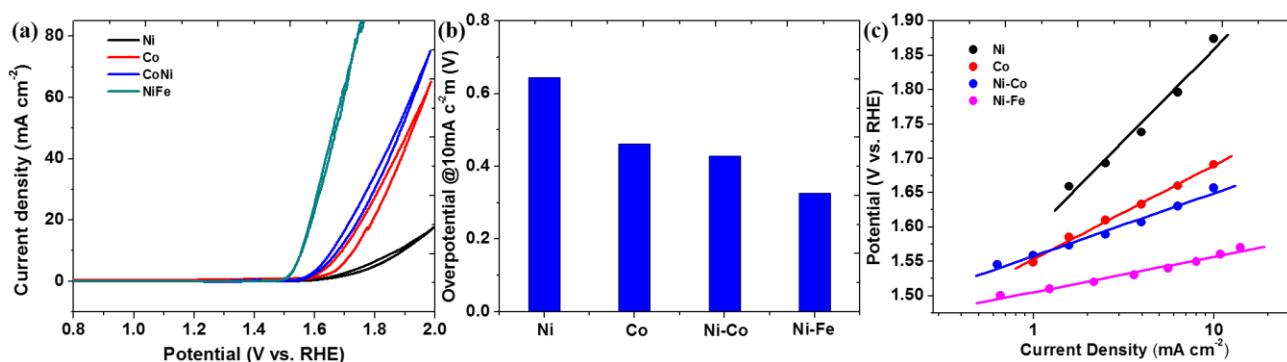


Figure 8.4 Cyclic voltammeteries (a), overpotential at a current density of 10 mA cm^{-2} (b) and Tafel plots (c) for Ni, Co, Ni-Co and Ni-Fe films on Au in 1M KOH.

Photoelectrochemical performance of Ni-Co/GaAs and Ni-Fe/GaAs was investigated in an aqueous solution containing $\text{K}_3\text{Fe}(\text{CN})_6/\text{K}_4\text{Fe}(\text{CN})_6$ under chopped light. Linear sweep voltammeteries for the Ni-Co/GaAs and Ni-Fe/GaAs films were shown in figure 8.5 (a). Both of the films show similar onset potential of 0.5V vs. RHE corresponding to a photovoltage of $\sim 0.39\text{V}$, while the saturated photocurrent density reaches 7.2 mA cm^{-2} at a $\sim 1.0 \text{ V}$ vs. RHE in either case. The similar photoelectrochemical performance for Ni-Co/GaAs and Ni-Fe/GaAs is attributed to the fact that the self-limiting deposited Ni-Co and Ni-Fe has close thickness and the junction created on the interface has similar behavior. The only difference is the photocurrent density for Ni-Fe/GaAs before saturation is higher than that of Ni-Co/GaAs with a maximum value of 0.8 mA cm^{-2} , which is attributed to the superior electrochemical catalytic activity of Ni-Fe film as aforementioned leading to a more rapid oxidation kinetics on the surface of the photoanode. Figure 8.5 (b) shows a comparison of stability between Ni/GaAs and Ni-Co/GaAs in the first 300s

potentialstatic measurements under the light at a potential of 1.23V vs. RHE with different deposition time of 0.2 s, 0.5 s and 1.0 s. For Ni/GaAs deposited for 0.2 s and 0.5 s, a rapid decay in photocurrent is shown in the first 30 seconds and a gradual decrease in photocurrent is present for the Ni/GaAs deposited for 1.0 s with a photocurrent retention of ~82.4 %. For Ni-Co/GaAs deposited for 0.2 s, an obvious photocurrent decay exhibits after 200 s, while for 0.5 s and 1.0 s deposited Ni-Co/GaAs, photocurrent decrease is minimum with a retention of ~ 91.8%. The stability of Ni-Fe/GaAs in the first 300s under the same condition is shown in figure 8.5 (c). 0.2s-deposited Ni-Fe exhibits a gradual decreased photocurrent in the first 300s measurement, while no obvious photocurrent decay is present for 0.5s and 1.0s-deposited Ni-Fe/GaAs and a maximum retention of 93.7% for 0.5s deposited Ni-Fe/GaAs is shown. It need to be noted that the 0.5s-deposited Ni-Fe/GaAs still retains a high photocurrent density of 7.6 mA cm⁻². Ni-Co and Ni-Fe films exhibit improved stability towards photocorrosion compared to pure Ni film, attributed to a smaller particle size and thus a higher density of nanoislands on the surface. Ternary Iron-group film containing Ni, Co, and Fe is then investigated on Au or GaAs substrate, aiming at further improving the electrochemical/photoelectrochemical performance towards water oxidation.

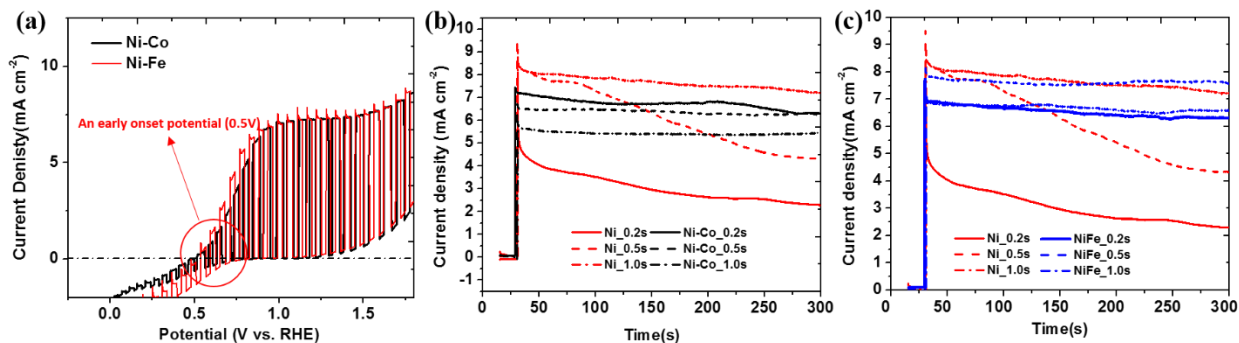


Figure 8.5 (a) Linear scanning voltammograms of Ni-Co and Ni-Fe under chopped irradiation of 100mW/cm² using AM 1.5G solar simulator in a K₃Fe(CN)₆/K₄Fe(CN)₆ solution. (b) Photocurrent transient for Ni/GaAs and Ni-Co/GaAs in the first 300s at 1.23V vs. RHE with various deposition time. (c) Photocurrent transient for Ni/GaAs and Ni-Fe/GaAs in the first 300s at 1.23V vs. RHE with various deposition.

8.3 Self-limiting deposition of ternary Iron-group alloys (Ni-Co-Fe)

XPS spectra for Ni-Co-Fe deposited on Au before/after 6 s of Ar sputtering were collected for Ni, Co, Fe and O, and are shown in figure 8.6 (a-d). Prior to Ar sputtering, a peak from metallic Ni is found at a bonding energy of 852.8 eV while there are multiple peaks locating at 855-856 eV and 861-862eV, possibly corresponding to Ni oxide/ (oxy) hydroxides. These peaks are hard to define since they show low intensity as the surface is highly oxidized in air and probably covered with absorbed water. After sputtering off a layer of ~ 1.5 nm, the spectrum shows a main peak located at a binding energy of 852.8 eV and another peak with intense counts at 870 eV associated with Ni 2p_{3/2} and Ni 2p_{1/2} in metallic Ni, while no other obvious peaks are shown. This implies that Ni mainly exists in the form of metal while no oxide/ (oxy) hydroxide is formed except on the surface, which further supports the self-limiting mechanism as the surface (oxy) hydroxides are not generated until the surface reaches coalescence. XPS spectrum of Co is shown in figure 8.6 (b),

where no distinguishable peak is shown prior to sputtering due to the small amount of Co and the highly oxidized surface. A peak located at a binding energy of 778.3 eV is present in the spectrum after sputtering, corresponding to metallic Co. No metallic Fe peak is shown on the surface before sputtering as can be seen in figure 8.6 (c), since Fe is also vulnerable to oxidation in air and the broad peak ranging from 711 eV to 713 eV can be probably assigned to FeOOH (711.3- 711.8 eV). A metallic peak from Fe for the post-sputtered Ni-Fe-Co film is shown while the broad peak from FeOOH still exists, because of the diffusion of surface oxygen to Fe. The Oxygen spectrum shown in figure 8.6 (d) further confirms the fact that the surface of the pre-sputtered Ni-Fe-Co film is mainly covered with absorbed water molecules and oxides, as the peak occurring at 531.6 eV is close to H-O-H bond (532.0 to 532.4 eV) or M-O-H (531 to 532 eV) and the peak occurring at 530.0 eV is corresponding to M-O-M bond (529.6 to 531.8 eV from common Ni oxides, Co oxides and Fe oxides). The peak at 531.6 eV disappears while the intensity of the peak at 530.0 eV decreases significantly after Ar sputtering, indicating that the film underneath the surface is mainly composed of metallic Ni, Co and Fe while there is still a small fraction of Fe oxyhydroxide due to the diffusion of oxygen.

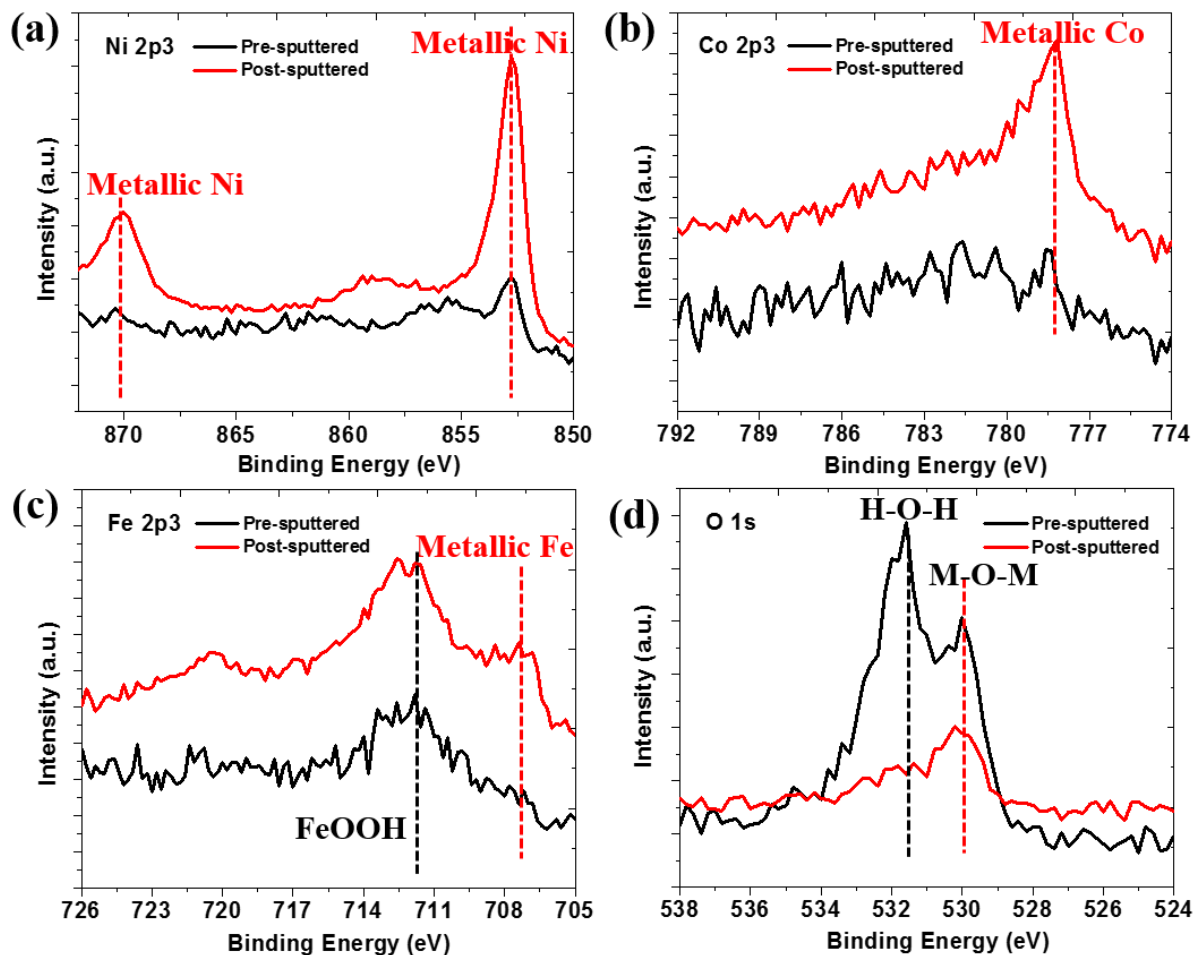


Figure 8.6 XPS spectrum of Ni (a), Co (b), Fe (c) and O (d) for the Ni-Fe-Co films on Au.

XPS depth profile depicting the elemental composition change along the depth of the Ni-Co-Fe film for different deposition time is shown in figure 8.7. Ni composition starts to decrease after the first sputtering and stays less than 5 At% when the milling depth is more than 18 nm as shown in figure 8.7 (a). The relative large thickness in the interface between Ni and Au is attributed to the interdiffusion similar to Ni-Co deposition. The composition profiles of films deposited for 10 to 60 s overlaps despite negligible deviations, indicating the independence of the film thickness towards deposition time. Figure 8.7 (b) exhibits the Fe composition profile for the films deposited

for 10 s to 60 s Ni-Fe-Co film. A plateau occurs for a depth of less than ~ 8 nm, and the composition starts to decrease as the interdiffusion between Fe and Au occurs. With regard to the Co depth profile shown in figure 8.7 (c), a decrease in the film intensity does not occur until the milling depth becomes larger than ~ 10 nm. The deviation between films deposited for 10 s and 60 s is relatively large, due to the relatively small amount of Co (~ 10 At %) in the film. The Au depth profile for the films deposited for 10 to 60 s are shown in figure 8.7 (d); the increase in composition with depth is owed to the interdiffusion while the similarity between the 10 s and 60 s films further verifies that the film thickness is independent of deposition time. Oxygen composition is dropping to zero at ~ 5 nm depth for both films with different deposition times, as shown in Figure 8.7 (e), which implies a thickness of surface oxide/(oxy)hydroxide layer of ~ 5 nm. Potential transient vs. deposition time in the first 3 s for the Ni-Fe-Co deposition is shown in figure 8.7 (f). A potential bump featuring the formation of hydroxide layer occurs at 1.5 s as marked out, which is longer than Ni (~ 0.6 s), Ni-Co (~ 0.8 s), and Ni-Fe (~ 0.8 s) deposition, as a result of a slower nucleation process by adding a third element.

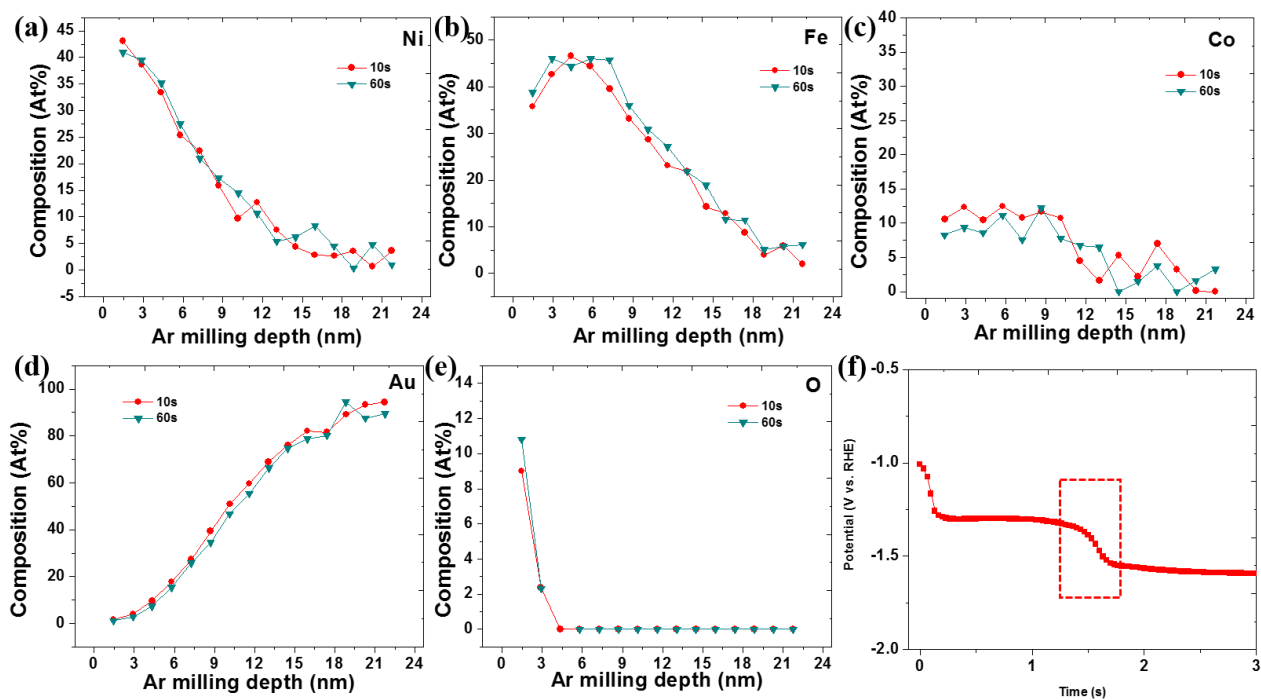


Figure 8.7 Elemental composition vs. Ar milling depth for Ni (a), Fe (b), Co (c), Au (d), and O (e) for Ni-Fe-Co/Au. (f) Potential transient of Ni-Fe-Co deposition on Au in the first 3 seconds.

8.4 Electrochemical/photoelectrochemical water oxidation on ternary Iron-group alloys

In order to investigate the electrochemical performance of the ternary alloy films, we performed linear scanning voltammeteries for various deposition times (1 s to 60 s) in 1 M KOH, the data are shown in figure 8.8 (a). The oscillation of the curves at higher potential ($\geq 1.6\text{V}$) is owed to the intense hydrogen bubble formation on the surface. The overpotential at 10 mA cm^{-2} for the Ni-Fe-Co film is 0.314V, 0.319V, 0.316V and 0.32V for a deposition time of 1s, 10s, 30s and 60s, respectively, as shown in figure 8.8 (b). Tafel measurements in 1M KOH were used to study the electrochemical kinetics of water oxidation on the surface of Ni-Fe-Co film; Tafel plots are shown in figure 8.8 (c). For all the films with different deposition time, the overpotential follows a good

linear relationship with the logarithm of current density, verifying that water oxidation is the main reaction in the selected potential range. A Tafel slope of 34.7, 37.9 and 38.4 mV/dec is respectively observed for 1s, 10s and 60s deposited films, showing a much-enhanced electrochemical kinetics compared to Ni-Fe (49 mV/dec), Ni-Co (93 mV/dec) and Ni (273 mV/dec). The slightly improved property of 1s deposited Ni-Fe-Co film compared to 10s deposited film is probably due to an increased resistance in the film with increased thickness as for a deposition time of 1s, the surface compact (oxy) hydroxide layer is not formed and the film thickness is still dependent on the deposition time. For a longer deposition time of 60 s, both the onset potential and the Tafel slope slightly increase as more pinholes are generated on the surface caused by the intense hydrogen evolution during the deposition.

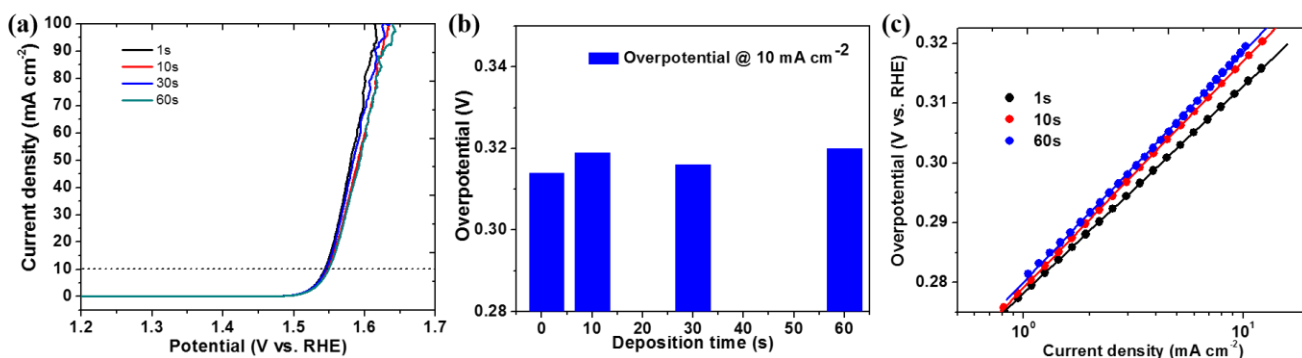


Figure 8.8 Linear scanning voltammeteries (a), overpotential at a current density of 10 mA cm^{-2} (b) and Tafel plots (c) for Ni-Fe-Co with deposition time ranging from 1s to 60s.

The photoelectrochemical performance of the Ni-Fe-Co deposited on GaAs with different deposition time is investigated in an aqueous Ferri/Ferro cyanide solution under AM 1.5G solar illumination with a power density of 100 mW/cm^2 . Linear scanning voltammeteries are shown in Figure 8.9 (a). The saturated photocurrent density for all the three films are similar with a value of

~4.7 mA cm⁻². For the 1s-deposited Ni-Fe-Co/GaAs, an onset potential of 0.58 V vs. RHE is obtained, corresponding to a photovoltage of 0.29V, while the onset potential is 0.70 V for both 10 s and 30 s deposited film as shown in figure 8.9 (b). The similar photoresponse for 10 s and 30 s deposited film is owed to the similar thickness and composition of the Ni-Fe-Co film when the self-limiting condition is fulfilled, while the Fermi level pinning effect when coalescence is reached leads to a late onset potential.⁴⁹ The stability of Ni-Fe-Co deposited GaAs is investigated by potentiostatic measurement at 1.23V vs. RHE under light and is compared with the previous results obtained on Ni/GaAs, Ni-Co/GaAs, Ni-Fe/GaAs. The optimal photocurrent retention of the different alloy-systems is shown in figure 8.9 (c), where Ni-Fe-Co/GaAs exhibits the optimum photocurrent retention (96.36%) compared to the binary alloy films or Ni film deposited on GaAs.

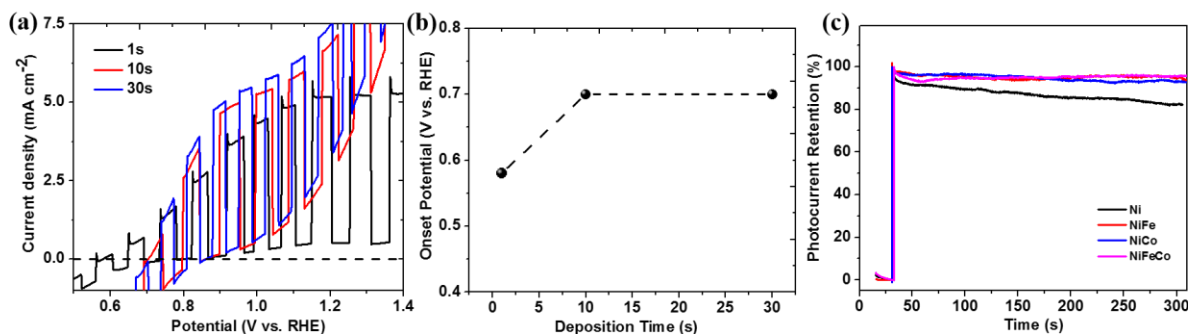


Figure 8.9 (a) Linear scanning voltammograms of Ni-Fe-Co/GaAs deposited with different time under chopped irradiation of 100mW/cm² using AM 1.5G solar simulator in a K₃Fe(CN)₆/K₄Fe(CN)₆ solution. (b) Onset potential of Ni-Fe-Co/GaAs deposited at various deposition time. (c) Comparison of photocurrent retention of Ni, Ni-Fe, Ni-Co and Ni-Fe-Co/GaAs in a 300s potentiostatic measurement under light.

8.5 Conclusions

In this chapter, the self-limiting electrodeposition of two binary Iron-group mutual alloy films (Ni-Co and Ni-Fe) and one ternary Iron-group mutual alloy film (Ni-Co-Fe) are investigated. The self-limiting mechanism is validated by potential transient during deposition, collection of XPS spectra and XPS depth profile, as the formation of (oxy) hydroxide/metal layer with low thickness, high coalescence is independent on deposition time. We also demonstrate that by adding an external element leads to a slower nucleation process, probably due to a smaller grain size of the deposited nanoislands as suggested by GI-XRD. The various Iron-group mutual alloy films deposited on Au substrate were further investigated as electrochemical catalysts for water oxidation in 1M KOH. Both binary and ternary Iron-group mutual alloy films exhibit improved water oxidation kinetics compared to pure Ni or Co film. In particular, an overpotential of 0.314 V at 10 mA cm⁻² and a Tafel slope of 34.7 mV/dec are obtained on the Ni-Fe-Co film. In addition, the Iron-group mutual alloys deposited on GaAs were further investigated as photoanodes in an aqueous Ferri/Ferrocyanide solution under light. The binary alloy films exhibit high photocurrent density (7.2 mA cm⁻²) with low onset potential (0.5 V vs. RHE) and an improved stability compared to pure Ni film, while the stability towards photocorrosion can be further improved by using the ternary alloy films with the cost of a reduced photoresponse (4.7 mA cm⁻²). This work provides a new deposition scheme to access continuous ultrathin Iron-group alloys with various composition, while to tailor the Ni-Fe-Co composition in the ternary alloy system it is possible to further improve the electrochemical/photoelectrochemical performance.

Chapter 9-Conclusions and future work

9.1 Conclusions

In the first part of the dissertation, various modification methods were thoroughly investigated to understand the relationship between the properties of the Ti-O based nanostructured materials and the photoelectrochemical performance towards water oxidation. Different reduction levels controlled by different synthesis methods allow the generation of various types of defects and doping levels. Argon-ammonia treatment provides a superior photoelectrochemical performance by introducing Ti³⁺/oxygen vacancies compared to surface laser modification, electrochemical doping and hydrogen treatment. Deposition of surface catalysts allows further improvement of the photoresponse by accelerating the oxidation kinetics only if the thickness is sufficiently low to maximize the absorption of the incident photons and the impact from trap states created during deposition is negligible. In the second part of this dissertation, electrodeposition of Iron-group metals and alloys on GaAs were investigated as a photoanode. Ultrathin film/nanoparticles of metal/ (oxy) hydroxides are produced from self-limiting deposition with enhanced photocurrent and photovoltage; the stability during photoelectrochemical water oxidation is improved simultaneously, but to a limited extent. More detailed conclusions are provided below:

Laser surface modification: Anodized TiO₂ nanotubes have been irradiated with a pulsed UV laser in DI water environment to introduce lattice disorder. As a result, the photocurrent improved by 1.6-fold under simulated sunlight compared with pristine TiO₂ nanotube arrays at 1.23V_{RHE}. For all samples the water oxidation reaction kinetics is determined to be the limiting step for the solar-to-current conversion at low bias (0.5-0.7 V_{RHE}), while modified nanotube arrays display a 78% water oxidation selectivity at 1.23 V_{RHE}, compared to 65% for the pristine TiO₂ nanotubes. The electronic density of states of the modified nanotubes is evaluated using electrochemical

impedance spectroscopy, revealing that selective laser irradiation improved the number density of shallow donors while reducing the density of deep trap states.

High temperature hydrogen reduction: Thermal annealing of anatase TiO₂ nanotube arrays under mixed hydrogen-argon atmosphere at high temperatures (>600°C) is employed to induce significant oxygen deficiency and phase transitions to substoichiometric structures (Magnéli phases), with the aim to limit interfacial recombination processes and increase the density of charge carriers. Particle-nanowire porous TiO₂ sub-stoichiometries are formed at 800°C, which is quantitatively investigated via X-ray diffraction and Rietveld refinement. The photocurrent of this Ti-O compounds is increased by 2.4-fold at 1.23V_{RHE} and the photoconversion efficiency is enhanced by 2.8-fold at a reduced bias under simulated solar illumination in comparison with pristine TiO₂ nanotube arrays. The improved performance is owed to a slower interfacial recombination, resulting in the increase of water oxidation selectivity from 65% to 92%, and by the increase in charge carrier density up to two orders of magnitude, as evaluated via electrochemical impedance spectroscopy. Finally, this method is compared to electrochemical hydrogen doping, with the latter exhibiting a significantly lower energy conversion efficiency.

Argon-nitrogen treatment: An Ar-NH₃-Ar treatment method is capable to introduce Ti³⁺ species in anodic self-ordered TiO₂ nanotube arrays for the synthesis of black TiO₂ nanotube arrays. The presence of Ti³⁺ is verified by XPS, EPR and EDS measurements while no detectable N is observed in the material. The modified TiO₂ exhibits a 5-fold enhancement in photocurrent compared to pristine TiO₂ at 1.23V vs. RHE due to the increased absorption of the solar spectrum. For the 4-hour treated sample, a photocurrent of 1 mA·cm⁻² is obtained at 1.18V vs. RHE, owing to the reduced flat band potential and the increased density of charge carriers evaluated using EIS measurements. The photocatalytic activity can be further optimized by increasing the layer

thickness, leading also to a cathodic shift of onset potential. Furthermore, the modified TiO₂ remains intact in air for no less than 1 week. This enhancement in photo-catalysis is proven closely relevant to the Ti³⁺ induced by the Ar-NH₃-Ar treatment.

Electrodeposited NiFe oxy-hydroxides catalysts: Ni-Fe (oxy) hydroxides with nanoflakes-structure are first electrodeposited on Au substrates; the as-deposited catalysts indicate enhanced oxygen evolution catalytic activity. The same deposition method is then applied at various TiO₂ nanotube systems. Specifically, mouths, walls and whole bodies of anodic TiO₂ nanotubes are electrodeposited with Ni-Fe (oxy) hydroxides and the corresponding photo response to water oxidation are investigated. We show that at relatively low applied potential ($\leq 1.5\text{V}$ vs. RHE) the Ni-Fe (oxy) hydroxides layer significantly reduces photon absorption and facilitates interfacial recombination, leading to a decreased photocurrent density. In contrast, at relatively high bias ($>1.5\text{V}$ vs. RHE), the oxygen evolution is enhanced due to the intrinsic electro-catalytic properties of the loaded catalysts. Synergistic effect are not found in the three Ni-Fe (oxy) hydroxide films deposited at TiO₂ nanotube systems.

Ni deposition on GaAs: A self-limiting electrodeposition method of Ni on GaAs is developed to either generate ultra-thin continuous film or nanoislands with high particle density by controlling deposition time. The self-limiting growth mechanism is validated by potential transients, XPS composition and depth profile measurements. This deposition method exhibits a rapid nucleation, forms an initial metallic layer followed by hydroxide/oxyhydroxide on the surface and is independent of layer thickness vs. deposition time when coalescence is reached. A photocurrent up to 8.9 mA cm^{-2} with a photovoltage of 0.11 V is obtained for continuous ultrathin films, while a photocurrent density of 9.2 mA cm^{-2} with a photovoltage of 0.50 V is reached for the discontinuous nanoislands layers in an aqueous solution containing $\text{K}_3\text{Fe}(\text{CN})_6/\text{K}_4\text{Fe}(\text{CN})_6$.

Iron-group-mutual-alloy deposition on GaAs: two binary Iron-group mutual alloy films (Ni-Co and Ni-Fe) and one ternary Iron-group mutual alloy film (Ni-Co-Fe) under self-limiting deposition condition are investigated and continuous ultrathin films with various composition are generated. The film thickness is independent of electrodeposition time when the self-limiting deposition condition is fulfilled, as verified by XPS depth profile. Each binary and ternary Iron-group mutual alloy film exhibits improved water oxidation kinetics compared to pure Ni or Co film. In particular, an overpotential of 0.314V at 10 mA cm⁻² and a Tafel slope of 34.7 mV/dec are obtained on the Ni-Fe-Co film. The Iron-group mutual alloy deposited on GaAs is further investigated for photoelectrochemical water oxidation. The stability towards photocorrosion under the light in an aqueous solution containing K₃Fe(CN)₆/K₄Fe(CN)₆ is significantly improved by electrodepositing the mutual alloy films while the optimum stability property is obtained for the ternary alloy film.

9.2 Future work

High-temperature hydrogen treatment on TiO₂ nanotubes has been demonstrated to generate various sub-stoichiometries with significant morphology change and improved photoresponse. The improvement, however, is mainly restricted to the UV region while improvement in the visible region is probably due to the fact that conductive TiO or Ti₂O₃ is not initially photo-active. It is possible to conduct a more thorough investigation of the relationship between the phase fraction and the photoresponse by a more accurate control of the reduction temperature and the partial pressure of hydrogen. This method provides a unique structure (microparticle-nanowire porous) with various Magneli phases which could be employed as the precursor for other modifications. Even though it has been demonstrated that electrochemical hydrogen doping cannot improve the photoelectrochemical performance of the reduced TiO compounds, other types of doping typically applied on Ti-O based materials including non-metal elements (carbon, nitrogen, iodine, sulfur,

etc.), and metal elements (copper, zinc, molybdenum, niobium, etc.) are yet to be understood.^{41,187–}

189

Ni-Fe oxy-hydroxide catalysts can be electrodeposited on various TiO₂ nanotube system with different surface morphology and the surface water oxidation kinetics is improved within a high voltage range, while the short individual nanotubes with large gaps exhibit the maximum improvement compared with the other two TiO₂ nanotube systems, possibly due to the minimum number of defects generated at the interface during electrodeposition. Nevertheless, the influence of the actually length of the nanotubes and the distribution density of the nanotubes on the surface has not been fully understood. There might exist an optimum condition for a maximized overall water oxidation activity, since a sparse distribution of the nanotubes leads to an improved electrochemical catalysis, but meanwhile limits the photoresponse and the surface area, while a compact alignment of the nanotubes results in a reduced electrochemical kinetics and more trap states that facilitate recombination. The investigation of a more accurate surface nanotube-distribution with controlled nanotube length could be achieved by controlling the water content, the reaction time and the applied potential during anodization.^{21,56}

Iron-group mutual metals electrodeposited onto GaAs has been investigated, including Ni, Ni-Fe, Ni-Co and Ni-Fe-Co; an optimum electrochemical/photoelectrochemical performance was obtained in the Ni-Fe-Co system in terms of the activity and the stability. However, the influence of various composition of Ni, Fe and Co was not reported. It is possible to further improve the electrochemical/photoelectrochemical performance of the Ni-Fe-Co system by controlling the composition of the three elements while understanding the changes in the film thickness, nucleation time and self-limiting deposition mechanism is also of interest. Despite the improved stability of the ternary alloy film in an aqueous electrolyte while testing the electrochemical

performance, long term operation as a photoanode for water splitting is still challenging. To deposit an additional protective layer between the GaAs substrate and the metal/(oxy)hydroxide layer may help further improve the stability. This additional layer should require high photo-transmittance, high charge transfer properties, and high resistance towards photocorrosion. An amorphous TiO₂ layer deposited by atomic layer deposition (ALD) is among the most promising candidates.^{160,190–192}

Acknowledgements

First of all, I would like to thank Dr. Giovanni Zangari, my PhD advisor. His diligent and rigorous attitude towards research shows me what makes a good researcher and greatly inspires me throughout the entire 5 years of my PhD study. Many of my efforts and findings would not be possible and paid off without his persistence, constant encouragement and word-by-word correction for each paper to be submitted. I truly appreciate and cherish the time working with him.

I also would like to thank all the professors on my committee for their support and valuable suggestions for my dissertation: Dr. Robert Kelly (chair of my committee), Dr. Joshua Choi (ChE, UVa); Dr. Petra Reinke; and Dr. Stephen McDonnell.

Our collaborators are highly appreciated as well, including Dr. David Klein and Dr. Sebastien Cap (FHI, Germany) for their help on the argon/ammonia treatment; Dr. Michael Melia and Dr. James Fitz-Gerald (UVA, MSE) for their efforts on the laser treatment; Dr. Keren Freedy, Meg Sales and Dr. McDonnell (UVA, MSE) for the support on E-beam deposition, and XPS measurements; Eric R. Hoglund for the help on TEM measurements; Dr. Zeming Sun, Arpan Sinha, Dr. Rasin Ahmed (UVA, ECE) for the help on solar simulator calibration; Dr. Sarah Bentley and Dr. David Cafiso (UVA, Chem) for the help on the EPR measurements.

My sincere thanks also go to all my former and current group members: Dr. Lok-kun Tsui, Dr. Marcel Mibus, Dr. Begum Unveroglu, Dr. Paloma Boeck, Dr. Rasin Ahmed, Dr. Fu Zhao, Dr. Amir Chamaani, Qiyuan Lin, Yunkai Sun, and Lee Kendall; and to my dear friends at UVa.

Last but certainly not least, I would like to thank my parents for their support on my study; A special thanks to my wife, Dr. Ge Song. It's a great blessing to meet her in my PhD career when

she was also pursuing her PhD in the ECE department at UVa. There have been many difficult times when I almost gave up, but her consistent support encourages me and keeps me carrying on. It is not possible for me to finish this long journey without having her on my side. It's another great blessing to meet Miss Luna Xu in my PhD, an 9-month-old lady who loves smiling. Her coming makes this journey even more meaningful, grateful and unforgettable.

Reference

- (1) Balat, M.; Balat, H. Biogas as a Renewable Energy Source—a Review. *Energy Sources, Part A* **2009**, *31* (14), 1280–1293.
- (2) Lewis, N. S.; Nocera, D. G. Powering the Planet: Chemical Challenges in Solar Energy Utilization. *Proc. Natl. Acad. Sci. U. S. Amer.* **2006**, *103* (43), 15729–15735.
<https://doi.org/10.1073/pnas.0603395103>.
- (3) Panwar, N. L.; Kaushik, S. C.; Kothari, S. Role of Renewable Energy Sources in Environmental Protection: A Review. *Renew. Sustain. Energy Rev.* **2011**, *15* (3), 1513–1524.
- (4) Kudo, A.; Miseki, Y. Heterogeneous Photocatalyst Materials for Water Splitting. *Chem. Soc. Rev.* **2009**, *38* (1), 253–278.
- (5) Gray, H. B. Powering the Planet with Solar Fuel. *Nat. Chem.* **2009**, *1* (1), 7.
- (6) Holladay, J. D.; Hu, J.; King, D. L.; Wang, Y. An Overview of Hydrogen Production Technologies. *Catal. today* **2009**, *139* (4), 244–260.
- (7) Nathan, S. L.; Crabtree, G.; Nozik, A. J.; Wasielewski, M. R.; Alivisatos, P. Basic Research Needs for Solar Energy Utilization. In *Report on the basic energy sciences workshop on solar energy utilization. Clo Technology*; 2005.
- (8) Jiao, Y.; Zheng, Y.; Jaroniec, M.; Qiao, S. Z. Design of Electrocatalysts for Oxygen-and Hydrogen-Involving Energy Conversion Reactions. *Chem. Soc. Rev.* **2015**, *44* (8), 2060–2086.
- (9) Gong, M.; Dai, H. A Mini Review of NiFe-Based Materials as Highly Active Oxygen Evolution Reaction Electrocatalysts. *Nano Res.* **2015**, *8* (1), 23–39.
- (10) Tahir, M.; Pan, L.; Idrees, F.; Zhang, X.; Wang, L.; Zou, J.-J.; Wang, Z. L. Electrocatalytic Oxygen Evolution Reaction for Energy Conversion and Storage: A Comprehensive Review. *Nano Energy* **2017**, *37*, 136–157.
- (11) Grätzel, M. Photoelectrochemical Cells. *Nature* **2001**, *414* (6861), 338–344.
<https://doi.org/10.1038/35104607>.
- (12) Tsui, L.; Zangari, G. Titania Nanotubes by Electrochemical Anodization for Solar Energy Conversion. *J. Electrochem. Soc.* **2014**, *161* (7), D3066–D3077.

<https://doi.org/10.1149/2.010407jes>.

- (13) Ni, M.; Leung, M. K. H.; Leung, D. Y. C.; Sumathy, K. A Review and Recent Developments in Photocatalytic Water-Splitting Using TiO₂ for Hydrogen Production. *Renew. Sustain. Energy Rev.* **2007**, *11* (3), 401–425. <https://doi.org/10.1016/j.rser.2005.01.009>.
- (14) Fujishima, A. Electrochemical Photolysis of Water at a Semiconductor Electrode. *Nature* **1972**, *238*, 37–38.
- (15) Lin, Z.; Orlov, A.; Lambert, R. M.; Payne, M. C. New Insights into the Origin of Visible Light Photocatalytic Activity of Nitrogen-Doped and Oxygen-Deficient Anatase TiO₂. *J. Phys. Chem. B* **2005**, *109* (44), 20948–20952. <https://doi.org/10.1021/jp053547e>.
- (16) Thompson, T. L.; Yates, J. T. Surface Science Studies of the Photoactivation of TiO₂--New Photochemical Processes. *Chem. Rev.* **2006**, *106* (10), 4428–4453. <https://doi.org/10.1021/cr050172k>.
- (17) He, Y.; Tilocca, A.; Dulub, O.; Selloni, A.; Diebold, U. Local Ordering and Electronic Signatures of Submonolayer Water on Anatase TiO₂(101). *Nat. Mater.* **2009**, *8* (7), 585–589. <https://doi.org/10.1038/nmat2466>.
- (18) Maeda, K. Direct Splitting of Pure Water into Hydrogen and Oxygen Using Rutile Titania Powder as a Photocatalyst. *Chem. Commun. (Camb)*. **2013**, *49* (75), 8404–8406. <https://doi.org/10.1039/c3cc44151b>.
- (19) Murphy, A. B.; Barnes, P. R. F.; Randeniya, L. K.; Plumb, I. C.; Grey, I. E.; Horne, M. D.; Glasscock, J. A. Efficiency of Solar Water Splitting Using Semiconductor Electrodes. *Int. J. Hydrogen Energy* **2006**, *31* (14), 1999–2017.
- (20) Tsui, L.; Saito, M.; Homma, T.; Zangari, G. Trap-State Passivation of Titania Nanotubes by Electrochemical Doping for Enhanced Photoelectrochemical Performance. *J. Mater. Chem. A* **2015**, *3* (1), 360–367. <https://doi.org/10.1039/C4TA05620E>.
- (21) Tsui, L.; Zangari, G. Titania Nanotubes by Electrochemical Anodization for Solar Energy Conversion. *J. Electrochem. Soc.* **2014**, *161* (7), D3066–D3077.
- (22) Houser, J. E.; Hebert, K. R. The Role of Viscous Flow of Oxide in the Growth of Self-Ordered Porous Anodic Alumina Films. *Nat. Mater.* **2009**, *8* (5), 415–420.

- (23) Hebert, K. R.; Albu, S. P.; Paramasivam, I.; Schmuki, P. Morphological Instability Leading to Formation of Porous Anodic Oxide Films. *Nat. Mater.* **2012**, *11* (2), 162–166.
- (24) Gong, D.; Grimes, C. A.; Varghese, O. K.; Hu, W.; Singh, R. S.; Chen, Z.; Dickey, E. C. Titanium Oxide Nanotube Arrays Prepared by Anodic Oxidation. *J. Mater. Res.* **2001**, *16* (12), 3331–3334.
- (25) Varghese, O. K.; Paulose, M.; Shankar, K.; Mor, G. K.; Grimes, C. A. Water-Photolysis Properties of Micron-Length Highly-Ordered Titania Nanotube-Arrays. *J. Nanosci. Nanotechnol.* **2005**, *5* (7), 1158–1165.
- (26) Macak, J. M.; Sirotna, K.; Schmuki, P. Self-Organized Porous Titanium Oxide Prepared in Na₂SO₄/NaF Electrolytes. *Electrochim. Acta* **2005**, *50* (18), 3679–3684.
- (27) Prakasam, H. E.; Shankar, K.; Paulose, M.; Varghese, O. K.; Grimes, C. A. A New Benchmark for TiO₂ Nanotube Array Growth by Anodization. *J. Phys. Chem. C* **2007**, *111* (20), 7235–7241.
- (28) Tighineanu, A.; Ruff, T.; Albu, S. P.; Hahn, R.; Schmuki, P. Conductivity of TiO₂ Nanotubes: Influence of Annealing Time and Temperature. *Chem. Phys. Lett.* **2010**, *494* (4–6), 260–263. <https://doi.org/10.1016/j.cplett.2010.06.022>.
- (29) Roy, P.; Berger, S.; Schmuki, P. TiO₂ Nanotubes: Synthesis and Applications. *Angew. Chemie Int. Ed.* **2011**, *50* (13), 2904–2939.
- (30) Diebold, U. The Surface Science of Titanium Dioxide. *Surf. Sci. Rep.* **2003**, *48* (5), 53–229. [https://doi.org/10.1016/S0167-5729\(02\)00100-0](https://doi.org/10.1016/S0167-5729(02)00100-0).
- (31) Chen, X.; Liu, L.; Yu, P. Y.; Mao, S. S. Increasing Solar Absorption for Photocatalysis with Black Hydrogenated Titanium Dioxide Nanocrystals. *Science* **2011**, *331* (6018), 746–750. <https://doi.org/10.1126/science.1200448>.
- (32) Zuo, F.; Wang, L.; Wu, T.; Zhang, Z.; Borchardt, D.; Feng, P. Self-Doped Ti³⁺ Enhanced Photocatalyst for Hydrogen Production under Visible Light. *J. Am. Chem. Soc.* **2010**, *132* (34), 11856–11857.
- (33) Zhou, X.; Häublein, V.; Liu, N.; Nguyen, N. T.; Zolnhofer, E. M.; Tsuchiya, H.; Killian, M. S.; Meyer, K.; Frey, L.; Schmuki, P. TiO₂ Nanotubes: Nitrogen-Ion Implantation at Low Dose Provides Noble-Metal-Free Photocatalytic H₂-Evolution Activity. *Angew. Chemie Int. Ed.* **2016**, *55* (11), 3763–3767.

- (34) Chen, X.; Liu, L.; Huang, F. Black Titanium Dioxide (TiO₂) Nanomaterials. *Chem. Soc. Rev.* **2015**, *44* (7), 1861–1885. <https://doi.org/10.1039/c4cs00330f>.
- (35) Zhou, X.; Liu, N.; Schmuki, P. Photocatalysis with TiO₂ Nanotubes: “Colorful” Reactivity and Designing Site-Specific Photocatalytic Centers into TiO₂ Nanotubes. *ACS Catal.* **2017**, *7* (5), 3210–3235.
- (36) Nowotny, J. Titanium Dioxide-Based Semiconductors for Solar-Driven Environmentally Friendly Applications: Impact of Point Defects on Performance. *Energy Environ. Sci.* **2008**, *1* (5), 565–572.
- (37) Cronmeyer, D. C. Infrared Absorption of Reduced Rutile Ti O₂ Single Crystals. *Phys. Rev.* **1959**, *113* (5), 1222.
- (38) He, J.; Behera, R. K.; Finnis, M. W.; Li, X.; Dickey, E. C.; Phillpot, S. R.; Sinnott, S. B. Prediction of High-Temperature Point Defect Formation in TiO₂ from Combined Ab Initio and Thermodynamic Calculations. *Acta Mater.* **2007**, *55* (13), 4325–4337.
- (39) Ghosh, A. K.; Wakim, F. G.; Addiss Jr, R. R. Photoelectronic Processes in Rutile. *Phys. Rev.* **1969**, *184* (3), 979.
- (40) Hossain, F. M.; Murch, G. E.; Sheppard, L.; Nowotny, J. Reactivity of Ideal and Defected Rutile TiO₂ (110) Surface with Oxygen. *Adv. Appl. Ceram.* **2007**, *106* (1–2), 95–100.
- (41) Asahi, R.; Morikawa, T.; Ohwaki, T.; Aoki, K.; Taga, Y. Visible-Light Photocatalysis in Nitrogen-Doped Titanium Oxides. *Science (80-)*. **2001**, *293* (5528), 269–271. <https://doi.org/10.1126/science.1061051>.
- (42) Choi, W.; Termin, A.; Hoffmann, M. R. The Role of Metal Ion Dopants in Quantum-Sized TiO₂: Correlation between Photoreactivity and Charge Carrier Recombination Dynamics. *J. Phys. Chem.* **1994**, *98* (51), 13669–13679.
- (43) Naldoni, A.; Allieta, M.; Santangelo, S.; Marelli, M.; Fabbri, F.; Cappelli, S.; Bianchi, C. L.; Psaro, R.; Dal Santo, V. Effect of Nature and Location of Defects on Bandgap Narrowing in Black TiO₂ nanoparticles. *J. Am. Chem. Soc.* **2012**, *134* (18), 7600–7603. <https://doi.org/10.1021/ja3012676>.
- (44) Nowotny, J.; Bak, T.; Alim, M. (High Temperature Materials Division Outstanding Achievement Award) Semiconducting Properties and Defect Disorder of Titanium Dioxide. *ECS Trans.* **2015**, *64*

- (46), 11–28.
- (45) Wang, T.; Gong, J. Single-Crystal Semiconductors with Narrow Band Gaps for Solar Water Splitting. *Angew. Chemie Int. Ed.* **2015**, *54* (37), 10718–10732.
- (46) Kenney, M. J.; Gong, M.; Li, Y.; Wu, J. Z.; Feng, J.; Lanza, M.; Dai, H. High-Performance Silicon Photoanodes Passivated with Ultrathin Nickel Films for Water Oxidation. *Science (80-.).* **2013**, *342* (6160), 836–840.
- (47) Hu, S.; Shaner, M. R.; Beardslee, J. A.; Lichterman, M.; Brunshwig, B. S.; Lewis, N. S. Amorphous TiO₂ Coatings Stabilize Si, GaAs, and GaP Photoanodes for Efficient Water Oxidation. *Science (80-.).* **2014**, *344* (6187), 1005–1009.
- (48) Wang, T.; Luo, Z.; Li, C.; Gong, J. Controllable Fabrication of Nanostructured Materials for Photoelectrochemical Water Splitting via Atomic Layer Deposition. *Chem. Soc. Rev.* **2014**, *43* (22), 7469–7484.
- (49) Hill, J. C.; Landers, A. T.; Switzer, J. A. An Electrodeposited Inhomogeneous Metal-Insulator-Semiconductor Junction for Efficient Photoelectrochemical Water Oxidation. *Nat. Mater.* **2015**, *14* (11), 1150–1155. <https://doi.org/10.1038/nmat4408>.
- (50) Nielander, A. C.; Bierman, M. J.; Petrone, N.; Strandwitz, N. C.; Ardo, S.; Yang, F.; Hone, J.; Lewis, N. S. Photoelectrochemical Behavior of N-Type Si (111) Electrodes Coated with a Single Layer of Graphene. *J. Am. Chem. Soc.* **2013**, *135* (46), 17246–17249.
- (51) Li, J.; Kim, S.; Edington, S.; Nedy, J.; Cho, S.; Lee, K.; Heeger, A. J.; Gupta, M. C.; Yates Jr, J. T. A Study of Stabilization of P3HT/PCBM Organic Solar Cells by Photochemical Active TiO_x Layer. *Sol. Energy Mater. Sol. Cells* **2011**, *95* (4), 1123–1130.
- (52) Liu, R.; Zheng, Z.; Spurgeon, J.; Yang, X. Enhanced Photoelectrochemical Water-Splitting Performance of Semiconductors by Surface Passivation Layers. *Energy Environ. Sci.* **2014**, *7* (8), 2504–2517. <https://doi.org/10.1039/C4EE00450G>.
- (53) Walter, M. G.; Warren, E. L.; McKone, J. R.; Boettcher, S. W.; Mi, Q.; Santori, E. A.; Lewis, N. S. Solar Water Splitting Cells. *Chem. Rev. (Washington, DC, United States)* **2010**, *110* (11), 6446–6473. <https://doi.org/10.1021/cr1002326>.
- (54) Kenney, M. J.; Gong, M.; Li, Y.; Wu, J. Z.; Feng, J.; Lanza, M.; Dai, H. High-Performance Silicon

- Photoanodes Passivated with Ultrathin Nickel Films for Water Oxidation. *Science* (80-.). **2013**, 342 (6160), 836–840. <https://doi.org/10.1126/science.1241327>.
- (55) Tsui, L. K.; Homma, T.; Zangari, G. Photocurrent Conversion in Anodized TiO₂ Nanotube Arrays: Effect of the Water Content in Anodizing Solutions. *J. Phys. Chem. C* **2013**, 117 (14), 6979–6989. <https://doi.org/10.1021/jp400318n>.
- (56) Kowalski, D.; Mallet, J.; Michel, J.; Molinari, M. Low Electric Field Strength Self-Organization of Anodic TiO₂ Nanotubes in Diethylene Glycol Electrolyte. *J. Mater. Chem. A* **2015**, 3 (12), 6655–6661.
- (57) Burke, M. S.; Zou, S.; Enman, L. J.; Kellon, J. E.; Gabor, C. A.; Pledger, E.; Boettcher, S. W. Revised Oxygen Evolution Reaction Activity Trends for First-Row Transition-Metal (Oxy) Hydroxides in Alkaline Media. *J. Phys. Chem. Lett.* **2015**, 6 (18), 3737–3742.
- (58) Scheck, C.; Evans, P.; Zangari, G.; Schad, R. Sharp Ferromagnet/Semiconductor Interfaces by Electrodeposition of Ni Thin Films onto n-GaAs(001) Substrates. *Appl. Phys. Lett.* **2003**, 82 (17), 2853–2855. <https://doi.org/10.1063/1.1571229>.
- (59) Vanpaemel, J.; Sugiura, M.; Cuypers, D.; Van Der Veen, M. H.; De Gendt, S.; Vereecken, P. M. Electrochemical Deposition of Subnanometer Ni Films on TiN. *Langmuir* **2014**, 30 (8), 2047–2053. <https://doi.org/10.1021/la404852m>.
- (60) Toby, B. H.; Von Dreele, R. B. GSAS-II: The Genesis of a Modern Open-Source All Purpose Crystallography Software Package. *J. Appl. Crystallogr.* **2013**, 46 (2), 544–549.
- (61) Gelderman, K.; Lee, L.; Donne, S. W. Flat-Band Potential of a Semiconductor: Using the Mott–Schottky Equation. *J. Chem. Educ.* **2007**, 84 (4), 685. <https://doi.org/10.1021/ed084p685>.
- (62) Bisquert, J.; Garcia-Belmonte, G.; Fabregat-Santiago, F.; Ferriols, N. S.; Bogdanoff, P.; Pereira, E. C. Doubling Exponent Models for the Analysis of Porous Film Electrodes by Impedance. Relaxation of TiO₂ Nanoporous in Aqueous Solution. *J. Phys. Chem. B* **2000**, 104 (10), 2287–2298. <https://doi.org/10.1021/jp993148h>.
- (63) Bisquert, J. Theory of the Impedance of Electron Diffusion and Recombination in a Thin Layer. *J. Phys. Chem. B* **2002**, 106 (2), 325–333.
- (64) Fabregat-Santiago, F.; Bisquert, J.; Garcia-Belmonte, G.; Boschloo, G.; Hagfeldt, A. Influence of

- Electrolyte in Transport and Recombination in Dye-Sensitized Solar Cells Studied by Impedance Spectroscopy. *Sol. Energy Mater. Sol. Cells* **2005**, *87* (1–4), 117–131.
- (65) Wang, Q.; Ito, S.; Grätzel, M.; Fabregat-Santiago, F.; Mora-Sero, I.; Bisquert, J.; Bessho, T.; Imai, H. Characteristics of High Efficiency Dye-Sensitized Solar Cells. *J. Phys. Chem. B* **2006**, *110* (50), 25210–25221.
- (66) Hanzu, I.; Djenizian, T.; Knauth, P. Electrical and Point Defect Properties of TiO₂ Nanotubes Fabricated by Electrochemical Anodization. *J. Phys. Chem. C* **2011**, *115* (13), 5989–5996. <https://doi.org/10.1021/jp1111982>.
- (67) Ali Yahia, S. A.; Hamadou, L.; Kadri, a.; Benbrahim, N.; Sutter, E. M. M. Effect of Anodizing Potential on the Formation and EIS Characteristics of TiO₂ Nanotube Arrays. *J. Electrochem. Soc.* **2012**, *159* (4), K83. <https://doi.org/10.1149/2.077204jes>.
- (68) Orazem, M. E.; Tribollet, B. *Electrochemical Impedance Spectroscopy*; John Wiley & Sons, 2011; Vol. 48.
- (69) Oskam, G.; Hoffmann, P. M.; Schmidt, J. C.; Searson, P. C. Energetics and Kinetics of Surface States at N-Type Silicon Surfaces in Aqueous Fluoride Solutions. *J. Phys. Chem.* **1996**, *100* (5), 1801–1806. <https://doi.org/10.1021/jp952129e>.
- (70) Oskam, G.; Hoffmann, P. M.; Searson, P. C. In Situ Measurements of Interface States at Silicon Surfaces in Fluoride Solutions. *Phys. Rev. Lett* **1996**, *76* (9), 1521–1524. <https://doi.org/10.1103/PhysRevLett.76.1521>.
- (71) Oskam, G.; Schmidt, J. C.; Hoffmann, P. M.; Searson, P. C. Electrical Properties of N-Type (111) Si in Aqueous K₄Fe(CN)₆ Solution I. Interface States and Recombination Impedance. *J. Electrochem. Soc.* **1996**, *143* (8), 2531–2537.
- (72) Park, Y.; Kang, D.; Choi, K.-S. Marked Enhancement in Electron–Hole Separation Achieved in the Low Bias Region Using Electrochemically Prepared Mo-Doped BiVO₄ Photoanodes. *Phys. Chem. Chem. Phys.* **2014**, *16* (3), 1238–1246.
- (73) McDonald, K. J.; Choi, K.-S. A New Electrochemical Synthesis Route for a BiOI Electrode and Its Conversion to a Highly Efficient Porous BiVO₄ Photoanode for Solar Water Oxidation. *Energy Environ. Sci.* **2012**, *5* (9), 8553–8557.

- (74) Shankar, K.; Basham, J. I.; Allam, N. K.; Varghese, O. K.; Mor, G. K.; Feng, X.; Paulose, M.; Seabold, J. A.; Choi, K.-S.; Grimes, C. A. Recent Advances in the Use of TiO₂ Nanotube and Nanowire Arrays for Oxidative Photoelectrochemistry. *J. Phys. Chem. C. Nanomater. Interfaces* **2009**, *113* (16), 6327.
- (75) Sarala, R.; Islam, M. A.; Rabin, S. B.; Stanburg, D. M. Aromatic Sulfonation by Sulfite and the Reduction Potential of the Sulfite Radical: Oxidation of Sulfite by the Tetraammine (Phenanthroline) Ruthenium (II) Cation. *Inorg. Chem.* **1990**, *29* (6), 1133–1142.
- (76) Stanbury, D. M. Reduction Potentials Involving Inorganic Free Radicals in Aqueous Solution. In *Advances in inorganic chemistry*; Elsevier, 1989; Vol. 33, pp 69–138.
- (77) Reber, J. F.; Meier, K. Photochemical Production of Hydrogen with Zinc Sulfide Suspensions. *J. Phys. Chem.* **1984**, *88* (24), 5903–5913.
- (78) Kim, T. W.; Choi, K.-S. Nanoporous BiVO₄ Photoanodes with Dual-Layer Oxygen Evolution Catalysts for Solar Water Splitting. *Science* (80-.). **2014**, *343* (6174), 990–994.
<https://doi.org/10.1126/science.1246913>.
- (79) Meekins, B. H.; Kamat, P. V. Got TiO₂ Nanotubes? Lithium Ion Intercalation Can Boost Their Photoelectrochemical Performance. *ACS Nano* **2009**, *3* (11), 3437–3446.
<https://doi.org/10.1021/nn900897r>.
- (80) Ke, S.-C.; Wang, T.-C.; Wong, M.-S.; Gopal, N. O. Low Temperature Kinetics and Energetics of the Electron and Hole Traps in Irradiated TiO₂ Nanoparticles as Revealed by EPR Spectroscopy. *J. Phys. Chem. B* **2006**, *110* (24), 11628–11634.
- (81) Yang, C.; Wang, Z.; Lin, T.; Yin, H.; Lü, X.; Wan, D.; Xu, T.; Zheng, C.; Lin, J.; Huang, F. Core-Shell Nanostructured “Black” Rutile Titania as Excellent Catalyst for Hydrogen Production Enhanced by Sulfur Doping. *J. Am. Chem. Soc.* **2013**, *135* (47), 17831–17838.
- (82) Leshuk, T.; Parviz, R.; Everett, P.; Krishnakumar, H.; Varin, R. A.; Gu, F. Photocatalytic Activity of Hydrogenated TiO₂. *ACS Appl. Mater. Interfaces* **2013**, *5* (6), 1892–1895.
- (83) Leshuk, T.; Linley, S.; Gu, F. Hydrogenation Processing of TiO₂ Nanoparticles. *Can. J. Chem. Eng.* **2013**, *91* (5), 799–807.
- (84) Lu, H.; Zhao, B.; Pan, R.; Yao, J.; Qiu, J.; Luo, L.; Liu, Y. Safe and Facile Hydrogenation of

- Commercial Degussa P25 at Room Temperature with Enhanced Photocatalytic Activity. *RSC Adv.* **2014**, *4* (3), 1128–1132.
- (85) Xu, Y.; Melia, M. A.; Tsui, L.; Fitz-Gerald, J. M.; Zangari, G. Laser-Induced Surface Modification at Anatase TiO₂ Nanotube Array Photoanodes for Photoelectrochemical Water Oxidation. *J. Phys. Chem. C* **2017**, *121* (32), 17121–17128.
- (86) Joya, Y. F.; Liu, Z. Formation of Ultraviolet Laser-Annealed Mesoporous Anatase Films by a Sol-Gel Process. *Scr. Mater.* **2009**, *60* (6), 467–470. <https://doi.org/10.1016/j.scriptamat.2008.11.037>.
- (87) Liu, L.; Yu, P. Y.; Chen, X.; Mao, S. S.; Shen, D. Z. Hydrogenation and Disorder in Engineered Black TiO₂. *Phys. Rev. Lett.* **2013**, *111* (6), 1–5. <https://doi.org/10.1103/PhysRevLett.111.065505>.
- (88) Lagemaat, J. Van De; Park, N.; Frank, a J. Influence of Electrical Potential Distribution , Charge Transport , and Recombination on the Photopotential and Photocurrent Conversion Efficiency of Dye-Sensitized Nanocrystalline TiO₂ Solar Cells : A Study by Electrical Impedance and Optical Modulation. *J. Phys. Chem. B* **2000**, *104*, 2044–2052. <https://doi.org/10.1021/jp993172v>.
- (89) Zhou, M.; Bao, J.; Bi, W.; Zeng, Y.; Zhu, R.; Tao, M.; Xie, Y. Efficient Water Splitting via a Heteroepitaxial BiVO₄ Photoelectrode Decorated with Co-Pi Catalysts. *ChemSusChem* **2012**, *5* (8), 1420–1425. <https://doi.org/10.1002/cssc.201200287>.
- (90) Wang, G.; Wang, H.; Ling, Y.; Tang, Y.; Yang, X.; Fitzmorris, R. C.; Wang, C.; Zhang, J. Z.; Li, Y. Hydrogen-Treated TiO₂ Nanowire Arrays for Photoelectrochemical Water Splitting. *Nano Lett.* **2011**, *11* (7), 3026–3033. <https://doi.org/10.1021/nl201766h>.
- (91) Chen, B.; Hou, J.; Lu, K. Formation Mechanism of TiO₂ Nanotubes and Their Applications in Photoelectrochemical Water Splitting and Supercapacitors. *Langmuir* **2013**, *29* (19), 5911–5919. <https://doi.org/10.1021/la400586r>.
- (92) Liu, N.; Schneider, C.; Freitag, D.; Hartmann, M.; Venkatesan, U.; Müller, J.; Spiecker, E.; Schmuki, P. Black TiO₂ Nanotubes: Cocatalyst-Free Open-Circuit Hydrogen Generation. *Nano Lett.* **2014**, *14* (6), 3309–3313. <https://doi.org/10.1021/nl500710j>.
- (93) Chen, X.; Liu, L.; Yu, P. Y.; Mao, S. S. Increasing Solar Absorption for Photocatalysis with Black Hydrogenated Titanium Dioxide Nanocrystals. *Science (80-.)*. **2011**, *331* (6018), 746–750. <https://doi.org/10.1126/science.1200448>.

- (94) Zhu, W.-D.; Wang, C.-W.; Chen, J.-B.; Li, D.-S.; Zhou, F.; Zhang, H.-L. Enhanced Field Emission from Hydrogenated TiO₂ Nanotube Arrays. *Nanotechnology* **2012**, *23* (45), 455204.
- (95) Xu, Y.; Lin, Q.; Ahmed, R.; Hoglund, E. R.; Zangari, G. Synthesis of TiO₂-Based Nanocomposites by Anodizing and Hydrogen Annealing for Efficient Photoelectrochemical Water Oxidation. *J. Power Sources* **2019**, *410*, 59–68.
- (96) Hanaor, D. A. H.; Sorrell, C. C. Review of the Anatase to Rutile Phase Transformation. *J. Mater. Sci.* **2011**, *46* (4), 855–874.
- (97) Tables, N.-J. T. ; ; Chase, MW, Jr., Ed. *J. Phys. Chem. Ref. Data* **1998**, 1952.
- (98) Cox, J. D.; Wagman, D. D.; Medvedev, V. A. *Codata Key Values for Thermodynamics*. New York **1984**.
- (99) Albu, S. P.; Tsuchiya, H.; Fujimoto, S.; Schmuki, P. TiO₂ Nanotubes–Annealing Effects on Detailed Morphology and Structure. *Eur. J. Inorg. Chem.* **2010**, *2010* (27), 4351–4356.
- (100) Wang, D.; Huang, C.; He, J.; Che, X.; Zhang, H.; Huang, F. Enhanced Superconductivity in Rock-Salt TiO. *ACS Omega* **2017**, *2* (3), 1036–1039.
- (101) Abbate, M.; Potze, R.; Sawatzky, G. A.; Schlenker, C.; Lin, H. J.; Tjeng, L. H.; Chen, C. T.; Teehan, D.; Turner, T. S. Changes in the Electronic Structure of Ti₄O₇ across the Semiconductor–Semiconductor-Metal Transitions. *Phys. Rev. B* **1995**, *51* (15), 10150.
- (102) McCafferty, E.; Wightman, J. P. Determination of the Concentration of Surface Hydroxyl Groups on Metal Oxide Films by a Quantitative XPS Method. *Surf. Interface Anal.* **1998**, *26* (8), 549–564.
- (103) Lazarus, M. S.; Sham, T. K. X-Ray Photoelectron Spectroscopy (XPS) Studies of Hydrogen Reduced Rutile (TiO_{2-x}) Surfaces. *Chem. Phys. Lett.* **1982**, *92* (6), 670–674.
- (104) Chen, X.; Liu, L.; Liu, Z.; Marcus, M. a; Wang, W.-C.; Oyler, N. a; Grass, M. E.; Mao, B.; Glans, P.-A.; Yu, P. Y.; et al. Properties of Disorder-Engineered Black Titanium Dioxide Nanoparticles through Hydrogenation. *Sci. Rep.* **2013**, *3*, 1510. <https://doi.org/10.1038/srep01510>.
- (105) Södergren, S.; Siegbahn, H.; Rensmo, H.; Lindström, H.; Hagfeldt, A.; Lindquist, S. Lithium Intercalation in Nanoporous Anatase TiO₂ Studied with XPS. *J. Phys. Chem. B* **1997**, *101* (16), 3087–3090. <https://doi.org/10.1021/jp9639399>.

- (106) Amano, F.; Nakata, M.; Yamamoto, A.; Tanaka, T. Effect of Ti³⁺ Ions and Conduction Band Electrons on Photocatalytic and Photoelectrochemical Activity of Rutile Titania for Water Oxidation. *J. Phys. Chem. C* **2016**, *120* (12), 6467–6474.
- (107) Mao, C.; Zuo, F.; Hou, Y.; Bu, X.; Feng, P. In Situ Preparation of a Ti³⁺ Self-Doped TiO₂ Film with Enhanced Activity as Photoanode by N₂H₄ Reduction. *Angew. Chemie Int. Ed.* **2014**, *53* (39), 10485–10489.
- (108) Schwingenschlögl, U.; Eyert, V. The Vanadium Magnéli Phases VnO_{2n-1}. *Ann. Phys.* **2004**, *13* (9), 475–510.
- (109) Valeeva, A. A.; Rempel, A. A.; Gusev, A. I. Structure and Specific Heat of Disordered and Ordered Titanium Monoxide TiO. *J. Struct. Chem.* **2003**, *44* (2), 235–242.
- (110) Denker, S. P. Electronic Properties of Titanium Monoxide. *J. Appl. Phys.* **1966**, *37* (1), 142–149.
- (111) Van de Walle, C. G.; Neugebauer, J. Universal Alignment of Hydrogen Levels in Semiconductors, Insulators and Solutions. *Nature* **2003**, *423* (6940), 626–628.
- (112) Ikram, A.; Sahai, S.; Rai, S.; Dass, S.; Shrivastav, R.; Satsangi, V. R. Improved Charge Transportation at PbS QDs/TiO₂ Interface for Efficient PEC Hydrogen Generation. *Phys. Chem. Chem. Phys.* **2016**, *18* (23), 15815–15821.
- (113) Tsui, L.; Zangari, G. Water Content in the Anodization Electrolyte Affects the Electrochemical and Electronic Transport Properties of TiO₂ Nanotubes: A Study by Electrochemical Impedance Spectroscopy. *Electrochim. Acta* **2014**, *121*, 203–209.
<https://doi.org/10.1016/j.electacta.2013.12.163>.
- (114) Tsui, L.; Xu, Y.; Dawidowski, D.; Cafiso, D.; Zangari, G. Efficient Water Oxidation Kinetics and Enhanced Electron Transport in Li-Doped TiO₂ Nanotube Photoanodes. *J. Mater. Chem. A* **2016**, *4* (48), 19070–19077.
- (115) Beranek, R.; Tsuchiya, H.; Sugishima, T.; Macak, J. M.; Taveira, L.; Fujimoto, S.; Kisch, H.; Schmuki, P. Enhancement and Limits of the Photoelectrochemical Response from Anodic TiO₂ Nanotubes. *Appl. Phys. Lett.* **2005**, *87* (24), 243114.
- (116) Bard, A. J.; Bocarsly, A. B.; Fan, F. R. F.; Walton, E. G.; Wrighton, M. S. The Concept of Fermi Level Pinning at Semiconductor/Liquid Junctions. Consequences for Energy Conversion Efficiency and

- Selection of Useful Solution Redox Couples in Solar Devices. *J. Am. Chem. Soc.* **1980**, *102* (11), 3671–3677.
- (117) Berger, T.; Lana-Villarreal, T.; Monllor-Satoca, D.; Gómez, R. Charge Transfer Reductive Doping of Nanostructured TiO₂ Thin Films as a Way to Improve Their Photoelectrocatalytic Performance. *Electrochem. commun.* **2006**, *8* (11), 1713–1718.
- (118) Wang, G.; Yang, Y.; Ling, Y.; Wang, H.; Lu, X.; Pu, Y.-C.; Zhang, J. Z.; Tong, Y.; Li, Y. An Electrochemical Method to Enhance the Performance of Metal Oxides for Photoelectrochemical Water Oxidation. *J. Mater. Chem. A* **2016**, *4* (8), 2849–2855.
<https://doi.org/10.1039/C5TA10477G>.
- (119) Wang, S.; Chen, P.; Yun, J. H.; Hu, Y.; Wang, L. An Electrochemically Treated BiVO₄ Photoanode for Efficient Photoelectrochemical Water Splitting. *Angew. Chemie - Int. Ed.* **2017**, *56* (29), 8500–8504. <https://doi.org/10.1002/anie.201703491>.
- (120) Ganduglia-Pirovano, M. V.; Hofmann, A.; Sauer, J. Oxygen Vacancies in Transition Metal and Rare Earth Oxides: Current State of Understanding and Remaining Challenges. *Surf. Sci. Rep.* **2007**, *62* (6), 219–270.
- (121) Zhou, X.; Liu, N.; Schmuki, P. Ar⁺-Ion Bombardment of TiO₂ Nanotubes Creates Co-Catalytic Effect for Photocatalytic Open Circuit Hydrogen Evolution. *Electrochem. commun.* **2014**, *49*, 60–64. <https://doi.org/10.1016/j.elecom.2014.09.013>.
- (122) Wang, Z.; Wen, B.; Hao, Q.; Liu, L.-M.; Zhou, C.; Mao, X.; Lang, X.; Yin, W.-J.; Dai, D.; Selloni, A. Localized Excitation of Ti³⁺ Ions in the Photoabsorption and Photocatalytic Activity of Reduced Rutile TiO₂. *J. Am. Chem. Soc.* **2015**, *137* (28), 9146–9152.
- (123) Ihara, T.; Miyoshi, M.; Iriyama, Y.; Matsumoto, O.; Sugihara, S. Visible-Light-Active Titanium Oxide Photocatalyst Realized by an Oxygen-Deficient Structure and by Nitrogen Doping. *Appl. Catal. B Environ.* **2003**, *42* (4), 403–409.
- (124) Di Valentin, C.; Pacchioni, G.; Selloni, A.; Livraghi, S.; Giamello, E. Characterization of Paramagnetic Species in N-Doped TiO₂ Powders by EPR Spectroscopy and DFT Calculations. *J. Phys. Chem. B* **2005**, *109* (23), 11414–11419.
- (125) Chen, X.; Lou, Y.; Samia, A. C. S.; Burda, C.; Gole, J. L. Formation of Oxynitride as the

- Photocatalytic Enhancing Site in Nitrogen-Doped Titania Nanocatalysts: Comparison to a Commercial Nanopowder. *Adv. Funct. Mater.* **2005**, *15* (1), 41–49.
- (126) Emeline, A. V.; Sheremetyeva, N. V.; Khomchenko, N. V.; Ryabchuk, V. K.; Serpone, N. Photoinduced Formation of Defects and Nitrogen Stabilization of Color Centers in N-Doped Titanium Dioxide. *J. Phys. Chem. C* **2007**, *111* (30), 11456–11462.
- (127) Batzill, M.; Morales, E. H.; Diebold, U. Influence of Nitrogen Doping on the Defect Formation and Surface Properties of TiO₂ Rutile and Anatase. *Phys. Rev. Lett.* **2006**, *96* (2), 26103.
- (128) Serpone, N. Is the Band Gap of Pristine TiO₂ Narrowed by Anion-and Cation-Doping of Titanium Dioxide in Second-Generation Photocatalysts? ACS Publications 2006.
- (129) Hoang, S.; Berglund, S. P.; Hahn, N. T.; Bard, A. J.; Mullins, C. B. Enhancing Visible Light Photo-Oxidation of Water with TiO₂ Nanowire Arrays via Cotreatment with H₂ and NH₃: Synergistic Effects between Ti³⁺ and N. *J. Am. Chem. Soc.* **2012**, *134* (8), 3659–3662.
<https://doi.org/10.1021/ja211369s>.
- (130) Chen, Y.; Cao, X.; Lin, B.; Gao, B. Origin of the Visible-Light Photoactivity of NH₃-Treated TiO₂: Effect of Nitrogen Doping and Oxygen Vacancies. *Appl. Surf. Sci.* **2013**, *264*, 845–852.
- (131) Irie, H.; Watanabe, Y.; Hashimoto, K. Nitrogen-Concentration Dependence on Photocatalytic Activity of TiO_{2-x}N_x Powders. *J. Phys. Chem. B* **2003**, *107* (23), 5483–5486.
- (132) Xu, Y.; Ahmed, R.; Klein, D.; Cap, S.; Freedy, K.; McDonnell, S.; Zangari, G. Improving Photo-Oxidation Activity of Water by Introducing Ti³⁺ in Self-Ordered TiO₂ Nanotube Arrays Treated with Ar/NH₃. *J. Power Sources* **2019**, 242–249. <https://doi.org/10.1016/j.jpowsour.2018.12.083>.
- (133) Liu, Y.; Wang, X.; Yang, F.; Yang, X. Excellent Antimicrobial Properties of Mesoporous Anatase TiO₂ and Ag/TiO₂ Composite Films. *Microporous Mesoporous Mater.* **2008**, *114* (1–3), 431–439.
- (134) Saha, N. C.; Tompkins, H. G. Titanium Nitride Oxidation Chemistry: An X-ray Photoelectron Spectroscopy Study. *J. Appl. Phys.* **1992**, *72* (7), 3072–3079.
- (135) Yates, H. M.; Nolan, M. G.; Sheel, D. W.; Pemble, M. E. The Role of Nitrogen Doping on the Development of Visible Light-Induced Photocatalytic Activity in Thin TiO₂ Films Grown on Glass by Chemical Vapour Deposition. *J. Photochem. Photobiol. A Chem.* **2006**, *179* (1–2), 213–223.
- (136) Shard, A. G. Detection Limits in XPS for More than 6000 Binary Systems Using Al and Mg K α X-

- rays. *Surf. Interface Anal.* **2014**, *46* (3), 175–185.
- (137) Anpo, M.; Che, M.; Fubini, B.; Garrone, E. Generation of Superoxide Ions at Oxide Surfaces. *Top. Catal.* **1999**, *8*, 189–198.
- (138) Kumar, C. P.; Gopal, N. O.; Wang, T. C.; Wong, M.-S.; Ke, S. C. EPR Investigation of TiO₂ Nanoparticles with Temperature-Dependent Properties. *J. Phys. Chem. B* **2006**, *110* (11), 5223–5229. <https://doi.org/10.1021/jp057053t>.
- (139) Di Valentin, C.; Finazzi, E.; Pacchioni, G.; Selloni, A.; Livraghi, S.; Paganini, M. C.; Giamello, E. N-Doped TiO₂: Theory and Experiment. *Chem. Phys.* **2007**, *339* (1–3), 44–56.
- (140) Livraghi, S.; Paganini, M. C.; Giamello, E.; Selloni, A.; Di Valentin, C.; Pacchioni, G. Origin of Photoactivity of Nitrogen-Doped Titanium Dioxide under Visible Light. *J. Am. Chem. Soc.* **2006**, *128* (49), 15666–15671.
- (141) Liu, C.; Dasgupta, N. P.; Yang, P. Semiconductor Nanowires for Artificial Photosynthesis. *Chem. Mater.* **2014**, *26* (1), 415–422. <https://doi.org/10.1021/cm4023198>.
- (142) Chen, Z.; Dinh, H. N.; Miller, E. Photoelectrochemical Water Splitting. *SpringerBriefs Energy, New York* **2013**, 49–61.
- (143) Govindaraju, G. V.; Wheeler, G. P.; Lee, D.; Choi, K.-S. Methods for Electrochemical Synthesis and Photoelectrochemical Characterization for Photoelectrodes. *Chem. Mater.* **2016**, *29* (1), 355–370.
- (144) Yang, Y.; Liu, G.; Irvine, J. T. S.; Cheng, H. Enhanced Photocatalytic H₂ Production in Core–Shell Engineered Rutile TiO₂. *Adv. Mater.* **2016**, *28* (28), 5850–5856.
- (145) Siuzdak, K.; Szkoda, M.; Sawczak, M.; Lisowska-Oleksiak, A.; Karczewski, J.; Ryl, J. Enhanced Photoelectrochemical and Photocatalytic Performance of Iodine-Doped Titania Nanotube Arrays. *RSC Adv.* **2015**, *5* (62), 50379–50391.
- (146) Grimes, C. A. Synthesis and Application of Highly Ordered Arrays of TiO₂ Nanotubes. *J. Mater. Chem.* **2007**, *17* (15), 1451. <https://doi.org/10.1039/b701168g>.
- (147) Ghicov, A.; Macak, J. M.; Tsuchiya, H.; Kunze, J.; Haeublein, V.; Frey, L.; Schmuki, P. Ion Implantation and Annealing for an Efficient N-Doping of TiO₂ Nanotubes. *Nano Lett.* **2006**, *6* (5), 1080–1082.

- (148) Das, C.; Roy, P.; Yang, M.; Jha, H.; Schmuki, P. Nb Doped TiO₂ Nanotubes for Enhanced Photoelectrochemical Water-Splitting. *Nanoscale* **2011**, *3* (8), 3094–3096.
<https://doi.org/10.1039/c1nr10539f>.
- (149) Beranek, R.; Macak, J. M.; Gärtner, M.; Meyer, K.; Schmuki, P. Enhanced Visible Light Photocurrent Generation at Surface-Modified TiO₂ Nanotubes. *Electrochim. Acta* **2009**, *54* (9), 2640–2646.
- (150) Goldsmith, Z. K.; Harshan, A. K.; Gerken, J. B.; Vörös, M.; Galli, G.; Stahl, S. S.; Hammes-Schiffer, S. Characterization of NiFe Oxyhydroxide Electrocatalysts by Integrated Electronic Structure Calculations and Spectroelectrochemistry. *Proc. Natl. Acad. Sci.* **2017**, *114* (12), 3050–3055.
- (151) Xu, Y.; Ahmed, R.; Lin, Q.; Zangari, G. (Photo) Electrochemical Water Oxidation at Anodic TiO₂ Nanotubes Modified by Electrodeposited NiFe Oxy-Hydroxides Catalysts. *Electrochim. Acta* **2019**, *308*, 91–98. <https://doi.org/10.1016/j.electacta.2019.04.018>.
- (152) Trotochaud, L.; Young, S. L.; Ranney, J. K.; Boettcher, S. W. Nickel–Iron Oxyhydroxide Oxygen-Evolution Electrocatalysts: The Role of Intentional and Incidental Iron Incorporation. *J. Am. Chem. Soc.* **2014**, *136* (18), 6744–6753.
- (153) Hu, J.-M.; Zhang, J.-Q.; Cao, C.-N. Oxygen Evolution Reaction on IrO₂-Based DSA® Type Electrodes: Kinetics Analysis of Tafel Lines and EIS. *Int. J. Hydrogen Energy* **2004**, *29* (8), 791–797.
- (154) Moulder, J. F.; Stickle, W. F.; Sobol, P. E.; Bomben, K. D. Handbook of X-Ray Photoelectron Spectroscopy: A Reference Book of Standard Spectra for Identification and Interpretation of XPS Data; Physical Electronics: Eden Prairie, MN, 1995. *Google Sch.* **2000**, 261.
- (155) Klaus, S.; Louie, M. W.; Trotochaud, L.; Bell, A. T. Role of Catalyst Preparation on the Electrocatalytic Activity of Ni_{1-x}Fe_xOOH for the Oxygen Evolution Reaction. *J. Phys. Chem. C* **2015**, *119* (32), 18303–18316.
- (156) Roginskaya, Y. E.; Morozova, O. V.; Lubnin, E. N.; Ulitina, Y. E.; Lopukhova, G. V.; Trasatti, S. Characterization of Bulk and Surface Composition of Co_xNi_{1-x}O_y Mixed Oxides for Electrocatalysis. *Langmuir* **1997**, *13* (17), 4621–4627.
- (157) Chigane, M.; Ishikawa, M. Characterization of Electrochromic Nickel Oxide Thin Films Prepared by Anodic Deposition. *J. Chem. Soc. Faraday Trans.* **1992**, *88* (15), 2203–2205.

- (158) Cai, W.; Nix, W. D. *Imperfections in Crystalline Solids*; Cambridge University Press, 2016.
- (159) Weber, M. F.; Dignam, M. J. Efficiency of Splitting Water with Semiconducting Photoelectrodes. *J. Electrochem. Soc.* **1984**, *131* (6), 1258–1265.
- (160) Hu, S.; Shaner, M. R.; Beardslee, J. A.; Lichterman, M.; Brunschwig, B. S.; Lewis, N. S. Amorphous TiO₂ Coatings Stabilize Si, GaAs, and GaP Photoanodes for Efficient Water Oxidation. *Science* (80-.). **2014**, *344* (6187), 1005–1009. <https://doi.org/10.1126/science.1251428>.
- (161) Ern , B. H.; Stchakovsky, M.; Ozanam, F.; Chazalviel, J. Surface Composition of N-GaAs Cathodes during Hydrogen Evolution Characterized by In Situ Ultraviolet-Visible Ellipsometry and In Situ Infrared Spectroscopy. *J. Electrochem. Soc.* **1998**, *145* (2), 447–456.
- (162) Ostermayer Jr, F. W.; Kohl, P. A. Photoelectrochemical Etching of P-GaAs. *Appl. Phys. Lett.* **1981**, *39* (1), 76–78.
- (163) Pourbaix, M. Atlas of Electrochemical Equilibria in Aqueous Solution. *NACE* **1974**, *307*.
- (164) Menezes, S.; Heller, A.; Miller, B. Metal Filmed-Semiconductor Photoelectrochemical Cells. *J. Electrochem. Soc.* **1980**, *127* (6), 1268–1273.
- (165) Allongue, P.; Souteyrand, E.; Allemand, L. Charge Transfer Process at Illuminated Semiconductor/Electrolyte Junctions Modified by Electrodeposition of Microscopic Metal Grain. *J. Electrochem. Soc.* **1989**, *136* (4), 1027–1033.
- (166) Guijarro, N.; Pr vot, M. S.; Sivula, K. Surface Modification of Semiconductor Photoelectrodes. *Phys. Chem. Chem. Phys.* **2015**, *17* (24), 15655–15674.
- (167) Nakato, Y.; Ueda, K.; Yano, H.; Tsubomura, H. Effect of Microscopic Discontinuity of Metal Overlayers on the Photovoltages in Metal-Coated Semiconductor-Liquid Junction Photoelectrochemical Cells for Efficient Solar Energy Conversion. *J. Phys. Chem.* **1988**, *92* (8), 2316–2324.
- (168) Rossi, R. C.; Lewis, N. S. Investigation of the Size-Scaling Behavior of Spatially Nonuniform Barrier Height Contacts to Semiconductor Surfaces Using Ordered Nanometer-Scale Nickel Arrays on Silicon Electrodes. *J. Phys. Chem. B* **2001**, *105* (49), 12303–12318.
- (169) Tung, R. T. Electron Transport at Metal-Semiconductor Interfaces: General Theory. *Phys. Rev. B* **1992**, *45* (23), 13509.

- (170) Vanpaemel, J.; van der Veen, M. H.; De Gendt, S.; Vereecken, P. M. Enhanced Nucleation of Ni Nanoparticles on TiN through H₃BO₃-Mediated Growth Inhibition. *Electrochim. Acta* **2013**, *109*, 411–418.
- (171) Gamburg, Y. D.; Zangari, G. *Theory and Practice of Metal Electrodeposition*; Springer Science & Business Media, 2011.
- (172) Vanpaemel, J.; van der Veen, M. H.; De Gendt, S.; Vereecken, P. M. Enhanced Nucleation of Ni Nanoparticles on TiN through H₃BO₃-Mediated Growth Inhibition. *Electrochim. Acta* **2013**, *109*, 411–418. <https://doi.org/10.1016/j.electacta.2013.07.111>.
- (173) Beyers, R.; Kim, K. B.; Sinclair, R. Phase Equilibria in Metal-gallium-arsenic Systems: Thermodynamic Considerations for Metallization Materials. *J. Appl. Phys.* **1987**, *61* (6), 2195–2202.
- (174) Guérin, R.; Guivarc’h, A. Metallurgical Study of Ni/GaAs Contacts. I. Experimental Determination of the Solid Portion of the Ni-Ga-As Ternary-phase Diagram. *J. Appl. Phys.* **1989**, *66* (5), 2122–2128.
- (175) Grosvenor, A. P.; Biesinger, M. C.; Smart, R. S. C.; McIntyre, N. S. New Interpretations of XPS Spectra of Nickel Metal and Oxides. *Surf. Sci.* **2006**, *600* (9), 1771–1779.
- (176) Chigane, M.; Ishikawa, M. XRD and XPS Characterization of Electrochromic Nickel Oxide Thin Films Prepared by Electrolysis–Chemical Deposition. *J. Chem. Soc. Faraday Trans.* **1998**, *94* (24), 3665–3670.
- (177) Scheck, C.; Evans, P.; Zangari, G.; Schad, R. Sharp Ferromagnet/Semiconductor Interfaces by Electrodeposition of Ni Thin Films onto n-GaAs (001) Substrates. *Appl. Phys. Lett.* **2003**, *82* (17), 2853–2855.
- (178) Scheck, C.; Evans, P.; Schad, R.; Zangari, G.; Williams, J. R. Structure and Magnetic Properties of Electrodeposited Ni Films on N-GaAs (001). **2002**, *14* (001), 12329–12338.
- (179) Allemand, L.; Froment, M.; Maurin, G.; Souteyrand, E. Structure of Nickel Thin Films Electrodeposited on N-GaAs Single Crystals. *Microsc. Microanal. Microstruct.* **1992**, *3* (5), 401–413.
- (180) Attenborough, K.; De Boeck, J.; Celis, J.-P.; Mizuguchi, M.; Akinaga, H. Enhanced Kerr Rotation in

- Electrodeposited Nickel Films. *IEEE Trans. Magn.* **1999**, *35* (5), 2985–2987.
- (181) Scheck, C.; Evans, P.; Schad, R.; Zangari, G.; Williams, J.; Isaacs-Smith, T. F. Structure and Magnetic Properties of Electrodeposited Ni Films on N-GaAs(001). *J. Phys. Condens. Matter* **2002**, *14* (47), 12329. <https://doi.org/10.1088/0953-8984/14/47/308>.
- (182) Wang, X.; Liu, X.; Tong, C.-J.; Yuan, X.; Dong, W.; Lin, T.; Liu, L.-M.; Huang, F. An Electron Injection Promoted Highly Efficient Electrocatalyst of FeNi₃@GR@Fe-NiOOH for Oxygen Evolution and Rechargeable Metal–Air Batteries. *J. Mater. Chem. A* **2016**, *4* (20), 7762–7771.
- (183) Digdaya, I. A.; Adhyaksa, G. W. P.; Trzeźniewski, B. J.; Garnett, E. C.; Smith, W. A. Interfacial Engineering of Metal-Insulator-Semiconductor Junctions for Efficient and Stable Photoelectrochemical Water Oxidation. *Nat. Commun.* **2017**, *8*, 15968.
- (184) Gangasingh, D.; Talbot, J. B. Anomalous Electrodeposition of Nickel-Iron. *J. Electrochem. Soc.* **1991**, *138* (12), 3605–3611. <https://doi.org/10.1149/1.2085466>.
- (185) Subbaraman, R.; Tripkovic, D.; Chang, K.-C.; Strmcnik, D.; Paulikas, A. P.; Hirunsit, P.; Chan, M.; Greeley, J.; Stamenkovic, V.; Markovic, N. M. Trends in Activity for the Water Electrolyser Reactions on 3d M (Ni, Co, Fe, Mn) Hydr (Oxy) Oxide Catalysts. *Nat. Mater.* **2012**, *11* (6), 550.
- (186) Friebel, D.; Louie, M. W.; Bajdich, M.; Sanwald, K. E.; Cai, Y.; Wise, A. M.; Cheng, M.-J.; Sokaras, D.; Weng, T.-C.; Alonso-Mori, R. Identification of Highly Active Fe Sites in (Ni, Fe) OOH for Electrocatalytic Water Splitting. *J. Am. Chem. Soc.* **2015**, *137* (3), 1305–1313.
- (187) Tang, X.; Li, D. Sulfur-Doped Highly Ordered TiO₂ Nanotubular Arrays with Visible Light Response. *J. Phys. Chem. C* **2008**, *112* (14), 5405–5409.
- (188) Su, W.; Zhang, Y.; Li, Z.; Wu, L.; Wang, X.; Li, J.; Fu, X. Multivalency Iodine Doped TiO₂: Preparation, Characterization, Theoretical Studies, and Visible-Light Photocatalysis. *Langmuir* **2008**, *24* (7), 3422–3428.
- (189) Thirupathi, B.; Smirniotis, P. G. Co-Doping a Metal (Cr, Fe, Co, Ni, Cu, Zn, Ce, and Zr) on Mn/TiO₂ Catalyst and Its Effect on the Selective Reduction of NO with NH₃ at Low-Temperatures. *Appl. Catal. B Environ.* **2011**, *110*, 195–206.
- (190) Moehl, T.; Suh, J.; Sévery, L.; Wick-Joliat, R.; Tilley, S. D. Investigation of (Leaky) ALD TiO₂ Protection Layers for Water-Splitting Photoelectrodes. *ACS Appl. Mater. Interfaces* **2017**, *9* (50),

43614–43622.

- (191) Guo, Z.; Ambrosio, F.; Pasquarello, A. Hole Diffusion across Leaky Amorphous TiO₂ Coating Layers for Catalytic Water Splitting at Photoanodes. *J. Mater. Chem. A* **2018**, *6* (25), 11804–11810.
- (192) Hu, S.; Richter, M. H.; Lichterman, M. F.; Beardslee, J.; Mayer, T.; Brunschwig, B. S.; Lewis, N. S. Electrical, Photoelectrochemical, and Photoelectron Spectroscopic Investigation of the Interfacial Transport and Energetics of Amorphous TiO₂/Si Heterojunctions. *J. Phys. Chem. C* **2016**, *120* (6), 3117–3129.